

**ADVANCED CONTROL SCHEMES FOR WIND POWER
PLANTS AND RENEWABLE ENERGY-BASED ISLANDED
MICROGRIDS**

By

Md Nasmus Sakib Khan Shabbir

A thesis submitted to the

School of Graduate Studies

in partial fulfillment of the requirements for the degree of

Doctor of Philosophy

Faculty of Engineering and Applied Science

Memorial University of Newfoundland

June 2021

St. John's

Newfoundland and Labrador

Canada

Abstract

Renewable energy sources are increasingly integrated in power grids, creating significant challenges for control and system operation. Among various renewable energy sources, wind power is one of the dominant forms, mainly generated from large-scale transmission-connected wind power plants (WPPs). The grid-connected WPPs are required to follow grid codes to maintain a predefined power factor range under normal operation and supply required reactive power under faulty conditions. To meet grid code requirements, a WPP control architecture is developed in this thesis. The control system consists of a central WPP controller and a local wind turbine generator (WTG) controller, both operate in the voltage control mode. Therefore, the controller can respond faster and is robust to communication failures. Under normal operating conditions, the proposed controller regulates the WPP's operation within its steady-state reactive power capability and meets the power factor limits. Under faulty conditions, the controller forces the WPP to its maximum capability to contribute more reactive power support to the grid. Two mathematical models representing the steady-state and maximum reactive power capability of the WPP are developed through regression and analytic approaches, respectively.

In the second part of the thesis, a model predictive control (MPC)-based distributed generation (DG) controller is proposed to regulate the voltage and frequency at the point of common coupling (PCC) in an islanded microgrid. A data-driven input-output Box-Jenkins polynomial predictive model for DG control is developed using the Gauss-Newton-based nonlinear least square method with the prediction optimization focus. The model inputs are direct- and quadrature-axis components of the control signal, and the model outputs are deviations of the voltage and frequency from their nominal values at the PCC. The proposed MPC controller operates using the

PCC data and does not require the microgrid's central controllers or DG-to-DG communication networks. It can effectively compensate voltage and frequency deviations at the PCC and ensure proportional reactive power sharing among DGs without a secondary controller and a virtual impedance loop. The integrated Kalman filter in the MPC structure enables a robust controller design when subjected to impedance variations and measurement noises.

Acknowledgments

First and foremost, I would like to convey sincere gratitude and respect to my supervisor Dr. Xiaodong Liang for her persistent support, scientific guidance, and constructive discussions throughout the development of this thesis.

I would like to thank my co-supervisor, Dr. Syed Imtiaz, and my supervisory committee member, Dr. John Quaicoe, for their support and suggestions.

I profoundly appreciate the financial support from the Natural Science and Engineering Research Council of Canada (NSERC) Discovery Grant and the Graduate Fellowship from Memorial University of Newfoundland. I would also like to thank Memorial University of Newfoundland for various support provided during this research.

Finally, I wish to thank my family members for their continual mental support and encouragement.

Table of Contents

Abstract	ii
Acknowledgments	iv
Table of Contents	v
List of Tables	xv
List of Figures	xvii
List of Abbreviations	xxiv
List of symbols.....	xxvi
Chapter 1	1
Introduction.....	1
1.1 Introduction.....	1
1.2 Motivation.....	2
1.2.1 Advanced Control Schemes for Grid-Connected Wind Power Plants.....	2
1.2.2 Model Predictive Control for Distributed Generation in Islanded Microgrids	3
1.3 Thesis Outline	6
1.4 Research Objectives	9
References	11
Chapter 2	14
Literature Review.....	14

2.1 Wind Power Plant Voltage Control	14
2.1.1 Voltage Control Approaches for WPP	14
2.1.2 The Maximum Reactive Power Capability Curve	15
2.1.3 Controllers Developed Using the Maximum Reactive Power Capability Model	17
2.2 Microgrid Control	18
2.2.1 Droop Control in Islanded Microgrid	18
2.2.2 Controller Used in Droop Control	22
2.2.3 Model Predictive Controller in Microgrid Control	22
2.3 Summary	23
2.3.1 Voltage Control Approaches for Grid Connected Wind Power Plants	23
2.3.2 Control of Islanded Microgrids	24
References	25
Chapter 3	31
A Novel Data-Driven Voltage Control Approach for Grid-Connected Wind Power Plants	31
3.1 Introduction	33
3.2 The WPP Under Study	38
3.3 Accuracy Evaluation for Regression Models	43
3.3.1 Goodness of Fit Assessment	43
3.3.2 Robustness Algorithm	44
3.4 Regression Models Development	45

3.4.1 Required Reactive Power at the POI.....	45
3.4.2 Reactive Power Capability of WPP	49
3.5 Two Controllers Design	51
3.5.1 Central WPP Controller	54
3.5.2 Capacitor Controller.....	58
3.6 Case Studies	60
3.6.1 Case 1 – Base Model without Controllers	60
3.6.2 Case 2 - Normal Operation with Power Factor Control.....	61
3.6.3 Case 3 - Under Voltage	63
3.6.4 Case 4 - Over Voltage.....	65
3.6.5 Case 5 – A 50% Voltage Sag at The POI	67
3.7 Sensitivity Studies.....	68
3.7.1 Scenario 1 - The Length of Transmission Lines	69
3.7.2 Scenario 2 - Communication Delay	70
3.7.3 Scenario 3 - X/R Ratio of the Utility Grid.....	72
3.8 Conclusion	74
Appendix.....	75
References.....	76
Chapter 4.....	84
Analytical Approach-Based Reactive Power Capability Curve for DFIG Wind Power Plants....	84

4.1 Introduction	85
4.2 System Modeling	88
4.2.1 Mechanical System Model	88
4.2.2 Active Power Generation	90
4.2.3 Reactive Power Generation	90
4.2.4 Steady-State Equivalent Circuit	91
4.3 Limiting Factors for Individual DFIG	93
4.3.1 Stator Current Limit	93
4.3.2 Rotor Current Limit	94
4.3.3 Rotor Voltage Limit:	96
4.3.4 Winding Factor	96
4.3.5 Magnetic Saturation	99
4.3.6 Reactive Power Capability of GSC	100
4.4 Plant level limiting factors	102
4.4.1 Determination of Power Coefficient	102
4.4.2 Wake Effect	103
4.4.3 Losses in Distribution Feeders	106
4.5 Plant-Level Reactive Power Capability Model	107
4.6 Summary of The Proposed Method	109
4.7 Validation of the Proposed Models	112

4.7.1 Individual WTG level Reactive Power Capability	112
4.7.2 Plant Level Reactive Power Capability	114
4.8 Conclusion	118
References	119
Chapter 5	124
An Adaptive Droop Coefficient Based Voltage Control Approach for Wind Power Plants through Enhanced Reactive Power Support.....	124
5.1 Introduction.....	126
5.2 The Proposed Control Approach.....	130
5.3 The System Under Analysis and Its Maximum Reactive Power Capability Model.....	133
5.3.1 Description of the WPP Model	133
5.3.2 Plant-Level Reactive Power Capability Model.....	137
5.4 Working Principle of the Developed Controller	139
5.4.1 The Central WPP controller	139
5.4.2 The RSC Controller	141
5.4.3 The GSC Controller	142
5.5 Case Studies	143
5.5.1 Case 1 – Base Model without the Proposed Controllers.....	144
5.5.2 Case 2 - Normal Operating Voltage (the controller is to maintain power factor).....	145
5.5.3 Case 3 - Connection and Disconnection of a Large Inductive Load	146

5.5.4 Case 4 - A Small Voltage Sag.....	147
5.5.5 Case 5 - A Deep Voltage Sag.....	148
5.6 Sensitivity Study	150
5.6.1 Communication Failure.....	150
5.6.2 SCR of the Grid.....	151
5.6.3 Washout Filter in the Central WPP Controller	152
5.7 Conclusion	153
References	155
Chapter 6.....	158
A Distributed Generation Control Algorithm for Islanded Microgrids: Development and Parameterization	158
6.1 Introduction.....	160
6.2 The Proposed Approach.....	163
6.2.1 Mathematical Formulation for the Proposed Approach.....	163
6.2.2 Stepwise Development Procedure of the Proposed Approach.....	167
6.3 Fundamental Theory	170
6.3.1 Box-Jenkins Model	170
6.3.2 Mathematical Formulation of Non-linear Least Square	170
6.3.3 Optimization Algorithms	171
6.3.4 The Objective Function.....	174

6.3.4 Model Quality Matrices	174
6.4 The Test System.....	175
6.5 Performance Analysis	177
6.5.1 Input Delay Calculation	178
6.5.2 Model Order Selection	178
6.5.3 Initialization Technique	179
6.5.4 Optimization Algorithms	179
6.6 The Final GN-Based Box-Jenkins Model.....	182
6.6.1 Residual Analysis.....	182
6.6.2 The Final Box-Jenkins Model.....	184
6.7 Conclusion	185
References	187
Chapter 7	191
A Novel Data-Driven Predictive Model for Distributed Generation Control in Islanded Microgrids	191
7.1 Introduction.....	193
7.2 The Proposed Approach.....	196
7.2.1 Mathematical Formulation for the Proposed Model	196
7.2.2 Main Idea of the Proposed Approach	199
7.3 Fundamental Theory	202

7.3.1 Box-Jenkins Model	202
7.3.2 Mathematical Formulation of Non-linear Least Square	202
7.3.3 The Gauss-Newton Method	203
7.3.4 Impact of Optimization Focus.....	203
7.3.5 Model Quality Matrices	206
7.4 The Test System.....	207
7.5 Performance analysis	209
7.5.1 Initialization Technique	210
7.5.2 Optimization Focus	211
7.6 The Final GN-Based Box-Jenkins Model.....	219
7.7 Conclusion	221
References:	222
Chapter 8.....	226
A Novel Design of Model Predictive Control-Based Distributed Generation Controller in Islanded Microgrids.....	226
8.1 Introduction.....	228
8.2 The Proposed Approach.....	231
8.2.1 Mathematical Formulation for Proposed Control System	231
8.2.2 Stepwise Evolution of the Proposed Controller.....	234
8.3 Fundamental Theory	238

8.3.1 System Identification	239
8.3.2 MPC Controller.....	241
8.4 The GN-Based Box-Jenkins Model	246
8.5 The MPC-Based DG Controller Design	249
8.6 Case Studies	250
8.6.1 Case Study 1: Comparison with the Existing Methods.....	251
8.6.2 Case Study 2: Equal Power Sharing	253
8.6.3 Case Study 3: Proportional Power Sharing.....	254
8.6.4 Case Study 4: Performance with one added DG.....	255
8.7 Robustness Analysis	256
8.7.1 Distribution Line Impedance Variation	256
8.7.2 Communication Delay	258
8.7.3 Measurement Noise.....	259
8.8 Conclusion	260
References.....	262
Chapter 9	266
Conclusions and Future Work.....	266
9.1 Summary and Conclusions.....	266
9.2 Major Contributions of the Research Work.....	268
9.3 Future Work	269

List of Publications (Since Fall 2017)..... 270

List of Tables

Table 3. 1: Simulation Parameters for the DFIG Model, Cables and Transformers.....	42
Table 3. 2: Coefficients of poly31 models with 95% confidence Bound	48
Table 3. 3: Goodness of fit data of poly31 models	48
Table 3. 4: Errors between simulated and calculated data.....	48
Table 3. 5: Goodness of fit data of poly51 models	50
Table 3. 6: Coefficients of the poly 51 model with 95% confidence range.....	50
Table 3. 7: Errors Between the Calculation and Field Measurement Actual Data	51
Table 3. 8: Simulated and calculated data for required reactive power to Compensate Different voltage condition at POI when SCR is 5	75
Table 4. 1: DFIG Parameter	113
Table 4. 2: Distribution Feeder Parameter	115
Table 5. 1: Simulation Parameters for the WTG Model, Cables and Transformers.....	136
Table 6. 1: Test System's Parameters	176
Table 6. 2: Data Fitting Accuracy (%) for Different Initialization Techniques for the Four Optimization Algorithms (GN, AGN, LM and TRR).....	179
Table 6. 3: The Model's Performance Matrices	181
Table 7. 1: Test System's Parameters	208
Table 7. 2: Simulation Accuracy (%) for Different Initialization Techniques	210
Table 7. 3: The Model's Performance Matrices for Different Initialization Techniques	211
Table 7. 4: First Order Optimality for Different Initialization Techniques	212
Table 7. 5: The Model's Performance Matrices for Noisy Dataset	217

Table 8. 1: Test System's Parameters	246
Table 8. 2: MPC controller's Parameters	249

List of Figures

Fig. 3. 1. Electrical single line diagram of a WPP currently in operation in Newfoundland and Labrador, Canada.....	39
Fig. 3. 2. SCADA field measurement data at the 66 kV POI of the WPP on March 1-5, 2016: (a) voltage in kV; (b) active power in MW; (c) reactive power in MVar.	40
Fig. 3. 3. The single line diagram of the equivalent WPP for controller design.....	41
Fig. 3. 4. Simulation model to determine the required reactive power at the POI.....	46
Fig. 3. 5. Poly31 model using “Bisquare”: (a) Surface fitting diagram; (b) Residuals.....	49
Fig. 3. 6. The developed poly51 model through surface fitting using LAR algorithm based on SCADA field measurement data at POI: (a) Surface fitting diagram; (b) Residuals.	51
Fig. 3. 7. The overview control block diagrams including both controllers.	55
Fig. 3. 8. Flowchart of the proposed Central WPP controller.....	56
Fig. 3. 9. Flowchart of the proposed capacitor controller.....	59
Fig. 3. 10. Simulation results vs. SCADA field measurements for the base WPP model without controllers for the 27 MW WPP in NL, Canada (Case 1): (a) voltage at the POI, (b) active power supplied by WTG, (c) reactive power supplied by WTG.	61
Fig. 3. 11. Simulation results (Case 2): (a) voltage at POI, (b) reactive power supplied by WTG, (c) active power supplied by WTG, and (d) PF at POI.....	63
Fig. 3. 12. Simulation results (Case 3): (a) voltage at POI, (b) reactive power supplied by WTG, (c) active power supplied by WTG, and (d) PF at POI.....	65
Fig. 3. 13. Simulation results (Case 4): (a) voltage at POI, (b) reactive power supplied by WTG, (c) active power supplied by WTG, and (d) PF at POI.....	66

Fig. 3. 14. Simulation results (Case 5): (a) voltage at POI, (b) reactive power supplied by WTG, (c) active power supplied by WTG, and (d) PF at POI.....	68
Fig. 3. 15. Simulation results (Scenario 1): (a) voltage at POI, (b) reactive power supplied by WTG, (c) active power supplied by WTG, and (d) PF at POI.....	70
Fig. 3. 16. Simulation results (Scenario 2): (a) voltage at POI, (b) reactive power supplied by WTG, (c) active power supplied by the WTG and (d) PF at POI.....	72
Fig. 3. 17. Simulation results (Scenario 3): (a) voltage at POI, (b) reactive power supplied by WTG, (c) active power supplied by WTG, and (d) PF at POI.....	73
Fig. 4. 1. Wind-Power characteristic curve of WTGs.....	89
Fig. 4. 2. Active power sharing between the stator and the RSC.....	91
Fig. 4. 3. The steady-state equivalent circuit of DFIGs referred to the stator.....	92
Fig. 4. 4. Reactive power capability of a DFIG considering stator current limit.....	93
Fig. 4. 5. Phasor diagrams of a DFIG [28].....	94
Fig. 4. 6. Rotor current in two modes of operations.	95
Fig. 4. 7. Effect of rotor current limit on reactive power capability of a DFIG.....	95
Fig. 4. 8. Effect of winding factor on reactive power capability of a DFIG: (a) overall capability; (b) the zoomed-in overexcited mode capability.....	98
Fig. 4. 9. Effect of magnetic saturation on reactive power capability of a DFIG.	100
Fig. 4. 10. Single-phase steady-state equivalent circuit of the GSC.....	101
Fig. 4. 11. Reactive power capability of a WTG.	102
Fig. 4. 12. Shadow cone of a WTG.....	103
Fig. 4. 13. Change of wind speed due to wake effect.	105
Fig. 4. 14. PI section distribution line.	106

Fig. 4. 15. Flow chart of the proposed method.	110
Fig. 4. 16. Comparison of reactive power capability of a DFIG: (a) overall capability; (b) the zoomed-in overexcited mode capability.	114
Fig. 4. 17. Single line diagram of WPP1.	116
Fig. 4. 18. Single line diagram of WPP2.	116
Fig. 4. 19. Comparison of reactive power capability: (a) WPP1; (b) WPP 2.	117
Fig. 5. 1. The flow chart of the proposed control approach.	132
Fig. 5. 2. The electrical single-line diagram of an actual WPP currently in operation in Newfoundland, Canada.	134
Fig. 5. 3. The active power generation of the WPP: (a) simulation model; and (b) SCADA field measurements.	135
Fig. 5. 4. The schematic diagram of the WPP simulation model.	136
Fig. 5. 5. The schematic diagram of the proposed central WPP controller.	140
Fig. 5. 6. The schematic diagram of the proposed power factor controller.	140
Fig. 5. 7. The schematic diagram of the proposed RSC controller.	142
Fig. 5. 8. The schematic diagram of the proposed GSC controller.	143
Fig. 5. 9. Simulation results vs. SCADA field measurements for the WPP's base model without the proposed controllers for the 27 MW WPP in Newfoundland, Canada: (a) active power supplied by WTG, (b) reactive power supplied by WTG, and (c) the voltage at the POI (Case 1).	144
Fig. 5. 10. Simulation results: (a) the voltage at the POI, (b) reactive power supplied by WTG, (c) active power supplied by WTG, and (d) power factor at the POI (Case 2).	146
Fig. 5. 11. Simulation results: (a) the voltage at the POI, (b) reactive power supplied by WTG, (c) active power supplied by WTG, and (d) I_{qGSC} (Case 3).	147

Fig. 5. 12. Simulation results: (a) the voltage at the POI, (b) reactive power supplied by WTG, (c) active power supplied by WTG, and (d) I_{qGSC} (Case 4).....	148
Fig. 5. 13. Simulation results: (a) the voltage at the POI, (b) reactive power supplied by WTG, (c) active power supplied by WTG, and (d) I_{qGSC} (Case 5).....	149
Fig. 5. 14. Simulation results: (a) the voltage at the POI, (b) reactive power supplied by WTG, (c) active power supplied by WTG, and (d) I_{qGSC}	151
Fig. 5. 15. Simulation results: (a) the voltage at the POI, (b) reactive power supplied by WTG, (c) active power supplied by WTG, and (d) I_{qGSC}	152
Fig. 5. 16. Simulation results: (a) the voltage at the POI, (b) reactive power supplied by WTG, (c) active power supplied by WTG, and (d) I_{qGSC}	153
Fig. 6. 1. The microgrid with a DG interfacing inverter.....	163
Fig. 6. 2. The flow chart of the proposed approach.	169
Fig. 6. 3. The test system simulation model.....	175
Fig. 6. 4. Input-output data: (a) the deviation of the voltage from the nominal value in pu, ΔV , (b) the deviation of the frequency from the nominal value in pu, Δf ; (c) the d-axis control signal, U_d , and (d) the q-axis control signal, U_q	177
Fig. 6. 5. The fitted models for four optimization algorithms along with their fitting accuracies for the training dataset: (a) $DelV$; (b) $DelF$	180
Fig. 6. 6. The fitted models for four optimization algorithms along with their fitting accuracies for the validation dataset: (a) $DelV$; (b) $DelF$	181
Fig. 6. 7. The residual plot of the final BJ model.	183
Fig. 6. 8. The cross-correlation readings for the final BJ model.....	183

Fig. 6. 9. Step response of the model along with the 3rd confidence bound: (a) Ud vs DelV; (b) Uq vs DelV; (c) Ud vs DelF; and (d) Uq vs DelF.	185
Fig. 7. 1. A microgrid with a DG's interfacing inverter.	196
Fig. 7. 2. Flow chart of the proposed approach.....	200
Fig. 7. 3. The test system's simulation model.....	207
Fig. 7. 4. Input-output data: (a) deviation of the voltage from the nominal value in pu, ΔV , (b) deviation of the frequency from the nominal value in pu, Δf ; (c) the d-axis control signal, Ud , and (d) the q-axis control signal, Uq	209
Fig. 7. 5. Initial states: (a) prediction focus; and (b) simulation focus.	211
Fig. 7. 6. Iteration wise variation of expected and achieved improvements: (a) DelV (prediction); (b) DelF (prediction); (c) DelV (simulation); (d) DelF (simulation); Iteration wise variation of step sizes: (e) DelV (prediction); (f) DelF (prediction); (g) DelV (simulation); and (h) DelF (simulation)	214
Fig. 7. 7. Fitted models for different optimization focus along with their fitting accuracies for noiseless training data: (a) DelV; (b) DelF.	214
Fig. 7. 8. Auto- and cross-correlation for the two optimization focus: (a) prediction focus; (b) simulation focus.	215
Fig. 7. 9. Fitted models for different optimization focus along with their fitting accuracies for noiseless validation data: (a) DelV; (b) DelF.	215
Fig. 7. 10. White Gaussian noise: (a) noise added to the ΔV data; and (b) noise added to the Δf data.....	217
Fig. 7. 11. Fitted models for different optimization focus along with their fitting accuracies for noisy training data: (a) DelV; (b) DelF.....	218

Fig. 7. 12. Auto- and cross-correlation for the two optimization focus: (a) prediction focus; (b) simulation focus.....	218
Fig. 7. 13. Fitted models for different optimization focus along with their fitting accuracies for noisy validation data: (a) DelV; (b) DelF.	219
Fig. 7. 14. Step responses of the model along with their 3rd confidence bound: (a) Ud vs DelV; (b) Uq vs DelV; (c) Ud vs DelF; and (d) Uq vs DelF.	220
Fig. 7. 15. One-step ahead prediction: (a) prediction fitting; (b) prediction error	221
Fig. 8. 1. A microgrid with an interfaced inverter system.	232
Fig. 8. 2. Flow chart of the proposed controller design.	236
Fig. 8. 3. Schematic diagram of the test system simulation model.....	237
Fig. 8. 4. The fitted model along with their fitting accuracies for different datasets: (a) training dataset; and (b) validation dataset.....	248
Fig. 8. 5. Change of plant state with line impedances.	250
Fig. 8. 6. The single line diagram of the test microgrid configuration.	251
Fig. 8. 7. Performance comparison of the proposed and two existing controllers; (a) PCC voltage in pu; (b) reactive power supplied by DGs in Var; (c) PCC frequency in pu; (d) active power supplied by DGs in W (Case Study 1).....	252
Fig. 8. 8. Controller performance: (a) PCC voltage deviation from the nominal in pu; (b) PCC voltage in pu; (c) Reactive power supplied by DGs in Var; (d) d-axis component of the control signal; (e) PCC frequency deviation from the nominal in pu; (f) PCC frequency in pu; (g) active power supplied by DGs in w; (h) q-axis component of the control signal (Case Study 2).	253
Fig. 8. 9. Controller performance: (a) PCC voltage deviation from the nominal in pu; (b) PCC voltage in pu; (c) Reactive power supplied by DGs in Var; (d) d-axis component of the control	

signal; (e) PCC frequency deviation from the nominal in pu; (f) PCC frequency in pu; (g) active power supplied by DGs in w; (h) q-axis component of the control signal (Case Study 3). 254

Fig. 8. 10. Controller performance: (a) PCC voltage deviation from the nominal in pu; (b) PCC voltage in pu; (c) Reactive power supplied by DGs in Var; (d) d-axis component of the control signal; (e) PCC frequency deviation from the nominal in pu; (f) PCC frequency in pu; (g) active power supplied by DGs in w; (h) q-axis component of the control signal (Case Study 4). 255

Fig. 8. 11. The proposed controller for uniform impedance variation of Line 1 and Line 2; (a) PCC voltage in pu; (b) Reactive power supplied by DGs in Var; (c) PCC frequency in pu; (d) active power supplied by DGs in W..... 257

Fig. 8. 12. The proposed controller for un-uniform impedance variation of Line 1 and Line 2; (a) PCC voltage in pu; (b) Reactive power supplied by DGs in Var; (c) PCC frequency in pu; (d) active power supplied by DGs in W. 258

Fig. 8. 13. The proposed controller for different communication delays; (a) PCC voltage in pu; (b) Reactive power supplied by DGs in Var; (c) PCC frequency in pu; (d) active power supplied by DGs in W. 259

Fig. 8. 14. The proposed controller with unfiltered measurement noises; (a) PCC voltage in pu; (b) Noisy deviation of voltage data, ΔV in pu; (c) Reactive power supplied by DGs in Var; (d) PCC frequency in pu; (e) Noisy deviation of frequency data, ΔF in pu; and (f) active power supplied by DGs in W. 260

List of Abbreviations

GHG	Greenhouse Gas
SDG	Sustainable Development Goal
RES	Renewable Energy Sources
DG	Distributed Generation
MPC	Model Predictive Control
WPP	Wind power plant
DFIG	Doubly-Fed Induction Generator
PMSG	Permanent Magnet Synchronous Generator
SCR	Short Circuit Ratio
SCADA	Supervisory control and data acquisition
TSK	Takagi–Sugeno–Kang
SSE	Sum Of Squares Due To Error
RMSE	Root-Mean-Squared Error
PI	Proportional Integral
MIMO	Multi-Input Multi-Output
SISO	Single-Input Single-Output
CPU	Central Processing Unit
GPU	Graphics Processing Unit
WTG	Wind Turbine Generator
IEEE	Institute of Electrical and Electronics Engineers
PCC	Point of Common Coupling
POI	Point Of Interconnection
SVC	Static Var Compensator
SG	Synchronous Generator
RSC	Rotor Side Converter

GSC	Grid Side Converter
DES	Distributed Energy Storage
NLS	Nonlinear Least Square
BJ	Box-Jenkins
GN	Gauss-Newton
AGN	Adaptive Gauss-Newton
LM	Levenberg-Marquardt
TRR	Trust Region Reflective

List of symbols

P	Active Power
Q	Reactive Power
S	Complex Power
f	Frequency
R	Distribution Line Resistance
X	Distribution Line Reactance
P_{mech}	Developed Mechanical Power by A WTG
C_p	Power Coefficient of the Wind Turbine
ρ	Air Density
v_{wind}	Wind Speed
v_{wake}	Wake Wind Speed
P_s	Active Power of the Stator
P_r	Active Power of the Rotor
V_s	Stator Voltage Per Phase
V_m	Magnetizing Voltage
V_{GSC}	Voltage Per Phase at the GSC
I_s	Stator Current
I_{fe}	Magnetizing Current
I_m	Iron Loss Current
R_s	Stator Resistance
$L_{\sigma s}$	Stator Leakage Inductance

$I_{s_{active}}$	Real Component of the Stator Current
V_r	Rotor Voltage
I_r	Rotor Current
R_r	Rotor Resistance
$L_{\sigma r}$	Rotor Leakage Inductance
V_{DC}	DC Link Voltage of the Back-to-Back Converter
K_s	Stator Winding Factor
K_r	Rotor Winding Factor
ψ_m	Mutual Flux
Q_{DFIG}	Reactive Power of the Stator
Q_r	Reactive Power of the Rotor
Q_{GSC}	Reactive Power of the GSC
Q_{WTG}	Reactive Power Capability of A WTG
$P_{RSC_{cond,switch}}$	Summed Conduction and Switching Losses for the RSC
$P_{GSC_{cond,switch}}$	Summed Conduction and Switching Losses for the GSC
δ	Power Angle
U_d	Direct Axis Control Signal
U_q	Quadrature Axis Control Signal
Δf	Deviation of Frequency
ΔV	Deviation of Voltage
m	Observed Data Points
θ	Estimated Model Coefficient
n	Number of Unknown Model Coefficients

$V(\theta)$	Objective Function
$r(t, \theta)$	Residual Function
$y_m(t)$	Measured Output
$y_s(t, \theta)$	The Simulated Response of the Model
p_k^{GN}	Search Direction of GN Method
p_k^{LM}	Search Direction of LM Method
α_k^{GN}	Step Size of GN Method
J	Jacobian Matrix
I	Unity Vector
g	Gradient Matrix
H	Hessian Matrix
D	Diagonal Scaling Matrices
$\ \ \ $	2-Norm

Note: Other symbols that are not mentioned in this list are defined in the text.

Chapter 1

Introduction

1.1 Introduction

Fossil fuel-based power generation causes nearly 75% of the total CO₂ emissions in the world [1], which leads to Greenhouse Gas (GHG) emissions and climate change. The United Nations is urging every nation in the world to comply with Sustainable Development Goals (SDGs) [2]. To slow down climate change, renewable energy sources are recommended to meet energy demands and reduce the per capita consumption. Many countries have complied with SDGs by framing a structure of adopting renewable energy sources (RES). RES is commonly utilized in two ways: one way is large-scale RES power plants, such as wind power plants, connected to power grids; and another way is multiple small capacity distributed RES, which can form a microgrid and operate in grid-connected and island modes.

Among the large-scale RES, wind power is a fast-growing technology and its deployment increases rapidly worldwide [3]. To reduce the dependency of modern power grids on fossil fuel-based power generation and accelerate the transformation towards renewable energy-based sustainable power generation, advanced control techniques for wind power plants and renewable energy-based microgrids are essential. Therefore, the research conducted in this thesis includes two parts: part 1 focuses on advanced control schemes developed for large wind power plants; part 2 focuses on Model Predictive Control (MPC) developed for renewable energy-based distributed generation (DG) units in islanded microgrids.

1.2 Motivation

1.2.1 Advanced Control Schemes for Grid-Connected Wind Power Plants

Wind power as a dominant form of renewable energy source plays a vital role in the modern mixed energy landscape [4]. Wind power plants (WPPs) are usually grid-connected and contribute both active and reactive power. The active power generation from wind turbine generators (WTGs) is defined by the wind speed, and pitch angle control; while through power electronic converters, the control of reactive power can be decoupled from the active power generation, and reactive power can be generated to the WTG's maximum residual limit with appropriate control actions. Adequate reactive power reserve of WPPs is critical to meet grid code requirements, handle steady-state and transient uncertainties, and maintain stability and power quality of the system. Among existing wind power technologies, only doubly-fed induction generator (DFIG) and permanent magnet synchronous generator (PMSG)-based wind turbines have the ability to supply reactive power to the grid [5]. Because of the intermittent nature of wind, significant penetration of wind power generation in the grid may lead to severe stability and power quality issues due to lack of ancillary services that are usually provided by conventional synchronous generators (SGs) [6]. To resolve these issues, many countries have enforced grid codes for WPPs [7]. Grid codes require that WPPs should have sufficient reactive power reserve; following a grid disturbance, a WPP must inject reactive power to the grid as rapidly as possible instead of tripping off. Meeting such requirements can compensate voltage sags and enhance voltage stability of the system [8]. Research has been conducted to ensure the maximum reactive power contribution following a fault [9], [10], and Ref [11] recommends that a WPP should have sufficient reserve to exchange reactive power under steady-state operation. Therefore, an accurate approximation of the maximum

reactive power capability of the WPP and a WPP controller competent to utilize this maximum reactive power capacity is crucial.

1.2.2 Model Predictive Control for Distributed Generation in Islanded Microgrids

Recently, decentralized energy generation has gained more popularity in the energy sector. Autonomous energy supply systems are diversely used in a variety of applications, ranging from emergency backup systems in hospitals to rural telecom tower stations, military applications, and powering off-grid islands. Due to the steady increase in fossil fuel prices and the simultaneous rise of energy demand in rural areas, the need for sustainable energy systems is rising. Consequently, a trend towards hybrid energy supply solutions, such as renewable energy-based microgrids, can be observed to reduce operating expenses.

Due to the integration of renewable energy sources in power grids, microgrids become a fundamental element in future smart grids enabling bidirectional power flow and advanced control for DG units and the load within them. A microgrid can operate in grid-connected or island mode: in grid-connected mode, the voltage and frequency are governed by the grid, and the function of the DG's controller is to perform power control; in island mode, the voltage and frequency are regulated by the DG's controller, dispatching necessary real and reactive power from DG units within the microgrid, if not successful, load shedding might occur.

The existing DG control techniques mostly adopt droop control to regulate the voltage and frequency by dispatching necessary active power [12]. Existing droop control algorithms are developed either for highly inductive or resistive distribution system [13], [14]. A control algorithm developed for highly inductive system, completely ignores the resistive parameters, and their subsequent impact and vice versa. In addition, inside the control architecture, impact of line parameters between the control and controlled variables are not considered. Although low voltage

microgrid are highly resistive [14], in practice, the impact of inductance should not be ignored. As a result, DG controllers developed from droop algorithms, suffer from steady-state errors in voltage and frequency, and cannot share reactive power accurately among DGs if feeder impedances are mismatched. To solve the challenges, conventional droop control is improved with secondary controller and virtual impedance loop [12], [15]. Although the improved droop control overcome the challenges, the size and complexity of the controller is substantially increased.

Existing DG control algorithms are usually applied in Proportional Integral (PI)-based controllers. PI-based controllers are low in price and easy to handle. However, the main drawback of PI-based controllers is that it cannot handle coupled relationship. Low voltage microgrids exhibit a coupled relationship between active and reactive power [16]. For ease of control and to implement it in PI-based controller, existing droop control architectures decouple the active and reactive power control and segmented the multi-input multi-output (MIMO) control structure into several single-input single-output (SISO) system. This increases the number of tunable parameters of the control structure. It requires continuous retuning of the controller due to the topological change of a microgrid, aging of DGs, and other real time dynamics encountered by the controller during operation [17]. With additional tuning parameters, retuning process become sophisticated and it requires delicate process with expert supervision [17]. Hardware based implementation of PI controller makes it harder. A microgrid is a weak network in nature, to automate its operation, an intelligent controller is required that can predict impacts of its current actions and adapt accordingly. PI controllers are completely lacks in such quality.

Therefore, a comprehensive DG control algorithm considering all influential parameters is necessary to develop. Unlike droop method, both inductance and resistance of the distribution line

and their relative impacts should be considered. This will keep active and reactive power coupled, which can be solved by adopting advanced intelligent controllers.

Model predictive control (MPC) is an advanced controller that uses a system model to predict the future response of the system because of its control actions within a predefined prediction horizon. The adopted system model used in MPC, can be coupled or decoupled MIMO or SISO model and should portray the relationship between control variables and controlled parameters. MPC solves the system model and set optimum trajectory for control parameters so that the system's stability and robustness can be ensured. Unlike other intelligent controllers, where the control moves are optimized and applied for the whole horizon, irrespective of the system response, MPC optimizes in a receding time window. Therefore, adaptive solutions depend on the system response, which enables the MPC to withstand a wide range of system uncertainty. The state observer used in MPC updates the system model in every control interval, therefore, MPC can track the changes of system dynamics and maintain the robust performance even though the system equilibrium is drifting away from the design point. Hence, MPC has the potential to fully automate the microgrid's operation, which is particularly important for remote communities, where continuous supervision from technical personnel is hard to maintain. Recent advancement in computer hardware further stimulates the MPC through parallel computing in CPU and GPU arena, which resolves the constraints resulted from excessive computational requirements of the MPC, as a result, MPC gains interest in airline, automotive and power system, where faster response is required. MPC along with an improved DG control algorithm can downsize the overall volume of DG controllers by directly handling the MIMO structure to achieve robust and reliable control. As a computer-based controller, updating or retuning due to topological change or aging become easier for MPC.

1.3 Thesis Outline

This manuscript-based thesis comprises six manuscripts. Two manuscripts have already been published and three have been submitted and are currently under review. One manuscript is in preparation and is yet to be submitted.

Chapter 1

In Chapter 1, the importance of the research topic and background information are introduced; and objectives of the research are provided.

Chapter 2

In Chapter 2, literature review is conducted for advanced control schemes for grid-connected wind power plants and distributed generation controllers in islanded microgrid.

Chapter 3

In Chapter 3, a data-driven voltage control approach is proposed for a grid-connected WPP. Two regression models are developed through surface fitting using MATLAB curve fitting toolbox: one model based on simulation data is to determine the required reactive power for grid voltage compensation; another model based on field measurement data is to determine the reactive power characteristics of the WPP. The reactive power compensation device is capacitors in this study. Two controllers, a central WPP controller and a capacitor controller, are designed, and their effectiveness is validated through several case and sensitivity studies. A version of this chapter has been published in IEEE Transactions on Industry Applications, July/August 2019 regular issue.

Chapter 4

In Chapter 4, an analytical approach to determine the reactive power capability of an individual doubly-fed induction generator (DFIG)-based wind turbine generators (WTGs) as well as plant level WPPs is proposed by considering several constraint variables. For ease of use, the proposed

approach is developed based on the well-known standard parameters, and individual WTGs reactive power capability model is validated by comparing with two existing methods whereas plant level capability model is validated by comparing with Supervisory Control and Data Acquisition (SCADA) field measurement data of two WPPs currently operating in Newfoundland, Canada. A version of this chapter has been published in Proceedings of 2020 IEEE Industry Applications Society Annual Meeting.

Chapter 5

In Chapter 5, to maximize the reactive power support from a wind power plant (WPP) and maintain the power factor at the point of interconnection (POI) within the acceptable limits, an adaptive droop coefficient-based WPP controller is proposed. The controller consists of a central WPP controller and a local wind turbine generator (WTG) controller. An integrated power factor controller enables the central WPP controller to regulate the power factor at the POI under normal operation. An updated droop coefficient model considering the depth of voltage deviation and the range of reactive power capability enables the controller to push the WTG more towards its maximum limit. To ensure faster and robust operation, both the central WPP controller and local WTG controllers are operated in voltage control mode. Additional reactive power is exported from the grid side converter (GSC) through a developed GSC controller. A version of this chapter is to be submitted for review.

Chapter 6

In Chapter 6, to regulate the voltage and frequency of an islanded microgrid, a novel control algorithm for Distributed Generation (DG) units is developed, where deviations of the voltage and frequency from their nominal values at the Point of Common Coupling (PCC) are correlated with direct- and quadrature-axis components of the control signal. It incorporates distribution line

parameters into the control algorithm and enables simultaneous P - f / Q - V and P - V / Q - f control. The proposed control algorithm eliminates the secondary controller and the virtual impedance loop from the DG controller, and substantially reduce the controller size and complexity. The polynomial input-output Box-Jenkins model is chosen as the model structure for the control algorithm, which is parameterized through data-driven system identification approach using Nonlinear Least Square (NLS) method. To initialize the parametric optimization, the Backcast technique is chosen after evaluating three initialization techniques (Zero, Estimate and Backcast). Four NLS optimization methods (Gauss-Newton (GN), Adaptive Gauss-Newton (AGN), Levenberg-Marquardt (LM), and Trust Region Reflective (TRR)) are considered and their performance in developing the model are evaluated for both training and validation datasets. GN shows consistent and superior performance over the others and is chosen as the suitable optimization technique in this study. A version of this chapter is to be submitted for review.

Chapter 7

In Chapter 7, a data-driven input-output Box-Jenkins polynomial predictive model for a Distributed Generation (DG) control in an islanded microgrid is developed using the Gauss-Newton-based nonlinear least square method to regulate the voltage and frequency at the Point of Common Coupling (PCC). The model inputs are direct- and quadrature-axis components of the control signal, and the model outputs are deviations of the voltage and frequency from their nominal values at the PCC. To initialize the iteration for nonlinear least square, the Backcast technique is chosen by comparing with Zero and Estimate techniques. Two optimization methodologies are evaluated: “simulation” focus and “prediction” focus. The prediction focus shows much better performance, such as a high prediction accuracy and faster convergence; it also avoids the necessity of data prefiltering by introducing a built-in weighted filter in the objective

function. The developed model is validated using noisy and noiseless datasets. A version of this chapter is to be submitted for review.

Chapter 8

In Chapter 8, to regulate the voltage and frequency at the Point of Common Coupling (PCC) in an islanded microgrid, a novel model predictive control (MPC)-based distributed generation (DG) controller is proposed. A data-driven predictive model that directly correlates deviations of the voltage and frequency at the PCC with direct- and quadrature-axis components of the control signal is used as MPC's plant model. This predictive model is developed using Gauss-Newton-based non-linear least-square approach with the prediction optimization focus. The proposed MPC controller operates using the PCC data and does not require microgrid's central controllers or DG-to-DG communication networks. It can effectively compensate voltage and frequency deviations at the PCC and ensure proportional power sharing among DGs without a secondary controller and a virtual impedance loop. The integrated Kalman filter in the MPC structure makes the controller robust to impedance variations and measurement noises. Effectiveness and robustness of the proposed MPC controller are validated through case studies and the robustness analysis. A version of this chapter is to be submitted for review.

Chapter 9

In Chapter 9, research outcomes are summarized, and future work is recommended.

1.4 Research Objectives

The main research objectives can be divided into two parts: part 1 is for grid-connected wind power plant control; part 2 is for DG control in islanded microgrids.

In part 1, the main objective is to develop advanced control schemes for wind power plants, which can be divided into several tasks as follows:

1. Develop a central WPP controller that ensures the maximum injection of reactive power to the grid during grid faults and regulates the reactive power injection from the WPP according to grid codes under normal operation. The WPP controller also ensures faster dispatch of reactive power to stabilize voltage deviations and protects individual DFIG within the WPP from overloading.
2. To assist the central WPP controller for reactive power compensation, develop a mathematical model that determines the required reactive power to compensate voltage deviations at the POI.

In part 2, the main objective is to develop a MPC-based DG controller to regulate voltage and frequency at the PCC in an islanded microgrid as follows:

1. Develop a DG control algorithm that directly correlates the deviation of voltage and frequency with the control signal. The model considers both resistance and reactance of the distribution line and their subsequent impacts.
2. Determine the most suitable initialization technique, optimization method and optimization focus to parameterize the developed control algorithm through data-driven system identification approach using nonlinear least square method.
3. To regulate voltage and frequency at the PCC of an islanded microgrid, develop a DG controller using the developed control algorithm and a model predictive controller (MPC).

References

- [1] S. Manish, I. R. Pillai, and R. Banerjee, “Sustainability analysis of renewables for climate change mitigation,” *Energy Sustain. Dev.*, vol. 10, no. 4, pp. 25–36, 2006.
- [2] R. M. Elavarasan *et al.*, “A Comprehensive Review on Renewable Energy Development, Challenges, and Policies of Leading Indian States With an International Perspective,” *IEEE Access*, vol. 8, pp. 74432–74457, 2020, doi: 10.1109/ACCESS.2020.2988011.
- [3] L. Ye *et al.*, “Hierarchical Model Predictive Control Strategy Based on Dynamic Active Power Dispatch for Wind Power Cluster Integration,” *IEEE Trans. Power Syst.*, vol. 34, no. 6, pp. 4617–4629, Nov. 2019, doi: 10.1109/TPWRS.2019.2914277.
- [4] H. Falaghi, M. Ramezani, C. Singh, and M. Haghifam, “Probabilistic Assessment of TTC in Power Systems Including Wind Power Generation,” *IEEE Syst. J.*, vol. 6, no. 1, pp. 181–190, Mar. 2012, doi: 10.1109/JSYST.2011.2163029.
- [5] A. M. Khalil and R. Iravani, “Enhanced Generic Nonlinear and Linearized Models of Wind Power Plants,” *IEEE Trans. Power Syst.*, vol. 32, no. 5, pp. 3968–3980, Sep. 2017, doi: 10.1109/TPWRS.2017.2654346.
- [6] J. Kim, E. Muljadi, J. Park, and Y. C. Kang, “Flexible IQ–V Scheme of a DFIG for Rapid Voltage Regulation of a Wind Power Plant,” *IEEE Trans. Ind. Electron.*, vol. 64, no. 11, pp. 8832–8842, Nov. 2017, doi: 10.1109/TIE.2017.2694408.
- [7] M. Tsili and S. Papathanassiou, “A review of grid code technical requirements for wind farms,” *IET Renew. Power Gener.*, vol. 3, no. 3, pp. 308–332, Sep. 2009, doi: 10.1049/iet-rpg.2008.0070.

- [8] H. Karbouj and Z. H. Rather, “Voltage Control Ancillary Service From Wind Power Plant,” *IEEE Trans. Sustain. Energy*, vol. 10, no. 2, pp. 759–767, Apr. 2019, doi: 10.1109/TSTE.2018.2846696.
- [9] D. Zhou and F. Blaabjerg, “Optimized Demagnetizing Control of DFIG Power Converter for Reduced Thermal Stress During Symmetrical Grid Fault,” *IEEE Trans. Power Electron.*, vol. 33, no. 12, pp. 10326–10340, Dec. 2018, doi: 10.1109/TPEL.2018.2803125.
- [10] D. Zheng, X. Xiong, J. Ouyang, Z. Zhang, and C. Xiao, “Control Method for Maximizing Fault Voltage of Wind Generation-Integrated Power Systems With Consideration of DFIG–Grid Coupling,” *IEEE Access*, vol. 7, pp. 894–905, 2019, doi: 10.1109/ACCESS.2018.2885988.
- [11] J. Ouyang, M. Li, Z. Zhang, and T. Tang, “Multi-Timescale Active and Reactive Power-Coordinated Control of Large-Scale Wind Integrated Power System for Severe Wind Speed Fluctuation,” *IEEE Access*, vol. 7, pp. 51201–51210, 2019, doi: 10.1109/ACCESS.2019.2911587.
- [12] B. Liu, Z. Liu, J. Liu, R. An, H. Zheng, and Y. Shi, “An Adaptive Virtual Impedance Control Scheme Based on Small-AC-Signal Injection for Unbalanced and Harmonic Power Sharing in Islanded Microgrids,” *IEEE Trans. Power Electron.*, vol. 34, no. 12, pp. 12333–12355, Dec. 2019, doi: 10.1109/TPEL.2019.2905588.
- [13] R. An, Z. Liu, and J. Liu, “Successive-Approximation-Based Virtual Impedance Tuning Method for Accurate Reactive Power Sharing in Islanded Microgrids,” *IEEE Trans. Power Electron.*, vol. 36, no. 1, pp. 87–102, Jan. 2021, doi: 10.1109/TPEL.2020.3001037.
- [14] J. Chen, D. Yue, C. Dou, L. Chen, S. Weng, and Y. Li, “A Virtual Complex Impedance Based V -Droop Method for Parallel-Connected Inverters in Low-Voltage AC Microgrids,”

IEEE Trans. Ind. Inform., vol. 17, no. 3, pp. 1763–1773, Mar. 2021, doi: 10.1109/TII.2020.2997054.

[15] X. Liang, C. Andalib-Bin-Karim, W. Li, M. Mitolo, and M. N. S. K. Shabbir, “Adaptive Virtual Impedance-Based Reactive Power Sharing in Virtual Synchronous Generator Controlled Microgrids,” *IEEE Trans. Ind. Appl.*, vol. 57, no. 1, pp. 46–60, Jan. 2021, doi: 10.1109/TIA.2020.3039223.

[16] C. Dou, Z. Zhang, D. Yue, and M. Song, “Improved droop control based on virtual impedance and virtual power source in low-voltage microgrid,” *IET Gener. Transm. Distrib.*, vol. 11, no. 4, pp. 1046–1054, 2017, doi: 10.1049/iet-gtd.2016.1492.

[17] L. Wang, Y. Qin, Z. Tang, and P. Zhang, “Software-Defined Microgrid Control: The Genesis of Decoupled Cyber-Physical Microgrids,” *IEEE Open Access J. Power Energy*, vol. 7, pp. 173–182, 2020, doi: 10.1109/OAJPE.2020.2997665.

Chapter 2

Literature Review

2.1 Wind Power Plant Voltage Control

For effective contribution to the voltage compensation by the WPP, accurate realization of the plant level reactive power reserve and its maximum dispatch during contingency through appropriate control architecture is crucial. To overcome technological limitations in estimating and extracting the maximum reactive power from a WPP, additional reactive power compensation equipment, such as capacitor banks and static var compensators (SVCs), is installed in WPPs. Although such secondary reactive power compensation equipment has increased reactive power competency of WPPs, dynamic synchronization between the WPP and such equipment is hard to achieve, which may cause voltage overshoot and cascaded tripping-off [1]. Therefore, to reduce the dependency on reactive power compensation equipment, research has been conducted to extract the maximum reactive power from wind turbine generators (WTGs) to control the WPP through the appropriate control architecture.

2.1.1 Voltage Control Approaches for WPP

Voltage control at the point of interconnection (POI) of a WPP can be categorized as hierarchical reactive power control-based approach [2]–[4] and voltage control-based approach [5]–[8]. In the former one, both central WPP controller and local WTG controller operate in reactive power control mode, where the central WPP controller sets a reactive power reference, and the local WTG controllers respond to it accordingly. Local WTG controllers cannot respond by itself and need continuous supervision from the central WPP controller. The central WPP

controller uses a communication network to communicate with the local WTG controllers. Therefore, the response of this method is slow and vulnerable to communication failures [6].

The voltage control-based approach can be classified into two categories. In the first category, the central WPP controller operates in voltage control mode, but local WTG controllers operate in reactive power control mode [9]. In this method, local WTG controllers are also completely supervised by the central WPP controller, therefore, exhibit sluggish response and remain vulnerable to communication network failures.

As a remedy, the voltage control mode-based central WPP controller and local WTG controllers have been developed [5]–[7], [10] (Second Category). In this approach, local WTG controller can respond immediately based on the voltage deviation sensed at the WTG terminal. Concurrently, the central WPP controller sends a voltage reference to local WTG controllers, which droops the WTG terminal voltage around its nominal value and brings the voltage at the POI back to the normal operating range by dispatching necessary reactive power [7]. This method has rapid response and can prevent a complete breakdown of the system during communication failures. Therefore, it has gained research interest gradually.

During contingency, to maximize the reactive power dispatch from a WPP using voltage control-based WPP controller, the maximum reactive power capability model of the WTG is a crucial parameter. Therefore, research have been conducted to develop such models similar to the conventional synchronous generators.

2.1.2 The Maximum Reactive Power Capability Curve

The slope of the $V - I$ characteristics, which is generally termed as inverse droop coefficient ($1/K_{Droop}$), regulates how far the rotor side controller (RSC) can push a WTG towards its

maximum reactive power capability. The maximum reactive power capability model of a WTG is an essential parameter in computing this droop coefficient. In practice, a wide range of limiting factors determine this capability model. The effectiveness of a controller depends heavily on how accurately the maximum reactive power capability model is developed.

In [11], [12], the reactive power capability of DFIGs is restricted by converter ratings only. However, due to additional constraints, such as the magnetic saturation, the controller of DFIGs cannot achieve the desired dynamic responses. An active power–reactive power (P-Q) diagram for DFIGs, similar to that for conventional SGs, is developed in [13]–[17] by considering: 1) converter current and heating limits in [14]; 2) only stator and rotor current limits in [15]; 3) stator and rotor current limits, and a rotor voltage limit in [16]; and 4) stator and rotor current limits, rotor voltage limits, and magnetic saturation in [17]. Although more constraints are considered in [17] than in [14]–[16], the detailed mathematical model is not provided in [17], it is hard to utilize the maximum reactive power capability under various operating conditions, and thus, limit its effectiveness.

In addition, the summation of individual WTGs capability does not represent the plant level reactive power capability. Additional constraints, such as wake effect and losses in distribution lines, impact the plant level capability. Lack of thorough consideration of a wide range of practical constraints has limited their real-life applications and resulted in improper controller actions. However, there are no in-depth models developed so far to estimate a WPP's maximum reactive power capability. Therefore, a comprehensive mathematical model is required considering practical limitations influencing individual and plant level reactive power capability of a DFIG-based WPP.

2.1.3 Controllers Developed Using the Maximum Reactive Power Capability Model

In a WPP, the RSC regulates the dispatch of reactive power from a WTG. The droop coefficient, which is the inverse of WTG's $V - I$ characteristics slope, estimated using its maximum reactive power capability model is used by the RSC to control this power flow [6]. In the literature, few controllers have been developed to utilize the maximum reactive power capacity of a WPP [2], [5], [6], [10], [18]. Among them, Ref [2] is developed using a hierarchical reactive power control, and the rest adopt the voltage control-based approach.

Among the published papers, some papers adopt the fixed droop coefficient [18], and other papers improve it by adopting an adaptive droop coefficient [5], [6], [10]. Due to the geographical position of WTGs within a WPP, active power generation from WTGs varies. In the adaptive droop coefficient-based approach, slopes (inverse droop coefficient) are chosen such that they maintain an inverse relationship with active power generation. The reactive power dispatch competency increases with a higher $V - I$ slope. Therefore, during contingency, controllers can extract more reactive power from WTGs by generating less active power. On the contrary, in a fixed slope-based approach, all WTGs contribute the same reactive power due to a fixed slope being assigned to all of them. For this reason, the adaptive slope-based approaches can contribute more reactive power than the fixed slope-based approach.

The adaptive droop coefficient estimation methods in [5], [6], [10] consider the available reactive power generation capacity only. Therefore, for the same active power generation, the coefficient estimated by these methods are the same irrespective of the depth of voltage deviations. During a deeper voltage sag, the controller cannot utilize the WTG's full capacity and consequently cannot maximize its contribution to the voltage compensation action.

In this research, an improved droop coefficient model is proposed to maximize the reactive power extraction from the WTG.

2.2 Microgrid Control

Microgrid is a combination of distributed generation (DG) units, distributed energy storages (DES), sensitive loads and centralized/decentralized control system, operating as a controllable subsystem [19]. Due to flexibilities provided by a microgrid from the aspects of efficiency, reliability, and expandability, microgrid is gaining popularity rapidly [20]. Control structures adopted in a microgrid can be categorized into grid feeding and grid forming controllers [21]. Grid feeding controllers are adopted when the microgrid is connected with the main utility grid, and they control the dispatch of active and reactive power only, irrespective of the voltage and frequency conditions. On the other hand, a microgrid adopts the grid forming control strategy when it is disconnected from the main grid and operates as an islanded microgrid. In the grid forming mode (islanded), controllers need to regulate the voltage and frequency, ensure economic operation by sharing active and reactive power among DGs and DES, and maintain continuity of power supply to critical loads. To meet these crucial criteria, droop is the most adopted primary control method for DGs in islanded microgrids [22].

2.2.1 Droop Control in Islanded Microgrid

Droop control is a primary control technique that mimics steady-state characteristics of synchronous generators. To compensate voltage or frequency deviations, droop control estimates adjustments of power flow by updating control signal references for voltage regulators [23] or current regulators [24] through its control architecture. Droop control is primarily developed for inductive feeder line (X) and adopts P - f / Q - V control methodology [25]. If $V_s \angle 0$ be the inverter terminal voltage of a DG, and $V_L \angle \delta$ be the common AC bus voltage of an islanded microgrid,

where δ is small, the active power and reactive power (P and Q) for an inductive line can be expressed as follows:

$$P = \frac{\delta V_s V_L}{X} \quad (1)$$

$$Q = \frac{V_s(V_s - V_L)}{X} \quad (2)$$

where δ is the power angle, V_s is the voltage at the inverter terminal V_L is the common bus voltage, X is distribution line reactance, P is active power and Q is reactive power.

According to (1) and (2), the phase angle (δ) and the system frequency (f) maintain a proportional relation with active power (P) dispatch; and the similar relationship is present between the converter output voltage V_s and reactive power (Q) [19]. Therefore, droop equations resulting from (1) and (2) can be expressed as follows:

$$f - f_0 = k_{p1}(P - P_0) \quad (3)$$

$$V_s - V_{s0} = k_{q1}(Q - Q_0) \quad (4)$$

where f and V_s are reference frequency and voltage, and f_0 and V_{s0} are nominal frequency and voltage, respectively; k_{p1} and k_{q1} are droop coefficient.

Converters developed from the conventional droop control method work properly in high or medium voltage system, but exhibits some drawbacks in low voltage microgrid [26], [27], such as

1. Conventional droop control does not fit with a low voltage microgrid, as low voltage microgrids are highly resistive.
2. A tradeoff present between the time constant of the controller and the frequency regulation.
3. A steady-state error present in the voltage and frequency.
4. Not suitable for nonlinear and single-phase load.

5. Poor power sharing among DGs due to unequal line impedance between DGs and loads.

To overcome these issues, and to make the droop algorithm compatible with low voltage microgrid, it has been improved and additional control layers have been added. A brief description about some of the improved droop control strategies are given below.

2.2.1.1 Real Power-Voltage / Reactive Power-Frequency Droop

In this method, droop equation is updated for a highly resistive distribution system [28]. It implements P - V / Q - f control, where active power and voltage, and reactive power and frequency are coupled. Active and reactive power in this method can be expressed as follows:

$$P = \frac{V_s(V_s - V_L)}{R} \quad (5)$$

$$Q = -\frac{\delta V_s V_L}{R} \quad (6)$$

Droop equations resulting from (5) and (6) can be expressed by

$$f - f_0 = k_{p1}(Q - Q_0) \quad (7)$$

$$V_s - V_{s0} = k_{q1}(P - P_0) \quad (8)$$

This method significantly improves power sharing accuracies in a low voltage microgrid, but cannot solve steady-state errors completely.

2.2.1.2 Reactive Power-Differential of Voltage Droop

The method was proposed in [29] where a $Q - V'$ control approach for reactive power sharing is adopted. The method is independent of the output line impedance, where a voltage restoration loop maintains constant output voltage by ensuring $V' = 0$. Control equations are expressed by

$$V'_s = V'_{s0} - n(Q_0 - Q) \quad (9)$$

$$V_s = V_{s0} + \int V'_s dt \quad (10)$$

where V_s and V_{s0} are the reference and nominal output voltage, respectively; V_s' is the rate of change of output voltage; n is the droop constant.

The method depends on initial conditions, if initial conditions are not tuned properly, it can destabilize the whole system [19].

2.2.1.3 Virtual Frame Transformation:

In this method, both active and reactive power equations are transformed into a new reference frame, where they are independent of the line impedance [30]. The method is easy to implement and facilitates the decoupled control of active and reactive power. However, the method requires the knowledge of line impedance. In addition, ensuring the same transformation angle for all DGs is hard to achieve [19].

2.2.1.4 Virtual Impedance Method

In this method, a virtual impedance is used in the feedback path of voltage control loop [31] and output voltage is controlled by adjusting the virtual impedance. The method shows superior reactive power sharing accuracy in mismatched feeder line system. Converter's output voltage reference is estimated by

$$V_{s,ref} = V_{s0} - Z_v i_0 \quad (11)$$

where V_{s0} is the no-load voltage, i_0 is the output current, and Z_v is the virtual impedance.

The method ensures accurate reactive power sharing among DGs. However, the bandwidth variation of active and reactive power controllers affects the voltage and frequency control [19].

All droop-based approaches are developed either for a highly inductive or resistive system and enforce either P - f / Q - V or P - V / Q - f control. However, a real distribution system contains both resistance and inductance, and requires simultaneous P - f / Q - V and P - V / Q - f control. As a result,

droop controllers always suffer from a steady-state error. As a remedy, in addition to improved droop methods, the secondary controller has also been integrated with the primary droop controller. The secondary controller adjusts the controller references so that additional power necessary for compensating steady-state errors are dispatched while ensuring active power sharing among DGs [32].

2.2.2 Controller Used in Droop Control

A wide variety of controllers, such as proportional-integral (PI) control, model-based control, robust control and sliding mode control, have been investigated to ensure the necessary dispatch of power in islanded microgrids [33]. However, these controllers are PI-based controllers. One major disadvantage of PI-based controllers is that it cannot handle a coupled relationship among control variables and controlled system parameters. Consequently, a multi-input multi-output (MIMO) system must be segmented into several single-input single-output (SISO) systems, and controllers need to be tuned for every individual segment to achieve the desired goal. This increases the overall volume of the control architecture. In addition, the microgrid's topological and parametric uncertainty requires continuous tuning of coefficients of the controller [34] and the conventional hardware-based implementation of PI controllers makes the retuning difficult, expensive, and time-consuming. Another major disadvantage of PI-based controllers is their inability to foresee the impact of their current actions.

2.2.3 Model Predictive Controller in Microgrid Control

The model predictive control has been used traditionally in the industrial process control, inverter control, and most recently in DG and microgrid control. In microgrids, MPC is mostly used for load forecasting[35], [36] and energy management [37], [38]; References [39]–[41]

implement MPC into a part of the overall DG's control loop. MPC is implemented at the secondary level controller in [39] to realize the secondary voltage control by incorporating forecasted behaviors of local and neighboring DGs, the secondary voltage and frequency control is regulated by MPC in [40], and eddy current losses are reduced by placing MPC in the inner control loop in [41].

In this research, a new control methodology for DG control in an islanded microgrid is proposed. A model predictive control-based DG controller is developed using the proposed control methodology. The proposed controller reduces the controller volume and complexity with improved performance.

2.3 Summary

In this section, limitations of the existing methods are summarized and how the conducted research has addressed the issues are pointed out.

2.3.1 Voltage Control Approaches for Grid Connected Wind Power Plants

2.3.1.1 Limitations of the Existing Methods

1. Unable to meet the power factor constraints.
2. No plant-level reactive power capability models available.
3. Limited constraints on developing the reactive power capability model for an individual WTG.
4. Existing controllers cannot utilize the maximum reactive power capability of a DFIG-based WPP.

2.3.1.2 Merits of the Proposed Method

1. A comprehensive maximum reactive power capability model for an individual WTG and the whole WPP.
2. A data driven steady-state reactive power capability model of a DFIG-based WPP.
3. A controller that can extract the maximum reactive power from a DFIG-based WPP.

2.3.2 Control of Islanded Microgrids

1.3.2.1 Limitations of the Existing Methods

1. Existing control algorithms consider either resistance or reactance of distribution lines, but not both.
2. Bigger and complex control structures.
3. System impedance dependent.
4. Require a secondary controller and a virtual impedance loop.
5. Require a communication network.
6. Cannot handle the coupled relationship and cannot predict the future state.

1.3.2.2 Merits of the Proposed Method

1. A novel DG control algorithm.
2. Considers both resistance and reactance of distribution lines.
3. A model predictive control (MPC)-based DG controller.
4. No secondary controllers, virtual impedance loops and DG-to-DG communication networks are required.

References

- [1] J. Ouyang, M. Li, Y. Diao, T. Tang, and Q. Xie, “Active control method of large-scale wind integrated power system with enhanced reactive power support for wind speed fluctuation,” *IET Gener. Transm. Distrib.*, vol. 12, no. 21, pp. 5664–5671, 2018, doi: 10.1049/iet-gtd.2018.5418.
- [2] A. Tapia, G. Tapia, and J. X. Ostolaza, “Reactive power control of wind farms for voltage control applications,” *Renew. Energy*, vol. 29, no. 3, pp. 377–392, Mar. 2004, doi: 10.1016/S0960-1481(03)00224-6.
- [3] A. D. Hansen, P. Sørensen, F. Iov, and F. Blaabjerg, “Centralised power control of wind farm with doubly fed induction generators,” *Renew. Energy*, vol. 31, no. 7, pp. 935–951, Jun. 2006, doi: 10.1016/j.renene.2005.05.011.
- [4] M. N. S. K. Shabbir, X. Liang, W. Li, N. Khan, and A. M. Le, “A Novel Data Driven Voltage Control Approach for Grid Connected Wind Power Plants,” *IEEE Trans. Ind. Appl.*, vol. 55, no. 4, pp. 3376–3393, 2019, doi: 10.1109/TIA.2019.2901732.
- [5] J. Kim, E. Muljadi, J.-W. Park, and Y. C. Kang, “Adaptive Hierarchical Voltage Control of a DFIG-Based Wind Power Plant for a Grid Fault,” *IEEE Trans. Smart Grid*, vol. 7, no. 6, pp. 2980–2990, 2016, doi: 10.1109/TSG.2016.2562111.
- [6] J. Kim, J.-K. Seok, E. Muljadi, and Y. C. Kang, “Adaptive Q–V Scheme for the Voltage Control of a DFIG-Based Wind Power Plant,” *IEEE Trans. Power Electron.*, vol. 31, no. 5, pp. 3586–3599, 2016, doi: 10.1109/TPEL.2015.2464715.
- [7] J. Kim, E. Muljadi, J.-W. Park, and Y. C. Kang, “Flexible IQ–V Scheme of a DFIG for Rapid Voltage Regulation of a Wind Power Plant,” *IEEE Trans. Ind. Electron.*, vol. 64, no. 11, pp. 8832–8842, 2017, doi: 10.1109/TIE.2017.2694408.

- [8] J. Martínez, P. C. Kjær, P. Rodriguez, and R. Teodorescu, "Design and Analysis of a Slope Voltage Control for a DFIG Wind Power Plant," *IEEE Trans. Energy Convers.*, vol. 27, no. 1, pp. 11–20, 2012, doi: 10.1109/TEC.2011.2170197.
- [9] M. E. Moursi, G. Joos, and C. Abbey, "A Secondary Voltage Control Strategy for Transmission Level Interconnection of Wind Generation," *IEEE Trans. Power Electron.*, vol. 23, no. 3, pp. 1178–1190, 2008, doi: 10.1109/TPEL.2008.921195.
- [10] S. Ghosh, Y. J. Isbeih, R. Bhattarai, M. S. E. Moursi, E. F. El-Saadany, and S. Kamalasan, "A Dynamic Coordination Control Architecture for Reactive Power Capability Enhancement of the DFIG-Based Wind Power Generation," *IEEE Trans. Power Syst.*, vol. 35, no. 4, pp. 3051–3064, 2020, doi: 10.1109/TPWRS.2020.2968483.
- [11] E. Vittal, M. O'Malley, and A. Keane, "A Steady-State Voltage Stability Analysis of Power Systems With High Penetrations of Wind," *IEEE Trans. Power Syst.*, vol. 25, no. 1, pp. 433–442, Feb. 2010, doi: 10.1109/TPWRS.2009.2031491.
- [12] G. F. Gontijo *et al.*, "Modeling, Control, and Experimental Verification of a DFIG With a Series-Grid-Side Converter With Voltage Sag, Unbalance, and Distortion Compensation Capabilities," *IEEE Trans. Ind. Appl.*, vol. 56, no. 1, pp. 584–600, Jan. 2020, doi: 10.1109/TIA.2019.2946950.
- [13] S. Mondal and D. Kastha, "Maximum Active and Reactive Power Capability of a Matrix Converter-Fed DFIG-Based Wind Energy Conversion System," *IEEE J. Emerg. Sel. Top. Power Electron.*, vol. 5, no. 3, pp. 1322–1333, Sep. 2017, doi: 10.1109/JESTPE.2017.2697038.

- [14] M. Z. Sujod, I. Erlich, and S. Engelhardt, "Improving the Reactive Power Capability of the DFIG-Based Wind Turbine During Operation Around the Synchronous Speed," *IEEE Trans. Energy Convers.*, vol. 28, no. 3, pp. 736–745, Sep. 2013, doi: 10.1109/TEC.2013.2272975.
- [15] H. Pulgar-Painemal, "Enforcement of Current Limits in DFIG-Based Wind Turbine Dynamic Models Through Capability Curve," *IEEE Trans. Sustain. Energy*, vol. 10, no. 1, pp. 318–320, Jan. 2019, doi: 10.1109/TSTE.2018.2831451.
- [16] J. Kim, J. Seok, E. Muljadi, and Y. C. Kang, "Adaptive Q–V Scheme for the Voltage Control of a DFIG-Based Wind Power Plant," *IEEE Trans. Power Electron.*, vol. 31, no. 5, pp. 3586–3599, May 2016, doi: 10.1109/TPEL.2015.2464715.
- [17] S. Engelhardt, I. Erlich, C. Feltes, J. Kretschmann, and F. Shewarega, "Reactive Power Capability of Wind Turbines Based on Doubly Fed Induction Generators," *IEEE Trans. Energy Convers.*, vol. 26, no. 1, pp. 364–372, Mar. 2011, doi: 10.1109/TEC.2010.2081365.
- [18] J. Martínez, P. C. Kjær, P. Rodriguez, and R. Teodorescu, "Design and Analysis of a Slope Voltage Control for a DFIG Wind Power Plant," *IEEE Trans. Energy Convers.*, vol. 27, no. 1, pp. 11–20, 2012, doi: 10.1109/TEC.2011.2170197.
- [19] S. K. Sahoo, A. K. Sinha, and N. K. Kishore, "Control Techniques in AC, DC, and Hybrid AC–DC Microgrid: A Review," *IEEE J. Emerg. Sel. Top. Power Electron.*, vol. 6, no. 2, pp. 738–759, Jun. 2018, doi: 10.1109/JESTPE.2017.2786588.
- [20] E. Espina, J. Llanos, C. Burgos-Mellado, R. Cárdenas-Dobson, M. Martínez-Gómez, and D. Sáez, "Distributed Control Strategies for Microgrids: An Overview," *IEEE Access*, vol. 8, pp. 193412–193448, 2020, doi: 10.1109/ACCESS.2020.3032378.

- [21] J. Rocabert, A. Luna, F. Blaabjerg, and P. Rodríguez, “Control of Power Converters in AC Microgrids,” *IEEE Trans. Power Electron.*, vol. 27, no. 11, pp. 4734–4749, Nov. 2012, doi: 10.1109/TPEL.2012.2199334.
- [22] “Stability and Control Aspects of Microgrid Architectures—A Comprehensive Review | IEEE Journals & Magazine | IEEE Xplore.” <https://ieeexplore-ieee-org.qe2a-proxy.mun.ca/document/9162105> (accessed Jun. 04, 2021).
- [23] B. Liu, Z. Liu, J. Liu, R. An, H. Zheng, and Y. Shi, “An Adaptive Virtual Impedance Control Scheme Based on Small-AC-Signal Injection for Unbalanced and Harmonic Power Sharing in Islanded Microgrids,” *IEEE Trans. Power Electron.*, vol. 34, no. 12, pp. 12333–12355, Dec. 2019, doi: 10.1109/TPEL.2019.2905588.
- [24] S. d J. M. Machado, S. A. O. da Silva, J. R. B. d A. Monteiro, and A. A. de Oliveira, “Network Modeling Influence on Small-Signal Reduced-Order Models of Inverter-Based AC Microgrids Considering Virtual Impedance,” *IEEE Trans. Smart Grid*, vol. 12, no. 1, pp. 79–92, Jan. 2021, doi: 10.1109/TSG.2020.3012475.
- [25] R. An, Z. Liu, and J. Liu, “Successive-Approximation-Based Virtual Impedance Tuning Method for Accurate Reactive Power Sharing in Islanded Microgrids,” *IEEE Trans. Power Electron.*, vol. 36, no. 1, pp. 87–102, Jan. 2021, doi: 10.1109/TPEL.2020.3001037.
- [26] J. M. Guerrero, J. C. Vasquez, J. Matas, L. G. de Vicuna, and M. Castilla, “Hierarchical Control of Droop-Controlled AC and DC Microgrids—A General Approach Toward Standardization,” *IEEE Trans. Ind. Electron.*, vol. 58, no. 1, pp. 158–172, Jan. 2011, doi: 10.1109/TIE.2010.2066534.

- [27] A. Bidram and A. Davoudi, "Hierarchical Structure of Microgrids Control System," *IEEE Trans. Smart Grid*, vol. 3, no. 4, pp. 1963–1976, Dec. 2012, doi: 10.1109/TSG.2012.2197425.
- [28] C. K. Sao and P. W. Lehn, "Control and Power Management of Converter Fed Microgrids," *IEEE Trans. Power Syst.*, vol. 23, no. 3, pp. 1088–1098, Aug. 2008, doi: 10.1109/TPWRS.2008.922232.
- [29] C.-T. Lee, C.-C. Chu, and P.-T. Cheng, "A New Droop Control Method for the Autonomous Operation of Distributed Energy Resource Interface Converters," *IEEE Trans. Power Electron.*, vol. 28, no. 4, pp. 1980–1993, Apr. 2013, doi: 10.1109/TPEL.2012.2205944.
- [30] Y. Li and Y. W. Li, "Power Management of Inverter Interfaced Autonomous Microgrid Based on Virtual Frequency-Voltage Frame," *IEEE Trans. Smart Grid*, vol. 2, no. 1, pp. 30–40, Mar. 2011, doi: 10.1109/TSG.2010.2095046.
- [31] W. Yao, M. Chen, J. Matas, J. M. Guerrero, and Z.-M. Qian, "Design and Analysis of the Droop Control Method for Parallel Inverters Considering the Impact of the Complex Impedance on the Power Sharing," *IEEE Trans. Ind. Electron.*, vol. 58, no. 2, pp. 576–588, Feb. 2011, doi: 10.1109/TIE.2010.2046001.
- [32] X. Liang, C. Andalib-Bin-Karim, W. Li, M. Mitolo, and M. N. S. K. Shabbir, "Adaptive Virtual Impedance-Based Reactive Power Sharing in Virtual Synchronous Generator Controlled Microgrids," *IEEE Trans. Ind. Appl.*, vol. 57, no. 1, pp. 46–60, Jan. 2021, doi: 10.1109/TIA.2020.3039223.
- [33] A. Tavakoli, M. Negnevitsky, and K. M. Muttaqi, "A Decentralized Model Predictive Control for Operation of Multiple Distributed Generators in an Islanded Mode," *IEEE Trans. Ind. Appl.*, vol. 53, no. 2, pp. 1466–1475, Mar. 2017, doi: 10.1109/TIA.2016.2616396.

- [34] L. Wang, Y. Qin, Z. Tang, and P. Zhang, "Software-Defined Microgrid Control: The Genesis of Decoupled Cyber-Physical Microgrids," *IEEE Open Access J. Power Energy*, vol. 7, pp. 173–182, 2020, doi: 10.1109/OAJPE.2020.2997665.
- [35] J. Sachs and O. Sawodny, "A Two-Stage Model Predictive Control Strategy for Economic Diesel-PV-Battery Island Microgrid Operation in Rural Areas," *IEEE Trans. Sustain. Energy*, vol. 7, no. 3, pp. 903–913, 2016.
- [36] A. Ouammi, H. Dagdougui, L. Dessaint, and R. Sacile, "Coordinated Model Predictive-Based Power Flows Control in a Cooperative Network of Smart Microgrids," *IEEE Trans. Smart Grid*, vol. 6, no. 5, pp. 2233–2244, Sep. 2015, doi: 10.1109/TSG.2015.2396294.
- [37] U. C. Yilmaz, M. E. Sezgin, and M. Gol, "A Model Predictive Control for Microgrids Considering Battery Aging," *J. Mod. Power Syst. Clean Energy*, pp. 1–9, 2019.
- [38] T. Pippia, J. Sijs, and B. D. Schutter, "A Single-Level Rule-Based Model Predictive Control Approach for Energy Management of Grid-Connected Microgrids," *IEEE Trans. Control Syst. Technol.*, pp. 1–13, 2019.
- [39] G. Lou, W. Gu, W. Sheng, X. Song, and F. Gao, "Distributed Model Predictive Secondary Voltage Control of Islanded Microgrids With Feedback Linearization," *IEEE Access*, vol. 6, pp. 50169–50178, 2018.
- [40] J. S. Gómez, D. Sáez, J. W. Simpson-Porco, and R. Cárdenas, "Distributed Predictive Control for Frequency and Voltage Regulation in Microgrids," *IEEE Trans. Smart Grid*, vol. 11, no. 2, pp. 1319–1329, 2020.
- [41] T. Nguyen, H. Yoo, and H. Kim, "Applying Model Predictive Control to SMES System in Microgrids for Eddy Current Losses Reduction," *IEEE Trans. Appl. Supercond.*, vol. 26, no. 4, pp. 1–5, 2016.

Chapter 3

A Novel Data-Driven Voltage Control Approach for Grid-Connected Wind Power Plants

Md Nasmus Sakib Khan Shabbir¹, *Student Member*, IEEE, Xiaodong Liang¹, *Senior Member*, IEEE, Weixing Li², *Senior Member*, IEEE, Nahidul Khan³, and Anh Minh Le¹

¹Department of Electrical and Computer Engineering, Memorial University of Newfoundland, St. John's, Newfoundland, Canada.

²Department of Electrical Engineering, Harbin Institute of Technology, Harbin, Hilongjiang, China.

³Newfoundland and Labrador Hydro System Operation and Planning, Energy Control Center, St John's, Canada

A version of this chapter has been published in IEEE Transactions on Industry Applications, July/August 2019 regular issue. MD Nasmus Sakib Khan Shabbir co-authored this paper under the supervision of Dr. Xiaodong Liang. Sakib's contributions are listed as follows:

- Performed literature searches required for the development of grid connected wind power plant controller.
- Analyzed the SCADA measurement data and developed the surface fitting models.
- Developed the wind power plant base model and evaluated the proposed controllers through MATLAB/Simulink simulation.
- Involved in the writing of the paper draft as the first author.

Dr. Xiaodong Liang provided continuous technical guidance, checked the results, and modified the manuscript. Dr. Weixing Li modified the manuscript. Dr. Nahidul Khan provided the SCADA

measurement data and necessary information about the wind power plant used in the analysis. Anh Minh Le helped in sorting and analyzing the SCADA measurement data.

In this chapter, the manuscript is presented with altered figure numbers, table numbers, and reference formats in order to match the thesis formatting guidelines set out by Memorial University of Newfoundland.

Abstract- Due to increasing penetration of wind power plants (WPP), power grids are facing significant power quality challenges at the point of interconnection (POI). To achieve stable and robust power system operation, reactive power plays a vital role. Reactive power needed to compensate voltage fluctuations at the POI of the WPP varies with a short circuit ratio (SCR). The reactive power capability of a WPP is also limited and largely depends on various operating conditions. In a physical system, it is difficult to find the correlation among critical parameters for voltage control. In this paper, a data-driven voltage control approach is proposed for a grid-connected WPP. Two regression models are developed through surface fitting using MATLAB curve fitting toolbox: one model based on simulation data is to determine the required reactive power for grid voltage compensation; another model based on field measurement data is to determine the reactive power characteristics of the WPP. The reactive power compensation device is capacitors in this study. Two controllers, a central WPP controller and a capacitor controller, are designed, their effectiveness is validated through several case and sensitivity studies.

Keywords- Power quality, reactive power control, short circuit ratio, surface fitting, voltage control.

3.1 Introduction

Over past decades, increasing penetration of wind power plants (WPPs) has created challenges towards stable operation of power grids. Wind power generation is intermittent due to the continuously changing wind. Power electronic converters interfacing with the utility for Types 3 and 4 wind turbine generators (WTGs) do not provide significant amount of fault currents. It weakens the grid strength and introduces a low short circuit ratio (SCR) at the point of interconnection (POI) of the WPP, which further affects grid dynamics and voltage control [1]. To govern wind power integration, grid codes have been established. Reactive power support from the WPP is required under normal and voltage sag conditions in grid codes [2]-[6]. Key characteristics to meet such requirements are reactive power capability of a WPP and continuously acting voltage control. Inadequate reactive power capability of WPPs can limit the potential of wind power generation [6][7]. WTGs alone may not be enough to provide the required reactive power at the plant level when the reactive power capability limit is reached at each WTG. Appropriate reactive power compensation can be implemented in the WPP to ensure acceptable voltage profiles across the system and sufficient reactive power available following major grid events [1][6]. In UK, the size of reactive power compensation equipment is recommended to be one-third of the nominal active power of a WPP [6].

Common reactive power compensation equipment includes capacitor banks, Static Var Compensator (SVC) and Static Synchronous Compensator (STATCOM). Due to cost consideration, capacitor banks are a viable lower cost option in a practical WPP [8]. The successful reactive power compensation can be realized through properly designed controllers operating with capacitor banks.

WPPs with Types 3 and 4 WTGs typically have a plant level control strategy, and each individual WTG has its own controls. The plant controller coordinates individual WTG level controls to ensure stable operation of the entire plant [1]. To maintain the voltage at the POI within a specified limit under normal and fault conditions, usually in the range of [0.95, 1.05] per unit, a central WPP controller can be implemented to send necessary set points for individual WTG controllers. The WPP controller can operate in either voltage control or reactive power control mode. Different variables, such as voltage deviation, available and required reactive power, and reactive power margin of the WPP, can be considered for the controller design [9]-[11].

A WPP supplies reactive power for under-voltage (voltage sags), and consumes reactive power for over-voltage (voltage swells) conditions to maintain the POI voltage. During under-voltage, the maximum voltage and reactive power generation capacity of a WPP depends on the rating of WTGs. During over-voltage, the minimum reactive power consumption capacity of a WPP depends on the negative reactive power margin at the POI [12]-[18]. It is important to validate a central WPP controller for both under- and over-voltage conditions.

There is an inverse relationship between active power generation and negative reactive power margin: a higher active power generation leads to a lower negative reactive power margin. A positive reactive power margin indicates an instable system, while a negative reactive power margin indicates a stable system [19]-[20].

The WPP controller can have reactive power control, and voltage control features. The voltage control is restricted by the reactive power capacity of WTGs [21]-[23]. Among various WPP controller design methods reported in the literature [24]-[29], Reference [24] proposes a controller that selects the required reactive current set point and sends it to a doubly-fed induction generator (DFIG) controller with a weighted factor, named “reactive power capability index”, which is the

ratio of instantaneous active power to average power supplied by each WTG. This index adjusts the required reactive power set point of a WTG based on its active power generation. A lower active power generation leads to a higher reactive power set point. However, this reactive current control scheme in [24] cannot react to a voltage dip immediately after a disturbance. A fixed reactive power-voltage magnitude (Q-V) control scheme is employed to control the grid voltage in [25]. The WPP controller calculates the reactive power set point using a coefficient named “slope”, which is a ratio between the voltage and reactive power deviation at the POI. However, the impact of active power on the reactive power generation capacity is neglected in [25]. Similarly, a static Q-V scheme is applied in the WPP controller in [27], where the upper limit of the reactive power injection of a WTG is set at 33% of the nominal active power regardless of different operating conditions. The issue is that a WTG cannot fully operate and its voltage control function at the POI is limited. To address this issue, a WPP controller using an adaptive Q-V characteristic curve to determine the required reactive power set point is proposed in [28][29].

Despite continuous effort for WPP controllers design, two critical aspects are missing in existing WPP controller design methods in the literature, which can hinder the controller’s performance: 1) the influence of the SCR is not considered [22]-[24],[26]-[28]; and 2) the reactive power capability of WTGs is not properly determined [22]-[24],[26].

The SCR represents grid strength, which is usually low at the POI of a WPP, for example, a SCR equal to 5 is not uncommon for a WPP. The influence of a lower SCR during disturbances is a higher voltage drop and a slower voltage recovery compared to the system with a higher SCR, which means an increased risk of system instability. The system with a low SCR shows strong dependency between voltage and reactive power [18]. It is recommended in [18] that the SCR equal to 5 can serve as a threshold, a WPP with a SCR less than 5 at the POI raises concerns that

the WPP may not operate correctly under disturbances. Therefore, it is essential that the SCR serves as a parameter for the WPP controller design.

The reactive power capability of WTGs and Q-V curves used in the literature [22]-[24],[26] are assumed typical characteristic curves. The control schemes are traditional model based techniques, which rely on physical models from first principles. The main drawback of these theoretically developed mathematical equation or assumed characteristics based controllers is that it cannot follow the nonlinearity and complexity of a real WPP. These models do not consider actual aerodynamic interactions among the WTGs, and environmental uncertainties. Therefore, their practical effectiveness is limited.

In contrast to traditional model based techniques, data-driven approaches by utilizing practical WPP data, such as the supervisory control and data acquisition (SCADA) measurement data, wind speed data etc, started gaining significant research interest a decade ago by wind power industry. By using practical data at WPPs, a fault-free and cost-efficient operation of WPPs can be achieved while the desired performance can be maintained.

To date, the work reported in the literature on data-driven research for wind power can be divided into four categories: 1) data-driven controller tuning or design for maximum energy extraction [30]-[36], various control techniques, such as Takagi–Sugeno–Kang (TSK) fuzzy model [30], anticipatory control [31], adaptive control [33], are implemented using control settings computed or tuned from optimization models, the main goal through the control is to realize the maximum wind power generation; 2) data-driven based operational cost reduction, wind farm scheduling and dispatch, and wind power forecasting [37]-[44], it is suggested in [39] that a novel statistical wind power forecast method, which leverages the spatio-temporal correlation in wind speed and direction data among geographically dispersed WPPs, can be integrated with an

economic dispatch framework, as a result, the total generation cost can be reduced up to 6% [39]; 3) data-driven condition monitoring and fault diagnosis [45]-[48], in this area, new signal processing methods [45] and various machine learning methods, such as a single hidden layer feedforward neural network [46] and random forests [48], are utilized; 4) data-driven modeling for wind turbines and power curve profile [49]-[53], wind turbine parameters including power output, drive-train vibratory acceleration, and tower vibratory acceleration can be modeled using machine learning techniques [50][52], in [53], the power curve profile can be accurately redefined under wind curtailment by effectively removing the abundant outliers caused by wind curtailment through a data-driven outlier elimination approach.

Although the data-driven approaches have been widely implemented in wind power industry during the past decade as discussed above, to the authors' best knowledge, there is no reported data-driven controller design for voltage control in the literature for WPPs so far.

For the very first time, this paper proposes a data-driven voltage controller design for a grid-connected WPP using SCADA measurement data at the POI. The SCADA data comprehend uncertainties, complexities, and aero-dynamic interactions associated with the WPP. The proposed voltage controllers are designed by directly analyzing the plant level data, and thus, stability, convergence and robustness of the system level control can be achieved. Two controllers, a central WPP controller and a capacitor controller, are designed using the proposed approach. The sample system is a 27 MW WPP currently in operation in Newfoundland and Labrador (NL), Canada. The reactive power compensation devices used in this paper are chosen to be capacitors. Presently, there are no reactive power compensation devices installed inside this WPP. The major contribution of this paper includes: 1) The SCR serves as a parameter of a regression model to determine the required reactive power to compensate voltage deviation at the POI, and this model

is obtained through surface fitting using simulation data with the SCR and voltage deviation as input parameters; 2) The reactive power capability of the WPP with collective effect of all WTGs can be determined by a regression model using SCADA measurement data at the POI of the WPP; 3) a central WPP controller is designed by integrating the required reactive power at the POI during a voltage deviation and the reactive power capability of the WPP determined by the real WPP data; and 4) a capacitor controller is design to properly manage on and off patterns of the capacitors.

The paper is arranged as follows: in Section 3.2, the WPP under study is described; a brief explanation about goodness fit evaluation and robustness algorithms for surface fitting are discussed in Section 3.3, which will be used to choose regression models; in Section 3.4, regression models of the required reactive power at the POI and reactive power capability of the WPP are developed; in Section 3.5, fundamental principles of the proposed central WPP controller and capacitor controller are elaborated; case and sensitivity studies are conducted in Sections 3.6 and 3.7; the conclusion is drawn in Section 3.8.

3.2 The WPP Under Study

In this study, a 27 MW WPP currently in operation in NL, Canada is adopted as a sample system. The electrical single line diagram of the WPP is shown in Fig. 3.1. There are a total of nine DFIGs. Each DFIG is rated at 3 MW and installed with a 3.5 MVA wye/delta step-up transformer with the voltage rating of 1 kV/25 kV. All WTGs are connected to a 25 kV plant main bus in a similar way. A 25 MVA wye/delta transformer further steps up the voltage from 25 kV to the 66 kV POI. Currently, no reactive power compensation equipment is installed in the WPP. The three phase short circuit MVA at the POI of the WPP is 135 MVA, and the X/R ratio is 3.259.

Operation requirements at the POI of the WPP from the local utility company include: 1) the voltage deviation should be within $\pm 5\%$ the nominal voltage of 66 kV; 2) the recommended power factor is within ± 0.95 . Other requirements include harmonics and flickers emission restrictions following IEEE Std. 519 and IEEE Std. 1453. Since our focus is voltage control, harmonics and flickers are not discussed in this paper.

The SCADA measurement data at the 66 kV POI recorded during the whole year of 2016 at the sampling rate of one sample per second are used to develop voltage control functions. As an example, plots of the voltage magnitude V in kV, active power P in MW, and reactive power Q in MVar vs. the time for March 1-5, 2016 are shown in Fig. 3.2.

The data analysis indicates that, during the whole year's operation, the voltage profile of the WPP varied in the range of [0, 69.96] kV or [0, 1.06] per unit (the voltage base is the nominal voltage of 66 kV). The measured active and reactive power were in the range of [-1.19, 27.23] MW and [-0.75, 13.03] MVar, respectively.

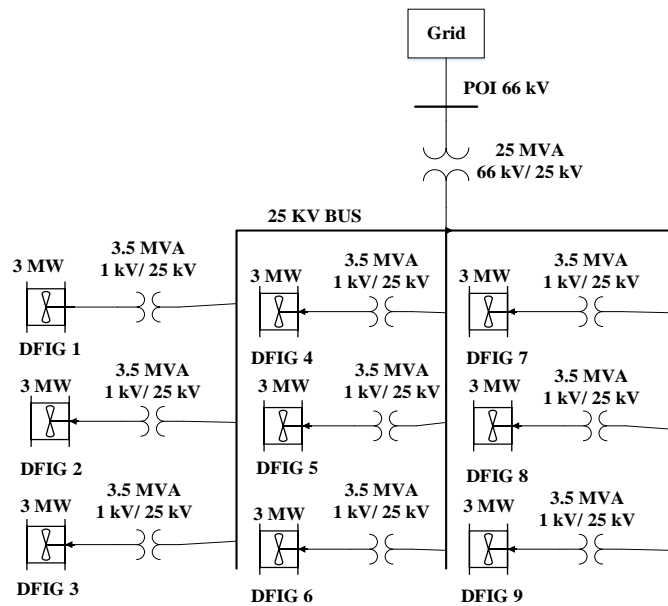


Fig. 3. 1. Electrical single line diagram of a WPP currently in operation in Newfoundland and Labrador, Canada.

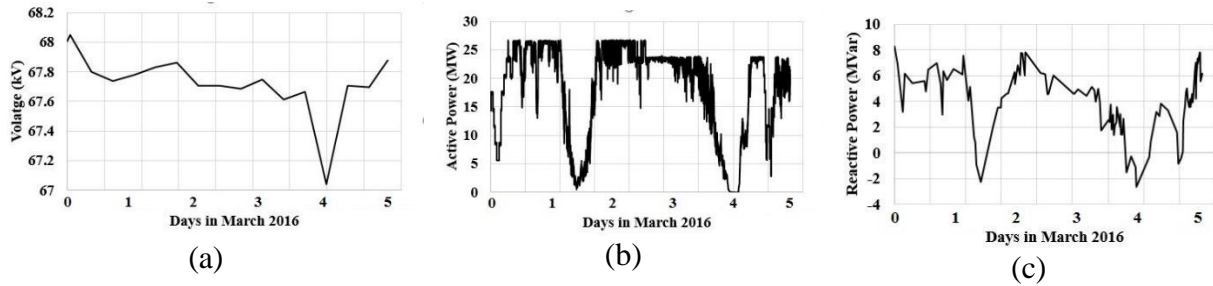


Fig. 3. 2. SCADA field measurement data at the 66 kV POI of the WPP on March 1-5, 2016: (a) voltage in kV; (b) active power in MW; (c) reactive power in MVar.

In this study, instead of modeling 9 individual WTGs in Fig. 3.1, an equivalent 27 MW DFIG operating in the reactive power control mode is modeled for the controller design. The DFIG model offered in MATLAB/Simulink is adopted. The electrical single-line diagram of the equivalent WPP used for the controller design is shown in Fig. 3.3.

The nominal apparent power capacity of the equivalent DFIG is 30 MVA. The maximum power of the grid and rotor side converters is 0.3 pu of the nominal power. These converters use forced commutated insulated-gate bipolar transistor (IGBT) switches to convey the conversion process. A DC bus capacitor of 90,000 μF is utilized between the converters in the model. The grid side converter (GSC) is connected to the grid through a coupling inductor with an inductance of 0.15 pu and an internal resistance of 0.015 pu. The active power output follows the power-rotor speed tracking characteristic. The active and reactive power regulators are used to reduce the error to zero compared to the corresponding active and reactive power references. The turbine has three blades with a pitch angle controller, where the maximum allowable pitch angle is 45° .

The DFIG is connected to the 25 kV plant main bus through an equivalent 31.5 MVA (9x3.5 MVA) wye/delta transformer (TL), as shown in Fig. 3.3. The distance between the equivalent DFIG and the 25 kV main bus is assumed to be 1.5 km. The 25 kV main bus is further connected

to the 66 kV grid through a 40 MVA, 25 kV/66 kV wye/delta transformer (TH). There is a 0.5 km transmission line used to connect between the transformer TL and 25 kV bus, and between the transformer TH and the 25 kV bus. In the simulation model, the two piece of lines are named as “Cable” as shown in Fig. 3.3. The detailed simulation parameters for the DFIG model, cables, and transformers are tabulated in Table 3.1.

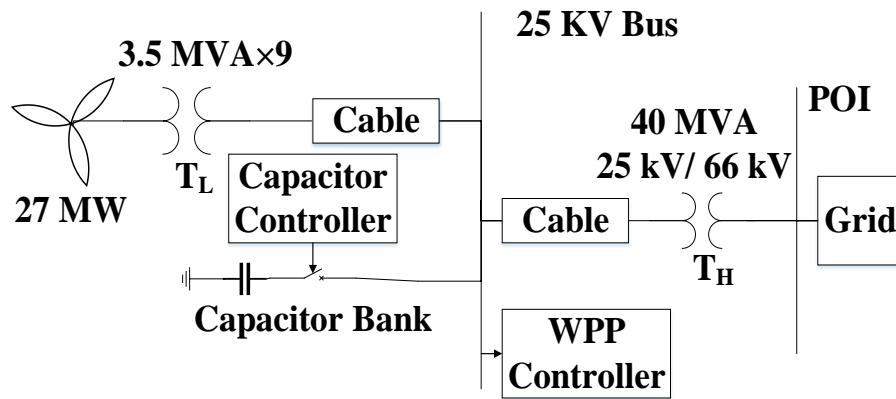


Fig. 3. 3. The single line diagram of the equivalent WPP for controller design.

Two controllers are proposed in this paper: a central WPP controller and a capacitor controller, both are connected to the 25 kV main bus as shown in Fig. 3.3. The central WPP controller senses a voltage deviation at the POI and calculates the required reactive power to compensate the voltage deviation. Currently, no reactive power compensation devices are installed in this WPP. To implement the proposed voltage control approach, six capacitor banks, each rated at 1.5 Mvar at 25 kV, are chosen to be connected to the 25 kV main bus for reactive power compensation. The size of capacitor banks is selected following the recommended practice in UK that reactive compensation equipment should be about one third of the plant’s nominal active power rating. The required reactive power is then divided between the WTG and

capacitor banks based on their operating capability. The capacitor controller controls the switching of capacitor banks in and out of the circuit

Table 3. 1: Simulation Parameters for the DFIG Model, Cables and Transformers

DFIG Data		DFIG Control Data		
Nominal apparent power	30 MVA	Regulator Name	Proportional Gain (K_P)	Integral Gain (K_I)
Nominal voltage	575 V	Reactive power (PI_1)	0.05	25
Stator resistance	0.00706 pu	Active power (PI_2)	1	100
Stator leakage inductance	0.171pu	DC bus voltage (PI_4)	0.002	0.05
Magnetizing inductance	2.9 pu	Grid-side converter current (PI_5)	1	100
Rotor resistance	0.005pu	Rotor-side converter current (PI_3)	0.3	8
Rotor leakage inductance	0.156pu	Pitch angle	500	None
System frequency	60 Hz			
Nominal DC bus voltage	1200 V			
Rated wind speed	12 m/s			
Cable Data				
Parameter Name		Positive Sequence		Zero Sequence
Resistance (Ω /km)		0.1153		0.413
Inductance (H/km)		1.05e-3		3.32e-3
Capacitance (F/km)		11.33e-009		5.01e-009
Transformer Data				
		T_L		T_H
Capacity (MVA)		9×3.5		40
Rated voltages (kV)		0.575/25		25/66
Resistance (pu)		0.025/30		0.003
Leakage Inductance (pu)		0.025		0.09

The central WPP controller communicates with the capacitor controller and individual WTG controller through a switched Ethernet based hierarchical communication network. It follows IEC 61400-25 standard to control and monitor the WPP. The link has a 1 Gbps bandwidth and it takes 1 ms to communicate with the individual WTG [54].

3.3 Accuracy Evaluation for Regression Models

In this paper, two regression models are developed through surface fitting using MATLAB curve fitting toolbox. The accuracy evaluation approach for regression models is firstly introduced in this section.

3.3.1 Goodness of Fit Assessment

Goodness of fit is to be studied to evaluate the accuracy of a developed regression model, which can be carried out graphically or statistically.

Residual analysis is a graphical analysis method. If the dataset are very scattered, the fitted surface model is not able to follow all data points. Higher randomness of data leads to higher amount of outliers. In a residual analysis, differences between actual and calculated values for a specific predictor are shown graphically. If residuals are following a pattern and are not random in nature, it means the model is poorly fit with the dataset [20]. In a prediction bound analysis, 95% upper and lower confidence surfaces are drawn along the actual fitted surface model. The prediction bound analyzes the number of data points the model can contain within its upper and lower bounds. More data points within the bounds indicate that the equation can follow the uncertainty of a system better.

In a statistical analysis, the goodness of fit evaluation process is conducted through the sum of squares due to error (SSE), root-mean-squared error (RMSE), R-square and adjusted R-square. SSE represents the cumulative deviation of calculated values from actual ones. RMSE represents standard error of a random data. A small SSE or RMSE indicates an accurate model. R-square and adjusted R-square show how properly a fitted model can explain the variance of an actual dataset, and a value closer to 1 indicates a better fit [20].

3.3.2 Robustness Algorithm

If a dataset contains randomly scattered data, a robustness algorithm can be used to improve the accuracy of a regression model. The algorithm can detect outliers and reduce their effect on the regression model, which allows the model to follow actual trend of the data set and disregard noisy data. Two robustness algorithms are considered in this paper, Bisquare and the least absolute residuals (LAR) [55][56].

The Bisquare algorithm develops the model based on a weighted factor. A weight is assigned to each data point, and its value is inversely proportional to the distance between the data point and the surface. The extreme values receive a zero weight, and thus, their impact on the model is eliminated [57]. The Least Square (LS) method is used to make an initial guess for a coefficient, the weight is then continuously updated according to the coefficient until the error is lowered down to a specified tolerance limit. The Bisquare algorithm develops a function through an iterative process, and residuals are calculated as follows [57]:

$$r = \frac{1}{n} \sum_{i=1}^{n-1} w_i (f(x_i) - y_i)^2 \quad (1)$$

Where, n is the number of data samples, w_i is the i^{th} element of the weights array for data samples, $f(x_i)$ is the y -value of the fitted model and y_i is the i^{th} element of the data set.

The LAR develops a surface equation based on absolute difference of the residuals. The absolute values higher than a specific threshold are disregarded, and thus, the influence of noises are minimized in the LAR algorithm. It put same emphasis on every data point within the threshold limit, and the influence of extreme values are lessened. LAR is also an iterative method but less sensitive than the least square method to extreme outliers. Therefore, LAR

performs better when the dataset has significant amount of outliers. The equation used to estimate least absolute deviation for LAR is [58]

$$\beta_{LAR} = \arg \min \sum_{i=1}^n |\varepsilon_i(\beta)| \quad (2)$$

Where, β_{LAR} is the absolute deviation estimator, $\varepsilon_i(\beta)$ is the error, and n is the number of data samples.

3.4 Regression Models Development

The development of the two regression models is demonstrated in this section. The 1st model is to determine a mathematical relationship for the required reactive power at the POI as a function of the SCR and the voltage deviation ΔU . The 2nd model is to develop a mathematical relationship for the reactive power capability in the WPP considering the collective effect of all WTGs as a function of the active power P and the voltage magnitude V.

3.4.1 Required Reactive Power at the POI

The SCR is defined as the ratio of the three-phase short circuit MVA at the POI to the WPP's nominal active power in MW, it can also be determined as the inverse of the impedance seen from the aggregate WTGs terminal to the POI [18].

$$SCR = \frac{\text{Three-phase Short Circuit MVA at POI}}{\text{WPP nominal power in MW}} \quad (3)$$

For the WPP under study in this paper, it is given by the local utility company that the WPP has a three phase short circuit MVA at the POI equal to 135 MVA, and a nominal active power rating of 27 MW, so the calculated SCR value at the POI for this WPP is 5 using Equ. (3).

Considering the SCR's effect, the control algorithm of a central WPP controller requires a mathematical relationship among the required reactive power, SCR, and voltage deviation at the

POI. To derive it, a set of data reflects the influence of these three parameters are needed, which can be obtained through computer simulation. The simulation model is shown in Fig. 3.4. Fictitious capacitor banks and inductors are connected through a 25 kV/66 kV wye/delta transformer to the 66 kV POI to obtain various under- and over-voltage situations. It is assumed that the reactive power is supplied or consumed by the grid.

In the simulation, the POI voltage varies from 0.9 pu to 1.1 pu, the SCR values varies from 3 to 15, and the X/R ratio is assumed to be 3.259, the same as the WPP under study in Section II. Regarding low SCR values, Reference [18] explains that most models are typically proven to be accurate for a SCR down to 5 but may or may not be accurate for a lower SCR between 3 and 5. The minimum SCR value is 3 in [59]. Therefore, the minimum SCR value is also chosen to be 3 in this paper. The simulation is conducted using MATLAB/ Simulink.

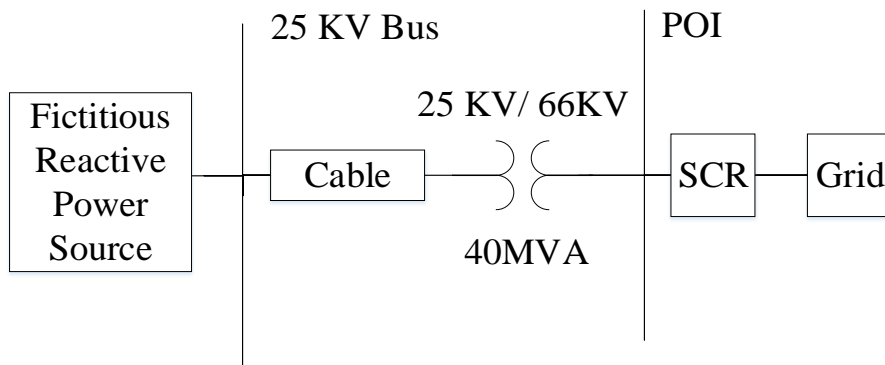


Fig. 3. 4. Simulation model to determine the required reactive power at the POI.

Using simulation data, the mathematical function of the required reactive power to compensate voltage deviation at the POI is obtained through polynomial surface fitting using the MATLAB curve fitting toolbox. The best fitted model is selected based on the goodness of fit and the percentage of errors between calculated and simulated data. Among the evaluated

mathematical models, the poly31 model shows accurate fitting with the dataset. The required reactive power in a poly31 model format can be expressed as follows:

$$Q(x, y) = p_{00} + p_{10}x + p_{01}y + p_{20}x^2 + p_{11}xy + p_{30}x^3 + p_{21}x^2y \quad (4)$$

Where, $Q(x,y)$ is the required reactive power at the POI in per unit to compensate the voltage deviation, x is the voltage deviation ΔU in per unit at the POI, and y is the SCR value at the POI. The power base is the WPP nominal active power rating, and the voltage base is the nominal voltage rating of the POI.

The LAR algorithm provides better goodness of fit results, but the fit computation cannot converge, therefore, only two types of poly31 models, “Bisquare” and “without robustness”, are considered. The coefficients with 95% confidence bound, the goodness of fit data, and the percentage of errors between calculated and simulated reactive power Q values are shown in Tables 3.2 to 3.4. A sample of simulation data together with the calculation data using the chosen fitting functions for SCR equal to 5 can be found in a table in Appendix.

R-square and adjusted R-square for poly31 models in Table 3.3 are similar using either “Bisquare” or “without robustness”. However, the Bisquare algorithm offers much less SSE and RMSE values, which indicates a better accuracy.

The percentage of errors between calculated and simulated Q in Table 3.4 for a case (SCR =15, $\Delta U = 0.95$) is 0.36% for “Bisquare” and 9.2% for “without robustness”. The “Bisquare” cases consistently show smaller errors than the “without robustness” in most cases. Therefore, the poly31 model using Bisquare algorithm is chosen as the final model.

The surface fitting graph and residuals of the final model are shown in Fig. 3.5. The coefficients of the model with 95% confidence bounds in Table 3.2 do not have zero crossing

points, and residuals in Fig. 3.5 (b) is random, both provide further proof that the chosen final model is a well fit of the dataset.

Table 3. 2: Coefficients of poly31 models with 95% confidence Bound

Coefficients	Bisquare	Without Robustness
P ₀₀	29.63 (14.03, 45.23)	81.28 (45.17, 117.4)
P ₁₀	-79.26 (-126, -32.52)	-230 (-338.2, -121.8)
P ₀₁	-1.89 (-2.115, -1.664)	-2.795 (-3.318, -2.273)
P ₂₀	69.53 (22.84, 116.2)	215.5 (107.4, 323.5)
P ₁₁	4.795 (4.343, 5.248)	6.648 (5.6, 7.695)
P ₃₀	-19.89 (-35.43, -4.344)	-66.75 (-102.7, -30.77)
P ₂₁	-2.906 (-3.133, -2.68)	-3.85 (-4.374, -3.326)

Table 3. 3: Goodness of fit data of poly31 models

Name	Bisquare	Without robustness
SSE	0.1277	0.684
RMSE	0.02246	0.05199
R-square	0.9988	0.9934
Adjusted R-square	0.9987	0.9933

Table 3. 4: Errors between simulated and calculated data

Voltage deviation ΔU at POI, p.u	SCR at POI	The required reactive power, p.u.			Errors – calculation vs. simulation, %	
		Calculated by Eq. (4)		Simulated	Bisquare	Without robustness
		Bisquare	Without robustness			
0.9	5	0.4737	0.5228	0.47	0.79	11.2
0.93	4	0.2892	0.3062	0.278	4.03	10.1
0.95	15	0.6694	0.7286	0.667	0.36	9.2
1.05	14	-0.7889	-0.7319	-0.8	-1.39	-8.5
1.06	6	-0.3859	-0.3284	-0.374	3.18	-12.2
1.1	15	-1.8747	-1.9198	-0.209	-10.30	-8.1

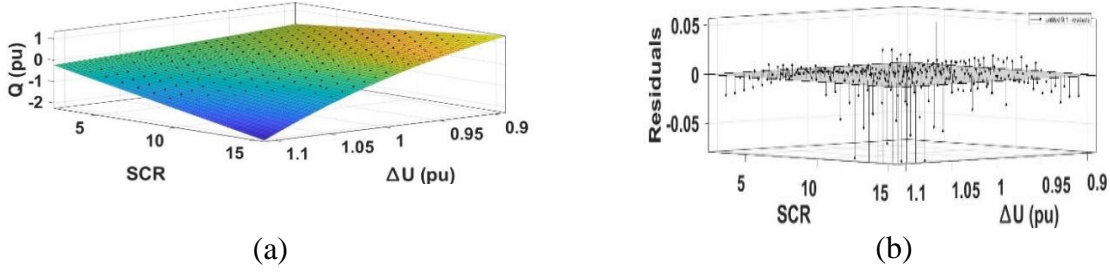


Fig. 3. 5. Poly31 model using “Bisquare”: (a) Surface fitting diagram; (b) Residuals.

3.4.2 Reactive Power Capability of WPP

The reactive power capability of the WPP with collective effect of all WTGs can be modeled through polynomial surface fitting using SCADA measurement data recorded in December 2016 at the POI. Among several models, poly51 is considered to be a suitable regression model as follows:

$$Q(x, y) = p_{00} + p_{10}x + p_{01}y + p_{20}x^2 + p_{11}xy + p_{30}x^3 + p_{21}x^2y + p_{40}x^4 + p_{31}x^3y + p_{50}x^5 + p_{41}x^4y \quad (5)$$

Where, $Q(x,y)$ is the reactive power capability of the WPP in per unit, x is the voltage magnitude V at the POI in per unit, and y is the active power P in per unit. The voltage and power base are the same as Eq. (4). “Bisquare”, “LAR”, and “without robustness” are considered in the surface fitting.

Since P and V values are scattered, to improve the accuracy of the model, V is normalized by a mean of 1.026 and a standard deviation of 0.003761; and P is normalized by a mean of 0.6957 and a standard deviation of 0.2377. To show the effect of the normalization, an example is provided as follows: for $P = 1$ pu and $V = 1.025575$ pu, the SCADA measured Q is 0.21831 pu. The normalized equation calculates Q equal to 0.2146 pu, which matches the measurement well, but the non-normalized equation calculates Q equal to $-9.6167e+04$ pu.

The goodness of fit results, coefficients with 95% confidence bounds, and the percentage of errors between calculated and measured data for the poly51 model are shown in Tables 3.5 to 3.7. As shown in Table 3.5, by using “LAR”, R-square and adjusted R-square for the poly51 model are significantly higher than using “Bisquare” and “without robustness”. Similarly, SSE and RMSE values by using “LAR” are also much smaller than using other two methods. Therefore, “LAR” offers a better surface fitting.

Table 3. 5: Goodness of fit data of poly51 models

Name	Without Robustness	Bisquare	LAR
SSE	254.7	276	138.3
RMSE	0.05734	0.05969	0.04225
R-square	0.4948	0.4525	0.7257
Adjusted R-square	0.4948	0.4524	0.7257

Table 3. 6: Coefficients of the poly 51 model with 95% confidence range.

Coefficients	Without Robustness	Bisquare	LAR
P ₀₀	0.1548 (0.1543, 0.1553)	0.1539 (0.1534, 0.1544)	0.1527 (0.1523, 0.153)
P ₁₀	0.01442(0.01359, 0.01525)	0.01394 (0.01308, 0.01481)	0.01197 (0.01136, 0.01259)
P ₀₁	0.05642 (0.05595, 0.05688)	0.05708 (0.0566, 0.05757)	0.05719 (0.05685, 0.05753)
P ₂₀	-0.006865 (-0.00735, -0.006381)	-0.008626 (-0.00913, -0.008121)	-0.01003 (-0.01039, -0.009671)
P ₁₁	0.003061 (0.00213, 0.003993)	0.002234 (0.001264, 0.003204)	0.007574 (0.006888, 0.008261)
P ₃₀	-0.003022 (-0.003202, -0.002841)	-0.003277 (-0.003464, -0.003089)	-0.004025 (-0.004158, -0.003892)
P ₂₁	-0.001009 (-0.001286, -0.000732)	-0.0005719 (-0.0008603, -0.0002835)	0.001953 (0.001749, 0.002157)
P ₄₀	0.0001382 (8.323e-5, 0.0001931)	0.000429 (0.0003718, 0.0004862)	0.001033 (0.0009926, 0.001074)
P ₃₁	-0.001587 (-0.001747, -0.001427)	-0.001675 (-0.001841, -0.001508)	-0.00307 (-0.003188, -0.002952)
P ₅₀	5.352e-05 (4.602e-5, 6.102e-5)	9.089e-05 (8.309e-05, 9.87e-05)	0.0001818 (0.0001763, 0.0001873)
P ₄₁	-0.0001972 (-0.0002195, -0.0001748)	-0.000217 (-0.0002403, -0.0001938)	-0.0004412 (-0.0004577,-0.0004248)

Table 3. 7: Errors Between the Calculation and Field Measurement Actual Data

Active Power, P, p.u.	Voltage V, p.u.	Reactive Power Capability, Q, p.u.			Measurements	Errors - Calculation vs. Measurements, %		
		Calculation				Without Robustness	LAR	Bisquare
		Without robustness	LAR	Bisquare				
1	1.025575	0.2159	0.2146	0.2129	0.21831	-1.10393	-1.69942	-2.47813
0.99	1.027094	0.2153	0.214	0.2123	0.235089	-8.41766	-8.97065	-9.69378
0.72	1.025481	0.2001	0.1969	0.197	0.189853	5.397334	3.711819	3.764491
0.39	1.020801	0.1814	0.1762	0.1784	0.178564	1.588226	-1.3239	-0.09184
0.3	1.027437	0.1763	0.1704	0.1732	0.15504	13.71259	9.907121	11.71311

Among five arbitrary chosen operating points in Table 3.7, “without robustness” case shows smallest percentage of errors for two operating points, and “LAR” case shows two smallest errors for the remaining two operating points. By considering both goodness of fit and percentage of errors evaluation, the poly 51 model using LAR is chosen as the final model.

The surface fitting graph and residuals of the final model are depicted in Fig. 3.6. From Table 3.5, coefficients with 95% confidence bounds do not have a zero crossing point, which means that the models are not over-fit. Residuals in Fig. 3.6(b) are random.

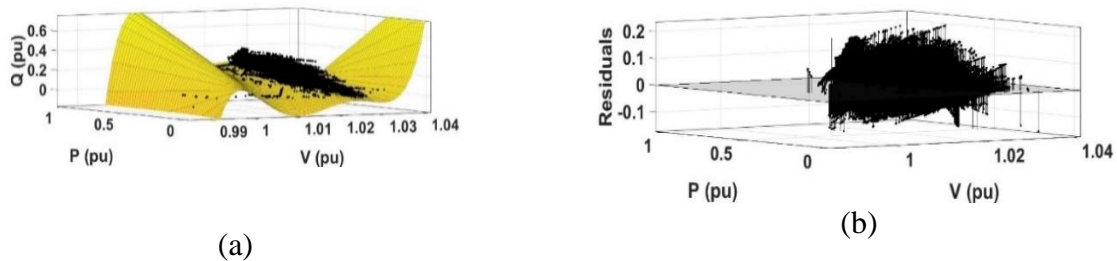


Fig. 3. 6. The developed poly51 model through surface fitting using LAR algorithm based on SCADA field measurement data at POI: (a) Surface fitting diagram; (b) Residuals.

3.5 Two Controllers Design

Two controllers, a central WPP controller and a capacitor controller, are designed in this paper. The overall control block diagram including both controllers is depicted in Fig. 3.7, which

can be divided into three parts, as shown in black, red and green colors. The black portion of the controller is adopted from MATLAB/Simulink toolbox, although this portion is not developed by the authors, it is tuned so that it can follow the characteristic equation developed in Eq. (5). The red and green portions are developed in this paper. The red portion represents the central WPP controller, which is a data driven regression equation based controller sensing a voltage deviation at the POI and determining a reactive power setting-point using Eq. (4). The green portion represents the capacitor controller, which is a program based controller regulating “on” or “off” status of the capacitor banks. The flowchart of the central WPP controller is shown in Fig. 3.8. The detailed design principles are introduced in this section.

In Fig. 3.7, the central WPP controller reads the voltage at the POI (U_{POI}) and compares it with the reference voltage (U_{POI_ref}). If the voltage deviation is within ± 0.05 pu, no voltage compensation action is required, in this case, the central WPP controller will not turn on any capacitor banks, and the WPP continues to supply reactive power to the grid according to its reactive power capability. The central WPP controller reads the operating condition and set reactive power reference (Q_{DFIG}) for the DFIG controller according to Eq. (5). The reactive power supplied by the DFIG to the grid (Q) is measured and compared with a reference (Q_{DFIG}). The error is passed through a reactive power regulator (PI1) and serves as a reference for the direct-axis (d-axis) rotor current (I_{drref}). I_{drref} is then compared with the d-axis rotor current (I_{dr}), and the error serves as an input of the rotor side current regulator (PI3). In the meantime, the speed of the rotor (ω_r) is measured and the reference for active power is calculated from the power-rotor speed tracking characteristics. The cumulative value of the measured active power output of the DFIG to the grid (P) and power losses (p_{loss}) is compared with the reference and the error passes through an active power regulator (PI2). The output of PI2 is the

quadrature-axis (q-axis) rotor current reference (i_{qrref}), which is then compared with the q-axis rotor current (I_{qr}), and the error serves as an input to the rotor-side converter current regulator (PI3). PI3 processes the d- and q-axis rotor currents (I_{dr} and I_{qr}) and provides the reference for the rotor voltage (V_r) to the PWM generator. PWM generator responds accordingly and regulates the switching of the rotor side converter (RSC).

If the voltage deviation at the POI is larger than 0.05 pu, the central WPP controller calculates the reactive power required ($Q_{required}$) to compensate the voltage deviation according to Eq. (4). If, $Q_{required}$ is larger than Q_{DFIG} , the central WPP controller turns on the capacitor controller to regulate switching of capacitor banks and supply additional required reactive power. If the central WPP controller still requires additional reactive power for the case that all capacitor banks are tuned on, this surplus power is supplied by the GSC. The central WPP controller sends the set point for the q-axis component of the GSC current (I_{q_GSC}), this current is compared with I_{qgc} , and the error serves as an input to the GSC current regulator (PI5). The voltage of the dc bus capacitor is controlled by a dc bus voltage regulator (PI4), which generates the reference for d-axis GSC current (I_{dgcref}). I_{dgcref} is then compared with I_{dgc} , the error serves as an input to the PI5. PI5 generates the reference for the GSC's voltage (V_{gc}) and maintains this voltage by adjusting the switching through PWM control.

The simulation of the two new controllers design is conducted using MATLAB/Simulink. The DFIG model in Fig. 3.7 is adopted from MATLAB/Simulink as mentioned in Section II, and the parameters used in the DFIG model are provided in Table 3.1. Other parameters related to the two new controllers are generated as discussed above. Eqs. (4) and (5) are used to determine these parameters.

3.5.1 Central WPP Controller

The central WPP controller maintains the voltage at the POI. Its operation can be divided into three scenarios: 1) normal operation: voltage deviation is within $\pm 5\%$ of the bus nominal voltage, [0.95, 1.05] pu; 2) under voltage: voltage deviation exceeds -5% of the bus nominal voltage (< 0.95 pu); and 3) over voltage: voltage deviation exceeds $+5\%$ of the bus nominal voltage (> 1.05 pu).

3.5.1.1 Normal Operation

According to grid requirements, the acceptable operating voltage at the POI is in the range of [0.95, 1.05] pu. As long as the voltage is in this range, the central WPP controller will not turn on external reactive power compensation. However, it must ensure that the power factor (PF) at the POI remains within the range of $[-0.95, +0.95]$. If the power factor exceeds the limit, the controller will adjust the reactive power set point accordingly. In this scenario, the central controller operates in the reactive power control mode.

3.5.1.2 Under Voltage

If the grid experiences an under voltage below 0.95 pu, the controller will operate in the voltage control mode as follows:

- 1) The required reactive power (Q_{required}) is determined by the central controller using Eq. (4) based on the SCR and ΔU values at the POI;

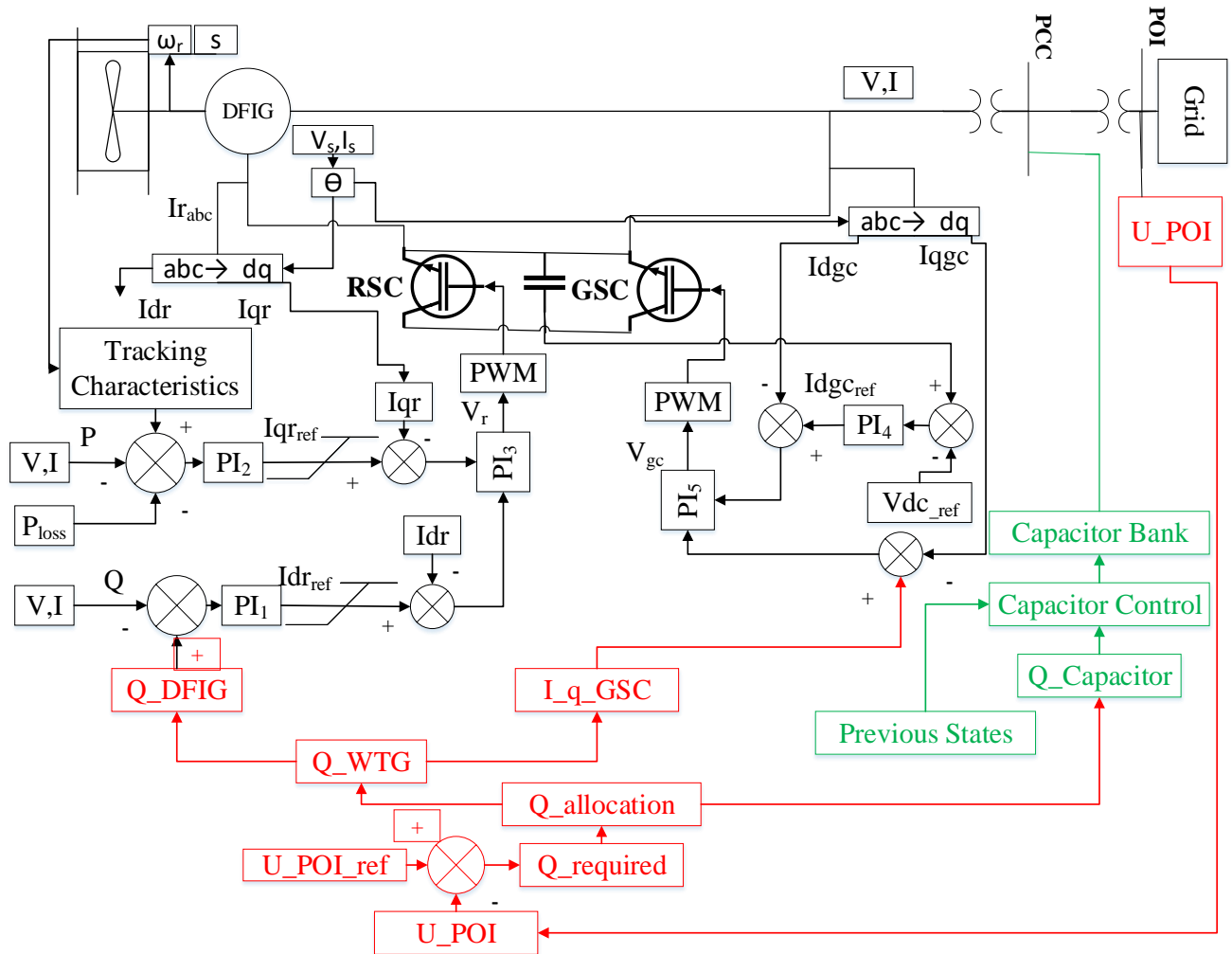


Fig. 3. 7. The overview control block diagrams including both controllers.

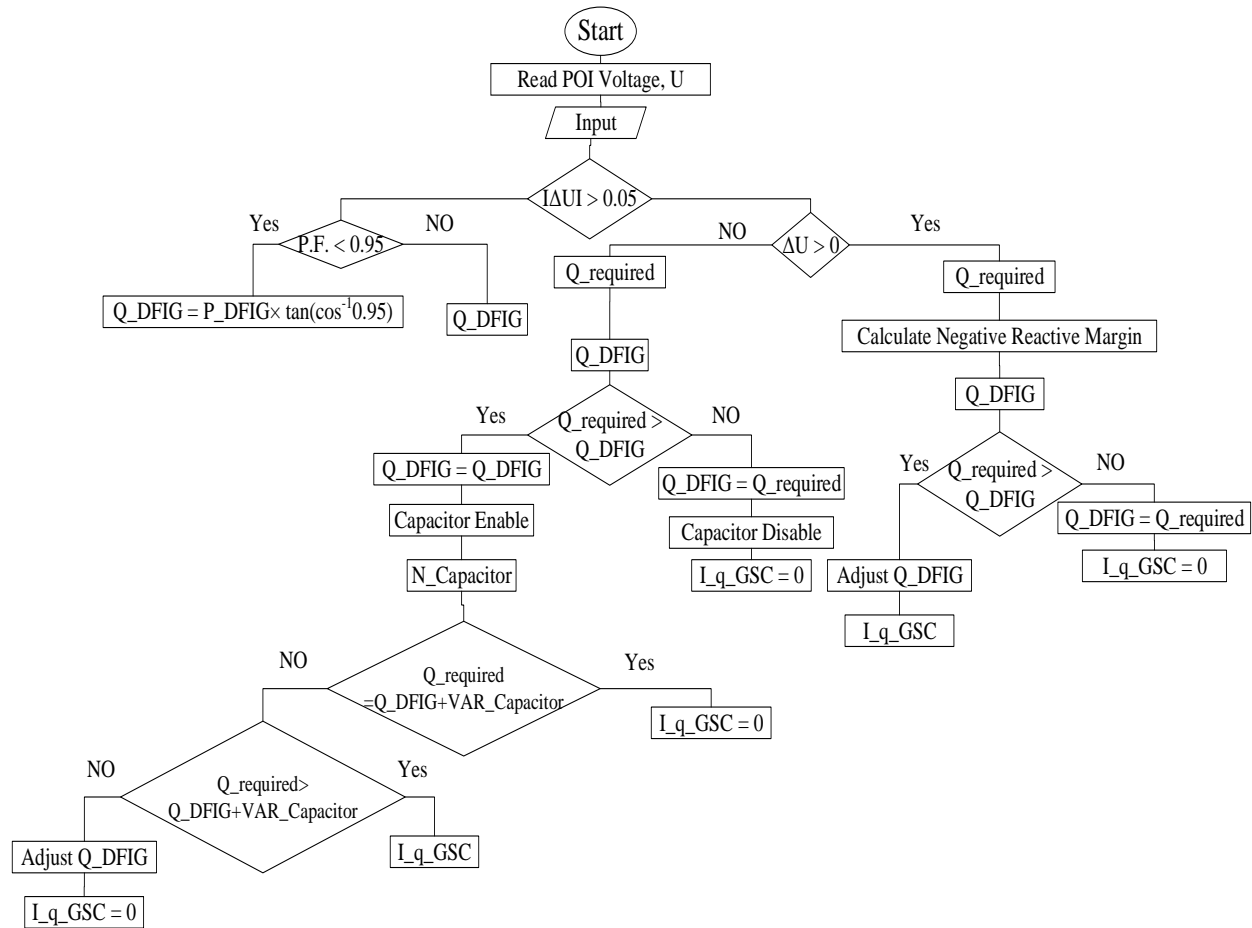


Fig. 3. 8. Flowchart of the proposed Central WPP controller.

2) The reactive power capability of the DFIG/WPP (Q_{DFIG}) is calculated using Eq. (5) based on P and V values at the POI.

3) Compare the two calculated parameters, $Q_{required}$ and Q_{DFIG} . If $Q_{required} < Q_{DFIG}$, the plant has enough capability to compensate the voltage deviation. In this case, Q_{DFIG} should be reduced according to $Q_{required}$. If $Q_{required} > Q_{DFIG}$, the WTGs do not have enough capability to compensate the voltage deviation, and additional reactive power compensation is required. In this case, the residual required reactive power, “residual $Q_{required}$ ”= $Q_{required} - Q_{DFIG}$, is supplied by capacitor banks.

4) To determine the number of capacitor banks, N_{CAP} , needs to turn on, the residual $Q_{required}$ is divided by the Var capacity of one capacitor bank, and the result is always rounded to the nearest larger integer. For example, a value of 0.4 is rounded to 1. By doing this, the total reactive power available in the system with capacitor banks can be calculated as follows:

$$Q_{total} = Q_{DFIG} + N_{CAP} \times (\text{Var capacity}_{per_capacitor_bank}) \quad (6)$$

It may not be equal to $Q_{required}$.

5) If $Q_{total} > Q_{required}$, the difference between them will be reduced from Q_{DFIG} . If $Q_{total} < Q_{required}$, it means after turning on all capacitor banks, the system reaches its maximum reactive power limit, and the grid still requires reactive power to compensate voltage deviation. In this case, the q-axis component of the GSC (I_{q_GSC}) can be turned on. The q-axis component of the rotor current, I_{qr} , controls the q-axis component of the rotor voltage, V_{qr} , which eventually controls the active power generation. Based on active power – voltage magnitude (P-V) curve, there is an inverse relationship between P and V in a stable operation region [60], i.e., the active power reduction results in the voltage increases, and consequently reduces the reactive power requirement. The central controller will continue the process until the POI voltage reaches its nominal voltage so that frequent switching of operational mode and capacitor banks can be avoided. When the voltage reaches one per unit, the central controller goes back to the normal operation status.

3.5.1.3 Over Voltage

Since the maximum allowable voltage swell is 1.05 pu, when the POI voltage exceeds 1.05 pu, the WPP consumes reactive power from the grid to bring it back to the acceptable limit. In this case, the central controller calculates the negative reactive margin of the WPP for a specific active power P to ensure that at least a 15% reactive power reserve is maintained so that the DFIG does

not become unstable. To find the negative reactive margin, the lowest point on the reactive power – voltage magnitude (Q-V) curve should be found first. Eq. (5) is differentiated with respect to the voltage magnitude V, and the first derivative of Q is made equal to zero:

$$\frac{dQ(x,y)}{dx} = (p_{10} + p_{11}y) + (2p_{20} + 2p_{21}y)x + (3p_{30} + 3p_{31}y)x^2 + (4p_{40} + 4p_{41}y)x^3 + (5p_{50})x^4 = 0 \quad (7)$$

Solve Equ. (7) and substitute the highest root below 1 pu in Eq. (5), the calculated reactive power capability is the negative reactive margin [60][61]. If $Q_{\text{required}} > Q_{\text{DFIG}}$, the central controller send a set point for I_{q_GSC} within its capability limit. Grid and rotor side converter can handle the maximum 0.5 pu of the nominal MVA of the WPP.

3.5.2 Capacitor Controller

When external reactive power compensation is required, the central WPP controller sends a signal to the capacitor controller. This signal contains the instruction whether the reactive power compensation system should be turned on (CAP_enable). If yes, the number of capacitor banks (N_CAP) should be brought online. In practical operation, frequent switching of a capacitor will affect its capability and durability, a capacitor controller can prevent this issue. The flowchart of the capacitor controller is shown in Fig. 3.9.

To prevent frequent switching, the capacitor controller ensure that a capacitor bank, which was turned on in previous state, will not be turned on in next state unless all other capacitor banks have been turned on and more external reactive power support is necessary. Therefore, the capacitor controller stores switching states of all capacitor banks in the form of 0 and 1, where 0 and 1 represent off and on, respectively. If no capacitor is turned on, then switching states are not stored and previous states (P.S.) remain on the memory. In the next state, the capacitor controller

generates a signal for capacitor banks by processing the following three parameters: CAP_enable, N_CAP and P.S. If the external reactive power is not required, capacitor banks are disconnected from the system. If the external reactive power is required, the capacitor controller reads previous states and reverse previous switching states. The number of 1 (N_ones) in the reversed states are counted and compares with the N_CAP. If they are equal, it means the required number of capacitor banks are available to bring online, the controller turns on respective capacitor banks and saves the switching states. If $N_CAP > N_ones$, it means more capacitor banks are needed than available, the controller searches for zero from the beginning of the inverted states and convert into 1. After each conversion, N_ones is counted and compared with N_CAP. Similarly, when $N_CAP < N_ones$, 1 is reversed. The process continues until $N_CAP = N_ones$. At this time, control signals are sent to the respective capacitor banks, and the states are saved to the memory.

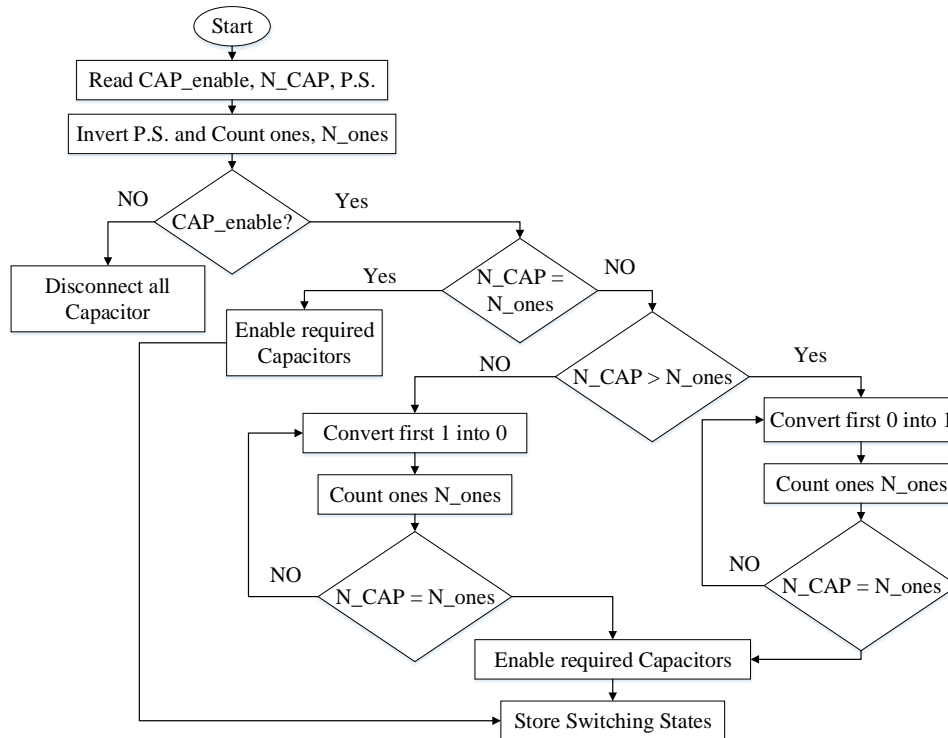


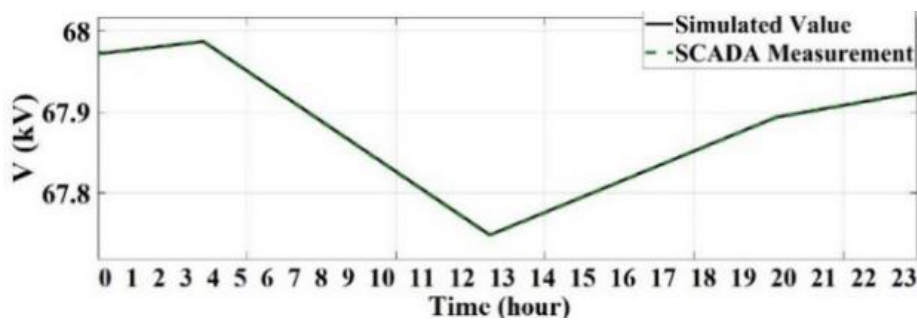
Fig. 3. 9. Flowchart of the proposed capacitor controller

3.6 Case Studies

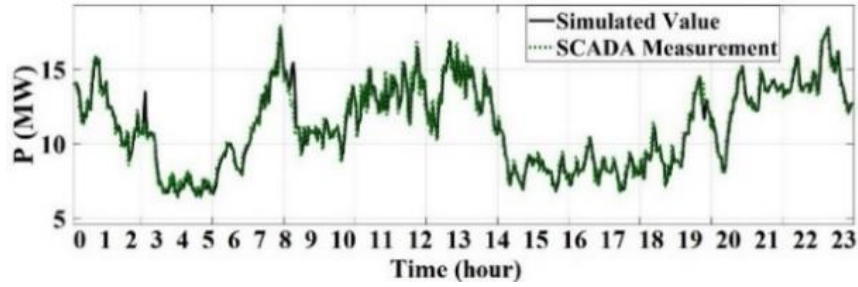
To validate the proposed data driven voltage control approach for WPPs, five case studies are conducted in this section. First of all, the WPP under study in Section II is used in Case I to validate the accuracy of our WPP base model without controllers. In this case, the base model simulation results are compared to SCADA field measurement data for a given voltage sag. After the base model is validated through Case 1, it can be used in the voltage controller design. The rest case studies are for the system under normal, under-voltage, and over-voltage conditions.

3.6.1 Case 1 – Base Model without Controllers

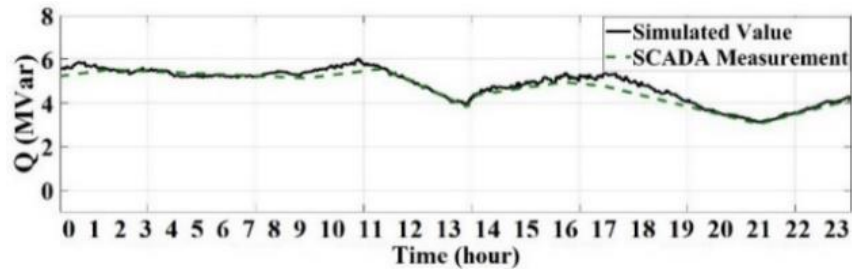
To evaluate the accuracy of the WPP base model without controller, Case 1 is conducted. The SCADA measurement data from 12 am to 23 pm on June 19, 2016 are compared with simulated values. The measured voltage at the POI and the active power generation of the WPP are entered in the base model according to SCADA measurement (Fig. 3.10 (a) and (b)), the simulated reactive power generation of the WPP is then compared with the SCADA measurement in Fig. 3.10 (c). It is clear from Fig. 3.10 (c) that the reactive power response of the WPP is closely following the SCADA measurement. Therefore, the base WPP model without controllers is considered to be accurately representing the real WPP.



(a)



(b)



(c)

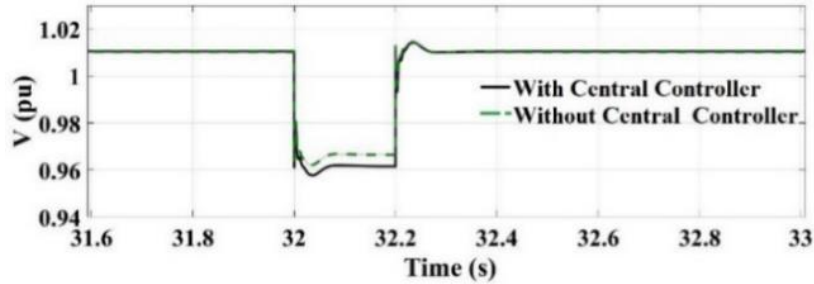
Fig. 3. 10. Simulation results vs. SCADA field measurements for the base WPP model without controllers for the 27 MW WPP in NL, Canada (Case 1): (a) voltage at the POI, (b) active power supplied by WTG, (c) reactive power supplied by WTG.

3.6.2 Case 2 - Normal Operation with Power Factor Control

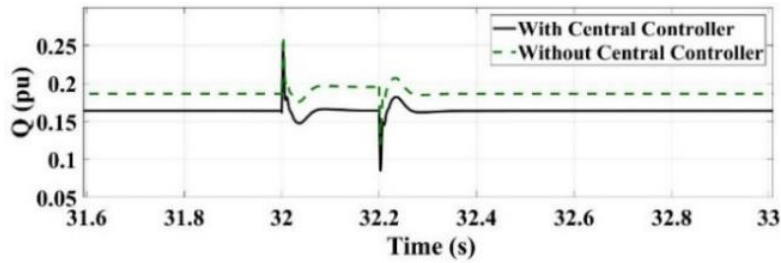
In Case 2, the simulation is conducted for the WPP model with controllers under normal operation. In this case, a 96% voltage sag at POI starts at 32 s and lasts for 0.2 ms.

Before the voltage disturbance, the voltage at POI is 1.01 pu (Fig. 3.11 (a)). The SCR is 5. The active power is 0.502 pu (Fig. 3.11 (c)). As the voltage remains within the permissible limit, no capacitor banks are turned on, and the WTG supplies reactive power according to the reference sent by the central controller. The main objective of the central controller in this case is to keep the power factor (PF) within ± 0.95 at the POI.

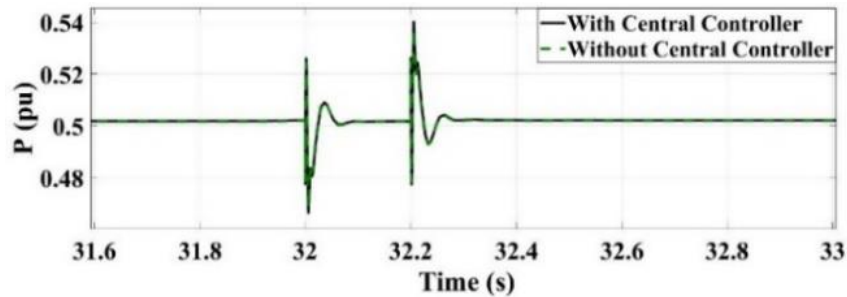
According to Eq. (5), the reactive power capability of the WTG is 0.185 pu in this case. Because the PF at the POI is around 0.935, which exceeds the permissible limit, the central controller adjusts the reactive power set point of the WPP to 0.165 pu so that +0.95 PF can be maintained (Fig. 3.11 (d)). Although the voltage profile is slightly better without any central controller, it cannot keep the PF at the POI within the permissible limit during and after the voltage sag. After the clearance of the voltage sag, the voltage at the POI goes back to 1.01 pu. The central controller still remains in the PF control mode and maintains a permissible PF by adjusting the reactive power reference of the WTG.



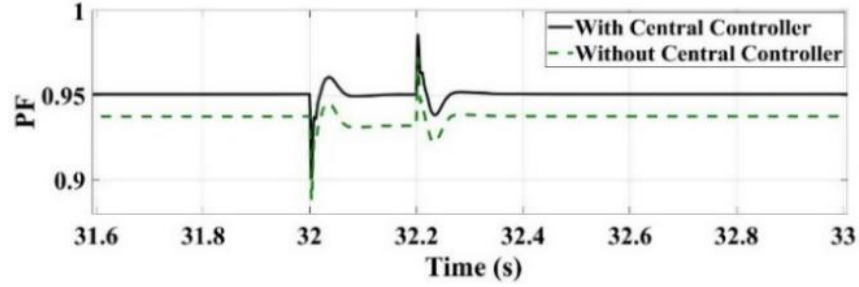
(a)



(b)



(c)



(d)

Fig. 3. 11. Simulation results (Case 2): (a) voltage at POI, (b) reactive power supplied by WTG, (c) active power supplied by WTG, and (d) PF at POI.

3.6.3 Case 3 - Under Voltage

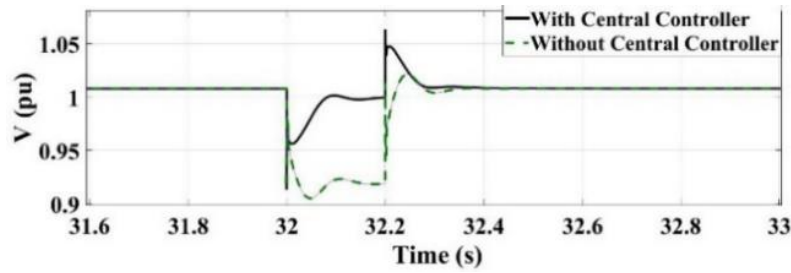
In Case 3, the simulation is conducted for the WPP model with controllers at under-voltage operation. A 92% voltage sag at the POI starts at 32 s and lasts for 0.2 ms. The pre-disturbance voltage is 1.01 pu. Before the voltage sag, the real power P supplied by the WPP at the POI is 0.3 pu. The SCR of the system is 5.

As the voltage at the POI is below 0.95 pu, the central WPP controller is at the voltage control mode. According to Eq. (4), the required reactive power at the POI, Q_{required} , is 0.3911 pu. The reactive power capability of the WPP, Q_{DFIG} , calculated by Eq. (5) is 0.1719 pu. The central WPP controller sends signals to the capacitor controller to turn on capacitor banks. Four capacitor banks, each rated at 1.5 MVar at 25 kV, with a total of 6 Mvar or 0.22 pu capacity are turned on based on the calculation. Therefore, the reactive power set point during the fault, Q_{DFIG} , is adjusted to be 0.1711 pu.

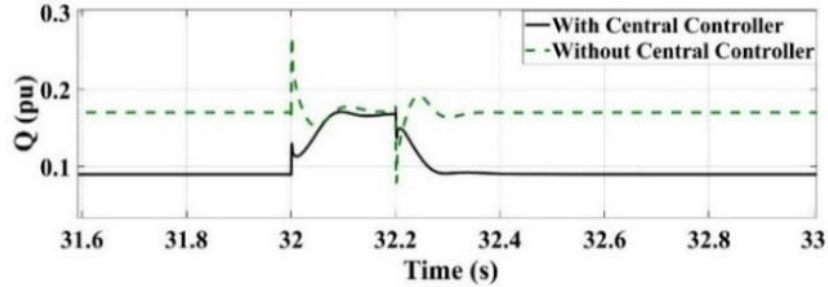
As shown in Fig. 3.12(b), before the voltage sag, the central controller ensures a 0.95 PF at the POI, and the corresponding active power supplied by the system is 0.3 pu, therefore, the central controller adjusts its reactive power set point to be 0.099 pu before the voltage sag. The total reactive power response during the fault can be found in Fig. 3.12(b).

As the total reactive power required to compensate the voltage sag is supplied by the WPP system, the GSC does not supply any reactive power.

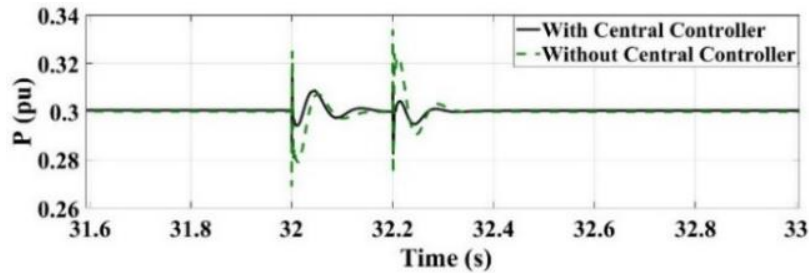
As shown in Fig. 3.12, immediately after the clearance of the voltage sag, because of the surplus injection of reactive power by capacitor banks, the voltage rises sharply. Once the controller enters the normal operating mode, the capacitor banks are turned off, and the POI voltage starts to decrease.



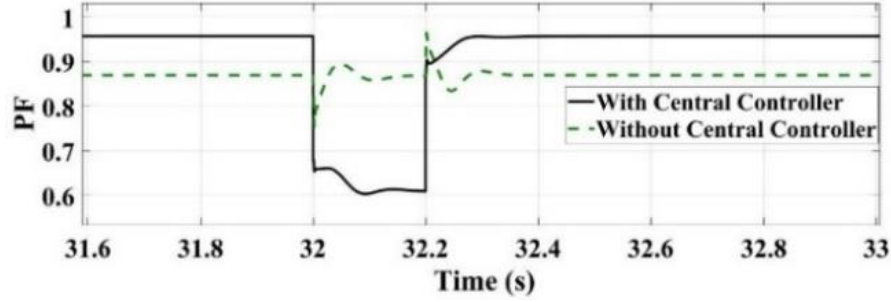
(a)



(b)



(c)



(d)

Fig. 3. 12. Simulation results (Case 3): (a) voltage at POI, (b) reactive power supplied by WTG, (c) active power supplied by WTG, and (d) PF at POI.

3.6.4 Case 4 - Over Voltage

In Case 4, the simulation is conducted for the WPP model with controllers under over-voltage operation. The voltage is raised at the POI by 0.06 pu at 32s and last for 0.2 s. The SCR at the POI is 5 and the active power P supplied by the WPP at the POI is 0.695 pu. Before this disturbance, the voltage at the POI is 1.01 pu, and the reactive power supplied by the WPP is 0.1956 pu.

As the voltage increases above 1.05 pu, the WPP starts to consume reactive power from the grid. Based on our central controller design principle, the controller secures at least 15% reserve from the negative reactive margin. During the voltage swell, the reactive power capability of the WPP, Q_{DFIG} , is -0.1948 pu without a central controller (calculated by Eq. (5)), which is very close to negative reactive margin (-0.1984 pu). As the negative reactive margin depends on P and V, therefore, for $P = 0.695$ pu, V is calculated using Eq. (7), substitute these P and calculated V values in Eq. (5), the negative reactive margin (-0.1984 pu) is calculated. With the central WPP controller, it secures 15% reserve from the negative reactive margin, and Q_{DFIG} is adjusted to -0.168 pu (Fig. 3.13(b)). As the reactive power capability (-0.1948 pu) is very close to its negative reactive margin (-0.1984 pu), the central WPP controller adjusts its reactive power capability to ($-0.1984 \times 0.85 = -0.168$ pu) to ensure a 15% reserve to its negative reactive margin. In this way,

the central WPP controller avoid the possibility of crossing the negative reactive margin. In Fig. 3.13 (d), the negative PF represents that the WPP system consumes reactive power from the grid.

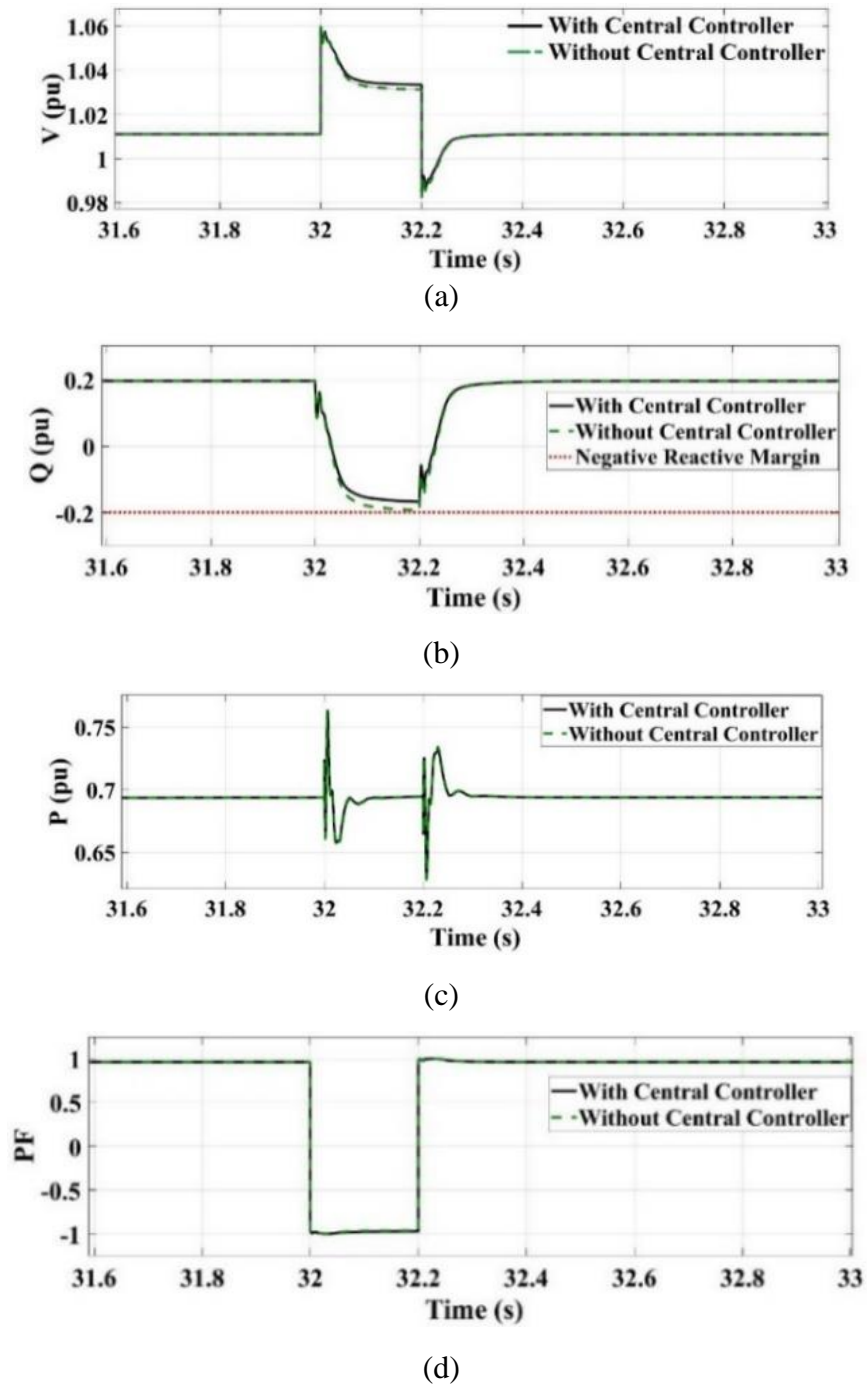
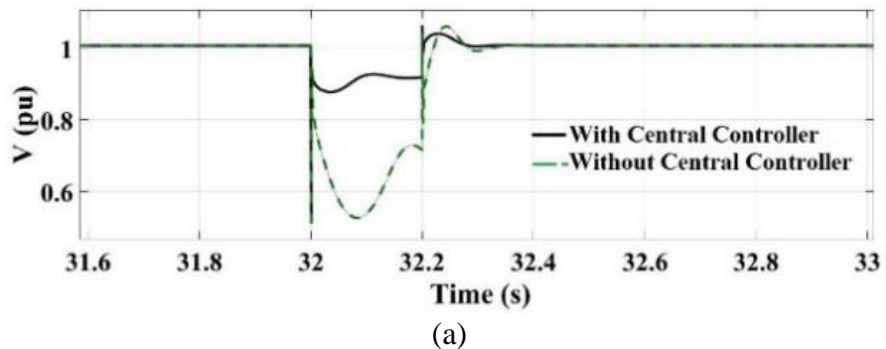


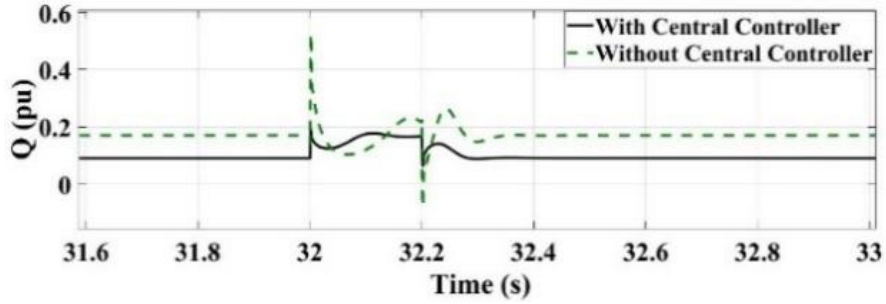
Fig. 3. 13. Simulation results (Case 4): (a) voltage at POI, (b) reactive power supplied by WTG, (c) active power supplied by WTG, and (d) PF at POI.

3.6.5 Case 5 – A 50% Voltage Sag at The POI

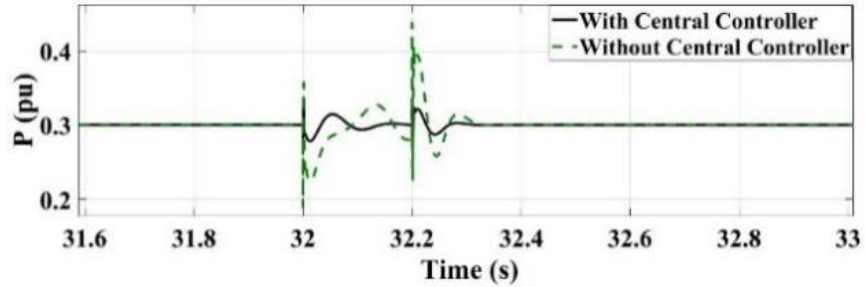
In Case 5, a severe voltage sag of 50% at the POI is applied, which starts at 32 s with a 0.2 s duration. Before the disturbance, the voltage at the POI is 1.01 pu, the real power supplied by the WPP at the POI is 0.3 pu, the central WPP controller adjusts the reactive power setting-point to 0.099 pu to meet the power factor limit of 0.95. The SCR of the system at the POI is assumed to be 15.

When the voltage sag occurs with the voltage at the POI below 0.95 pu, the central WPP controller is at the voltage control mode. According to Eq. (4), the required reactive power at the POI, Q_{required} , is 1.6112 pu. The reactive power capability of the WPP, Q_{DFIG} , calculated by Eq. (5) is 0.1741 pu. The central WPP controller turns on six 1.5 MVar capacitor banks through the capacitor controller that supply 9 MVar or 0.33 pu of reactive power. Although it cannot fully compensate the voltage deviation during the fault as the system cannot supply the required amount of reactive power, it significantly improves the voltage profile at the POI as shown in Fig. 3.14 (a).

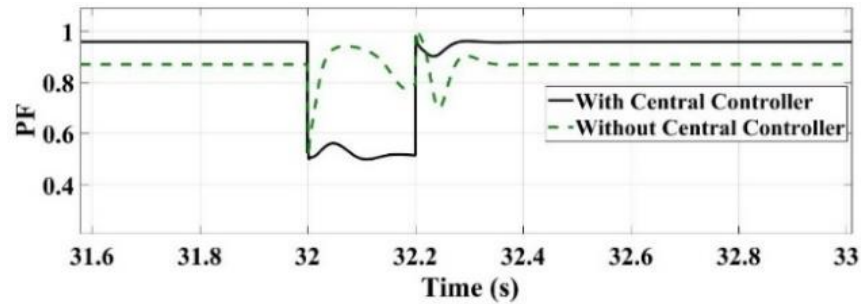




(b)



(c)



(d)

Fig. 3. 14. Simulation results (Case 5): (a) voltage at POI, (b) reactive power supplied by WTG, (c) active power supplied by WTG, and (d) PF at POI.

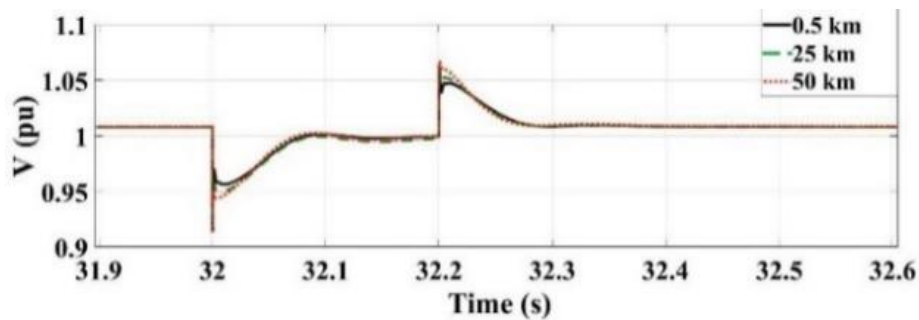
3.7 Sensitivity Studies

In this section, sensitivity studies are conducted to evaluate impacts of several parameters on dynamic performance of the proposed control scheme. The parameters include: 1) the length of transmission lines, 2) communication delay, and 3) X/R ratio of the utility grid. For all cases, a 92% voltage sag is applied at 32 s and cleared at 32.2 s. A total of 0.3911 pu reactive power is required to compensate the voltage deviation, therefore, four capacitor banks, each rated at 1.5 MVar are turned on, the rest of the reactive power is supplied by WTGs.

3.7.1 Scenario 1 - The Length of Transmission Lines

WPPs are generally located in a remote location and connected to the utility grid through a transmission line. To evaluate the impact of the length of interconnection transmission lines in the proposed voltage control operation, three sets of lengths are considered: 0.5 km (short), 25 km (medium) and 50 km (long). A 92% voltage sag is applied for the three configurations. The resistance of the transmission line is $0.1153 \Omega/\text{km}$, and the reactance is $0.3958 \Omega/\text{km}$ (See Table 3.1 Cable Data). The impact of the length of transmission lines on the power grid voltage, WTG active and reactive power generation and PF at the POI are shown in Fig. 3.15.

Fig. 3.15 indicates that the steady-state performance of the three configurations are similar although the transient performance is slower and flatter for the long transmission line than the short and medium ones. For the short transmission line, the WPP system responds immediately due to voltage variations in the grid. With the initiation of the voltage sag, the WTG increases its reactive power generation right away, hence the voltage recovery process at the POI starts faster than medium and long transmission lines. Similar characteristics are also visible for the active power P and power factor during and after the voltage sag.



(a)

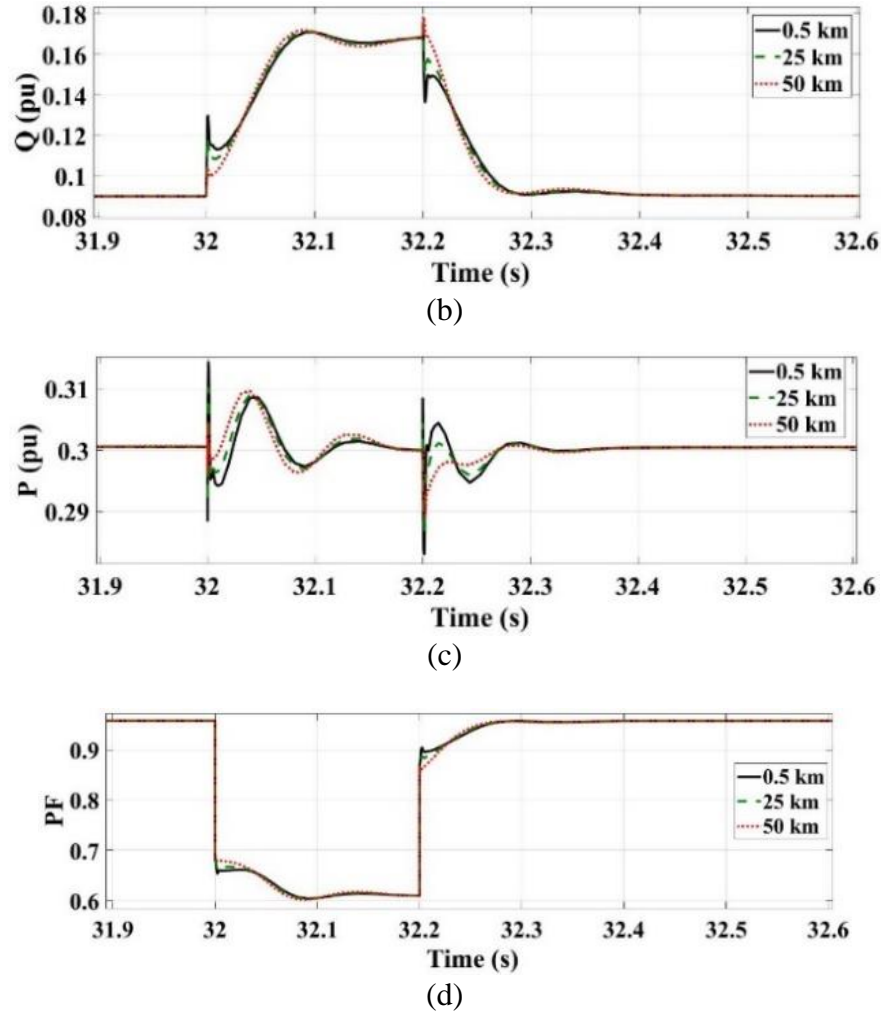
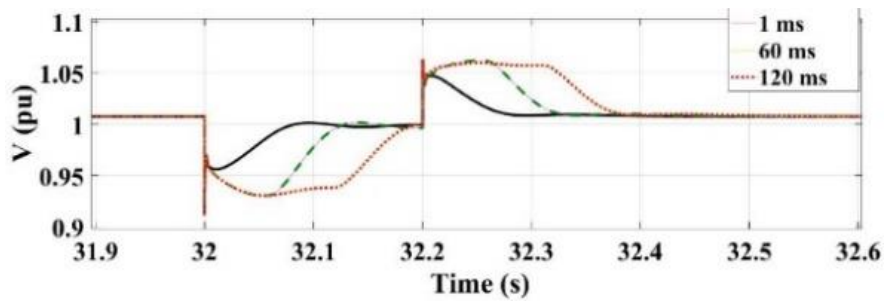


Fig. 3. 15. Simulation results (Scenario 1): (a) voltage at POI, (b) reactive power supplied by WTG, (c) active power supplied by WTG, and (d) PF at POI.

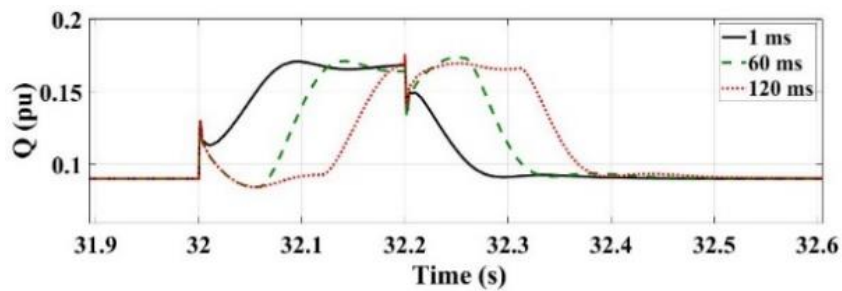
3.7.2 Scenario 2 - Communication Delay

Communication delay is a major concern in WPP operation. Because of the geographic span of the WPP and the bandwidth of the communication link, there is always a communication delay between the central controller and the individual WTG. To evaluate the impact of communication delay in voltage control operation, three sets of communication delay are considered, 1 ms, 60 ms and 120 ms. A 92% voltage sag is applied. The influence of communication delay on the grid voltage, WTG active and reactive power generation, and the PF at the POI are shown in Fig. 3.16.

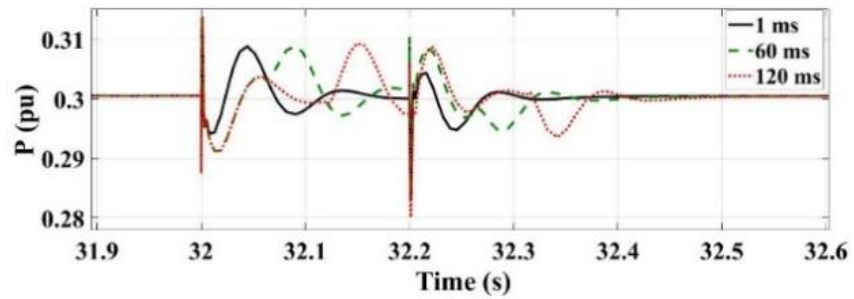
Fig. 3.16 indicates that communication delay can significantly affect dynamic characteristics of the WPP using the proposed control scheme. As the communication delay increases, the time required to stabilize the voltage during and after the disturbance increases. A communication delay is greater than 120 ms cannot compensate the voltage during the disturbance. For all three different delays, the magnitude of the active power fluctuation during and after the disturbance are the same, but it takes a longer time to return to the normal value with a longer communication delay. Fig. 3.16 (c) shows that the active power of the WTG experiences more fluctuation with the increase of communication delay. The 60 ms and 120 ms delays pose similar performance for the PF at the POI, and it takes longer time than the 1ms delay to get back to +0.95 PF limit after the voltage sag clearance. To make an effective contribution in the voltage control process, communication delay between central and WTG controllers should be kept as small as possible. The delay must not be greater than 120 ms.



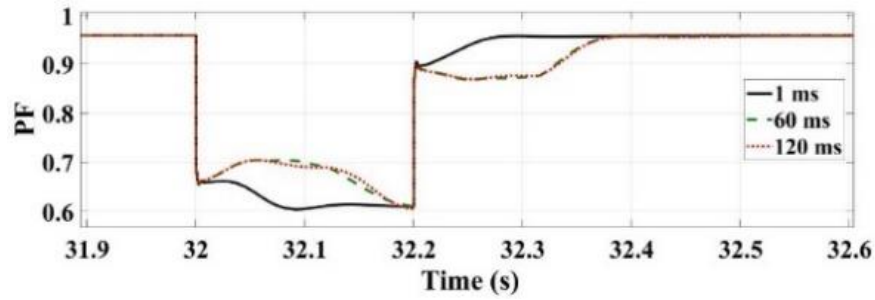
(a)



(b)



(c)



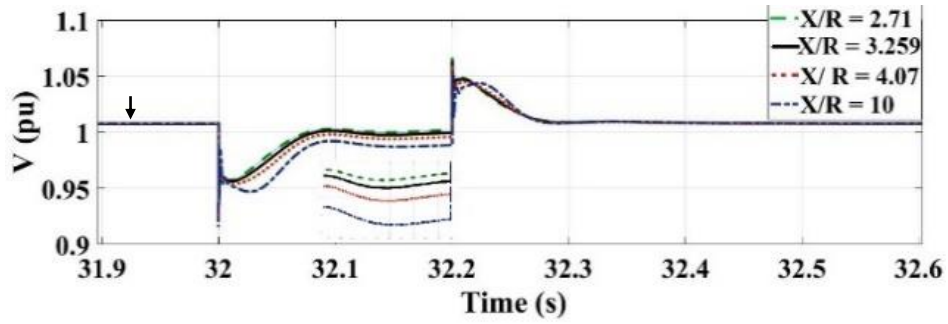
(d)

Fig. 3. 16. Simulation results (Scenario 2): (a) voltage at POI, (b) reactive power supplied by WTG, (c) active power supplied by the WTG and (d) PF at POI.

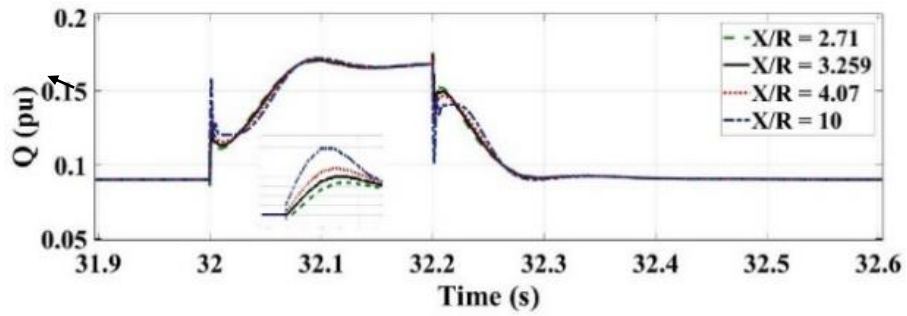
3.7.3 Scenario 3 - X/R Ratio of the Utility Grid

To evaluate the impact of X/R ratio of the utility grid in voltage control operation, four sets of X/R ratio are considered, 2.71, 3.259, 4.07 and 10. The effect of X/R ratio on the grid voltage, WTG active and reactive power generation, and the PF at the POI are shown in Fig. 3.17.

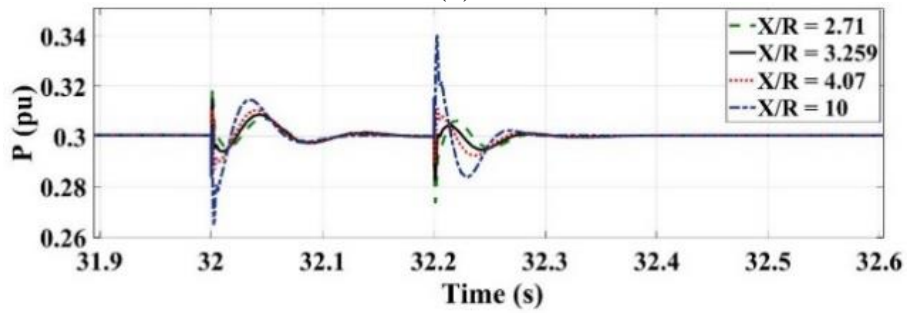
Fig. 3.17 indicates that the X/R ratio of the utility grid has influence on dynamic characteristics of the system. Fig. 3.17 (a) shows that the voltage compensation performance for various X/R ratios. Although the impacts of X/R ratio are similar on active and reactive power during stable situations, but by the inception of a voltage change, WTGs connected to a grid with a higher SCR experience a larger peak. Therefore, caution should be exercised when the WPP is connected to a utility grid with a higher X/R ratio.



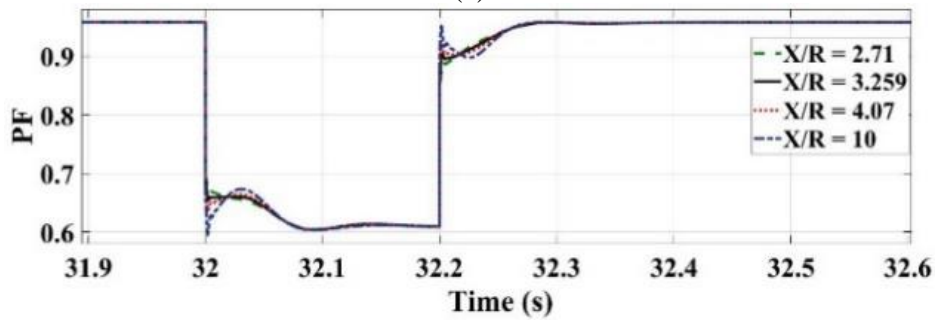
(a)



(b)



(c)



(d)

Fig. 3. 17. Simulation results (Scenario 3): (a) voltage at POI, (b) reactive power supplied by WTG, (c) active power supplied by WTG, and (d) PF at POI.

3.8 Conclusion

In this paper, a data-driven voltage control approach for grid-connected WPPs is proposed and implemented by designing a central WPP controller and a capacitor controller on a sample 27 MW WPP currently in operation in Newfoundland and Labrador, Canada. Although many data-driven based research in wind power industry were reported in the literature during the past decade, this paper is the very first one to propose a data-driven controllers designed for the voltage control.

The controller design is carried out using the SCADA field measurements recorded in 2016 at the POI of the sample WPP. Two factors are considered as the parameters for the controller design in the proposed method, which have not been done in the literature: one factor is the SCR at the POI, another factor is the reactive power capability of the WPP. Each factor is included in the form of a mathematical equation, which can be easily implemented in the controller design scheme. These equations are regression models developed using simulation data and SCADA measurement data through MATLAB curve fitting toolbox.

The reactive power compensation devices are capacitor banks in this study, it offers a lower cost solution and superior dynamic performance through the combination of the new central WPP controller and capacitor controller, working together with the existing individual WTG controllers. The proposed data-driven based voltage controllers are extensively validated through several case and sensitivity studies.

Appendix

Table 3. 8: Simulated and calculated data for required reactive power to Compensate Different voltage condition at POI when SCR is 5

Voltage deviation ΔU at POI, p.u	SCR at POI	The required reactive power, p.u.		
		Calculated		Simulated
		Bisquare	Without robustness	
1.10	5	-0.5571	-0.5128	-0.544
1.09	5	-0.4933	-0.442	-0.481
1.08	5	-0.4315	-0.3756	-0.424
1.07	5	-0.3716	-0.3132	-0.365
1.06	5	-0.3134	-0.2544	-0.309
1.05	5	-0.2569	-0.1988	-0.252
1.04	5	-0.2019	-0.1461	-0.196
1.03	5	-0.1484	-0.0957	-0.143
1.02	5	-0.0961	-0.0473	-0.0907
1.01	5	-0.045	-5.67E-04	-0.04
1.00	5	0.005	0.045	0.00
0.99	5	0.0541	0.0898	0.063
0.98	5	0.1024	0.1341	0.107
0.97	5	0.15	0.1785	0.156
0.96	5	0.197	0.2233	0.2
0.95	5	0.2436	0.2688	0.252
0.94	5	0.2898	0.3156	0.296
0.93	5	0.3358	0.364	0.337
0.92	5	0.3817	0.4144	0.381
0.91	5	0.4276	0.4672	0.422
0.9	5	0.4737	0.5228	0.47

References

- [1] “Integrating Inverter-Based Resources into Weak Power Systems”, Reliability Guideline, The North American Electric Reliability Corporation (NERC), 3353 Peachtree Road NE, Suite 600, North Tower, Atlanta, GA, United States, July 2017.
- [2] “Requirements for offshore grid connections in the grid of Tennet TSO GmbH”, Tennet, Germany, pp. 1–14, 2012.
- [3] M.Mohseni and S. M. Islam, “Review of international grid codes for wind power integration: diversity, technology and a case for global standard”, *Renew. Sustain. Energy Rev.*, vol. 16, no. 6, pp. 3876–3890, Aug. 2012.
- [4] M. Tsili and S. Papathanassiou, "A review of grid code technical requirements for wind farms," *IET Renew. Power Gener.*, vol. 3, no. 3, pp. 308-332, Sept. 2009.
- [5] “Grid Code: High and Extra High Voltage”, E. ON Netz GmbH, Bayreuth, Germany, Aug. 2006.
- [6] “Cracking the grid code with reactive power compensation,” ABB, <http://www.abb.com/cawp/seitp202/8c8b05431439be2fc125794100410c36.aspx>, visited at 1:10 pm on March 30, 2018.
- [7] N. R. Ullah, K. Bhattacharya and T. Thiringer, "Wind farms as reactive power ancillary service providers - technical and economic issues," *IEEE Trans. Energy Convers.*, vol. 24, no. 3, pp. 661-672, Sept. 2009.
- [8] W. Edmondson and S. Mukherjee, "Adaptive capacitor switching for wind energy generation," *2017 IEEE Ind. Appl. Soc. Annu. Meeting*, Cincinnati, OH, USA, 2017, pp. 1-6.

- [9] H. Xu, J. Hu, and Y. He, "Operation of wind-turbine-driven DFIG systems under distorted grid voltage conditions: analysis and experimental validations," *IEEE Trans. Power Electron.*, vol. 27, no. 5, pp. 2354–2366, May 2012.
- [10] M. Mohseni, and S. M. Islam, "Transient control of DFIG-based wind power plants in compliance with the Australian grid code," *IEEE Trans. Power Electron.*, vol. 27, no. 6, pp. 2813–2824, Jun. 2012.
- [11] A. Camacho, M. Castilla, J. Miret, R. Guzman, and A. Borrell, "Reactive power control for distributed generation power plants to comply with voltage limits during grid faults," *IEEE Trans. Power Electron.*, vol. 29, no. 11, pp. 6224–6234, Nov. 2014.
- [12] D. R. Simon, H. Ergun, D. V. Hertem, and J. Driesen. "Grid impact of voltage control and reactive power support by wind turbines equipped with direct-drive synchronous machines." *IEEE Trans. Sustainable Energy*, vol. 3, no. 4, pp. 890-898, Oct. 2012.
- [13] W. Qiao and R. G. Harley, "Grid connection requirements and solutions for DFIG wind turbines," *2008 IEEE Energy 2030 Conference*, Atlanta, GA, USA, 2008, pp. 1-8.
- [14] C. Feltes, S. Engelhardt, J. Kretschmann, J. Fortmann, F. Koch, and I. Erlich, "High voltage ride-through of DFIG-based wind turbines," *Proc. IEEE Power and Energy Soc. General Meeting*, Pittsburgh, PA, USA, 2008, pp. 1–8.
- [15] K. K. Yagnik and V. Ajjarapu, "Consideration of the wind and solar generation reactive power capability on grid voltage performance," *2012 IEEE Power and Energy Soc. General Meeting*, San Diego, CA, USA, 2012, pp. 1-7.
- [16] M. H. Hassan, D. Helmi, M. Elshahed and H. Abd-Elkhalek, "Improving the capability curves of a grid-connected wind farm: Gabel El-Zeit, Egypt," *2017 Nineteenth Int. Middle East Power Syst. Conf. (MEPCON)*, Cairo, Egypt, 2017, pp. 300-307.

- [17] R. S. Moura, A. C. Zambroni de Souza, B. I. L. Lopes and F. W. Mohn, "Effects of QV curves in the dynamic behaviour of power systems," *IET Gener. Transm. Distrib.*, vol. 10, no. 12, pp. 2861-2870, May 2016.
- [18] "Wind turbine plant capabilities report: 2013 wind integration studies," AEMO (Australian Energy Market Operator), Australia, 2013.
- [19] Z. Huang, L. Bao, and W. Xu, "A method to measure QV curves and its applications in power systems," *Elect. Power Energy Syst.*, vol. 29, no. 2, pp. 147–154, Feb. 2007.
- [20] A. Chowdhury, X. Liang, N. Khan, and H. Zhang. "Determine Q–V characteristics of grid-connected wind farms for voltage control using a data-driven analytics approach." *IEEE Trans. Ind. Appl.*, vol. 53, no.5, pp. 4162-4175, Sept. 2017.
- [21] A. D. Hansen, M. Altin and N. A. Cutululis, "Modelling of wind power plant controller, wind speed time series, aggregation and sample results," Technical University of Denmark, Lyngby, Denmark, *DTU Wind Energy E-0064*, 2015.
- [22] A. Tapia, G. Tapia, and J. X. Ostolaza, "Reactive power control of wind farms for voltage control applications," *Renew. Energy*, vol. 29, no. 3, pp. 377–392, Mar. 2004.
- [23] D. Hansen, P. Sorensen, F. Iov, and F. Blaabjerg, "Centralised power control of wind farm with doubly fed induction generators," *Renew. Energy*, Vol. 31, No. 7, pp. 935–951, Jun. 2006.
- [24] M. E. Moursi, G. Joos, and C. Abbey, "A secondary voltage control strategy for transmission level interconnection of wind generation," *IEEE Trans. Power Electron.*, Vol. 23, No. 3, pp. 1178–1190, May 2008.

- [25] J. Martínez, P. Kjaer, P. Rodriguez, and R. Teodorescu, "Design and analysis of a slope voltage control for a DFIG wind power plant," *IEEE Trans. Energy Convers.*, vol. 27, no. 1, pp. 11–20, Mar. 2012.
- [26] L. Petersen, F. Kryezi and F. Iov, "Design and tuning of wind power plant voltage controller with embedded application of wind turbines and STATCOMs," *IET Renew. Power Gener.*, vol. 11, no. 3, pp. 216-225, Feb. 2017.
- [27] J. Fortmann and I. Erlich, "Use of a deadband in reactive power control requirements for wind turbines in European grid code," *Proc. 11th Int. Workshop Large-Scale Integr. Wind Power Syst.*, Lisbon, Portugal, 2012, pp. 13–15.
- [28] J. Kim, J. Seok, E. Muljadi, and Y. C. Kang "Adaptive Q–V scheme for the voltage control of a DFIG-based wind power plant", *IEEE Trans. Power Electron.*, Vol. 31, no. 5, pp. 3586-3599, May 2016.
- [29] J. Kim, E. Muljadi, J. Park, and Y. C. Kang. "Flexible I_Q –V scheme of a DFIG for rapid voltage regulation of a wind power plant." *IEEE Trans. Ind. Electron.*, Vol. 64, no. 11, pp. 8832-8842, Nov. 2017.
- [30] V. Galdi, A. Piccolo, and P. Siano, "Designing an adaptive fuzzy controller for maximum wind energy extraction," *IEEE Trans. Energy Convers.*, vol. 23, no. 2, pp. 559 – 569, Jun. 2008.
- [31] A. Kusiak, Z. Song, and H. Zheng, "Anticipatory control of wind turbines with data-driven predictive models," *IEEE Trans. Energy Convers.*, vol. 24, no. 3, pp. 766 - 774, Sept. 2009.
- [32] A. Kusiak, Z. Zhang, and M. Li, "Optimization of wind turbine performance with data-driven models," *IEEE Trans. Sustainable Energy*, vol. 1, no. 2, pp. 66 - 76, Jul. 2010.

- [33] A. Kusiak, and Z. Zhang, "Adaptive control of a wind turbine with data mining and swarm intelligence," *IEEE Trans. Sustainable Energy*, vol. 2, no. 1, pp. 28 - 36, Jan. 2011.
- [34] Z. Zhang, Q. Zhou, and A. Kusiak, "Optimization of wind power and its variability with a computational intelligence approach," *IEEE Trans. Sustainable Energy*, vol. 5, no. 1, pp. 228 - 236, Jan. 2014.
- [35] J. Park, and K. H. Law, "Bayesian ascent: a data-driven optimization scheme for real-time control with application to wind farm power maximization," *IEEE Trans. Control Syst. Technol.*, vo. 24, no. 5, pp. 1655 – 1668, Sept. 2016.
- [36] C. Kim, Y. Gui, and C. C. Chung, "Maximum power point tracking of a wind power plant with predictive gradient ascent method," *IEEE Trans. Sustainable Energy*, vol. 8, no. 2, pp. 685 - 694, Apr. 2017.
- [37] A. Kusiak, and Z. Zhang, "Short-horizon prediction of wind power: a data-driven approach," *IEEE Trans. Energy Convers.*, vol. 25, no. 4, pp. 1112 - 1122, Dec. 2010.
- [38] A. Kusiak, Z. Zhang, and G. Xu, "Minimization of wind farm operational cost based on data-driven models," *IEEE Trans. Sustainable Energy*, vol. 4, no. 3, pp. 756 - 764, Jul. 2013.
- [39] L. Xie, Y. Gu, X. Zhu, and M. G. Genton, "Short-term spatio-temporal wind power forecast in robust look-ahead power system dispatch," *IEEE Trans. Smart Grid*, vol. 5, no. 1, pp. 511 - 520, Jan. 2014.
- [40] S. T. Navalkar, E. v. Solingen, and J.-W. v. Wingerden, "Wind tunnel testing of subspace predictive repetitive control for variable pitch wind turbines," *IEEE Trans. Control Syst. Technol.*, vol. 23, no. 6, pp. 2101 - 2116, Nov. 2015.
- [41] C. Zhao, and Y. Guan, "Data-driven stochastic unit commitment for integrating wind generation", *IEEE Trans. Power Syst.*, vol. 31, no. 4, pp. 2587 - 2596, Jul. 2016.

- [42] W. Wei, N. Li, J. Wang, and S. Mei, "Estimating the probability of infeasible real-time dispatch without exact distributions of stochastic wind generations," *IEEE Trans. Power Syst.*, vol. 31, no. 6, pp. 5022 - 5032, Nov. 2016.
- [43] S. Fang, and H.-D. Chiang, "Improving supervised wind power forecasting models using extended numerical weather variables and unlabelled data," *IET Renew. Power Gener.*, vol. 10, no. 10, pp. 1616 - 1624, Jun. 2016.
- [44] F. Qiu, Z. Li, and J. Wang, "A data-driven approach to improve wind dispatchability," *IEEE Trans. Power Syst.*, vol. 32, no. 1, pp. 421 - 429, Jan. 2017.
- [45] W. Yang, C. Little, P. J. Tavner, and R. Court, "Data-driven technique for interpreting wind turbine condition monitoring signals," *IET Renew. Power Gener.*, vol. 8, no. 2, pp. 151 – 159, 2014.
- [46] P. Qian, X. Ma, and P. Cross, "Integrated data-driven model-based approach to condition monitoring of the wind turbine gearbox," *IET Renew. Power Gener.*, vol. 11, no. 9, pp. 1177 - 1185, Mar. 2017.
- [47] G. Jiang, P. Xie, H. He, and J. Yan, "Wind Turbine Fault Detection Using a Denoising Autoencoder with Temporal Information," *IEEE/ASME Trans. Mechatronics*, vol. 23, no. 1, pp. 89 - 100, Feb. 2018.
- [48] D. Zhang, L. Qian, B. Mao, C. Huang, B. Huang, and Y. Si, "A data-driven design for fault detection of wind turbines using random forests and XGboost," *IEEE Access*, vol. 6, pp. 21020 - 21031, May 2018.
- [49] A. Kusiak, and W. Li, "Virtual models for prediction of wind turbine parameters," *IEEE Trans. Energy Convers.*, vol. 25, no. 1, pp. 245 - 252, Mar. 2010.

- [50] X. Kong, X. Liu, K. Y. Lee, "Data-driven modelling of a doubly fed induction generator wind turbine system based on neural networks," *IET Renew. Power Gener.*, vol. 8, no. 8, pp. 849 - 857, Feb. 2014.
- [51] H. Long, L. Wang, Z. Zhang, Z. Song, and J. Xu, "Data-driven wind turbine power generation performance monitoring," *IEEE Trans. Ind. Electron.*, vol. 62, no. 10, pp. 6627 - 6635, Oct. 2015.
- [52] M. Tan, and Z. Zhang, "Wind turbine modeling with data-driven methods and radially uniform designs," *IEEE Trans Ind. Informat.*, vol. 12, no. 3, pp. 1261 - 1269, Jun. 2016.
- [53] Y. Zhao, L. Ye, W. Wang, H. Sun, Y. Ju, and Y. Tang, "Data-driven correction approach to refine power curve of wind farm under wind curtailment," *IEEE Trans. Sustainable Energy*, vol. 9, no. 1, pp. 95 - 105, Jan. 2018.
- [54] M. A. Ahmed, and Y.-C. Kim. "Hierarchical communication network architectures for offshore wind power farms." *Energies*, vol. 7, no. 5, pp. 3420-3437, Jun. 2014.
- [55] O. Polat, "A robust regression based classifier with determination of optimal feature set." *J. Appl. Res. Technol.*, vol. 13, no. 4, pp. 443-446, Aug. 2015.
- [56] C. Chen, "Robust Regression and Outlier Detection with the ROBUSTREG Procedure," *Proc. 27th SAS Users Group Int. Conf.*, Cary, NC, USA, 2002, pp. 1-13.
- [57] D. C. Hoaglin, F. Mosteller and J. W. Tukey, *Exploring Data Tables, Trends, and Shapes*, John Wiley & Sons, 2011, Vol. 101.
- [58] F. H. Thanoon, "Robust regression by least absolute deviations method," *Int. J. Statist. Appl.*, vol. 5, no. 3, pp. 109-112, 2015.

- [59] R. Reginatto, and C. R. M. da Rocha. "Minimum short-circuit ratios for grid interconnection of wind farms with induction generators," *8th Latin-American Congr. Electricity Generation and Transmission-CLAGTEE 2009*, Ubatuba, SP, Brazil, 2009, pp. 1-8.
- [60] B. Leonardi and V. Ajjarapu, "Investigation of various generator reactive power reserve (GRPR) definitions for online voltage stability/security assessment," *2008 IEEE Power and Energy Soc. General Meeting - Convers. Del. Electrical Energy in the 21st Century*, Pittsburgh, PA, USA, 2008, pp. 1-7.
- [61] M.N.S.K. Shabbir, X. Liang, W. Li, A.M. Le, and N. Khan, "A Data-Driven Voltage Control Approach for Grid-Connected Wind Power Plants," *Proc. 2018 IEEE Ind. Appl. Soc. (IAS) Annu. Meeting*, Portland, OR, USA, 2018, pp. 1-14.

Chapter 4

Analytical Approach-Based Reactive Power Capability Curve for DFIG Wind Power Plants

Md Nasmus Sakib Khan Shabbir¹, *Student Member*, IEEE, Xiaodong Liang², *Senior Member*, IEEE, Weixing Li³, *Senior Member*, IEEE, and Nahidul Khan⁴

¹Department of Electrical and Computer Engineering, Memorial University of Newfoundland, St. John's, Newfoundland, Canada.

²Department of Electrical and Computer Engineering, University of Saskatchewan, Saskatoon, Saskatchewan, Canada.

³Department of Electrical Engineering, Harbin Institute of Technology, Harbin, Hilongjiang, China.

⁴Newfoundland and Labrador Hydro System Operation and Planning, Energy Control Center, St John's, Canada

A version of this chapter has been published in Proceedings of 2020 IEEE Industry Applications Society Annual Meeting. Md Nasmus Sakib Khan Shabbir developed this work under the supervision of Dr. Xiaodong Liang. Sakib's contributions in this paper are listed as follows:

- Performed literature review for maximum reactive power capability models of doubly-fed induction generator.
- Developed the analytical model of maximum reactive power capability for DFIG wind power plant.
- Examined results and reported findings.
- Involved in writing the paper draft as the first author.

Dr. Xiaodong Liang provided continuous technical guidance, checked the results, and modified the manuscript. Dr. Weixing Li modified the manuscript. Dr. Nahidul Khan provided the SCADA measurement data and necessary information about the wind power plant used in the analysis.

In this chapter, the manuscript is presented with altered figure numbers, table numbers, and reference formats to match the thesis formatting guidelines set out by Memorial University of Newfoundland.

Abstract- In this paper, an analytical approach to determine the reactive power capability of an individual doubly-fed induction generator (DFIG)-based wind turbine generators (WTGs) as well as plant level WPPs is proposed by considering several constraint variables. For ease of use, the proposed approach is developed based on the well-known standard parameters, and individual WTGs reactive power capability model is validated by comparing with two existing methods whereas plant level capability model is validated by comparing with Supervisory Control and Data Acquisition (SCADA) field measurement data of two WPPs currently operating in Newfoundland, Canada.

Keywords- Doubly-fed induction generator, reactive power capability, wake effect, wind power plant.

4.1 Introduction

Wind power as a dominant form of renewable energy source plays an important role in the modern mixed energy landscape [1][2]. Wind power plants (WPPs) are usually grid-connected, adequate reactive power reserve of WPPs is critical to meet grid code requirements, handle steady-state and transient uncertainties, and maintain stability and power quality of the system. Among

existing wind power technologies, only doubly-fed induction generator (DFIG) and permanent magnet synchronous generator (PMSG)-based wind turbines have the ability to supply reactive power to the grid [3]-[6]. Although the generation capacity of wind turbine generators (WTGs) has been developed up to 8 MW [7], 2 to 3 MW DFIGs are still considered the most optimum type due to partial-rated power electronic converters [8]-[14]. This paper focuses on DFIG-based WPPs.

Because of the intermittent nature of wind, significant penetration of wind power generation in the grid may lead to severe stability and power quality issues due to lack of ancillary services that are usually provided by conventional synchronous generators (SGs) [15]. To resolve these issues, many countries have enforced grid codes for WPPs [16]. Grid codes require that WPPs should have sufficient reactive power reserve; following a grid disturbance, a WPP must inject reactive power to the grid as rapidly as possible instead of tripping off. Meeting such requirements can compensate voltage sags and enhance voltage stability of the system [17]. Research has been conducted to ensure the maximum reactive power contribution following a fault [14][18][19], and Ref [20] recommends that a WPP should have sufficient reserve to exchange reactive power under steady-state operation as well.

Reactive power contribution from a WPP is based on the plant-level reactive power reserve and the voltage at the point of common coupling (PCC). Reactive power compensation equipment, such as capacitor banks and static var compensators (SVCs), can be installed in WPPs, but dynamic synchronization between the WPP and such equipment is hard to achieve, which may cause voltage overshoot and cascaded tripping-off [21]. Therefore, research has been conducted to enhance reactive power extraction from WTGs and reduce the dependency on reactive power compensation

equipment. In a practical WTG, several constraints are related to the reactive power capability [22]. A capability model without properly including these constraints may be less effective.

The plant-level reactive power capability may affect voltage compensation, controller operation, and is directly related to the system's stability and power quality. However, in the literature, there is no work reported so far on reactive power capability curve at the plant-level of WPPs, while only the reactive power capability curve development for individual DFIGs was reported in several papers. To support voltage compensation, reactive power capability of DFIGs is restricted by converter ratings [23][24]. However, due to additional constraints, such as magnetic saturation, the controller of DFIGs cannot achieve the desired dynamic responses. An active power–reactive power (P-Q) diagram for DFIGs, similar to that for conventional SGs, is developed in [22],[25]-[28] by considering: 1) converter current and heating limits in [25]; 2) only stator and rotor current limits in [26]; 3) stator and rotor current limits, and a rotor voltage limit in [27]; and 4) stator and rotor current limits, rotor voltage limits, and magnetic saturation in [28]. Although more constraints are considered in [28] than in [25]-[27], the detailed mathematical model is not provided in [28].

In this paper, for the very first time, a mathematical model to determine reactive power capability curve at the plant-level of DFIG-based WPPs is developed. The reactive power capability of a DFIG is derived first in this study. To obtain the plant-level mathematical formulation, simple summation of individual WTGs' reactive power capability is not proper. Several constraints affecting reactive power capability at both individual DFIGs and the plant-level are considered. Parameters that affect the plant-level reactive power capability include wake effect and distribution feeder losses. A WPP usually spans over a large geographic area and is connected to the PCC through long distribution lines, where significant losses may occur. For ease

of use, our developed model is formulated using the well-known standard parameters. To validate the proposed model of reactive power capability at individual DFIGs, it is compared with two existing methods reported in [26][27]. Since there is no existing model for the reactive power capability curve at the plant-level, it is validated by comparing with SCADA field measurements of two WPPs currently operating in Newfoundland, Canada.

The main contribution of the paper includes: 1) develop an analytical approach to calculate reactive power capability at the plant-level for DFIG-based WPPs; and 2) evaluate reactive power capability at individual DFIGs. The plant-level reactive power capability curve assists the WPP central controller to accurately estimate the plant's reactive power reserve and ensure robust voltage compensation. Grid operators can also use it to estimate the network's competency for sudden voltage fluctuations. To avoid WTG overloading, reactive power capability curve of individual WTGs can be used by the WPP central controller to distribute reactive power setting points proportionally among WTGs based on operating conditions.

The paper is arranged as follows: the proposed method and its implementation procedure are introduced in Section 4.2; the steady-state WPP system model is derived in Section 4.3; constraints affecting reactive power capability calculation at individual DFIGs and the plant-level are discussed in Sections 4.4 and 4.5, respectively; the reactive power capability model is developed in Section 4.6 and validated in Section 4.7; conclusions are drawn in Section 4.8.

4.2 System Modeling

4.2.1 Mechanical System Model

To account for the wake effect, the well-established wind speed-power equation is adopted as follows [21]:

$$P_{mech} = \frac{\pi R^2 C_p \rho v_{wind}^3}{2} \quad (1)$$

Where P_{mech} is the developed mechanical power, R is the radius of the wind turbine, C_p is the power coefficient of the wind turbine, ρ is the air density, and v_{wind} is the wind speed. For downstream WTGs, v_{wind} in (1) is replaced by the wake wind speed (v_{wake}), and its calculation is discussed in Section IV. Eq. (1) is depicted in Fig. 4.1.

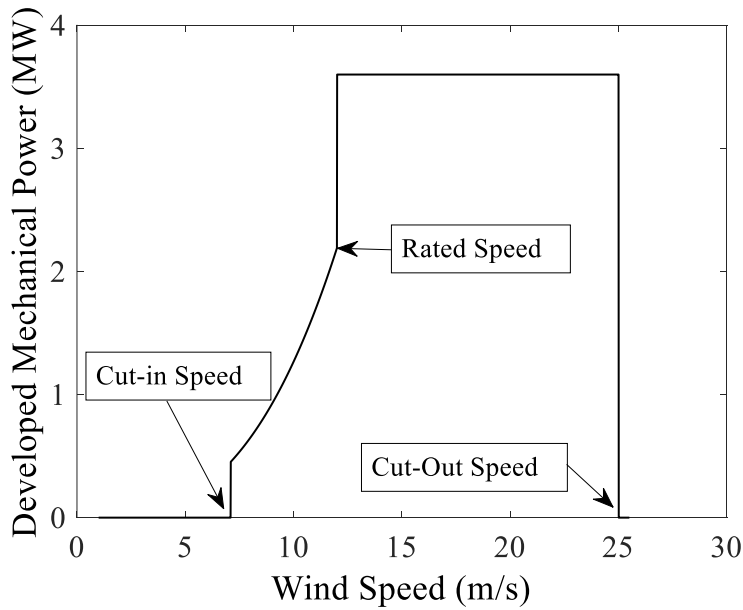


Fig. 4. 1. Wind-Power characteristic curve of WTGs

In this paper, two WPPs currently in operation in Newfoundland, Canada are used to validate the proposed method. The following data are used in the study: 1) based on historical wind profiles (published by Government of Canada) [29] of the two WPPs, the cut-in, rated, and cut-out wind speeds for wind turbines are determined to be 7.099, 12, and 25 m/s, respectively; 2) the rated slips in super- and sub-synchronous modes for WTGs are -0.2 and 0.3 , respectively, which are calculated from the rated and cut-in wind speeds using (39); and 3) a gearbox ratio of wind turbines

is 57.468. Although these parameters are not directly related to the maximum reactive power capability, they are crucial to relate active power generation with wind speed.

4.2.2 Active Power Generation

To determine the reactive power capability at the plant-level of DFIG-based WPPs, the reactive power capability of a DFIG must be determined first. In a sub-synchronous mode, the rotor rotational speed is below the synchronous speed, and it results in a sub-synchronous generated voltage and current; in this case, the rotor side converter (RSC) provides additional excitation to speed up the rotor to the synchronous speed. In a super-synchronous mode, the rotor rotational speed is above the synchronous speed, the RSC consumes excess excitation and keeps the system into synchronism. By neglecting losses occurred in DFIGs, the relation between active power and mechanical power of the stator and the rotor are expressed by

$$P_r = -sP_s \quad (2)$$

$$P_{mech} = (1 - s)P_s = 3V_s I_{s_{active}} \quad (3)$$

Where P_s and P_r are active power of the stator and the rotor, respectively (Note: the active power of the rotor P_r is the same as the active power of the RSC); s is the slip; V_s is the stator voltage per phase; and $I_{s_{active}}$ is the real component of the stator current. The relationship represented by Eqs. (1), (2) and (3) is depicted in Fig. 4.2.

4.2.3 Reactive Power Generation

In a DFIG, both the stator and the grid side converter (GSC) have the potential to generate or consume reactive power. As reactive power generation from the stator and the GSC is controlled separately, reactive power can be extracted from the stator and/or the GSC to their maximum limits

when needed. Therefore, the reactive power capability of a WTG, Q_{WTG} , can be determined by (4), where reactive power of the stator, Q_{DFIG} , is controlled by the rotor based on (5), while the GSC controller controls the GSC's reactive power, Q_{GSC} .

$$Q_{WTG} = Q_{DFIG} + Q_{GSC} \quad (4)$$

$$Q_{DFIG} = -\frac{3Q_r}{s} \quad (5)$$

Where Q_{DFIG} , Q_r and Q_{GSC} are reactive power of the stator, the rotor and the GSC, respectively. Q_{WTG} is the reactive power capability of a WTG.

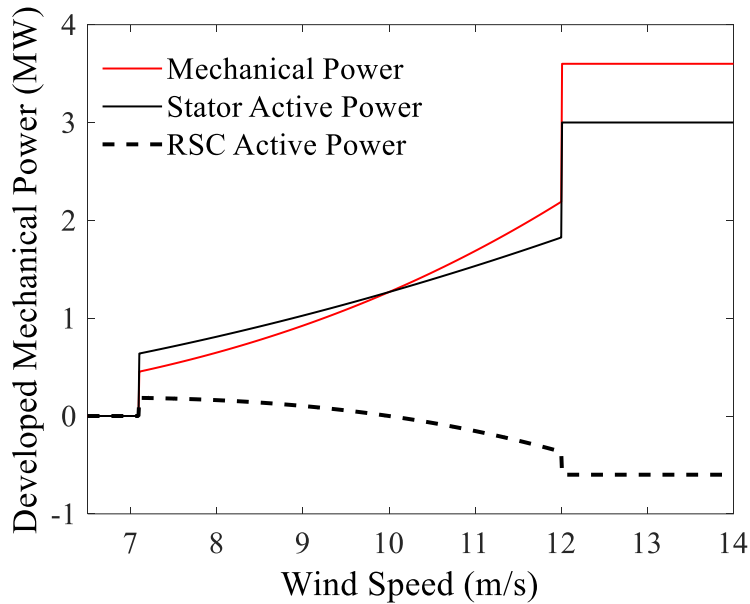


Fig. 4. 2. Active power sharing between the stator and the RSC.

4.2.4 Steady-State Equivalent Circuit

The steady-state T equivalent electric circuit of a DFIG is shown in Fig. 4.3 with the following assumptions:

- 1) Both stator and rotor windings are connected in wye;

2) The stator is connected to a three phase AC grid, which is balanced and remains at its nominal voltage and frequency.

3) The rotor is connected to a three phase AC grid, which is balanced and remains at its nominal voltage and frequency, by a back-to-back voltage source converter.

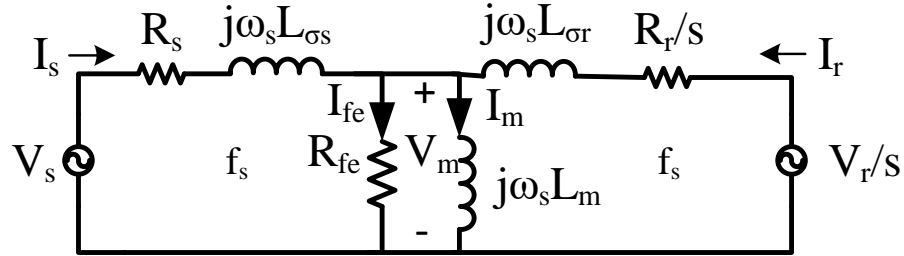


Fig. 4. 3. The steady-state equivalent circuit of DFIGs referred to the stator.

In Fig. 4. 3, steady-state voltage equations of the stator and the rotor can be written as follows:

$$V_s = V_m - (R_s + j\omega_s L_{\sigma s})I_s \quad (6)$$

$$\frac{V_r}{s} = V_m - \left(\frac{R_r}{s} + j\omega_s L_{\sigma r}\right)I_r \quad (7)$$

$$I_{fe} + I_m = I_s + I_r \quad (8)$$

Where V_s is the stator voltage; V_m is the magnetizing voltage; I_s is the stator current; I_{fe} and I_m are the magnetizing and iron loss current, respectively; R_s and $L_{\sigma s}$ are the resistance and leakage inductance of the stator, respectively; V_r , I_r , R_r , and $L_{\sigma r}$ are the voltage, current, resistance, and inductance of the rotor referred to the stator, respectively. The relationship between actual rotor parameters and rotor parameters referred to the stator side is shown below:

$$z_r = \frac{Z_r}{N^2} \quad (9)$$

$$i_r = I_r N \quad (10)$$

$$v_r = \frac{V_r}{N} \quad (11)$$

Where N is a constant factor; Z_r , I_r and V_r are the impedance, current, and voltage of the rotor referred to the stator side, respectively; z_r , i_r and v_r are the actual rotor impedance, current and voltage, respectively.

4.3 Limiting Factors for Individual DFIG

4.3.1 Stator Current Limit

The stator current mainly limits the reactive power capability of the system at the under-excited mode. The impact of the stator current at this aspect can be evaluated by varying the phase angle while keeping the magnitude of the stator current constant at the rated value. DFIG reactive power capability due to the stator current limit is shown in Fig. 4.4. Although the stator current shapes the reactive power capability at both over- and under-excited modes in Fig. 4.4, with additional limiting variables, its influence at the over-excited mode is omitted.

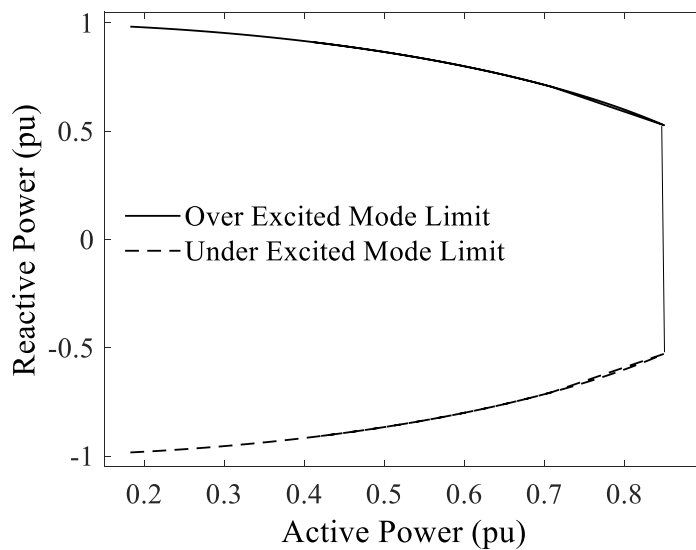


Fig. 4. 4. Reactive power capability of a DFIG considering stator current limit.

4.3.2 Rotor Current Limit

In the over-excited mode, the rotor's flux generation increases rapidly as shown in Fig. 4.5 [28]. In Fig. 4.6, to accommodate additional fluxes required to generate reactive power within the stator current constraint, the rotor current exceeds its rated value in the over-excited mode; while it remains way below its rated value in the under-excited mode. Therefore, the rotor current becomes a limiting variable, and is required to be within its rating in the over-excited mode. The rated slip in the super-synchronous mode determines the converter's power rating as the converter handles the maximum power in this state [30]. The reactive power capability within the rotor current limit is drawn in Fig. 4.7.

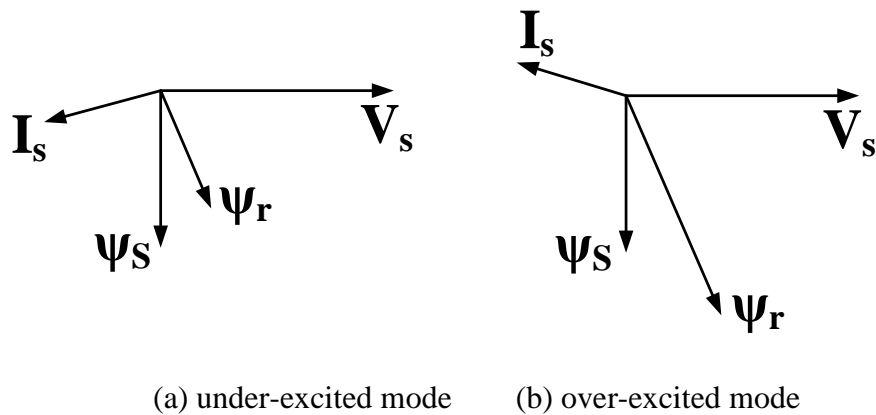


Fig. 4. 5. Phasor diagrams of a DFIG [28].

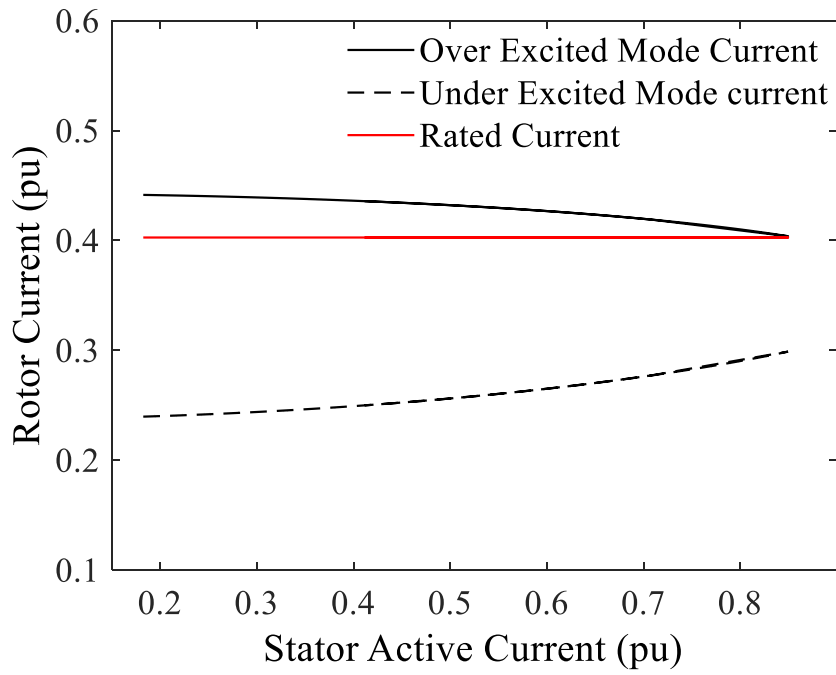


Fig. 4. 6. Rotor current in two modes of operations.

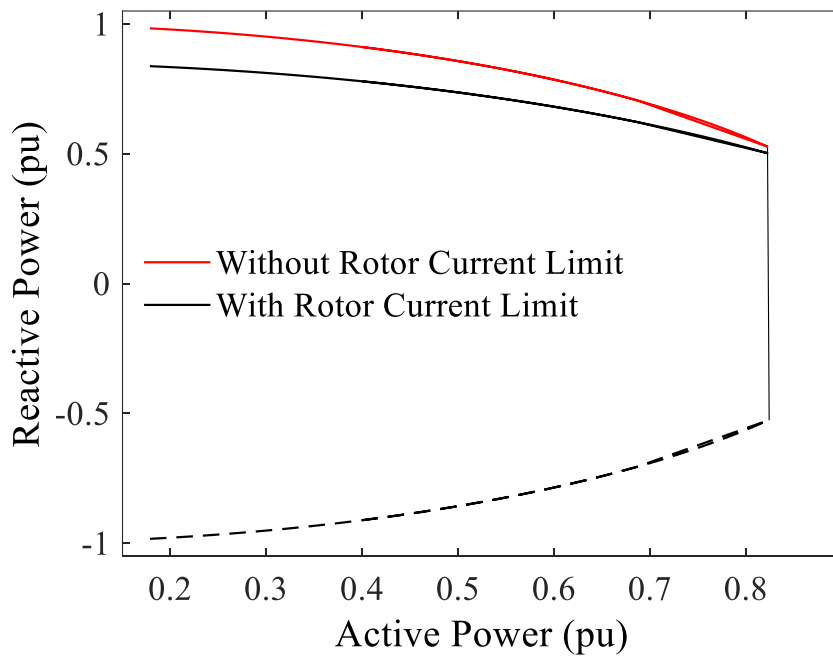


Fig. 4. 7. Effect of rotor current limit on reactive power capability of a DFIG.

4.3.3 Rotor Voltage Limit:

The maximum permissible voltage of the rotor is:

$$v_{r_{max}} = \frac{V_{DC}D_{max}}{\sqrt{2}\sqrt{3}} \quad (12)$$

Where V_{DC} is the DC link voltage, and D_{max} is the maximum allowable duty cycle of the RSC.

According to [27], the complex power (S) of a DFIG in terms of stator and rotor voltages can be written as follows:

$$S = -3V_s \left(\frac{V_s(Z_r + Z_m) - \frac{V_r}{s}Z_m}{(Z_r + Z_s)Z_m + Z_sZ_r} \right) \quad (13)$$

Where V_s and V_r are the stator and rotor voltage, respectively, Z_s , Z_r and Z_m are the impedance of the stator, rotor and magnetic circuit, respectively.

To understand the impact of the rotor voltage on the reactive power capability of a DFIG, the phase angle of the rotor voltage in (13) is varied, while its magnitude is kept at the rated value, resulting in a circle with a large negative offset on the imaginary axis [27]. Therefore, the rotor voltage becomes a limiting variable in the over-excited mode when the absolute value of the slip is high [27]. A capacitor is placed between the back to back converters (RSC and GSC) as showed in Fig. 4.10, and the nominal capacitor voltage is set based on the peak rotor voltage to avoid voltage over-surge.

4.3.4 Winding Factor

The stator and rotor windings of a DFIG are coupled with mutual flux, ψ_m . According to Faraday's law, the induced electromotive force (e.m.f.) in the stator (Vs) is

$$V_s = \sqrt{2}\pi K_s n_s f_s \psi_m \quad (14)$$

Where K_s is the stator winding factor, n_s is the number of turns in the stator, f_s is the operating frequency, and ψ_m is the mutual flux. Similarly, the induced e.m.f. in the rotor referred to the rotor side is

$$v_r' = \sqrt{2}\pi K_r n_r f_r \psi_m \quad (15)$$

Where K_r is the rotor winding factor, n_r is the number of turn in the rotor, and f_r is the frequency in the rotor circuit.

The relation of frequencies between the induced voltage of the stator and the rotor is:

$$f_r = s f_s \quad (16)$$

By combining (14), (15), and (16), we have

$$\frac{V_s}{v_r'} = N = \frac{1}{s} \frac{K_s n_s}{K_r n_r} \quad (17)$$

Where N is the constant factor that defines the relation between the stator and the rotor induced e.m.f.s at zero speed ($s = 1$); n_s/n_r is the stator to rotor turns ratio. Winding factors are calculated by

$$K_w = K_d K_p \quad (18)$$

Where K_w , K_d , and K_p are winding factor, distribution factor and pitch factor for both stator and rotor, respectively. K_d arises because armature windings in each phase are distributed in a number of slots, and the voltage induced in each slots cannot be in the same phase. K_p arises when the slot pitch is smaller than the pole pitch. According to [31] and [32], for DFIGs, the approximation is $\frac{K_s}{K_r} \approx 1$. However, in real life, $\frac{K_s}{K_r}$ can be slightly higher or lower than 1. According to (17), this change of winding factor ratio from its nominal value holds a proportional relationship with N . However,

N limits DFIG reactive power capability only when N is increased, as this will increase rotor current as well, and as a result, rotor current reaches to its maximum value for comparatively lower value of stator current. Therefore, the influence of winding factors cannot be neglected.

In this research, it shows that winding factors have impact on the overall performance of the DFIG; therefore, it should be considered while developing characteristics equations. Fig. 4.8 (b), depicts that the reactive power capacity is reduced by 0.0067 pu, 0.0134 pu and 0.0232 pu when K_s/K_r is change from 1 to 1.005, 1.01 and 1.02, respectively.

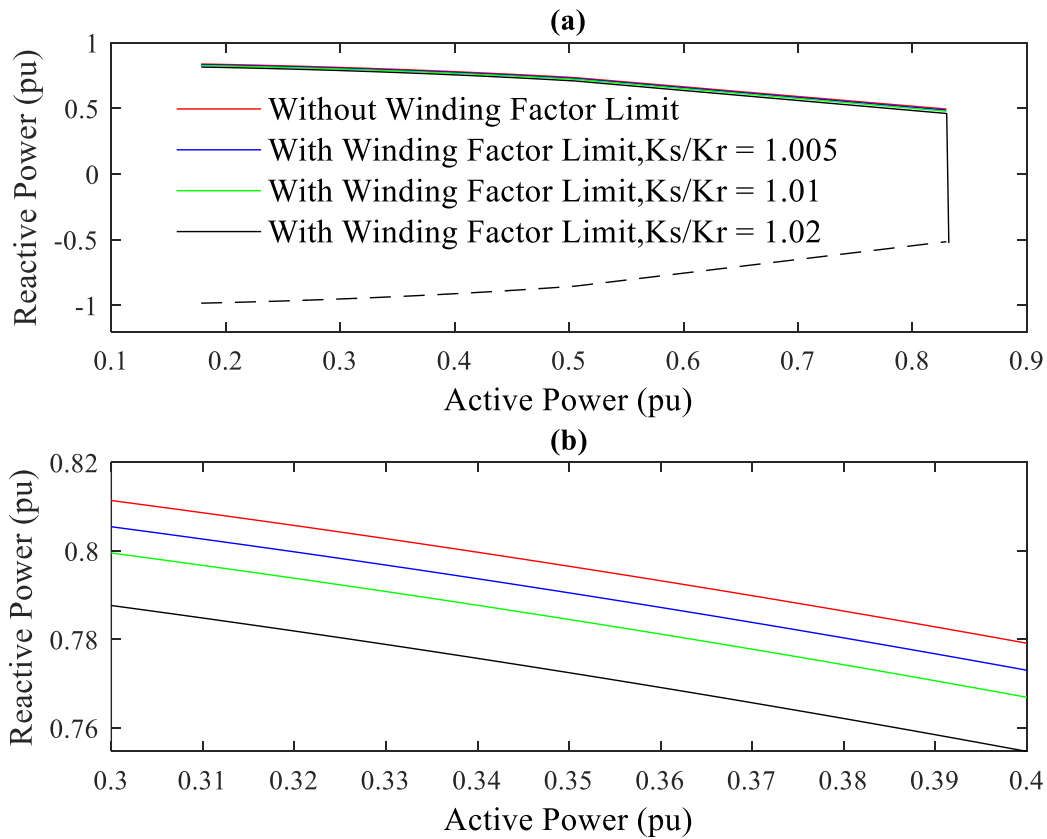


Fig. 4. 8. Effect of winding factor on reactive power capability of a DFIG: (a) overall capability; (b) the zoomed-in overexcited mode capability.

4.3.5 Magnetic Saturation

A DFIG is partially saturated under the nominal operating condition [28]. Magnetic saturation of the core brings a practical limit on the maximum achievable magnetic fields in a DFIG. Saturation starts when the magnetic current exceeds the saturation current. The impact of magnetic saturation should be considered in reactive power capability calculation of DFIGs. If saturated, the mutual inductance (L_m) of the DFIG experiences a non-linear variation, which can be expressed by

$$L_m = \begin{cases} L_m, & I_m < I_{m_{sat}} \\ k(I_m)L_m, & I_m \geq I_{m_{sat}} \end{cases} \quad (19)$$

Where I_m is the magnetic current, $I_{m_{sat}}$ is the magnetic saturation current, $K(I_m)$ is a saturation constant, expressed by

$$k(I_m) = \begin{cases} 1, & I_m < I_{m_{sat}} \\ \frac{2}{\pi} \left[\sin^{-1} \frac{I_{m_{sat}}}{I_m} + \frac{1}{2} \sin(2 \sin^{-1} \frac{I_{m_{sat}}}{I_m}) \right], & I_m \geq I_{m_{sat}} \end{cases} \quad (20)$$

The reduction of the available reactive power due to magnetic saturation of the core is shown in Fig. 4.9.

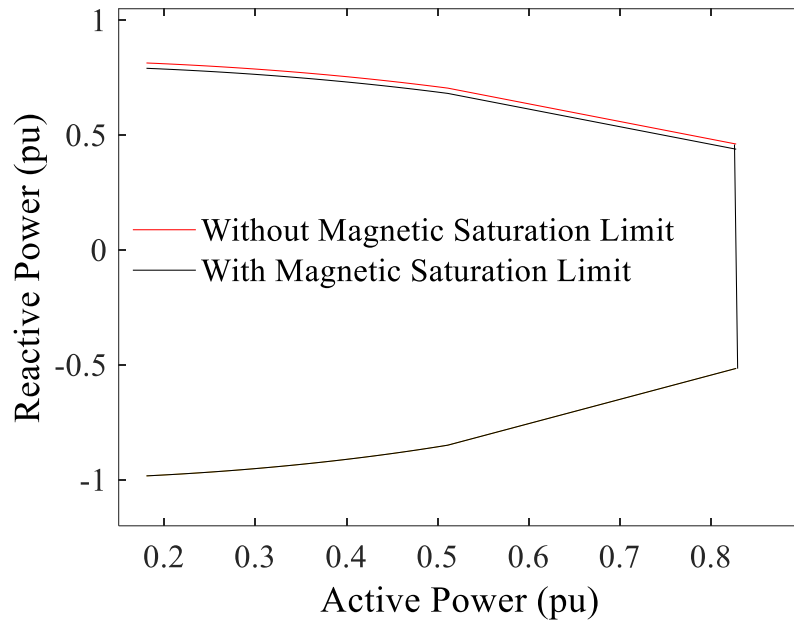


Fig. 4. 9. Effect of magnetic saturation on reactive power capability of a DFIG.

4.3.6 Reactive Power Capability of GSC

In a DFIG, reactive power can be exported from the GSC through proper control algorithms [7]. Under steady-state, the GSC supports slip power to the DFIG based on operating conditions. Therefore, the rated and active currents of the GSC determine the available reactive power flow from the GSC.

In Section II, it is assumed that the rotor is fed by a three phase AC grid, which is balanced and remains at its nominal voltage and frequency, through the RSC. Conduction and switching losses associated with the RSC have not been considered so far. To keep the DC link voltage (V_{DC}) at its nominal value, active power of RSC and GSC must be the same. Since the operating voltage and current of RSC and GSC are different, their losses are also different. To properly formulate the GSC reactive power limit, losses associated with the RSC and the GSC must be considered. From

the equivalent circuit of the GSC shown in Fig. 4.10, the expression for available reactive current from the GSC ($I_{GSC_{reactive}}$) can be expressed by (21). The converter steady-state conduction and switching losses can be calculated according to [28].

$$I_{GSC_{reactive}} = \sqrt{I_{GSC_{rated}}^2 - \left(\frac{P_r - P_{RSC_{cond,switch}} - P_{GSC_{cond,switch}}}{V_{GSC}} \right)^2} \quad (21)$$

Where V_{GSC} is the voltage per phase at the GSC, $P_{RSC_{cond,switch}}$ and $P_{GSC_{cond,switch}}$ are summed conduction and switching losses for the RSC and GSC switches, respectively. $I_{GSC_{rated}}$ is the rated current of the GSC and can be calculated by

$$I_{GSC_{rated}} = - \frac{\max|3v_r i_r \cos \theta_r|}{3V_{GSC}} \quad (22)$$

Where $\cos \theta_r$ is the rotor power factor, and v_r follows the boundary stated in (12).

The steady-state relation between V_{GSC} and V_s can be written as follows:

$$V_{GSC} = V_s + (R_{GSC} + j\omega_s L_{GSC}) I_{GSC} \quad (23)$$

Where V_{GSC} and I_{GSC} are the voltage per phase and the current of the GSC, respectively; R_{GSC} and L_{GSC} are the resistance and inductance per phase of the GSC, respectively. By combining the DFIG and the GSC, the resultant reactive power capability of a DFIG is drawn in Fig. 4.11.

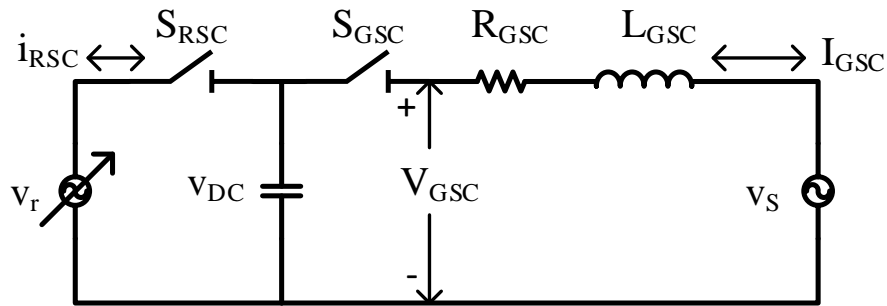


Fig. 4. 10. Single-phase steady-state equivalent circuit of the GSC.

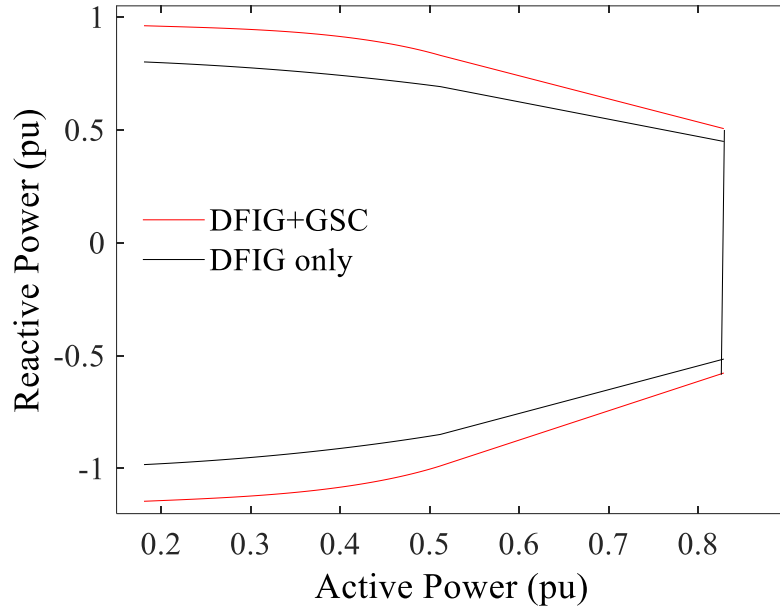


Fig. 4. 11. Reactive power capability of a WTG.

4.4 Plant level limiting factors

4.4.1 Determination of Power Coefficient

Power coefficient is a measure for the wind turbine efficiency, expressed by

$$C_p(\lambda, \beta) = c_1 \left(\frac{c_2}{\lambda_i} - c_3 \beta - c_4 \right) e^{-c_5/\lambda_i} + c_6 \lambda \quad (24)$$

Where, for the previously mentioned range of the operating wind speed and turbine capacity, standard value of coefficients c_1 to c_6 are 0.5176, 116, 0.4, 5, 21, and 0.0068, respectively [34].

The maximum power coefficient of the studied DFIG, $C_{p_max} = 0.48$, is achieved when β is 0 degree, and λ is 8.1.

However, to accurately calculate power coefficients, profile and swirl losses should be considered. The profile loss is associated with the drag of the profile and directly proportional to the tip speed ratio (λ). The swirl loss is triggered by the vortex formed around the tip of the turbine

and inversely proportional to the product of the number of turbine blades and the tip speed ratio (λ) [33]. The optimum power coefficient (C_{p_opt}) with profile and swirl losses can be determined by [33]

$$C_{p_opt} = \frac{16}{27} \left(1 - \frac{0.219}{\lambda^2} - \frac{0.106}{\lambda^4} - \frac{2 \ln \lambda^2}{9 \lambda^2} \right) \quad (25)$$

The corresponding effective power coefficient of a wind turbine is calculated as follows:

$$C_{pth} = C_p(\lambda, \beta) \frac{C_{p_opt}}{C_{p_max}} \quad (26)$$

4.4.2 Wake Effect

WTGs generate electricity by extracting energy from the wind, resulting in a subsequent reduction of energy density in the downstream air. This phenomenon is known as “wake effect”. The wake effect is directly associated with active power generation, and indirectly associated with reactive power generation. To develop a realistic representation of the reactive power capability curve of a WPP, wake effect should be considered [27].

In this paper, the Jensen wake model is used to represent wake effect as shown in Fig. 4.12. According to Jensen wake model, the wake flow is linear for the downstream wind turbines [35].

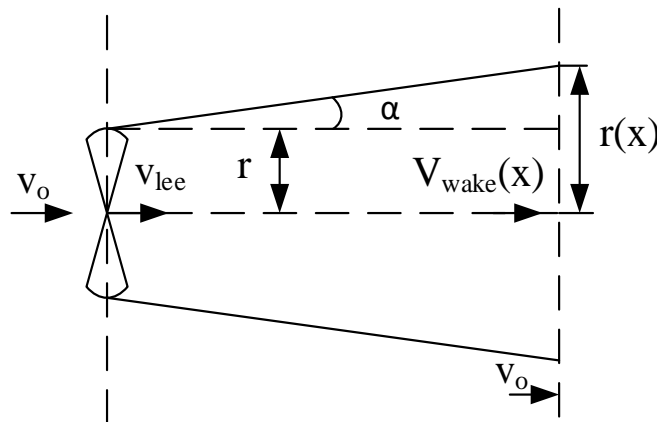


Fig. 4. 12. Shadow cone of a WTG.

To simplify the calculation, the wake wind speed due to one upstream WTG is calculated first. The wake wind speed $v_{wake}(x)$ at a radial distance x from an upstream WTG can be calculated as follows:

$$v_{wake}(x) = v_o + (v_{lee} - v_o) \left(\frac{r}{r(x)} \right)^2 \quad (27)$$

Where v_o and v_{lee} are the free wind speed and the lee side wind speed, respectively. Depending on the value of power coefficient, expressions for the lee side wind speed are written as follows [33]:

$$v_{lee} = \begin{cases} v_o \frac{4 \cos(\Phi/3) - 1}{3}, & C_{pth} < \frac{8}{27} \\ -v_o \frac{4 \cos(4\pi - \Phi/3) - 1}{3}, & C_{pth} \geq \frac{8}{27} \end{cases} \quad (28)$$

Where

$$\Phi = \cos^{-1} \left(1 - \frac{27}{8} C_{pth} \right) \quad (29)$$

In (27), r and $r(x)$ are the radius of the upstream WTG and the radius of the shadow cone at the distance x , respectively. $r(x)$ can be calculated by

$$r(x) = r + x \tan \alpha \quad (30)$$

Where, depending on the surface roughness of the WPP, $\tan \alpha$ is associated with two values: $\tan \alpha$ is set to 0.04 for wind turbines with free wind; $\tan \alpha$ is set to 0.08 for other wind turbines affected by wake effect [27]. WTGs are usually arranged in rows in a WPP, and WTGs standing in the first row to the direction of the airflow face the free wind.

In practical applications, the wake wind speed at a downstream WTG is the result of cumulative shadowing of multiple upstream WTGs. Therefore, for the proper wake wind speed calculation, the collective impact of multiple shadowing is calculated by [27]

$$v_{wake_j} = v_{j0} - \sqrt{\sum_{\substack{i=1 \\ i \neq j}}^n \beta_i (v_{lee_i}(x_{ij}) - v_{j0})^2} \quad (31)$$

Where v_{wake_j} is the wake wind speed of the WTG_j , v_{j0} is the incoming wind speed at WTG_j without any shadowing, x_{ij} is the radial distance between WTG_i and WTG_j , β_i is the ratio of the area of WTG_j under the shadow of WTG_i to its total area, $v_{lee_i}(x_{ij})$ is the speed of the wind approaching WTG_j from the shadowing WTG_i , and n is the total number of WTGs.

The wake wind speed, calculated using (31) for the three WTGs in the first column of the WPP currently operating in Newfoundland (Fig. 4.18), is shown in Fig. 4.13.

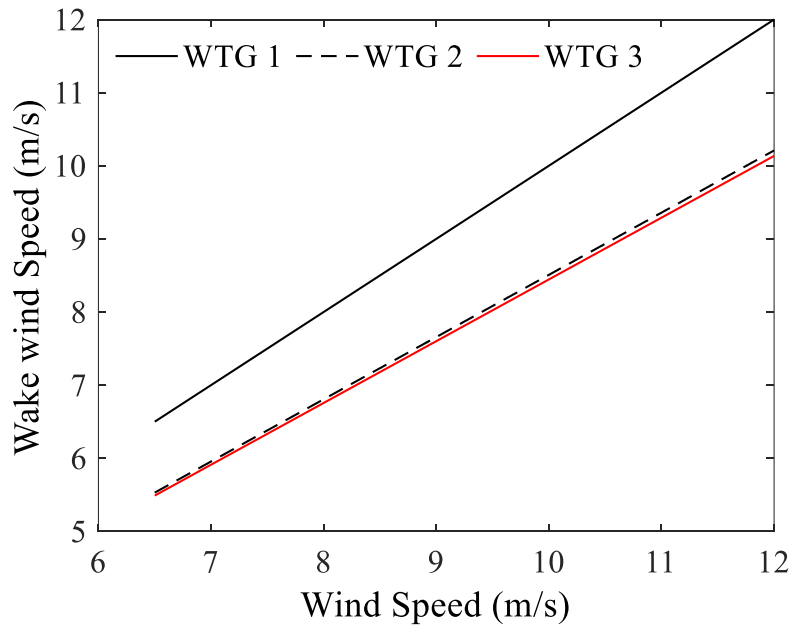


Fig. 4. 13. Change of wind speed due to wake effect.

4.4.3 Losses in Distribution Feeders

A WPP system may have a long distribution feeder as it is usually distributed over a large area. Therefore, losses occurred in lines and transformers of the feeder should be considered for accurate prediction of the plant-level reactive power capacity. In this paper, to account for distribution losses, a lumped PI section distribution line shown in Fig. 4.14 is adopted from MATLAB. The positive- and zero-sequence quantities for the line resistance used in this study are 0.1153 Ω/km and 0.413 Ω/km ; for the inductance are 1.05 mH/km and 3.32 mH/km; and for the capacitance are 11.33 nF/km and 5.01 nF/km, respectively [36]. The negative-sequence parameters are assumed to be same as the positive-sequence values.

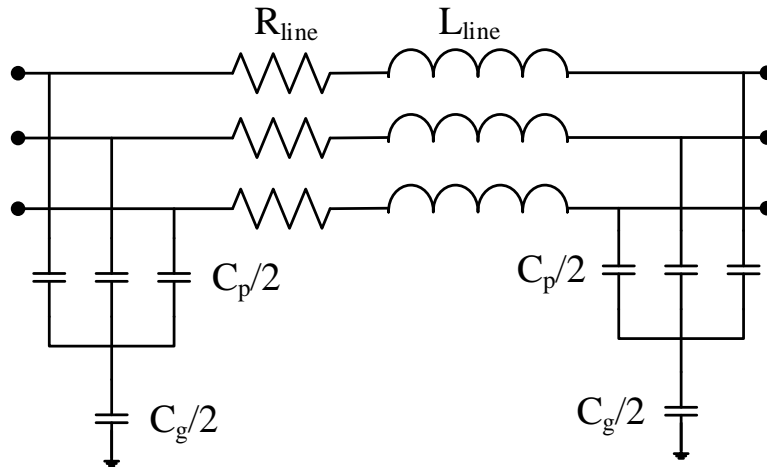


Fig. 4. 14. PI section distribution line.

The line parameters are calculated by assuming a balanced three-phase system. The relations are given as follows:

$$A_+ = a_+ L_{line} k_{z+} \quad (32)$$

$$A_0 = a_0 L_{line} k_{z0} \quad (33)$$

Where a represents the line inductance, capacitance or resistance per km; the subscripts, + and 0, represent positive- and zero-sequence quantities, respectively; L_{line} is the line length; k_z is hyperbolic correction factors, which are assumed to be 1 for a line shorter than 50 km; and A represents the aggregated sequence parameters. The RLC line section parameters can be computed by

$$A_s = (2A_+ + A_0)/3 \quad (34)$$

$$C_p = C_+ \quad (35)$$

$$C_g = \frac{3C_+C_0}{(C_+ - C_0)} \quad (36)$$

Where C is the capacitance, the subscripts, p and g, represent parallel and ground.

4.5 Plant-Level Reactive Power Capability Model

In this paper, based on limiting factors, we have derived the mathematical model for reactive power capability at the plant-level for DFIG-based WPPs for the very first time. For the sake of convenience, the model is developed based on the well-known standard parameters, i.e., the stator voltage, wind speed, and the nominal power. A clear relation among constraint variables and the plant-level reactive power capability is deduced. The developed model can be applied to WPPs with various capacities, WTG's geographical locations and voltage ranges.

The reactive power capability model at the plant-level (Q_{Total}) can be determined as follows:

$$Q_{Total} = \sum_{i=1}^n (Q_{DFIG}^i + Q_{GSC}^i - Q_{line}^i - Q_{transformer}^i) \quad (37)$$

Where n is the number of WTGs in the WPP; the superscript i represents the quantities for the i th WTG; Q_{DFIG}^i and Q_{GSC}^i are the reactive power capability of the i^{th} DFIG and its GSC, respectively;

Q_{line}^i and $Q_{transformer}^i$ are the associated line and transformer losses for the i^{th} WTG, respectively. Q_{DFIG}^i is calculated by

$$Q_{DFIG}^i = 3|V_s| \sqrt{I_{S_{rated}}^2 - \frac{\pi R^2 C_p \rho (v_{wake}^i)^3}{6(1-s^i)V_s}} \quad (38)$$

$$s^i = \frac{\omega_s R - r_{gb} v_{wake} \lambda p}{\omega_s R} \quad (39)$$

Where ω_s is the synchronous speed, r_{gb} is the gear box ratio, p is the number of pole pairs, and $I_{S_{rated}}$ is the rated stator current, which can be calculated as follows:

$$I_{S_{rated}} = \begin{cases} \frac{S_{rated}}{3|V_s|}, & i_r \leq i_{r_{rated}} \\ \left| \frac{|V_m|}{R_{fe}} + \frac{|V_m|}{j\omega_s L_m} - \frac{i_{r_{active}}}{N} \pm j \frac{1}{N} \sqrt{i_{r_{rated}}^2 - i_{r_{active}}^2} \right|, & i_r > i_{r_{rated}} \end{cases} \quad (40)$$

Where v_{wake} , V_m , L_m are the wake wind speed, magnetizing voltage, and mutual inductance calculated by (31), (41), and (19), respectively; $i_{r_{rated}}$ and $i_{r_{active}}$ are the actual rated rotor current and its real component, respectively. The magnetizing voltage V_m can be calculated by

$$V_m = V_s - |I_s| Z_s \quad (41)$$

$$Q_{GSC}^i = 3|V_s| \sqrt{I_{GSC_{rated}}^2 - \left(\frac{P_r^i - P_{kSC_{cond,switch}}^i - P_{GSC_{cond,switch}}^i}{3V_{GSC}} \right)^2} \quad (42)$$

Where,

$$P_r^i = 3v_r^i i_r^i \cos \theta_r^i \quad (43)$$

$$Q_{line}^i = im \left(|I_{line}^i|^2 (Z_{line}^i) \right) \quad (44)$$

$$Q_{transformer}^i = im \left(|I_{line}^i|^2 (Z_{transformer}^i) \right) \quad (45)$$

Where Z_{line}^i and $Z_{transformer}^i$ are the line impedance and the equivalent impedance of the transformer between WTG^i and the PCC, and I_{line} is the line current for WTG^i and can be calculated by

$$I_{line}^i = I_s^i + I_{GSC}^i \quad (46)$$

The reactive power capability model at the individual WTG (Q_{WTG}) can be determined by (4), where Q_{DFIG} and Q_{GSC} are calculated by (38) and (42), respectively.

4.6 Summary of The Proposed Method

The proposed method and its implementation procedure are summarized in this section. To accurately estimate reactive power capability at individual WTGs and at the plant-level, six variables (the maximum capacity of stator current, the maximum capacity of rotor current, rotor voltage, winding factor, magnetic saturation, and reactive power of the GSC) have been identified affecting reactive power capability of individual WTGs, while three variables (the turbine's power coefficient, wake effect, and feeder system losses) affecting reactive power capability at the plant-level. The procedure to implement the proposed method is shown in Fig. 4.15.

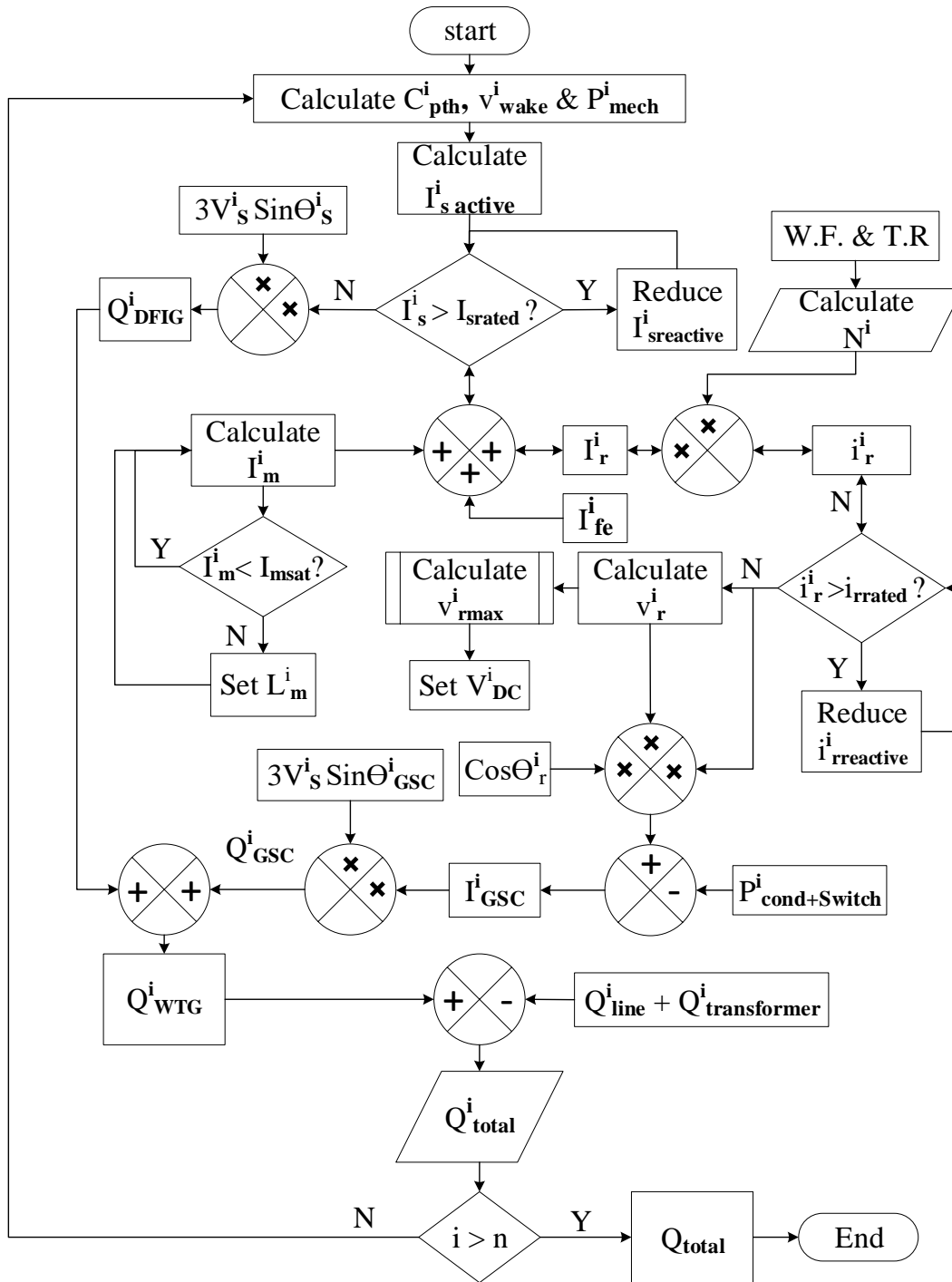


Fig. 4. 15. Flow chart of the proposed method.

To estimate the plant-level reactive power capability of a WPP, the reactive power capability of individual WTGs (Q_{WTG}^i) must be calculated first by the following 6 steps:

1) Based on the geographic location of the i th WTG, the power coefficient of the wind turbine (C_{pth}^i), the wake wind speed (v_{wake}^i), and the developed mechanical power (P_{mech}^i) are calculated by (26), (31) and (1), respectively.

2) From P_{mech}^i and (3), the stator active current ($I_{sactive}^i$) is computed. Afterward, the stator reactive current ($I_{sreactive}^i$) is calculated by (40), keeping I_s within its rated value.

3) The magnetizing current (I_m^i) and the iron loss current (I_{fe}^i) depend on V_m^i , and V_m^i is determined by (41). To calculate I_m^i , the magnetic saturation level of $DFIG^i$ is crucial. The magnetizing current can be calculated by (19), and the saturation constant can be calculated by (20).

4) Finally, I_r^i is calculated by (8), which is further converted to i_r^i by (10). In (10), the constant factor (N^i), which depends on the stator-rotor turn ratio (T.R= n_s/n_r) and the winding factor (W.F., K_s and K_r), the winding factor is calculated by (18). During the operation, if i_r^i exceeds its rated value, its reactive component ($i_{rreactive}^i$) is lowered down, and bring i_r^i to its rated value. Lowering $i_{rreactive}^i$ affects $I_{sreactive}^i$, consequently, which can be estimated by (40). Updated i_r^i is then used to calculate v_r^i by (10), (7), and (11), consecutively.

5) In this work, the reactive power capability is calculated by keeping the WTG's terminal voltage and active power generation unchanged. Limiting the rotor voltage would change the terminal voltage, and further change the active power generation. Therefore, instead of limiting the rotor voltage, the DC link voltage (V_{DC}^i) is modeled based on the maximum rotor voltage (v_{rmax}^i) by (12).

6) The reactive power of a DFIG (Q_{DFIG}^i) is calculated by (38). The reactive power capability of the GSC is calculated concurrently by (42). At this point, Q_{WTG}^i is calculated by (4).

Distribution losses associated with Q_{WTG}^i is computed using (44) and (45). Finally, reactive power contribution of WTG^i at the PCC (Q_{total}^i) is estimated by (37). This process continues until the plant-level reactive power capability (Q_{total}) is calculated by summing up Q_{total}^i for all WTGs.

4.7 Validation of the Proposed Models

4.7.1 Individual WTG level Reactive Power Capability

To validate the proposed reactive power capability model for individual WTGs, the proposed model is compared with two existing methods:

Method 1: in [26], a reactive power capability curve is developed within the constraints of stator and rotor current limits only. The impact of rotor voltage, magnetic saturation, winding factor or losses in the stator or the rotor circuit is not considered. Moreover, to calculate individual WTG level capability, it does not consider the reactive power capability of GSC as well.

Method 2: [28] consider a wide range of limiting factors like, stator and rotor current limit, rotor voltage limit, and magnetic saturation for a reactive power capability curve, however, the impact of winding factor is overlooked. The method consider GSCs reactive power capability to draw individual WTGs capability curve.

Proposed method: The proposed method considers the impact of stator and rotor current limit, rotor voltage limit, magnetic saturation and winding factor for reactive power capability curve. In addition, the GSCs maximum capability is also been added to draw the individual WTGs capability curve.

The comparison of reactive power capability of a DFIG is conducted using the three methods (the proposed method and the two existing methods) and the same simulation parameters shown in Table 4.1. In addition, for the two existing methods, constant factor N is set to 0.34 whereas, for the proposed method, it is set to (0.34×1.02) . The results are shown in Fig. 4.16. It is found that the method 1 underestimate the WTG level capability by not considering the GSCs capability, on the contrary, although method 2 consider GSCs maximum reactive power capability, however, overestimate the WTGs reactive power capability by not considering the winding factor, which limits their applicability in practical applications and can lead to faulty controller operation. The average difference between the existing Method 1 and the proposed method in over-excited and under-excited mode are 0.1122 pu and 0.1395 pu with an standard deviation of 0.0461 pu and 0.0424 pu respectively. Whereas the existing Method 2 and the proposed method hold the same value in under-excited mode but maintains a constant difference of 0.0263 pu in over-excited mode.

Table 4. 1: DFIG Parameter

Parameter Name	Value
Rated active power (MW)	3
Rated apparent power (MVA)	3.5
Rated stator voltage (kV)	1
Rated stator current (kA)	2.0207
Rated rotor current (A)	814
Rated GSC current (A)	350
Stator resistance (Ω)	0.0026
Stator leakage inductance (mH)	0.087
Magnetizing inductance (mH)	2.5
Rotor resistance (Ω)	0.0261
Rotor leakage inductance (mH)	0.783
Operating frequency (Hz)	60
Operating slip	-0.2 to 0.3

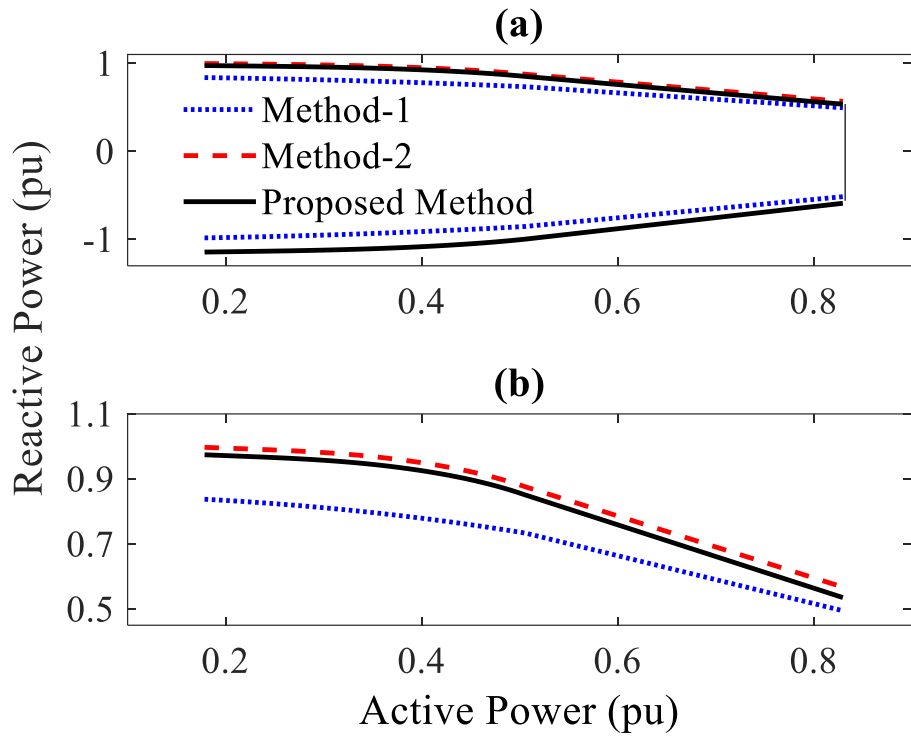


Fig. 4. 16. Comparison of reactive power capability of a DFIG: (a) overall capability; (b) the zoomed-in overexcited mode capability.

4.7.2 Plant Level Reactive Power Capability

The developed reactive power capability model at the plant-level using the proposed method is validated by comparing with SCADA measurement data of two WPPs currently operating in Newfoundland, Canada. The SCADA measurement data at the 66 kV PCC of the WPPs were recorded at the sampling rate of one sample per second in 2016 for the whole year. Each WPP has a nameplate capacity of 27 MW with nine DFIGs, and each DFIG is rated at 3 MW. Each DFIG is connected with a 3.5 MVA, 1 kV/25 kV wye/delta step-up transformer. The first WPP shown in Fig. 4.17 is connected with the grid at the PCC through a 30 MVA, 25 kV/66 kV wye/delta transformer, while the second WPP shown in Fig. 4.18 uses a 25 MVA, 25 kV/66 kV wye/delta

transformer connected to the grid. In addition to Table 4.1, simulation parameters for cables and transformers are shown in Table 4.2. Also, while calculating plant level reactive power capability using the proposed method, constant factor N is set to (0.34×1.02) for all WTGs.

Table 4. 2: Distribution Feeder Parameter

Cable Parameters	Positive Sequence	Zero Sequence
Resistance (Ω /km)	0.1153	0.413
Inductance (H/km)	1.05e-3	3.32e-3
Capacitance (F/km)	11.33e-009	5.01e-009
Transformer Data	TL	TH
Capacity (MVA)	3.5	40
Rated voltages (kV)	0.575/25	25/66
Resistance (pu)	0.025/30	0.003
Leakage Inductance (pu)	0.025	0.09

Under normal steady-state, the two WPPs follow grid code and run far below its reactive power capability based on SCADA data of a whole year in 2016. In fact, the operational SCAD data only occupy a narrow range. However, during contingencies, like grid faults or sudden off-lining of a power plant, the WPPs can be pushed to theses maximum limit through appropriate controller actions and maximize their contribution to the voltage deviation compensation process. In addition to this, it helps the grid operators scheduling power plants operations and calculating reactive power reserve of the grid to handle any unforeseen situation.

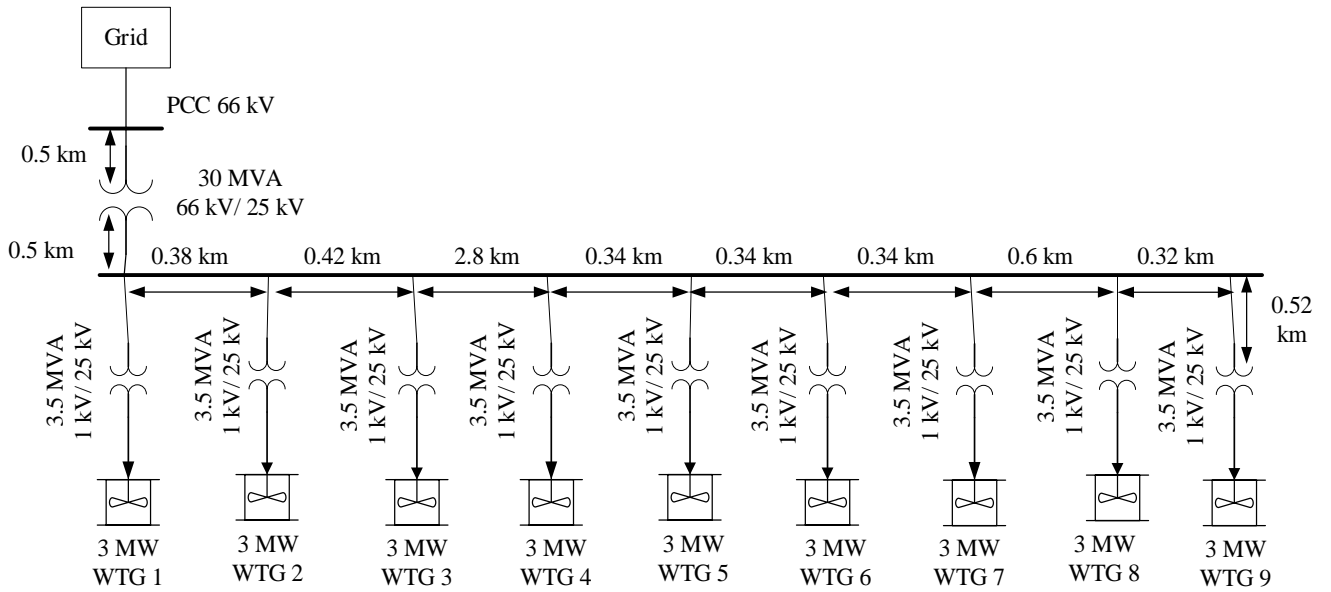


Fig. 4. 17. Single line diagram of WPP1.

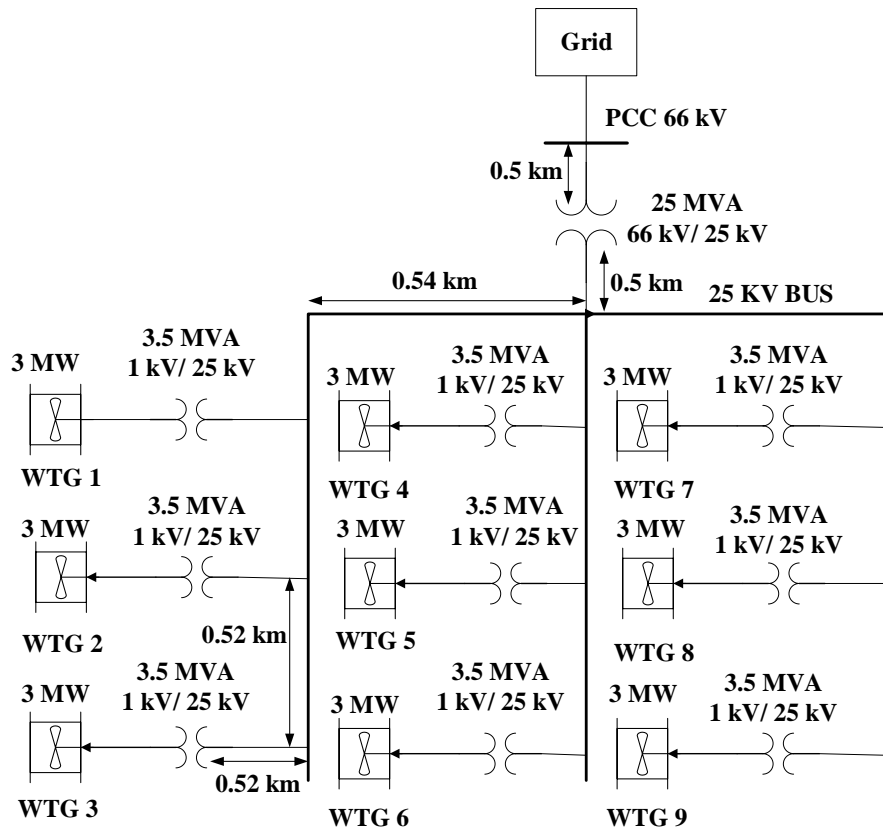


Fig. 4. 18. Single line diagram of WPP2.

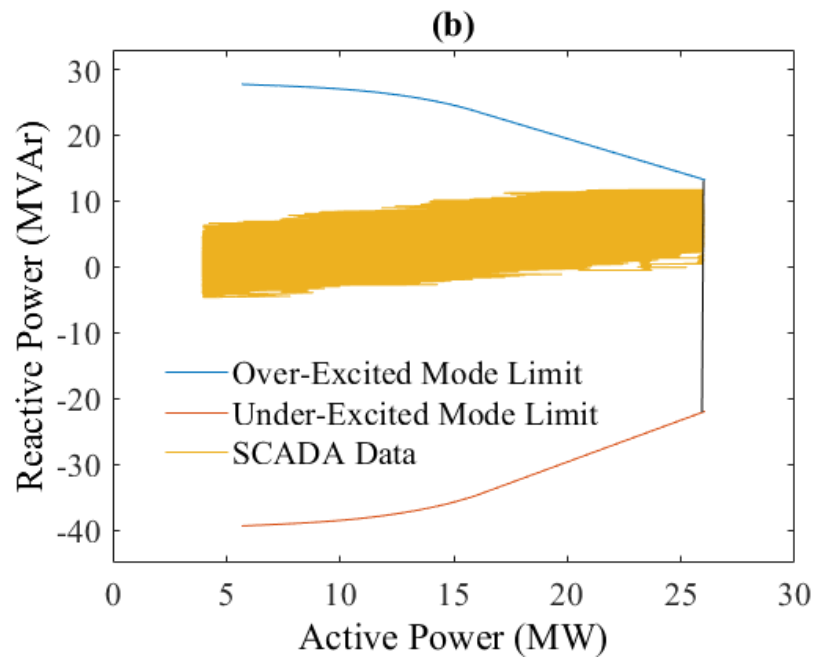
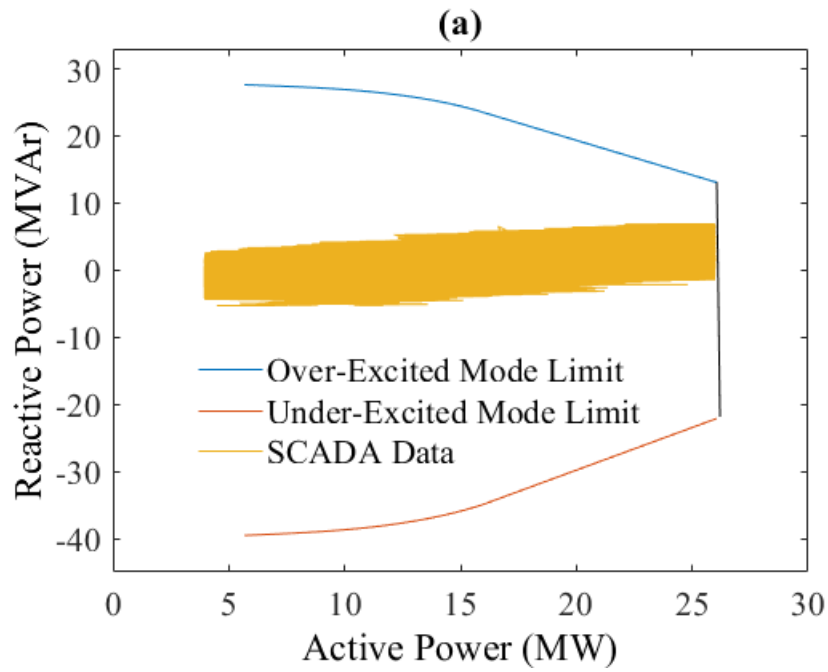


Fig. 4. 19. Comparison of reactive power capability: (a) WPP1; (b) WPP 2.

4.8 Conclusion

In this paper, an analytical model for reactive power capability curve at the plant-level of DFIG-based WPPs is proposed by considering several constraint variables at DFIGs and the plant-level. The reactive power capability curve for individual WTGs is derived first by including effect of stator current, rotor current, rotor voltage, winding factor, magnetic saturation, losses associated with converter switches, the stator and rotor circuits. The proposed method considers maximum capability of the GSC to realize maximum capability of individual of WTG. The proposed model for individual WTGs is validated by comparing with two existing methods; while the proposed model at the plant-level is compared with SACDA measurement data of two WPPs currently operating in Newfoundland, Canada for the whole year of 2016.

References

- [1] H. Falaghi, M. Ramezani, C. Singh and M. Haghifam, "Probabilistic Assessment of TTC in Power Systems Including Wind Power Generation," in *IEEE Syst. J.*, vol. 6, no. 1, pp. 181-190, Mar. 2012.
- [2] Z. H. Rather, Z. Chen, P. Thøgersen and P. Lund, "Dynamic Reactive Power Compensation of Large-Scale Wind Integrated Power System," in *IEEE Transactions on Power Syst.*, vol. 30, no. 5, pp. 2516-2526, Sept. 2015.
- [3] A. M. Khalil and R. Iravani, "Enhanced Generic Nonlinear and Linearized Models of Wind Power Plants," in *IEEE Trans. on Power Syst.*, vol. 32, no. 5, pp. 3968-3980, Sept. 2017.
- [4] A. M. Khalil and R. Iravani, "Power System Coherency Identification Under High Depth of Penetration of Wind Power," in *IEEE Trans. on Power Syst.*, vol. 33, no. 5, pp. 5401-5409, Sept. 2018.
- [5] M. P. S. Gryning, Q. Wu, Ł. Kocewiak, H. H. Niemann, K. P. H. Andersen and M. Blanke, "Stability Boundaries for Offshore Wind Park Distributed Voltage Control," in *IEEE Trans. on Control Syst. Technol.*, vol. 25, no. 4, pp. 1496-1504, Jul. 2017.
- [6] A. E. M. Operator, "Wind Turbine Plant Capabilities Report," *Wind Integration Studies*, 2013.
- [7] D. Zhou, F. Blaabjerg, M. Lau and M. Tønnes, "Optimized Reactive Power Flow of DFIG Power Converters for Better Reliability Performance Considering Grid Codes," in *IEEE Trans. on Ind. Electron.*, vol. 62, no. 3, pp. 1552-1562, Mar. 2015.
- [8] F. Blaabjerg, Zhe Chen and S. B. Kjaer, "Power electronics as efficient interface in dispersed power generation Syst.," in *IEEE Trans. on Power Electron.*, vol. 19, no. 5, pp. 1184-1194, Sept. 2004.

- [9] J. M. Carrasco *et al.*, "Power-Electronic Systems for the Grid Integration of Renewable Energy Sources: A Survey," *IEEE Trans. on Ind. Electron.*, vol. 53, (4), pp. 1002-1016, 2006. .
- [10] J. M. Guerrero *et al.*, "Distributed Generation: Toward a New Energy Paradigm," in *IEEE Ind. Electron. Mag.*, vol. 4, no. 1, pp. 52-64, Mar. 2010.
- [11] R. Cardenas, R. Pena, S. Alepuz and G. Asher, "Overview of Control Systems for the Operation of DFIGs in Wind Energy Applications," in *IEEE Trans. on Ind. Electron.*, vol. 60, no. 7, pp. 2776-2798, Jul. 2013.
- [12] M. J. Hossain, T. K. Saha, N. Mithulananthan and H. R. Pota, "Control Strategies for Augmenting LVRT Capability of DFIGs in Interconnected Power Systems," in *IEEE Trans. on Ind. Electron.*, vol. 60, no. 6, pp. 2510-2522, Jun. 2013.
- [13] M. Liserre, R. Cardenas, M. Molinas and J. Rodriguez, "Overview of Multi-MW Wind Turbines and Wind Parks," in *IEEE Trans. on Ind. Electron.*, vol. 58, no. 4, pp. 1081-1095, Apr. 2011.
- [14] A. Luna, F. K. A. Lima, D. Santos, P. Rodriguez, E. H. Watanabe and S. Arnaltes, "Simplified Modeling of a DFIG for Transient Studies in Wind Power Applications," in *IEEE Trans. on Ind. Electron.*, vol. 58, no. 1, pp. 9-20, Jan. 2011.
- [15] J. Kim, E. Muljadi, J. Park and Y. C. Kang, "Flexible IQ–V Scheme of a DFIG for Rapid Voltage Regulation of a Wind Power Plant," in *IEEE Trans. on Ind. Electron.*, vol. 64, no. 11, pp. 8832-8842, Nov. 2017.
- [16] M. Tsili and S. Papathanassiou, "A review of grid code technical requirements for wind farms," in *IET Renewable Power Generation*, vol. 3, no. 3, pp. 308-332, Sept. 2009.

- [17] H. Karbouj and Z. H. Rather, "Voltage Control Ancillary Service From Wind Power Plant," in *IEEE Trans. on Sustain. Energy*, vol. 10, no. 2, pp. 759-767, Apr. 2019.
- [18] D. Zheng, X. Xiong, J. Ouyang, Z. Zhang and C. Xiao, "Control Method for Maximizing Fault Voltage of Wind Generation-Integrated Power Systems With Consideration of DFIG-Grid Coupling," in *IEEE Access*, vol. 7, pp. 894-905, 2019.
- [19] D. Zhou and F. Blaabjerg, "Optimized Demagnetizing Control of DFIG Power Converter for Reduced Thermal Stress During Symmetrical Grid Fault," in *IEEE Trans. on Power Electron.*, vol. 33, no. 12, pp. 10326-10340, Dec. 2018.
- [20] J. Ouyang, M. Li, Z. Zhang and T. Tang, "Multi-Timescale Active and Reactive Power-Coordinated Control of Large-Scale Wind Integrated Power System for Severe Wind Speed Fluctuation," in *IEEE Access*, vol. 7, pp. 51201-51210, 2019.
- [21] J. Ouyang, M. Li, Y. Diao, T. Tang and Q. Xie, "Active control method of large-scale wind integrated power system with enhanced reactive power support for wind speed fluctuation," in *IET Generation, Transmission & Distribution*, vol. 12, no. 21, pp. 5664-5671, 27 11 2018.
- [22] S. Mondal and D. Kastha, "Maximum Active and Reactive Power Capability of a Matrix Converter-Fed DFIG-Based Wind Energy Conversion System," in *IEEE J. of Emerg. and Sel. Topics in Power Electron.*, vol. 5, no. 3, pp. 1322-1333, Sept. 2017.
- [23] E. Vittal, M. O'Malley and A. Keane, "A Steady-State Voltage Stability Analysis of Power Systems With High Penetrations of Wind," in *IEEE Trans. on Power Syst.*, vol. 25, no. 1, pp. 433-442, Feb. 2010.
- [24] G. F. Gontijo *et al.*, "Modeling, Control and Experimental Verification of a DFIG with a Series-Grid-Side Converter with Voltage Sag, Unbalance and Distortion Compensation Capabilities," in *IEEE Trans. on Ind. Appl.*.

- [25] M. Z. Sujod, I. Erlich and S. Engelhardt, "Improving the Reactive Power Capability of the DFIG-Based Wind Turbine During Operation Around the Synchronous Speed," in *IEEE Trans. on Energy Convers.*, vol. 28, no. 3, pp. 736-745, Sept. 2013.
- [26] H. Pulgar-Painemal, "Enforcement of Current Limits in DFIG-Based Wind Turbine Dynamic Models Through Capability Curve," in *IEEE Trans. on Sustain. Energy*, vol. 10, no. 1, pp. 318-320, Jan. 2019.
- [27] J. Kim, J. Seok, E. Muljadi and Y. C. Kang, "Adaptive Q–V Scheme for the Voltage Control of a DFIG-Based Wind Power Plant," in *IEEE Trans. on Power Electron.*, vol. 31, no. 5, pp. 3586-3599, May 2016.
- [28] S. Engelhardt, I. Erlich, C. Feltes, J. Kretschmann and F. Shewarega, "Reactive Power Capability of Wind Turbines Based on Doubly Fed Induction Generators," in *IEEE Trans. on Energy Convers.*, vol. 26, no. 1, pp. 364-372, Mar. 2011.
- [29] [Online] Available:
https://climate.weather.gc.ca/climate_data/hourly_data_e.html?hlyRange=2006-01-23%7C2020-06-28&dlyRange=2006-12-01%7C2020-06-28&mlyRange=2006-12-01%7C2007-07-01&StationID=45567&Prov=NL&urlExtension=_e.html&searchType=stnProv&optLimit=yearRange&StartYear=2016&EndYear=2017&selRowPerPage=25&Line=61&1stProvince=NL&timeframe=1&Year=2016&Month=3&Day=28#. Accessed on: June 29, 2020.
- [30] B. Wu *et al*, *Power Conversion and Control of Wind Energy Systems*. 201176.
- [31] D. Xu, F. Blaabjerg, W. Chen, and N. Zhu, "Advanced Control of Doubly Fed Induction Generator for Wind Power Systems," pp. 69, Wiley-IEEE Press, 2018.

- [32] G. Abad, J. Lopez, M. Rodriguez, L. Marroyo, and G. Iwanski, Doubly fed induction machine: modeling and control for wind energy generation, vol. 85. John Wiley & Sons, 2011.
- [33] F. Koch, M. Gresch, F. Shewarega, I. Erlich and U. Bachmann, "Consideration of wind farm wake effect in power system dynamic simulation," *2005 IEEE Russia Power Tech*, St. Petersburg, 2005, pp. 1-7.
- [34] [Online] Available:
<https://www.mathworks.com/help/phymod/sps/powersys/ref/windturbine.html>. Accessed on: June 29, 2020.
- [35] N. O. Jensen, *A Note on Wind Generator Interaction*. 1983.
- [36] [Online] Available:
<https://www.mathworks.com/help/phymod/sps/owersys/ref/threephasepisectionline.html>. Accessed on: June 29, 2020.

Chapter 5

An Adaptive Droop Coefficient Based Voltage Control Approach for Wind Power Plants through Enhanced Reactive Power Support

Md Nasmus Sakib Khan Shabbir¹, *Student Member*, IEEE, Xiaodong Liang², *Senior Member*, IEEE, and Saikat Chakrabarti³, *Senior Member*, IEEE

¹Department of Electrical and Computer Engineering, Memorial University of Newfoundland, St. John's, Newfoundland, Canada.

²Department of Electrical and Computer Engineering, University of Saskatchewan, Saskatoon, Saskatchewan, Canada.

³Department of Elect Electrical Engineering, Indian Institute of Technology Kanpur, Kanpur, Uttar Pradesh, India.

A version of this chapter is to be submitted to a journal. MD Nasmus Sakib Khan Shabbir co-authored this paper under the supervision of Dr. Xiaodong Liang. Sakib's contributions are listed as follows:

- Performed literature searches required for the development of grid connected wind power plant controller.
- Developed the wind power plant base model and evaluated the proposed controller through MATLAB/Simulink simulations.
- Involved in the writing of the paper draft as the first author.

Dr. Xiaodong Liang provided continuous technical guidance, checked the results, and modified the manuscript. Dr. Saikat Chakrabarti modified the manuscript.

In this chapter, the manuscript is presented with altered figure numbers, table numbers, and reference formats in order to match the thesis formatting guidelines set out by Memorial University of Newfoundland.

The wind power plant controller presented in this chapter is an improved version of the controller presented in Chapter 3. The controller presented in this chapter operates in the voltage control mode, and when needed, it can extract the maximum amount of reactive power from the wind turbine generators. However, the controller presented in Chapter 3 operates in the reactive power control mode and extracts reactive power within the wind turbine generator's steady state reactive power capability.

Abstract- To maximize the reactive power support from a wind power plant (WPP) and maintain the power factor (PF) at the point of interconnection (POI) within the acceptable limits, an adaptive droop coefficient-based WPP controller is proposed in this paper. The controller consists of a central WPP controller and a local wind turbine generator (WTG) controller. An integrated power factor controller enables the central WPP controller to regulate the power factor at the POI under normal operation. An updated droop coefficient model considering the depth of voltage deviation and the range of reactive power capability enables the controller to push the WTG more towards its maximum limit. To ensure faster and robust operation, both the central WPP controller and local WTG controllers are operated in voltage control mode. Additional reactive power is exported from the grid side converter (GSC) through a developed GSC controller. The effectiveness of the proposed controller is validated through case and sensitivity studies in MATLAB/Simulink environment.

Keywords- Adaptive droop coefficient, $P - Q$ diagram, voltage control, reactive power.

5.1 Introduction

Due to environmental concerns from fossil fuel-based large central power generation, and rapid technology advancement and price reduction of renewable energy sources, wind and solar power generation have been increasingly integrated to our modern power grids [1],[2]. Wind power offers about a quarter of global renewable generation capacity, serving as one of the major forms of renewable energy sources. Wind power is mainly generated by utility-scale transmission-connected power plants. Despite all the benefits, due to uncertainties associated with the wind, high penetration of wind power plants (WPPs) into the grid makes the grid vulnerable [3]. As a result, grid codes are imposed for WPPs to ensure stability and power quality of power grids. Grid codes require that WPPs should supply ancillary services instead of tripping off and bring the system back to normal operating condition during a contingency [4]–[6].

Typically, the utility company requires that the voltage deviation is within ± 0.05 in pu around the nominal value under normal operation, and the corresponding power factor is within the range of $[-0.95, +0.95]$ at the POI. For voltage deviations beyond the above limits, rapid dispatch of reactive power within the WPP's capability is required to compensate voltage deviations. Another important aspect is that being spanned over a wide area, WPPs rely heavily on communication networks, and an interruption in communication could have severe impact on the performance and stability of the system. Therefore, WPP controllers are required to be equipped with a contingency plan so that a communication failure does not lead to a complete failure of a WPP.

The first two generations of wind power technologies, Types 1 and 2, do not have the reactive power generation competency, therefore, they cannot contribute to the voltage compensation action. Although the third and fourth generation of wind power technologies, Types 3 and 4, are developed with the reactive power handling competency [7], [8], due to technological constraints,

their reactive power competency cannot be utilized properly. As a result, WPPs require additional reactive power support, such as capacitor banks or static var compensators (SVCs) [9]. However, dynamic synchronization between a WPP and reactive power compensation equipment is a complicated process; it may cause significant voltage overshoot and cascaded tripping-off if not properly designed [10]. Therefore, research has been conducted to reduce dependence on such equipment by maximizing reactive power extraction from the WPPs through appropriate control actions and to ensure effective contribution to voltage control at the POI.

Voltage control at the POI of a WPP by dispatching reactive power can be categorized into: 1) hierarchical reactive power control-based approach [9], [11], [12]; and 2) voltage control-based approach [13]–[16]. In the first approach, a reactive power control mode is used in both central WPP controller and local WTG controllers, where the central WPP controller sets references for local WTG controllers. However, excessive dependence on the communication system between the central WPP controller and local WTG controllers results in slow response, and the system is vulnerable to communication failures [14].

The voltage control-based approach can be classified into two categories. In the first category, the central WPP controller operates in voltage control mode, but the local WTG controller operates on the reactive power control mode [17]. In this method, local controllers are also completely supervised by the central WPP controller, therefore, they exhibit sluggish response and remains vulnerable to communication failures.

As a remedy, in the second category, the voltage control mode-based central WPP controller and local WTG controllers are developed in [13]–[15], [18], where local WTG controllers response immediately based on voltage deviations sensed at the WTG terminal. Concurrently, the central WPP controller sends a voltage reference to local WTG controllers, which droops the WTG

terminal around its nominal value and brings the voltage at the POI back to the normal operating range by dispatching necessary reactive power [15]. This approach enables fast response and prevents the complete system breakdown during communication failures. In this approach, local WTG controllers involve either a rotor side converter (RSC) alone [14]; or both RSC and grid side converter (GSC) combined [15]. In the former one, no reactive power is harnessed from the GSC, while in the second one, both RSC and GSC's reactive power competency are utilized. In the core of the control of reactive power dispatch through the RSC, Ref [19] adopts a constant slope for the WTG's $V - I$ characteristics; while Ref [14] improved [19] by adopting an adaptive slope. Due to geographical positions of WTGs within a WPP, the active power generation from WTGs varies. Therefore, in the adaptive slope-based approach, slopes are chosen in such a way that an inverse relationship with active power generation is maintained. Because reactive power dispatch increases with a higher $V - I$ slope, during a contingency, controllers extract more reactive power from WTGs that generate less active power. For this reason, the adaptive slope-based approach can contribute more reactive power than the fixed slope-based approach, as all WTGs contribute same reactive power when a fixed slope is assigned to all of them.

The slope of the $V - I$ characteristics, known as “inverse droop coefficient” ($1/K_{Droop}$), regulates how far the RSC controller can push the WTG towards its maximum capability. This droop coefficient used in [14], [18] varies only with the amount of active power being dispatched by the respective WTG. Therefore, the RSC controller estimates the same droop coefficient regardless of the depth of voltage deviations. Consequently, controllers cannot take the full leverage of the WTG's maximum reactive power capacity during a deeper voltage sag.

To overcome this issue, in this paper, an adaptive droop coefficient model that varies with the active power generation and the depth of voltage deviations is proposed. The proposed RSC controller can ensure more reactive power contribution from the WTG during contingency.

The maximum reactive power capability model of a WTG is crucial in computing its droop coefficient. The maximum current carrying capacity of the stator and rotor, and the maximum allowable voltage for the rotor circuit are mostly used factors to define the maximum reactive power capability of a WTG [13], [14], [18]. However, parameters, such as winding factors and magnetic saturation, are ignored, which reduced the model's accuracy. To overcome this issue, we have developed the maximum reactive power capability curve for WTG by considering comprehensive parameters including winding factors and magnetic saturation [20]. In this paper, we will use this result directly in the new controller design.

In this paper, in addition to the RSC controller, a GSC controller is also developed to utilize its reactive power competency. The effectiveness of the developed controller is studied in a Simulink equivalent model of a real WPP currently operating in Newfoundland, Canada.

The major contributions of the paper include: 1) developing a novel adaptive droop coefficient-based WPP controller to maximize reactive power dispatch; 2) integrating the developed maximum reactive power capability model to estimate droop coefficients of a WTG; and 3) developing an adaptive droop coefficient model that varies with active power dispatch and the depth of voltage deviations at the POI.

The paper is arranged as follows: the proposed control approach is introduced in Section 5.2; the system under analysis, and its maximum reactive power capability model is described in Section 5.3; the detailed working principles of the developed controller is elaborated in Section 5.4; case studies are conducted in Section 5.5, showing comparison between existing methods and

the proposed controller under various normal and abnormal operating conditions; sensitivity studies by considering several influential factors are conducted in Section 5.6; and conclusions are drawn in Section 5.7.

5.2 The Proposed Control Approach

To meet requirements of grid codes, a novel hierarchical control approach for a DFIG-based WPP is proposed, where both the central WPP controller and local WTG controller operate in voltage control mode. Local WTG controllers consist of an RSC controller and a GSC controller. The central WPP controller communicates with local WTG controllers by a switched Ethernet-based hierarchical communication network.

Depending on the depth of voltage deviations, the central WPP controller droops the WTG voltage up to 5% around its nominal value through local WTG controllers. In the event of a communication failure, subjected to available reactive power capability, local WTG controllers maintain the nominal voltage at the WTG terminal, which keeps the POI voltage within the normal operation limits and prevents cascaded WPP failures.

The proposed controller regulates the WPP's reactive power generation in the following five steps as depicted in Fig. 5.1.

Step 1: *Detection of voltage deviations.* The central WPP controller monitors the voltage at the POI and compares it with the reference. If a deviation is detected, the controller first measures the depth of voltage deviation (ΔU).

Step 2: *Power factor control.* Voltage deviations ΔU up to ± 0.05 in pu around the nominal is counted as normal operating conditions, and WPPs are required to maintain $[-0.95, +0.95]$ power factor at the POI. Therefore, the central WPP controller turns the power factor (PF) controller on

in this case. The PF controller reads the dispatched active power at the POI and generate ΔU_{Adj} , which is added up with ΔU to generate ΔU_{Ref} . ΔU_{Ref} is the adjusted reference for local WTG controllers to ensure the required power factor at the POI. If the depth of voltage deviations is more than ± 0.05 , ΔU_{Adj} is set to “zero”, instead of maintaining power factor, the system is required to bring the voltage back to a normal operating range by supplying sufficient reactive power.

Step 3: Updating K_{Droop} . Based on the depth of voltage deviations, and active power supplied by the individual WTG, The RSC controller updates K_{Droop} and computes $I_{dRSC,Ref}$. Simultaneously, the GSC controller computes $I_{qGSC,Ref}$, which regulates GSC’s reactive power generation, where $I_{dRSC,Ref}$ and $I_{qGSC,Ref}$ are direct(d)- and quadrature(q)-axis reference current of RSC and GSC, respectively.

Step 4: Reference adjustment. The RSC computes $I_{RSC,Ref}$ using the computed $I_{dRSC,Ref}$ and $I_{qRSC,Ref}$, and compares with $I_{RSC,Max}$. If the net reference current ($I_{RSC,Ref}$) exceeds the maximum current capacity ($I_{RSC,Max}$), $I_{qRSC,Ref}$ is reduced until the reference and the maximum current capacity matches. $I_{qRSC,Ref}$ is the q-axis reference current of the RSC. Similarly, if the estimated net reference current for GSC ($I_{GSC,Ref}$) exceeds GSC’s maximum current carrying capacity ($I_{GSC,Max}$), the GSC controller reduces $I_{qGSC,Ref}$ to match $I_{GSC,Ref}$ with $I_{GSC,Max}$.

Step 5: Control signal generation. Based on final values of $I_{dRSC,Ref}$ and $I_{qRSC,Ref}$, the RSC generates the control signal, V_{RSC} , and pass it to the PWM generator. Concurrently, the GSC generates its control signal, V_{GSC} , using $I_{dGSC,Ref}$ and $I_{qGSC,Ref}$ and passes it to the PWM generator.

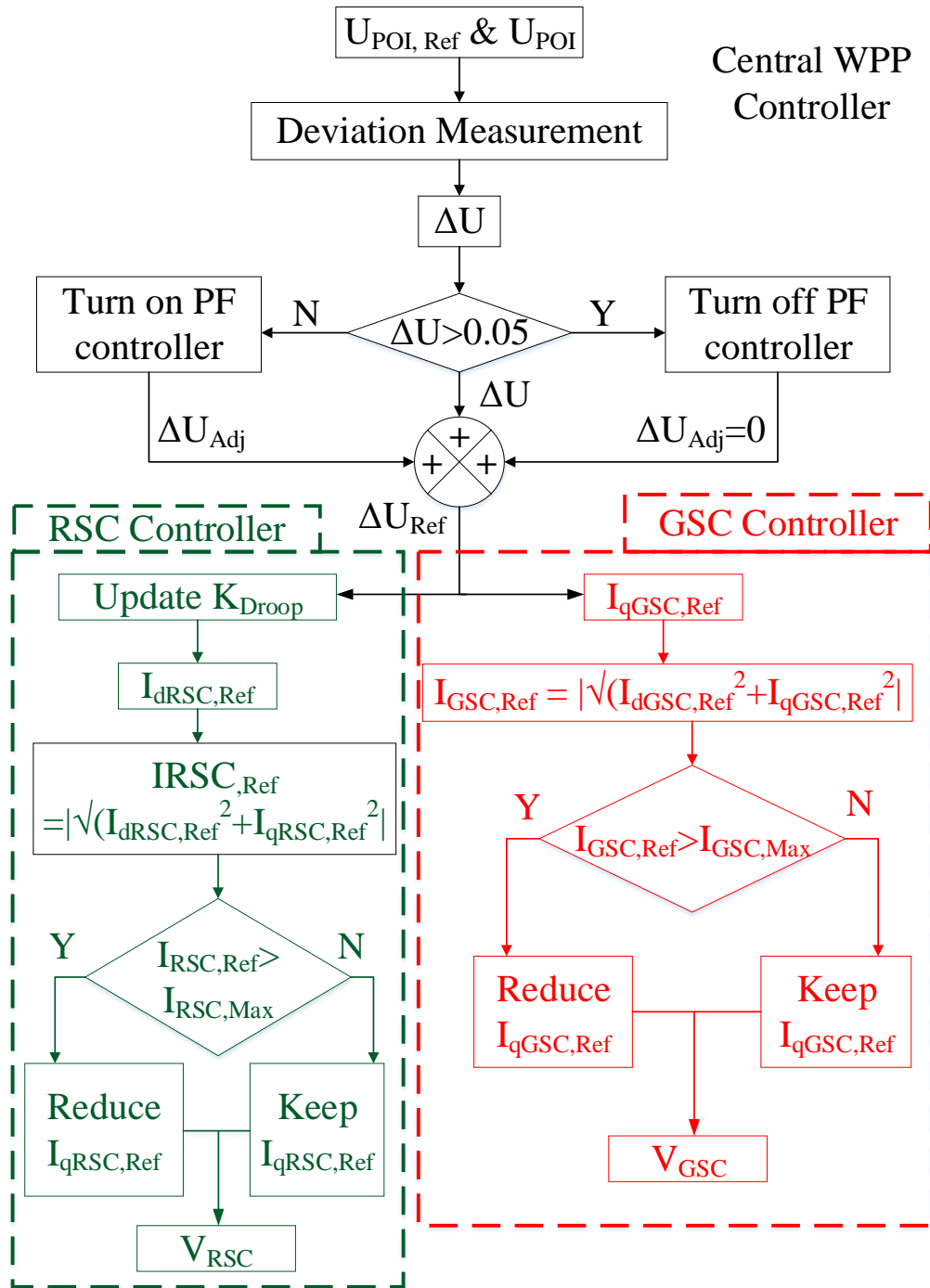


Fig. 5. 1. The flow chart of the proposed control approach.

5.3 The System Under Analysis and Its Maximum Reactive Power Capability Model

In this section, the WPP used in the analysis is introduced, and the maximum reactive power capability model for the WPP is explained.

5.3.1 Description of the WPP Model

The simulation model used in this paper represents an actual WPP currently operating in Newfoundland, Canada. It has a 27 MW nameplate rating, with 9 doubly-fed induction generators (DFIGs), each rated at 3 MW. Each WTG is connected with a 25 kV plant main bus with a 3.5 MVA, 1 kV/25 kV, wye/delta step-up transformer, which is further connected with the 66 kV POI through a 25 MVA wye/delta transformer. Provided by Newfoundland Hydro, the three-phase short circuit MVA at the POI of the WPP is 135 MVA and the X/R ratio is 3.259. The electrical single-line diagram of this actual WPP is depicted in Fig. 5.2.

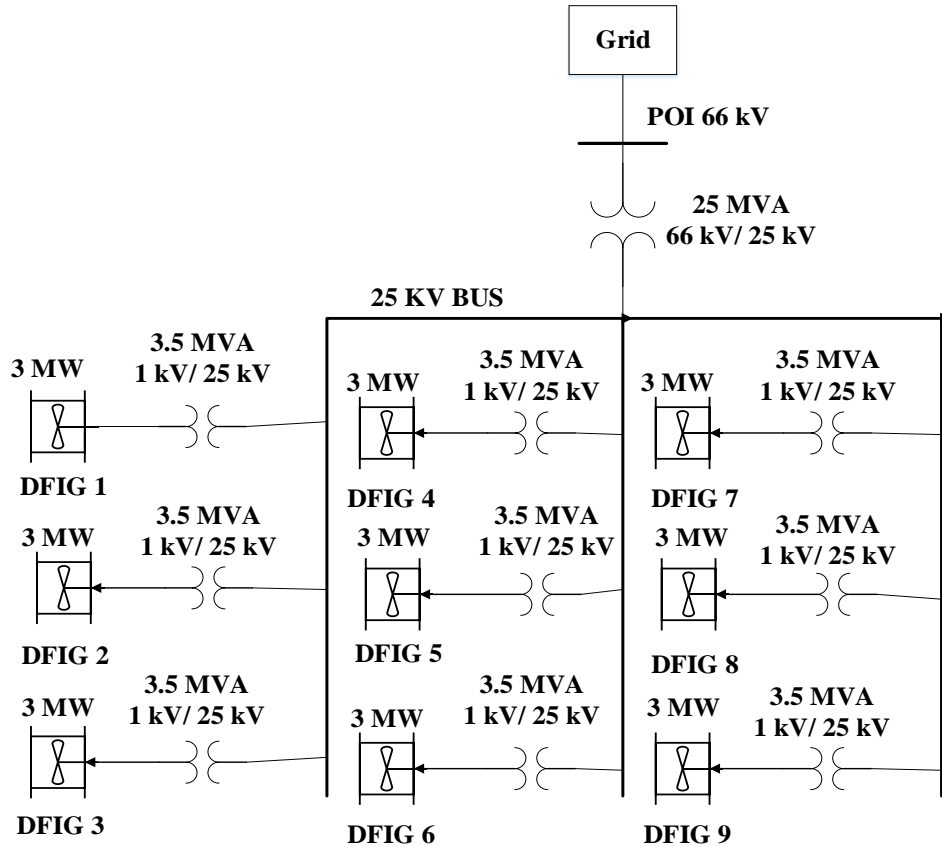


Fig. 5. 2. The electrical single-line diagram of an actual WPP currently in operation in Newfoundland, Canada.

In this study, instead of using a full detailed model, a lumped WPP model with a nameplate capacity of 30 MVA is developed. The model parameters are tuned so that its responses match with the SCADA field measurements of the WPP at the POI. The real power generation simulated by the lumped model of the WPP, and SCADA field measurements recorded from 18 to 23 pm on January 16, 2016 are compared in Fig. 5.3. From the figure it can be inferred that active power characteristics of both the simulation model and the actual WPP show a similar exponential shape, which got flattened at the same pick value.

More detailed comparison between the simulated values and SCADA field measurement data for voltage, active power, and reactive power of the WPP are provided in Case 1 in Section V.

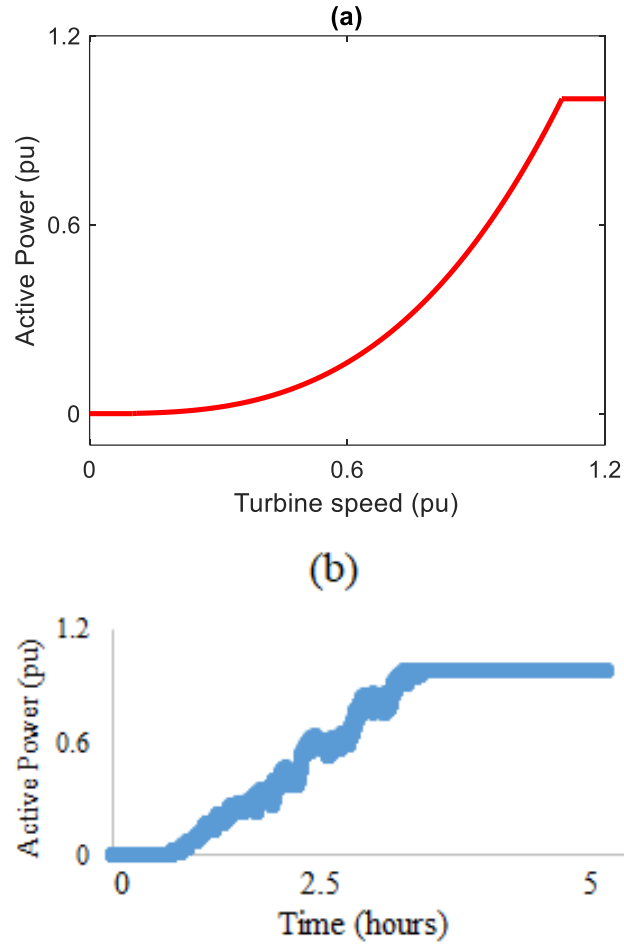


Fig. 5. 3. The active power generation of the WPP: (a) simulation model; and (b) SCADA field measurements.

The schematic diagram of the WPP simulation model is given in Fig. 5.4. The lumped model is connected to the 66 kV grid through a 40 MVA wye/delta transformer. Two layers of controllers, a central WPP controller and a local WTG controller, are present in the system. The central WPP controller reads the voltage at the POI and droops the local WTG controllers. The local WTG controller located at each WTG consists of a GSC controller and an RSC controller. Both layers of the controllers are operated in voltage control mode. The details of simulation parameters are tabulated in Table 5.1. More detailed description of the simulation model for the actual WPP can be found in our previous research published in [9].

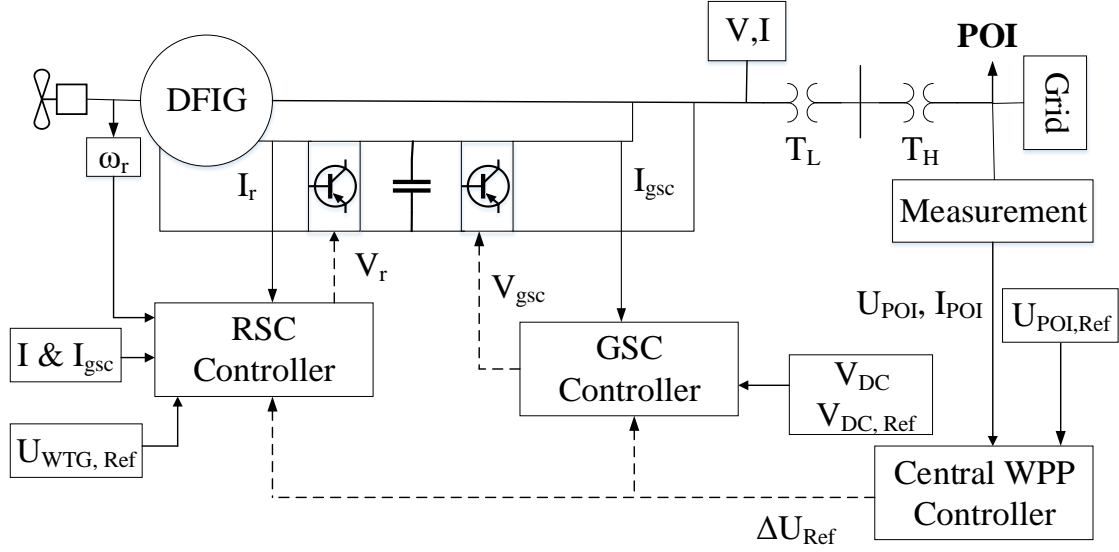


Fig. 5. 4. The schematic diagram of the WPP simulation model.

Table 5. 1: Simulation Parameters for the WTG Model, Cables and Transformers

DFIG Data		DFIG Control Data		
Nominal apparent power	30 MVA	Regulator Name	Proportional Gain (K _P)	Integral Gain (K _I)
Nominal voltage	575 V	RSC voltage Regulator (PI ₁)	1.25	80
Stator resistance	0.00706 pu	RSC Power Regulator (PI ₂)	1	100
Stator leakage inductance	0.171pu	RSC Current Regulator (PI ₃)	0.38	8
Magnetizing inductance	2.9 pu	DC voltage (PI ₄)	0.002	0.5
Rotor resistance	0.005pu	GSC current Regulator (PI ₅)	1	100
Rotor leakage inductance	0.156pu	Pitch angle	500	None
System frequency	60 Hz			
Nominal DC bus voltage	1200 V			
Rated wind speed	12 m/s			

Cable Data		
Parameter Name	Positive Sequence	Zero Sequence
Resistance (Ω /km)	0.1153	0.413
Inductance (H/km)	1.05e-3	3.32e-3
Capacitance (F/km)	11.33e-009	5.01e-9
Transformer Data		
	T _L	T _H
Capacity (MVA)	9×3.5	40
Rated voltages (kV)	0.575/25	25/66
Resistance (pu)	0.025/30	0.003
Leakage Inductance (pu)	0.025	0.09

5.3.2 Plant-Level Reactive Power Capability Model

We have developed a mathematical model to realize the maximum reactive power capability of a DFIG-based WPP by considering a wide range of factors affecting both the plant level and individual WTG in [20]. Factors that are considered in the model affecting the individual WTG's capacity are the maximum capacity of stator and rotor currents, rotor voltage, winding factor, magnetic saturation, and reactive power of the GSC. In addition, the wind turbine's power coefficient, wake effect, and feeder system losses are the factors considered that limit the plant level's reactive power capacity. The detailed mathematical derivation process and description of the limiting factors can be found in [20].

The reactive power capability model at the plant-level (Q_{total}) can be determined as follows:

$$Q_{Total} = \sum_{i=1}^n (Q_{WTG}^i + Q_{GSC}^i - Q_{line}^i - Q_{transformer}^i) \quad (1)$$

where n is the number of WTGs in the WPP; the superscript i represents the quantities for the i th WTG; Q_{WTG}^i and Q_{GSC}^i are the reactive power capability of the i th WTG and its GSC, respectively; Q_{line}^i and $Q_{transformer}^i$ are the associated line and transformer losses for the i th WTG, respectively. Q_{WTG}^i is calculated by,

$$Q_{WTG}^i = 3|V_s| \sqrt{I_{S_{rated}}^2 - \frac{\pi R^2 C_p \rho (v_{wake}^i)^3}{6(1-s^i)V_s}} \quad (2)$$

$$s^i = \frac{\omega_s R - r_{gb} v_{wake} \lambda p}{\omega_s R} \quad (3)$$

where ω_s is the synchronous speed, r_{gb} is the gear box ratio, p is the number of pole pairs, and $I_{S_{rated}}$ is the rated stator current, which can be calculated as follows:

$$I_{S_{rated}} = \begin{cases} \frac{S_{rated}}{3|V_s|}, & i_r \leq i_{r_{rated}} \\ \left| \frac{|V_m|}{R_{fe}} + \frac{|V_m|}{j\omega_s L_m} - \frac{i_{r_{active}}}{N} \pm j \frac{1}{N} \sqrt{i_{r_{rated}}^2 - i_{r_{active}}^2} \right|, & i_r > i_{r_{rated}} \end{cases} \quad (4)$$

where v_{wake} , V_m , L_m are the wake wind speed, magnetizing voltage, and mutual inductance; $i_{r_{rated}}$ and $i_{r_{active}}$ are the actual rated rotor current and its real component, respectively. The magnetizing voltage V_m can be calculated by,

$$V_m = V_s - |I_s| Z_s \quad (5)$$

The reactive power capability of the GSC can be formulated as follows:

$$Q_{GSC}^i = 3|V_s| \sqrt{I_{GSC_{rated}}^2 - \left(\frac{P_r^i - P_{RSC_{cond,switch}}^i - P_{GSC_{cond,switch}}^i}{3V_{GSC}} \right)^2} \quad (6)$$

where,

$$P_r^i = 3v_r^i i_r^i \cos \theta_r^i \quad (7)$$

$$Q_{line}^i = im \left(|I_{line}^i|^2 (Z_{line}^i) \right) \quad (8)$$

$$Q_{transformer}^i = im \left(|I_{line}^i|^2 (Z_{transformer}^i) \right) \quad (9)$$

where Z_{line}^i and $Z_{transformer}^i$ are the line impedance and the equivalent impedance of the transformer between WTGⁱ and the PCC, and I_{line}^i is the line current for WTGⁱ and can be calculated by,

$$I_{line}^i = I_s^i + I_{GSC}^i \quad (10)$$

5.4 Working Principle of the Developed Controller

The detailed working principle of the proposed controller in this paper is presented in this section.

5.4.1 The Central WPP controller

The central WPP controller monitors voltage at the POI and supervises the WPP operation. In the event of a voltage sag, it sets the voltage reference (ΔU_{Ref}) for WTGs following grid codes. The schematic diagram of the proposed central WPP controller is shown in Fig. 5.5.

To avoid any persisting post-fault over-surge voltage, a washout filter has been added. The filter washes up any low frequency components, and thus, removes accumulated values in the integrator. This way, the controller can adjust ΔU_{Ref} with changing dynamics faster. Despite having the washout filter, the central WPP controller cannot prevent the post-fault voltage spike due to the presence of the communication latency with local WTG controllers but can bring it back to the nominal value faster than the case without a washout filter.

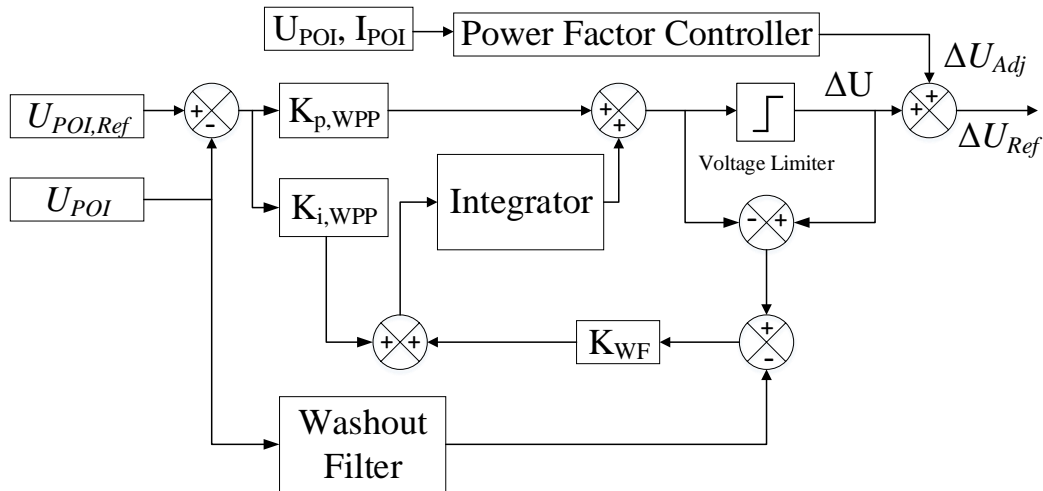


Fig. 5. 5. The schematic diagram of the proposed central WPP controller.

To meet the power factor requirements at the POI during normal operation, a power factor controller has been added with the central WPP controller as shown in Fig. 5.5. The added power factor controller reads active and reactive power values at the WTG terminal and generate the signal of ΔU_{Adj} , which adjusts ΔU_{Ref} to meet the power factor requirements. The power factor controller makes no adjustment and sends “zero” for ΔU_{Adj} , if the voltage deviation is beyond the normal range of ± 0.05 pu. The schematic diagram of the proposed power factor controller is given in Fig. 5.6.

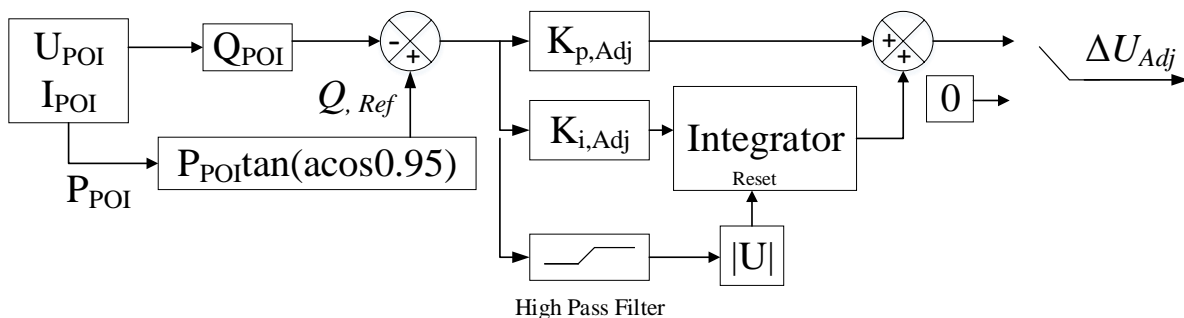


Fig. 5. 6. The schematic diagram of the proposed power factor controller.

5.4.2 The RSC Controller

The RSC controller, located at each of individual WTGs, regulates reactive power flow from WTGs, and operates in voltage control mode. It reads the voltage set point at the WTG terminal ($U_{WTG,Ref}$), adjusts it with the received ΔU_{Ref} , and generates U_{Ref} . The parameter (U_{Ref}) is then compared with the measured voltage at the WTG terminal, and the droop voltage, U_{Droop} . U_{Droop} is estimated by multiplying the line current (I) with K_{Droop} . The droop coefficient, K_{Droop} , regulates how deep the RSC controller can push the WTG towards its maximum reactive power limit. To calculate K_{Droop} , the following equation is used:

$$K_{Droop} = \frac{\Delta U_{max}}{\sqrt{3}(Q_{max} - Q_{min})(\Delta U + U_{WTG,Ref})} \quad (11)$$

where ΔU_{max} is the maximum allowable voltage deviation around the nominal in pu, which is 0.05 in this paper; $(Q_{max} - Q_{min})$ is the difference between the maximum and minimum reactive power capability in pu, retrieved from the maximum reactive power capability model; and ΔU is the depth of voltage deviations at the POI.

The parameter $1/K_{Droop}$ is the slope of the WTG's $V - I$ characteristics. In (11), $(Q_{max} - Q_{min})$ depends on the amount of active power being supplied by the WTG, and $(\Delta U + U_{WTG,Ref})$ depends on the depth of voltage deviations at the POI. For the same amount of active power supply, the deeper the voltage sag is, the higher is the $1/K_{Droop}$ and the more the RSC controller can push the WTG towards its maximum reactive power capacity. If the net reference current ($I_{RSC,Ref}$) reaches the RSC's maximum current limit ($I_{RSC,Max}$), the RSC controller curbs down I_{qr} that regulates the active power flow to contribute more to reactive power compensation by dispatching more reactive power. The schematic diagram of the proposed RSC controller is shown in Fig. 5.7.

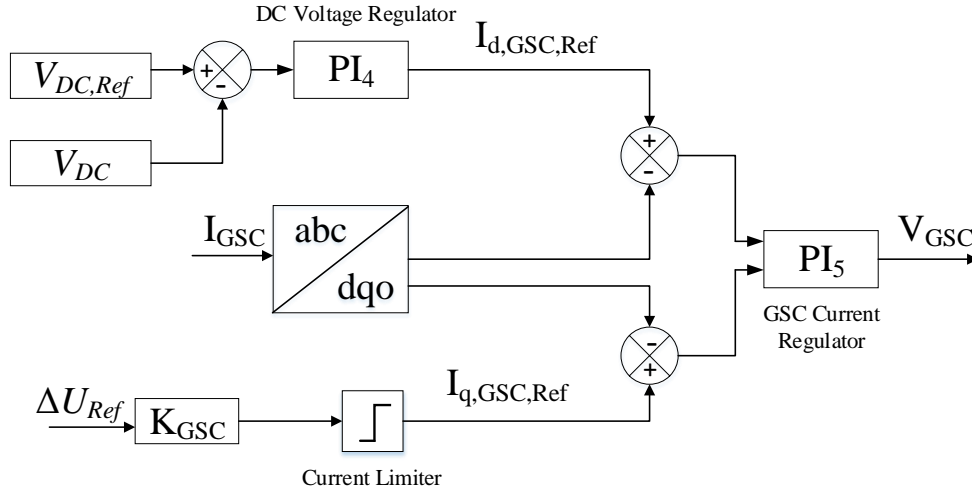


Fig. 5. 8. The schematic diagram of the proposed GSC controller.

5.5 Case Studies

In this section, the proposed controller is exposed to different operating conditions, and its performance is analyzed and compared with two existing controllers. For all case studies, the SCR of the grid is set to 5 and the active power supply is 0.3 pu. A short description of the two existing controllers is given below.

Method 1: In our previous research work published in [9], the WPP controller regulates the WPP's voltage according to the steady-state reactive power capability model developed from SCADA field measurement data of the real WPP operating in Newfoundland, Canada through curve fitting techniques. Both the central WPP controller and local WTG controllers are operating in reactive power control mode, and the central WPP controller is equipped with a power factor controller. Reactive power competency of both RSC and GSC are utilized. However, Method 1 is only effective under steady-state normal operating conditions.

Method 2: In [14], an adaptive $Q - V$ slope ($1/K_{Droop}$)-based voltage management approach is used. Both the central WPP controller and local WTG controllers are operated in voltage control

mode, and no power factor controller is integrated with the central WPP controller. In addition, the method in [14] exports no reactive power from the GSC.

5.5.1 Case 1 – Base Model without the Proposed Controllers

To evaluate the tuning accuracy of the WPP’s base model, Case 1 is conducted. To do so, SCADA measurement data from 8 am of January 16, 2016 to 6 am of January 17, 2016 for the WPP (currently operating in Newfoundland, Canada) are compared with the simulated values as shown in Fig. 5.9. The base model of the WPP does not have the proposed controllers, which matches the system configuration during SCADA field measurements in 2016. The system parameters are tuned until the simulated voltage and the SCADA measurement voltage at the POI matches. Fig. 5.9 (c) shows that the simulated voltage and SCADA measured voltage at the POI closely match each other. Therefore, the WPP’s base model is considered to be accurately representing the real WPP.

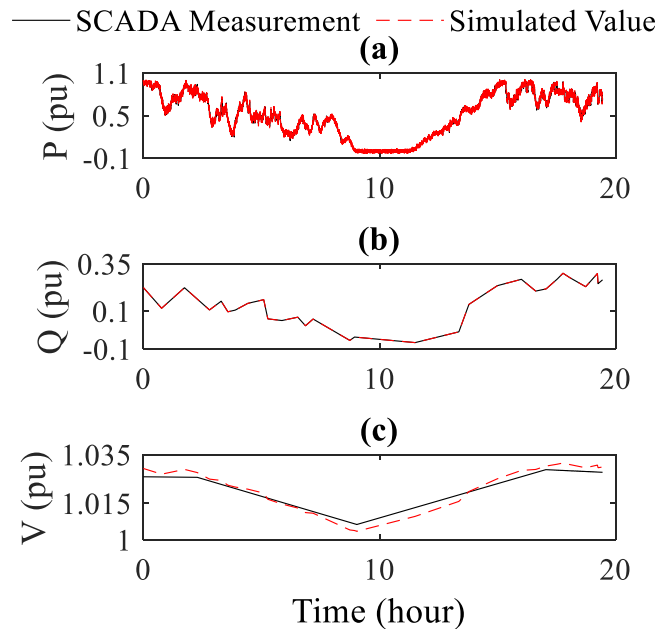


Fig. 5. 9. Simulation results vs. SCADA field measurements for the WPP’s base model without the proposed controllers for the 27 MW WPP in Newfoundland, Canada: (a) active power supplied by WTG, (b) reactive power supplied by WTG, and (c) the voltage at the POI (Case 1).

5.5.2 Case 2 - Normal Operating Voltage (the controller is to maintain power factor)

In Case 2, the simulation is conducted for the WPP model with the proposed controllers under normal operation. A 96% voltage sag at the POI starts at 32 s and lasts for 0.2 ms.

According to grid codes, voltage deviations up to ± 0.05 pu is counted as normal operating conditions. Therefore, the proposed controller attempts to maintain the power factor at the POI instead of compensating the voltage deviation. At 32 s, the voltage sag starts at the POI; as soon as after reading the depth of voltage deviations, the central WPP controller turns the power factor controller on. The power factor controller immediately adjusts ΔU_{Ref} , which subsequently adjusts its reactive power generation (Fig. 5.10 (b)) and brings the power factor back to 0.95 (Fig. 5.10 (d)).

The performance of the proposed controller is compared with the two existing methods, Methods 1 and 2, as shown in Fig. 5.10 in this case study. Because the proposed controller is an improvement to our previous work in Method 1, they show similar characteristics during normal operation, and their response during normal operation overlaps with each other. However, due to the absence of power factor controller, Method 2 makes no adjustment to its reactive power dispatch (Fig. 5.10 (b)), as a result, it cannot maintain the required power factor at the POI as depicted in Fig. 5.10 (d).

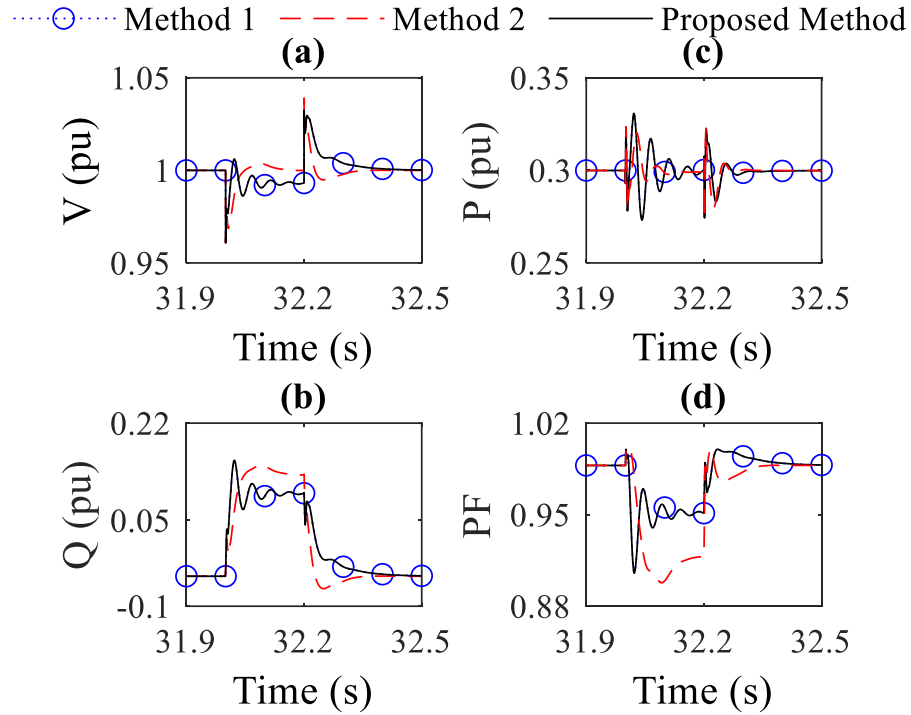


Fig. 5. 10. Simulation results: (a) the voltage at the POI, (b) reactive power supplied by WTG, (c) active power supplied by WTG, and (d) power factor at the POI (Case 2).

5.5.3 Case 3 - Connection and Disconnection of a Large Inductive Load

In Case 3, the simulation is conducted for the WPP model with the proposed controllers at an under-voltage operation due to the sudden connection and disconnection of a larger inductive load. A 10 MVA inductive load is connected with the system at 32 s and disconnected at 32.2 s.

The connection of the load drops the voltage to 94%, which is out of the normal operation voltage range, and the controller responses immediately to compensate the voltage deviation by swiftly dispatching the required reactive power. K_{Droop} is 0.014 in this case. From Fig. 5.11 (b), it can be seen that, due to the adaptive droop gain, the proposed controller can ensure more reactive power support than the two existing methods, and thus, can compensate the voltage deviation completely. In addition, as shown in Fig. 5.11 (d), the GSC supports the recovery by supplying additional reactive power.

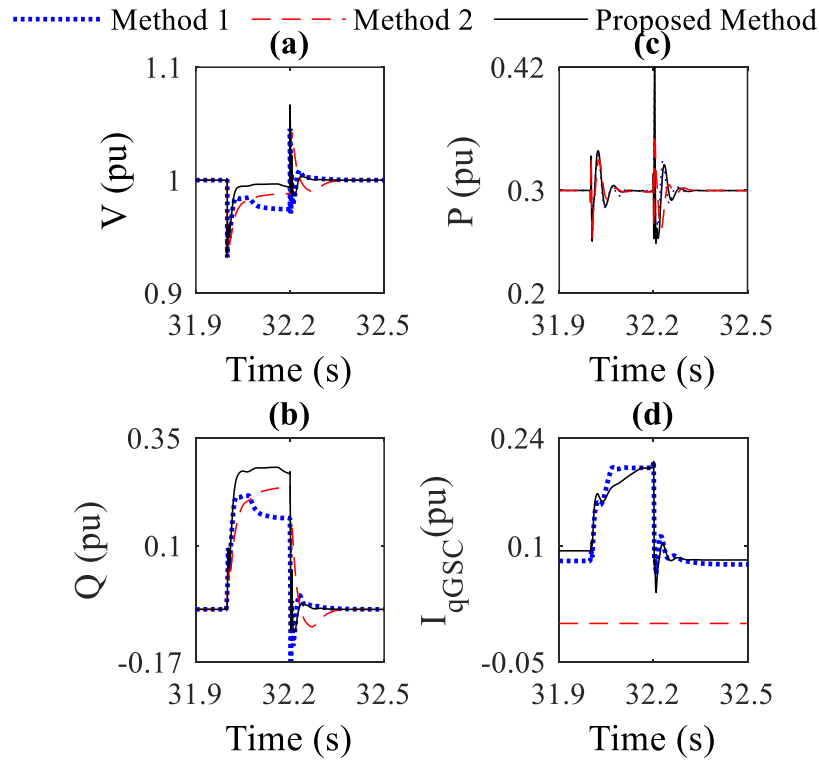


Fig. 5. 11. Simulation results: (a) the voltage at the POI, (b) reactive power supplied by WTG, (c) active power supplied by WTG, and (d) I_{qGSC} (Case 3).

5.5.4 Case 4 - A Small Voltage Sag

In Case 4, the simulation is conducted for the WPP model with the proposed controllers at an under-voltage operation due to a three-phase-to-ground fault that is far away from the POI. A 92% voltage sag at the POI starts at 32 s and lasts for 0.2 ms.

As the fault drives the voltage away from the normal operating range, the proposed controller responds immediately by supplying adequate reactive power (Fig. 5.12 (b) and (d)) to compensate it. K_{Droop} is 0.013 in this case. Reactive power dispatched by the proposed controller is higher than the two existing two methods (Fig. 5.12 (b)). As the RSC's total current reference does not exceed its maximum rating, the active power supply remains unchanged (Fig. 5.12 (c)). The GSC

provides additional 0.11 pu of reactive current, as a result, the voltage is completely compensated by the proposed controller, whereas the controllers in existing methods lag behind (Fig. 5.12 (a)).

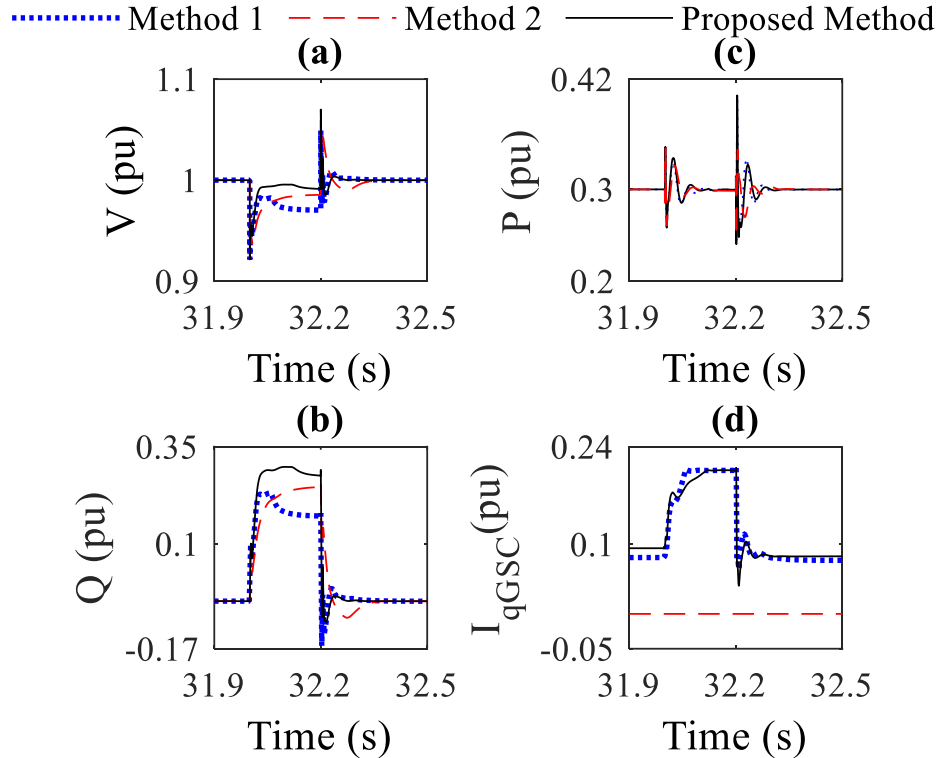


Fig. 5. 12. Simulation results: (a) the voltage at the POI, (b) reactive power supplied by WTG, (c) active power supplied by WTG, and (d) I_{qGSC} (Case 4).

5.5.5 Case 5 - A Deep Voltage Sag

In Case 5, a severe 60% voltage sag is applied at the POI at 32 s and continues for 0.2 s for the WPP model with the proposed controller. Immediately after the initiation of the voltage sag, the central WPP controller sends references to local WTG controllers. K_{Droop} is 0.01 in this case. The net current reference for the RSC exceeds its maximum rating, therefore, the active current ($I_{qr,Ref}$) is reduced, which can be seen in the active power supply in Fig. 5.13 (c). With the

additional capacity attained by the reduction of active power supply, the RSC pushes the WTG to its full capacity (Fig. 5.13 (b)). Although Method 2 adopts adaptive droop coefficients, as it does not vary its droop coefficient with the depth of voltage deviations, it cannot utilize the WTG's maximum capacity during a large voltage sag (Fig. 5.13(b)). In addition, no reactive power is exported from the GSC in Method 2 (Fig. 5.13 (d)). Although Method 1 exports reactive power through the GSC (Fig. 5.13 (d)), due to its reliance on the steady-state reactive power capability model, the controller cannot export enough during contingency (Fig. 5.13 (b)). The proposed controller properly utilizes both the RSC and GSC; so, its voltage compensation performance is significantly better than the two existing methods as shown in Fig. 5.13 (a).

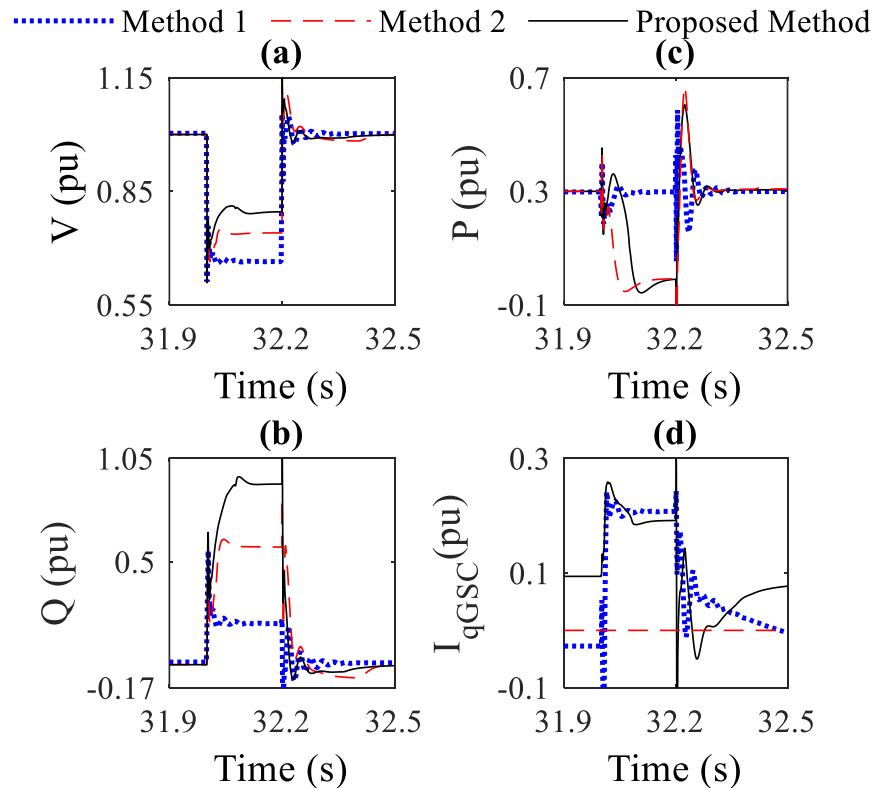


Fig. 5. 13. Simulation results: (a) the voltage at the POI, (b) reactive power supplied by WTG, (c) active power supplied by WTG, and (d) I_{qGSC} (Case 5).

5.6 Sensitivity Study

5.6.1 Communication Failure

Being spanned over a wider area, WPPs depend heavily on communication networks, and a failure in communication networks can lead to complete failure to the whole WPP. Therefore, unlike our previous research work in [9], a contingency mechanism against the complete WPP failure during a communication failure is added in the proposed controller. In this approach, instead of directly supervising the local WTG controllers, the central WPP controller droops local WTG controllers' voltage up to 5% around their nominal value. As a result, during a communication failure, depending on the availability of reactive power, local WTG controllers can still ensure a nominal voltage at the WTG terminal independently. Due to the communication failure, local WTG controllers receive no ΔU_{Ref} , and it cannot droop WTG's voltage around its nominal. As a result, reactive power support from both RSC and GSC is reduced (Fig. 5.14 (b) and (d)), however, the support is enough to keep the POI voltage within the normal operating range (Fig. 5.14 (a)) by keeping the WTG voltage at the nominal. This way, the proposed controller resists the collapse of the whole WPP during a communication failure and keeps the voltage within the acceptable range.

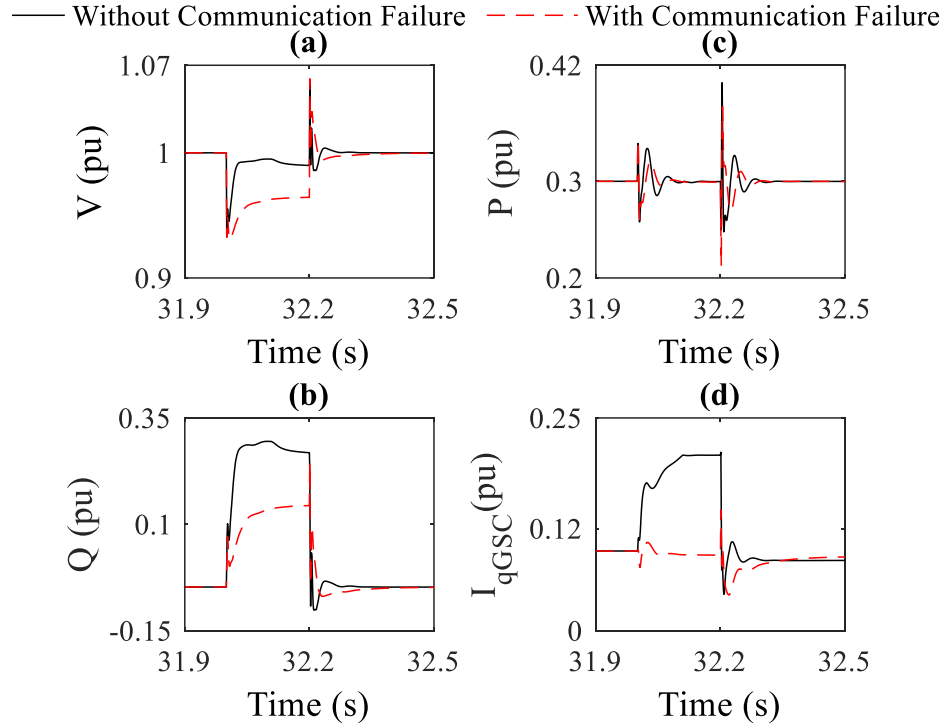


Fig. 5. 14. Simulation results: (a) the voltage at the POI, (b) reactive power supplied by WTG, (c) active power supplied by WTG, and (d) I_{qGSC} .

5.6.2 SCR of the Grid

The SCR represents the strength of a power grid. The voltage compensation performance of a WPP controller varies with the WPP's nameplate capacity and the grid's strength. To study the performance of the proposed controller for different SCR values, the small voltage sag applied in Case 4 is used here. From Fig. 5.15 (b) and (d), it can be inferred that the proposed controller automatically adapts itself with the change of SCR. With a stronger grid (corresponding to a higher SCR), although the controller dispatches more reactive power, the voltage compensation becomes harder due to excessive reactive power requirements (Fig. 5.15 (a)). With a larger WPP, better voltage compensation can be achieved.

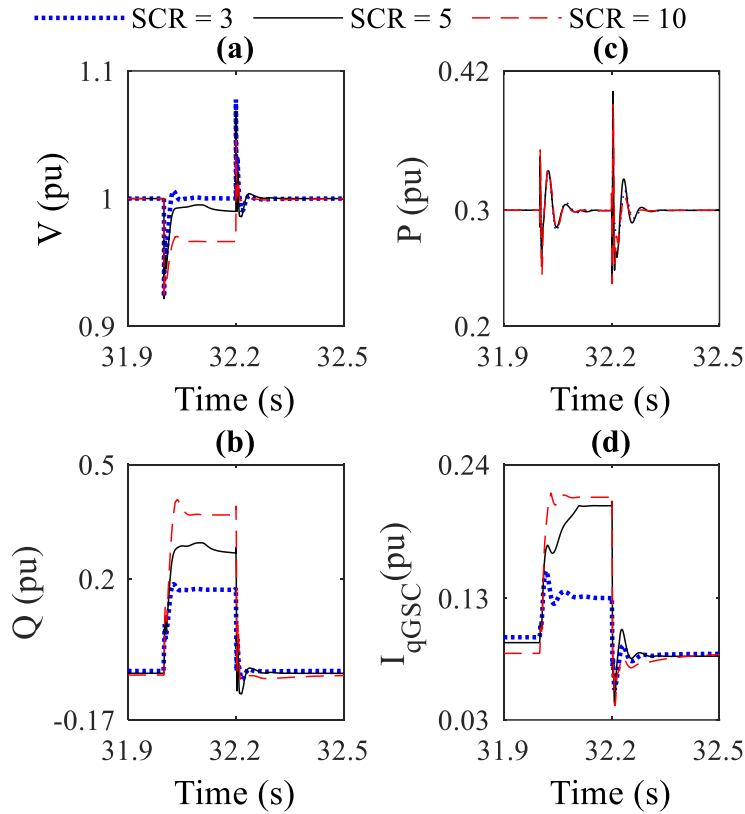


Fig. 5. 15. Simulation results: (a) the voltage at the POI, (b) reactive power supplied by WTG, (c) active power supplied by WTG, and (d) I_{qGSC} .

5.6.3 Washout Filter in the Central WPP Controller

To demonstrate the effectiveness of the integrated washout filter in the central WPP controller, a deep voltage sag applied in Case 5 is used here. From Fig. 5.16, it can be inferred that the washout filter improves the performance of the proposed controller significantly.

Without the washout filter, the voltage and reactive power exhibit a voltage over-surge for a considerable amount of time (Fig. 5.16 (a) and (b)), which is caused by the integrator in the central WPP controller taking more than a second after the clearance of the fault to drive the accumulated values completely away from it.

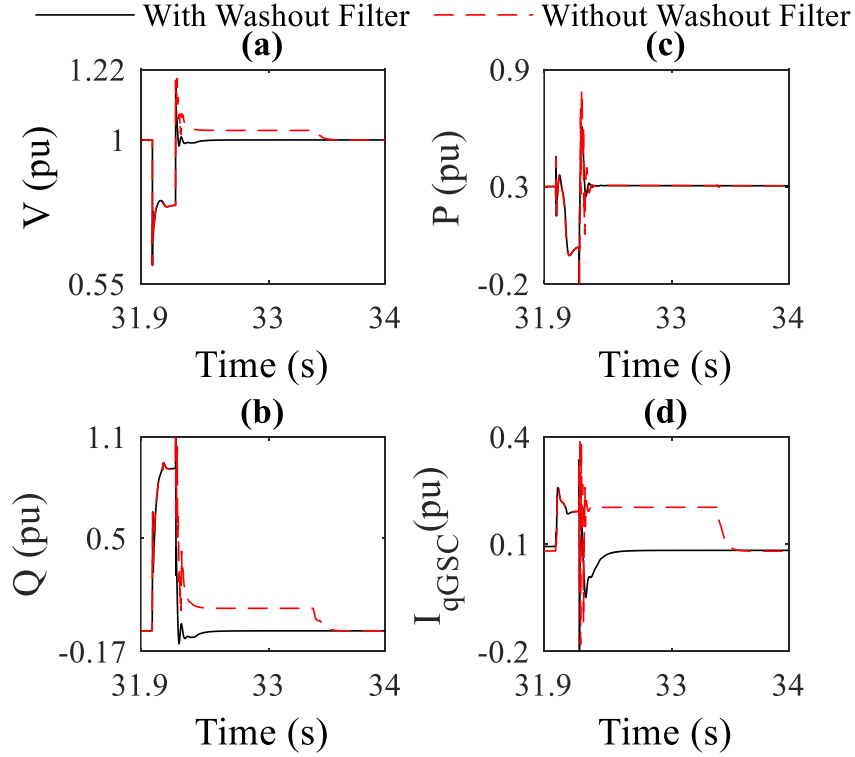


Fig. 5. 16. Simulation results: (a) the voltage at the POI, (b) reactive power supplied by WTG, (c) active power supplied by WTG, and (d) I_{qGSC} .

5.7 Conclusion

In this paper, a novel hierarchical wind power plant controller is developed, consisting of the central WPP controller and the local wind turbine generator controller, both operating in voltage control mode. The proposed controller ensures excellent performance under both normal and abnormal operating conditions. Under normal operation, the control is associated with the data-driven method previously developed using WPP's SCADA field measurement data through curve fitting techniques. Under abnormal operation, the maximum reactive power capability model of the WPP is integrated in the controller design. The combination of the data-driven method using SCADA data under steady-state normal operation, and the maximum reactive power capability model of WPP under dynamic abnormal operation enables the proposed controller design to offer excellent performance consistently through a much wider operation range of a WPP.

In the proposed controller, the central WPP controller monitors the voltage at the point of interconnection and droops the local WTG controller up to 5% around its nominal voltage. A power factor controller integrated with the central WPP controller keeps the power factor within the acceptable limit during normal operation. An adaptive droop coefficient-based RSC controller is developed that ensures enhanced reactive power support during contingency. To improve the effectiveness of the proposed controller, a comprehensive $P - Q$ model of a DFIG-based WPP is adopted to estimate the droop coefficient. Reactive power competency of the GSC is also utilized to further enhance the reactive power support.

The proposed method is compared with two existing methods in [9], [14] and demonstrates much improved performance. It is also robust during communication failures.

References

- [1] J. Ouyang, T. Tang, J. Yao, and M. Li, "Active Voltage Control for DFIG-Based Wind Farm Integrated Power System by Coordinating Active and Reactive Powers Under Wind Speed Variations," *IEEE Trans. Energy Convers.*, vol. 34, no. 3, pp. 1504–1511, 2019.
- [2] "Almost All New US Power Plants Built in 2021 Will Be Carbon-Free." <https://www.greentechmedia.com/articles/read/almost-all-new-us-power-plants-in-2021-will-be-carbon-free> (accessed May 31, 2021).
- [3] H. Karbouj and Z. H. Rather, "Voltage Control Ancillary Service From Wind Power Plant," *IEEE Trans. Sustain. Energy*, vol. 10, no. 2, pp. 759–767, 2019.
- [4] M. Tsili and S. Papathanassiou, "A review of grid code technical requirements for wind farms," *IET Renew. Power Gener.*, vol. 3, no. 3, pp. 308–332, Sep. 2009.
- [5] A. Camacho, M. Castilla, J. Miret, R. Guzman, and A. Borrell, "Reactive Power Control for Distributed Generation Power Plants to Comply With Voltage Limits During Grid Faults," *IEEE Trans. Power Electron.*, vol. 29, no. 11, pp. 6224–6234, 2014.
- [6] C. Liu, D. Xu, N. Zhu, F. Blaabjerg, and M. Chen, "DC-Voltage Fluctuation Elimination Through a DC-Capacitor Current Control for DFIG Converters Under Unbalanced Grid Voltage Conditions," *IEEE Trans. Power Electron.*, vol. 28, no. 7, pp. 3206–3218, 2013.
- [7] Z. Dong, Z. Li, Y. Xu, X. Guo, and Z. Ding, "Surrogate-Assisted Cooperation Control of Network-Connected DFIG Wind Farm with Maximized Reactive Power Capacity," *IEEE Trans. Ind. Inform.*, pp. 1–1, 2021.
- [8] S. Das and B. Subudhi, "A Robust Active and Reactive Power Control Scheme for a PMSG-Based Wind Energy Conversion System," *IEEE Trans. Energy Convers.*, vol. 33, no. 3, pp. 980–990, 2018.

- [9] M. N. S. K. Shabbir, X. Liang, W. Li, N. Khan, and A. M. Le, "A Novel Data Driven Voltage Control Approach for Grid Connected Wind Power Plants," *IEEE Trans. Ind. Appl.*, vol. 55, no. 4, pp. 3376–3393, 2019.
- [10] J. Ouyang, M. Li, Y. Diao, T. Tang, and Q. Xie, "Active control method of large-scale wind integrated power system with enhanced reactive power support for wind speed fluctuation," *IET Gener. Transm. Amp Distrib.*, vol. 12, no. 21, pp. 5664–5671, Nov. 2018.
- [11] A. Tapia, G. Tapia, and J. X. Ostolaza, "Reactive power control of wind farms for voltage control applications," *Renew. Energy*, vol. 29, no. 3, pp. 377–392, Mar. 2004.
- [12] A. D. Hansen, P. Sørensen, F. Iov, and F. Blaabjerg, "Centralised power control of wind farm with doubly fed induction generators," *Renew. Energy*, vol. 31, no. 7, pp. 935–951, Jun. 2006.
- [13] J. Kim, E. Muljadi, J.-W. Park, and Y. C. Kang, "Adaptive Hierarchical Voltage Control of a DFIG-Based Wind Power Plant for a Grid Fault," *IEEE Trans. Smart Grid*, vol. 7, no. 6, pp. 2980–2990, 2016.
- [14] J. Kim, J.-K. Seok, E. Muljadi, and Y. C. Kang, "Adaptive Q–V Scheme for the Voltage Control of a DFIG-Based Wind Power Plant," *IEEE Trans. Power Electron.*, vol. 31, no. 5, pp. 3586–3599, 2016.
- [15] J. Kim, E. Muljadi, J.-W. Park, and Y. C. Kang, "Flexible IQ–V Scheme of a DFIG for Rapid Voltage Regulation of a Wind Power Plant," *IEEE Trans. Ind. Electron.*, vol. 64, no. 11, pp. 8832–8842, 2017.
- [16] J. Martínez, P. C. Kjær, P. Rodriguez, and R. Teodorescu, "Design and Analysis of a Slope Voltage Control for a DFIG Wind Power Plant," *IEEE Trans. Energy Convers.*, vol. 27, no. 1, pp. 11–20, 2012.

- [17] M. E. Moursi, G. Joos, and C. Abbey, "A Secondary Voltage Control Strategy for Transmission Level Interconnection of Wind Generation," *IEEE Trans. Power Electron.*, vol. 23, no. 3, pp. 1178–1190, 2008.
- [18] S. Ghosh, Y. J. Isbeih, R. Bhattarai, M. S. E. Moursi, E. F. El-Saadany, and S. Kamalasan, "A Dynamic Coordination Control Architecture for Reactive Power Capability Enhancement of the DFIG-Based Wind Power Generation," *IEEE Trans. Power Syst.*, vol. 35, no. 4, pp. 3051–3064, 2020.
- [19] J. Martínez, P. C. Kjær, P. Rodriguez, and R. Teodorescu, "Design and Analysis of a Slope Voltage Control for a DFIG Wind Power Plant," *IEEE Trans. Energy Convers.*, vol. 27, no. 1, pp. 11–20, 2012.
- [20] M. N. Sakib, K. Shabbir, X. Liang, W. Li, and N. Khan, "Analytical Approach-Based Reactive Power Capability Curve for DFIG Wind Power Plants," in *2020 IEEE Industry Applications Society Annual Meeting*, 2020, pp. 1–9.

Chapter 6

A Distributed Generation Control Algorithm for Islanded Microgrids: Development and Parameterization

Md Nasmus Sakib Khan Shabbir¹, *Student Member, IEEE*, Xiaodong Liang², *Senior Member, IEEE*, Weixing Li³, *Senior Member, IEEE*, and Syed Imtiaz⁴

¹Department of Electrical and Computer Engineering, Memorial University of Newfoundland, St. John's, Newfoundland, Canada.

²Department of Electrical and Computer Engineering, University of Saskatchewan, Saskatoon, Saskatchewan, Canada.

³Department of Electrical Engineering, Harbin Institute of Technology, Harbin, Hilongjiang, China.

⁴Department of Process Engineering, Memorial University of Newfoundland, St. John's, Newfoundland, Canada.

A version of this chapter is to be submitted to a journal. Md Nasmus Sakib Khan Shabbir co-authored the paper under the supervision of Dr. Xiaodong Liang. Sakib's contributions in this paper are listed as follows:

- Performed literature review for droop control algorithms for islanded microgrid control and data driven system identification approaches for distributed generation system.
- Developed the novel control structure for distributed generation control.
- Examined results and reported findings.
- Involved in writing the paper draft as the first author.

Dr. Xiaodong Liang provided continuous technical guidance, checked the results, reviewed the manuscript, provided suggestions to accomplish the work, and modified the final version of the manuscript. Dr. Weixing Li modified the manuscript. Dr. Syed Imtiaz reviewed the manuscript, and provided suggestions.

In this chapter, the manuscript is presented with altered figure numbers, table numbers and reference formats in order to maintain the thesis formatting guidelines set out by the Memorial University of Newfoundland.

Abstract- To regulate the voltage and frequency of an islanded microgrid, a novel control algorithm for Distributed Generation (DG) units is developed in this paper, where deviations of the voltage and frequency from their nominal values at the Point of Common Coupling (PCC) are correlated with direct- and quadrature-axis components of the control signal. It incorporates distribution line parameters into the control algorithm and enables simultaneous P-f/Q-V and P-V/Q-f control. The proposed control algorithm eliminates the secondary controller and the virtual impedance loop from the DG controller, and substantially reduces the controller size and complexity. The polynomial input-output Box-Jenkins model is chosen as the model structure for the control algorithm, which is parameterized through data-driven system identification approach using Nonlinear Least Square (NLS) method. To initialize the parametric optimization, the Backcast technique is chosen after evaluating three initialization techniques (Zero, Estimate and Backcast). Four NLS optimization methods (Gauss-Newton (GN), Adaptive Gauss-Newton (AGN), Levenberg-Marquardt (LM), and Trust Region Reflective (TRR)) are considered and their performance in developing the model are evaluated for both training and validation datasets. GN shows consistent and superior performance over the others and is chosen as the suitable optimization technique in this study.

Keywords- Adaptive Gauss-Newton, Box-Jenkins model, distributed generation, Gauss-Newton, Levenberg-Marquardt, nonlinear least square, Trust Region Reflective.

6.1 Introduction

Due to power losses associated with conventional high voltage transmission networks, the concept of localized distributed generation (DG) in low voltage distribution networks, particularly renewable energy-based DGs, has attracted significant research interest. However, a single DG unit is less reliable [1], and microgrid is an effective building block to integrate DGs in smart distribution systems. The self-adequate microgrid can host a number of DGs and operate in grid-connected or island mode [2]. In island mode, the voltage and frequency of the microgrid is controlled solely by DG controllers [3].

In a microgrid, droop control is most commonly used to dispatch active and reactive power from DGs. Droop control imitates steady-state characteristics of a synchronous generator, and is usually applied in proportional-integral (PI)-based controllers. Although the control of the voltage and frequency (V and f), and active and reactive power (P and Q) in a low voltage microgrid are coupled [4], PI controllers' incompetency to handle such coupled relationship forces droop control to treat active and reactive power as uncoupled, and either P - f / Q - V [5] or P - V / Q - f control [6] is adopted. When connected DGs have mismatched line impedances, droop control shows deteriorate performance. As a result, primitive droop controllers exhibit steady-state errors in voltage and frequency, and have disproportional reactive power sharing issue among DGs.

To overcome these limitations, the secondary controller and the virtual impedance loop are integrated with droop controllers [7]. Although such added layers improve the droop controller's performance, controllers' size and complexity are also increased substantially. During operation,

to cope with the microgrid topological changes and parametric variations, controllers need continuous retuning, and these added layers make the retuning process difficult and time consuming [8].

The performance of a DG controller depends on accurate estimation of its control signals, a simple but effective estimation process is essential to avoid the complex process introduced by existing controller technologies. Therefore, in this paper, for the first time, a simple control model, directly correlating the deviation of voltage and frequency (outputs) with direct (d)- and quadrature (q)-axis components (U_d and U_q) of the DG control signal (inputs) is proposed. The proposed model considers both resistance and reactance of the distribution line into its control algorithm, and consequently enforces simultaneous P-f/Q-V and P-V/Q-f control, which enables the proper handling of coupled relationship. As a result, the model overcomes the necessity of the complex secondary controller and the virtual impedance loop. To avoid estimating distribution line parameters, the proposed control model is parameterized through a data-driven system identification approach.

The data-driven system identification is an emerging approach that has been used in modeling dynamic characteristics of active and reactive power of a DG or microgrid [9]-[11]. To parameterize a data-driven model, nonlinear least-square (NLS) is an effective and robust approach. NLS adopts optimization algorithms to obtain optimum coefficients of the system model. Algorithms used in NLS can be broadly categorized as line search-based and trust region-based approaches. The line search-based approach is to find a new iterative point along a decent direction at each iteration; while the trust region-based approach is to find a new iterative point within a trusted region centered at the current iterate. Among the line search-based algorithms, Gauss-Newton (GN) [12] and Adaptive Gauss-Newton (AGN), and among the trust region-based

algorithms, Levenberg-Marquardt (LM) [13] and Trust Region Reflective (TRR) [14], are widely accepted robust optimization algorithms. All these methods use truncated approximation of the Hessian matrix, and thus, significantly reduce the computational burden without deteriorating data fitting accuracies. With the appropriate initialization, GN and AGN show quadratic convergence near the minima [15]; LM shows the robust performance against the ill-conditioned Jacobian [16]; and TRR shows the superior performance in the case of negative definite Hessian[17]. Therefore, these methods have been adopted to solve NLS problems in a wide range of areas [17]–[19].

In this research, a polynomial Box-Jenkins model structure is adopted, and a quantitative comparison among the above NLS algorithms in developing the proposed data-driven model is conducted. Being a variant of GN methods, all four methods show excellent performance in developing the model, however, GN consistently maintains a better performance in all performance matrices used in the analysis.

The main contributions of this paper include: 1) develop a data-driven DG control model by directly correlating the deviation of voltage and frequency at the PCC with the d- and q-axis components of the DG control signal, this model eliminates the need of the secondary controller and the virtual impedance loop; and 2) select the best nonlinear least square optimization algorithm, and demonstrate the effectiveness of GN over AGN, LM and TRR to parameterize the model.

The paper is arranged as follows: the mathematical derivation of the proposed model, and steps to obtain the proposed model through the data-driven system identification approach are covered in Section 6.2; fundamental theories are explained in Section 6.3; the test system is given in Section 6.4; the key steps during the model development are explained in Sections 6.5; the final model is developed in Section 6.6; and conclusions are drawn in Section 6.7.

6.2 The Proposed Approach

The mathematical derivation of the proposed model, and the stepwise evolution of the final data-driven Box-Jenkins model development is described in this section.

6.2.1 Mathematical Formulation for the Proposed Approach

The generated active and reactive power at the point S in the microgrid in Fig. 6.1 can be written as follows:

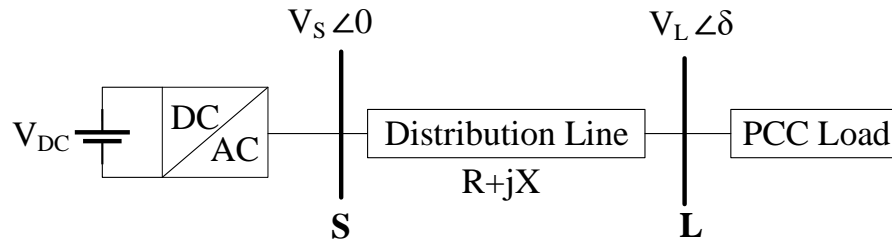


Fig. 6. 1. The microgrid with a DG interfacing inverter.

$$P = \frac{V_s}{R^2+X^2} [R(V_s - V_L \cos \delta) + XV_L \sin \delta] \quad (1)$$

$$Q = \frac{V_s}{R^2+X^2} [X(V_s - V_L \cos \delta) - RV_L \sin \delta] \quad (2)$$

Let's assume that the power angle, δ , is very small, and thus, (1) and (2) can be rewritten as follows:

$$\delta = \frac{1}{XV_L} \left[\frac{R^2+X^2}{V_s} P - R(V_s - V_L) \right] \quad (3)$$

$$V_s - V_L = \frac{1}{X} \left(\frac{R^2+X^2}{V_s} Q + RV_L \delta \right) \quad (4)$$

Eqs. (3) and (4) can be further solved considering δ and $V_s - V_L$ as two variables, then we have

$$\delta = \frac{1}{V_s V_L} (XP - RQ) \quad (5)$$

$$V_s - V_L = \frac{1}{V_s}(XQ + RP) \quad (6)$$

From (5) and (6), fundamental formulas of the conventional droop equations are derived as shown in (7). Eq. (7.1) is derived by assuming $X \gg R$ (a highly inductive feeder line) and ignoring R , which leads to the P-f/Q-V control. Eq. (7.2) is derived by assuming $R \gg X$ and (a highly resistive feeder line) ignoring X , which leads to the P-V/Q-f control.

$$\delta, (V_s - V_L) = \begin{cases} \frac{XP}{V_s V_L}, \frac{XQ}{V_s}, \text{ when } X \gg R & (7.1) \\ -\frac{RQ}{V_s V_L}, \frac{RP}{V_s}, \text{ when } R \gg X & (7.2) \end{cases}$$

Generally, the control of the power angle, δ , dynamically controls the system frequency. Therefore, the droop equation developed from (7.1) can be expressed by

$$f - f_0 = -k_p(P - P_0) \quad (8)$$

$$V_s - V_{s0} = -k_q(Q - Q_0) \quad (9)$$

In (8) and (9), the parameter X is no longer present in the control algorithm. As a result, the control structures developed from (8) and (9) cannot comprehend the impact of feeder line impedances, and cannot overcome the virtual impedance loop requirement [20].

Although feeder lines of a low voltage microgrid are predominantly highly resistive, some degree of inductance is always present. Therefore, droop equations in (5) and (6) with both feeder line impedance parameters considered can be expressed by

$$f - f_0 = -k_{p1}(P - P_0) + k_{p2}(Q - Q_0) \quad (10)$$

$$V_s - V_{s0} = -k_{q1}(Q - Q_0) - k_{q2}(P - P_0) \quad (11)$$

Eqs. (10) and (11) indicate that the DG control algorithm having both R and X in it. To control the voltage V in (11), both active power P and reactive power Q must be regulated simultaneously, which are P-V and Q-V control; similarly, to control the frequency f in (10), both active power P and reactive power Q must be regulated simultaneously as well, which are P-f and Q-f control. Therefore, Eqs. (10) and (11) ensure simultaneous P-f/Q-V and P-V/Q-f control, but conventional droop equations in (7) only focus on one type of control, either P-f/Q-V or P-V/Q-f, not both, which restricts the droop controller to comprehend the control signal, leading to steady-state errors in voltage and frequency. To overcome this issue, the secondary controller is employed. The active and reactive power can be written by

$$P = \frac{3}{2}(U_d I_d + U_q I_q) \quad (12)$$

$$Q = \frac{3}{2}(-U_d I_q + U_q I_d) \quad (13)$$

Where subscript d and q represent the d- and q-axis components of respective parameters. Eqs. (12) and (13) transform (5) and (6) into the following expressions:

$$\delta = \frac{3}{2} \frac{1}{V_s V_L} [(X I_d + R I_q) U_d + (X I_q - R I_d) U_q] \quad (14)$$

$$V_s - V_L = \frac{3}{2} \frac{1}{V_s} [(R I_d - X I_q) U_d + (R I_q + X I_d) U_q] \quad (15)$$

To simplify the problem, we assume that alterations of U_d and U_q will not have impact on I_d and I_q . Therefore, the control formulas developed from (14) and (15) can be expressed by

$$f - f_0 = \frac{3}{2} \frac{1}{V_s V_L} [(X I_d + R I_q)(U_d - U_{d0}) + (X I_q - R I_d)(U_q - U_{q0})] \quad (16)$$

$$V_L - V_{L0} = \frac{3}{2} \frac{1}{V_s} [(R I_d - X I_q)(U_d - U_{d0}) + (R I_q + X I_d)(U_q - U_{q0})] \quad (17)$$

Where f and V_L are the reference voltage and frequency, and f_0 and V_{L0} are the nominal voltage and frequency, respectively. U_d and U_q are the reference of the respective parameters at f and V_L , and U_{d0} and U_{q0} are the references of the respective parameters at f_0 and V_{L0} .

The major challenge to implement the formulas is that they require a proper quantification of the resistance and reactance of a distribution line. To solve the issue, a data-driven system identification approach is adopted. To do so, U_d and U_q are varied over a short-range, which is large enough to influence the system dynamics while small enough to ignore the nonlinearities, and subsequent impacts on the voltage and frequency at the PCC are recorded in the datasets. Using the recorded data, two system identification models for voltage and frequency are developed as follows:

$$\Delta f = k_1 \Delta U_d + k_2 \Delta U_q \quad (18)$$

$$\Delta V = k_3 \Delta U_d + k_4 \Delta U_q \quad (19)$$

Where coefficients k_1 to k_4 are derived through data-driven system identification approach.

This way, the proposed models no longer need the exact values of the feeder line parameters, their impact is reflected in the model through the datasets. Because the impact of feeder line impedances are included in the model in (18) and (19), the secondary controller and the virtual impedance loop are no longer needed in the controller design. From (18) and (19), and (10) and (11), it is found that a complete compensation of voltage and frequency by directly regulating U_d and U_q lead to indirect dispatching necessary active and reactive power.

As the model exhibits the coupled relationship among input-output parameters, therefore, the model requires a controller, which is able to handle the coupled relationship, to control a system.

6.2.2 Stepwise Development Procedure of the Proposed Approach

To develop a data-driven Box-Jenkins model for DG control in an islanded microgrid to regulate the voltage and frequency, the following 10 steps are required, which are also shown in the flowchart in Fig. 6.2:

Step 1: *Data acquisition for system identification.* To obtain the required datasets for developing the proposed data-driven model, d- and q-axis components of the DG control signal (U_d and U_q) in the simulation model are varied, and the corresponding deviations of the voltage and frequency from the nominal values in pu at the PCC (ΔV and Δf) are recorded. Details about the input-output data are provided in Section IV.

Step 2: *Calculation of input delay.* Input delay is an intrinsic property of a physical system that represents the time laps between the actuation of an input variable and reflection of its impact on output variables. Accurate measurement and inclusion of the input delay into a mathematical model developed out of a dataset is crucial if the model is intended to control the physical system. A MATLAB function named “delayest” is used to measure the input delay from the input-output data.

Step 3: *Selection of model order.* To best fit the model with the data, a Box-Jenkins model has the flexibility to independently choose a suitable order for each of the model coefficients including the noise model. Therefore, all possible combinations up to the 8th model order are examined, and the most suitable one is chosen based on data fitting accuracies.

Step 4: *Selection of initialization technique.* Initialization is crucial in developing a data driven model using NLS method. Therefore, three initialization techniques, Zero, Estimate and Backcast, are considered in this paper and the most suitable technique is chosen by evaluating their

performance matrices. Among the underlying methods, “zero” set the initial condition to zero regardless of the data trend; “estimate” treat the initial condition as an independent estimation parameter, and “backcast” estimate the initial condition by the “auto-regressive with external input” method.

Step 5: *Model fitting.* Using the measured input delay, chosen model order and initialization technique, models are developed using four optimization algorithms, GN, AGN, LM and TRR.

Step 6: *Performance analysis.* To study the performance of the optimization algorithms, the data fitting accuracies, Normalized Root Mean Square Error (NRMSE) and Mean Square Error (MSE), of their respective models are analyzed.

Step 7: *Model validation.* Models developed by the four optimization algorithms, GN, AGN, LM and TRR, are validated with a validation dataset. Validation shows the efficacy of the developed model to capture system characteristics for a different combination of input-output.

Step 8: *Selection of suitable optimization algorithm.* Based on the analysis conducted in Steps 6 and 7, the most suitable optimization algorithm is chosen. If no suitable model resulted, the analysis jumps to the next suitable initialization technique and Steps 5, 6 and 7 are repeated.

Step 9: *Residual analysis for the model.* To check data overfitting, a residual analysis on the final Box-Jenkins model is conducted. If overfitting detected, the analysis jumps to the next suitable optimization algorithm and Step 9 is repeated.

Step 10: *Development of the final Box-Jenkins model.* The final Box-Jenkins model is developed for a given system.

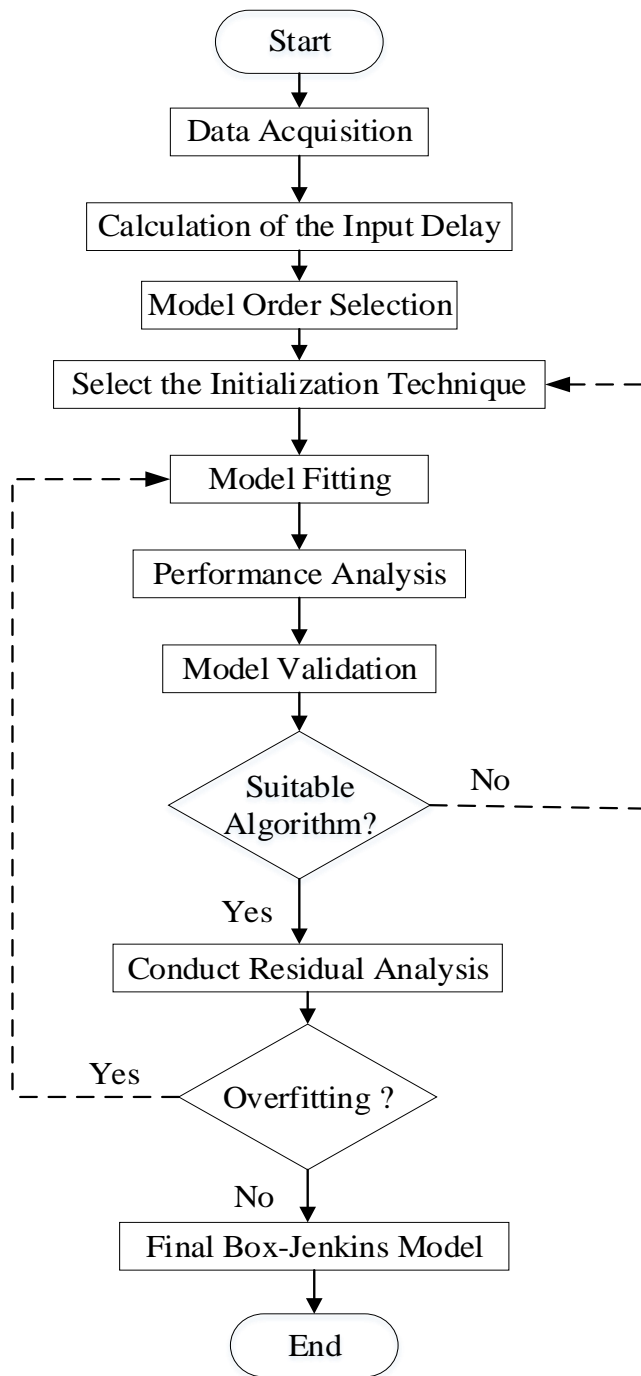


Fig. 6. 2. The flow chart of the proposed approach.

6.3 Fundamental Theory

6.3.1 Box-Jenkins Model

The polynomial input-output Box-Jenkins model structure has been widely adopted to formulate a data-driven system identification model because of its flexibility in parameterizing the system's dynamics and associated noises independently [21]. The general expression of the Box-Jenkins model with nu inputs and ny outputs can be written as follows:

$$\sum_{i=1}^{nu} \sum_{j=1}^{ny} A_{ij}(q) y_j(t) = \sum_{i=1}^{nu} \sum_{j=1}^{ny} \frac{B_{ij}(q)}{F_{ij}(q)} u_i(t - nk_{ij}) + \sum_{j=1}^{ny} \frac{C_j(q)}{D_j(q)} e_t(t) \quad (20)$$

Where A, B, C, D, and F are polynomial coefficients; q is the time shift operator; $u(t)$ and $y(t)$ are the input and the output of the model, respectively; nk_{ij} is the transport delay in between the i^{th} input and the j^{th} output; and $e_t(t)$ is the noise. C and D are noise coefficients; B and F are the system model coefficients. The dimension of A, B, F, and K matrices depends on the number of inputs and outputs; and the dimension of C and D depends on the number of outputs only. A, B, C, D, and F are obtained by the nonlinear least-square approach.

6.3.2 Mathematical Formulation of Non-linear Least Square

During the parametric optimization, the polynomial mathematical model, $y = f(\theta, t)$, with n unknown model coefficients $\theta = [\theta_1, \theta_2, \dots, \theta_n]^T$, is used to fit a set of m observed data points $(t_1, y_1), (t_2, y_2), \dots, (t_m, y_m)$, where $m > n$. The optimum model coefficients (θ) are obtained by optimizing an objective function, $V(\theta)$. In NLS, $V(\theta)$ is formulated as the sum of the squared residual functions, $r_i(t, \theta)$ of the m observed data. The minimum point of θ , θ^* , is calculated by.

$$\theta^* = \arg \min_{\theta} V(\theta) \quad (21)$$

6.3.3 Optimization Algorithms

The pattern of optimizing an objective function draws the distinction between the line search-based and trust region-based approaches. Line search-based approaches first select the search direction (p_k) of the optimization, and then decide the step size (α_k), which determines how far θ will move towards the selected direction in every iteration. On the contrary, trust region-based approaches work exactly opposite, it first decides the trusted region, which is the step size (α_k), and then select the search direction (p_k). A brief description about the chosen line and trust region-based methods are given below.

6.3.3.1 Line Search-Based Approaches

Two line search based approaches, known as “Gauss-Newton” (GN) and “Adaptive Gauss-Newton” (AGN), are chosen in this analysis.

6.3.3.1.1 The Gauss-Newton Approach

GN is a quasi-newton approach. For a search direction of p_k^{GN} and the step size of α_k^{GN} , the iterative equation of GN can be expressed as follows[12]:

$$\theta_{k+1} = \theta_k + \alpha_k p_k^{GN} \quad (22)$$

GN approximates the objective function’s Hessian matrix to its truncated form of $J(\theta_k)^T J(\theta_k)$, and the search direction p_k^{GN} is given by

$$p_k^{GN} = -[J(\theta_k)^T J(\theta_k)]^{-1} J(\theta_k)^T r(\theta_k) \quad (23)$$

Where $J \in \mathbb{R}^{m \times n}$ is the Jacobian of $r(\theta)$.

While computing p_k^{GN} , any singular value of the Jacobian matrix smaller than $J_{threshold} * \max(\text{size}(J)) * \text{norm}(J) * \text{eps}$ are disregarded and the search direction is computed for the

remaining subspace. If the sufficient improvement cannot be attained through this direction, GN follows the gradient direction.

6.3.3.1.2 The Adaptive Gauss-Newton Approach

AGN is an adaptive subspace of Gauss-Newton method. AGN follows (22) and (23), but any eigenvalues less than $\gamma * \max(sv)$ of the Hessian are ignored, where sv contains the singular values of the Hessian. Whenever the search fails to find a lower value of the criterion in fewer than five bisections, the parameter γ is increased by x_step . On the contrary, the parameter is decreased by twice the size of x_step if the search is successful without any bisection. x_step is the size of the Levenberg-Marquardt step.

6.3.3.2 Trust Region-Based Approaches

The Levenberg-Marquardt (LM) and trust region reflective (TRR) have been selected as the trust region-based approaches.

6.3.3.2.1 The Levenberg-Marquardt Method

LM is a hybrid technique that uses both Gradient Descent (GD) and Gauss-Newton method [22]. The LM equation for the search direction can be expressed by

$$p_k^{LM} = [J(\theta_k)^T J(\theta_k) + \mu_k I]^{-1} g(\theta_k) \quad (24)$$

Where $\mu_k > 0$ and termed as Lagrange parameter and I is a unity vector.

Smaller values of μ_k guide LM to follow GN method, whereas a larger μ_k results in the gradient descent method. LM first uses GD to traverse to a potential solution area, and then adopt GN to quickly find the minimum. At the beginning, μ_k is initialized with larger values to counter the initialization problem, and LM follows the steepest-descent direction. μ_k decreases with $V(\theta +$

$s) < V(\theta)$, and finally with sufficiently small μ_k , LM jumps into the GN direction and accelerates to the minimum.

6.3.3.2.2 The Trust Region Reflective Method

The TRR optimizes the objective function $V(\theta)$ by approximating it with a quadratic function $q(s)$ that reasonably reflects the characteristics exhibited by $V(\theta)$ in a neighborhood N around the point θ [14]. This neighborhood is addressed as the trust region, and the process to approximate $q(s)$ is the trust region sub-problem. In TRR, a trial step s is computed by solving the sub-problem over the trusted region N , and the current point is updated from θ to $\theta + s$ if and only if $V(\theta + s) < V(\theta)$. Otherwise, the current point remains unchanged, but the trusted region N is shrunken, and the trial step computation is repeated. Mathematically, the trust region sub-problem can be expressed as follows:

$$\min_s \left\{ \frac{1}{2} s^T H s + s^T g \text{ such that } \|Ds\| \leq \Delta \right\} \quad (25)$$

Where g is the gradient of V ; H and D are the Hessian and diagonal scaling matrices, respectively; Δ is the radius of the trusted region > 0 ; and $\| \cdot \|$ is the 2-norm.

The TRR restricts the subproblem into a two-dimensional subspace. The gradient (g) sets the direction of one of the dimensions, whereas the other follows the Gauss-Newton direction of the function $\min \|Js + v\|$, where J is the Jacobian of v , and v is a vector valued function of V . The subspace is then used to solve (25) to determine the trial step s , which is then used to obtain optimized coefficients.

6.3.4 The Objective Function

The objective used to parameterize the model coefficients using the nonlinear least square approach can be expressed by

$$V(\theta) = \frac{1}{N} \sum_{t=1}^N r^T(t, \theta) W(\theta) r(t, \theta) \quad (26)$$

Where N is the number of data samples, and $W(\theta)$ is a weighted semi-definite matrix of the vector parameter θ , and $r(t, \theta)$ is the residual function.

The general expression to compute the residuals can be expressed by

$$r(t, \theta) = y_m(t) - y_s(t, \theta) \quad (27)$$

Where $y_m(t)$ is the measured output, $y_s(t, \theta)$ is the simulated response of the model.

The current measured inputs and initial states are used to estimate the simulated response. The general expression to estimate the simulated response can be written as follows:

$$y_s(t, \theta) = f(u_m(t), u_m(0); y_m(0)) \quad (28)$$

Where $u_m(t)$ is the current measured input; and $u_m(0)$ and $y_m(0)$ are the initial states.

6.3.4 Model Quality Matrices

The model quality matrices used in this paper include Normalized Root-Mean-Square Error (NRMSE), Mean Square Error (MSE), and the model data fitting accuracy. The NRMSE represents the normalized square root of the second sample moment of the difference between the model's predicted and observed values. The MSE is a non-negative quality matrix of an estimated model and the second moment of the error. The MSE incorporates both the variance and the bias

of an estimated model. A better model comes with lower NRMSE and MSE values, and higher data fitting accuracies.

6.4 The Test System

The schematic diagram of the islanded microgrid, used to generate input-output data is depicted in Fig. 6.3. The DG in the microgrid is a PV system rated at 10 kVA, modeled as a constant DC voltage source. System parameters used in the simulation are tabulated in Table 6.1.

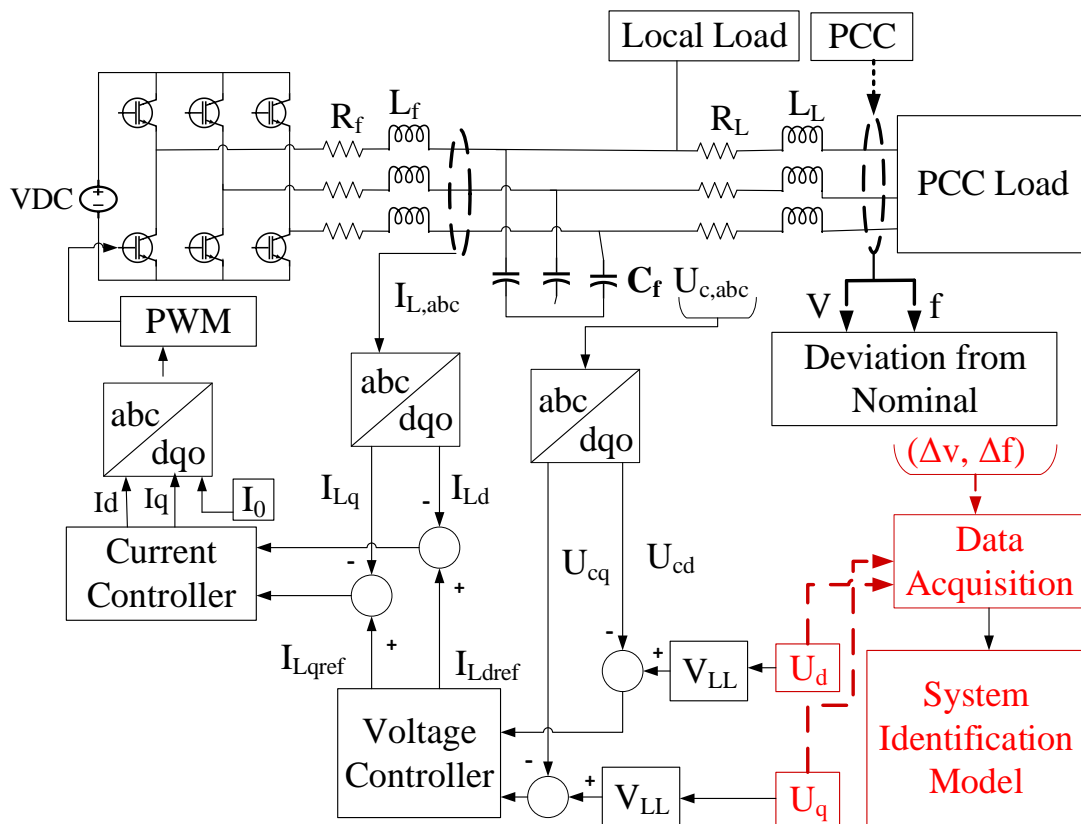


Fig. 6. 3. The test system simulation model.

Table 6. 1: Test System's Parameters

Parameters		Values
Nominal DC bus voltage (V)		700
Nominal AC bus RMS line voltage (V)		380
AC system frequency (f)		50
DG's Nameplate capacity (kVA)		10
Local Load		5 kW, 1 kVar
PCC Load		2 kW, 0.4 kVar
Inverter filter	Resistance, $R_f(\Omega)$	0.2
	Inductance, $L_f(\text{H})$	3×10^{-3}
	Capacitance, $C_f(\text{F})$	15×10^{-6}
Line impedance	Line resistance, $R_L(\Omega)$	0.641
	Line reactance, $X_L(\Omega)$	0.08

Before starting the experiment, the simulation model is initialized to the nominal steady-state conditions. Based on the initialization, the d-axis component (U_d) of the DG's control signal is set to 0.821, and the q-axis component (U_q) is set to 0.07. Next, to generate the training dataset for system identification, a step variation of ± 0.05 and ± 0.005 around the nominal values of U_d and U_q , are applied, respectively. The ranges are carefully chosen so that the system dynamics are influenced without initiating the nonlinearity. Variations of U_d and U_q and the corresponding deviations of the voltage and frequency from nominal values in pu at the PCC (ΔV and ΔF) are tabulated. The step duration is 0.5 s, and the data acquisition frequency is 10 kHz. Similarly, step magnitudes for U_d and U_q to generate the validation dataset are set to ± 0.04 and ± 0.004 , respectively. The duration of the step input and data acquisition frequency remain the same as they

are for the training dataset. The input-output data collection points are drawn in red as shown in Fig. 6.3.

The islanded microgrid is assumed as a balanced system. The triangular carrier signal in pulse-width modulation (PWM) in the DG's interfacing converter has a switching frequency of 10 kHz and a peak value of 1.03. The input-out data used in the analysis are depicted in Fig. 6.4.

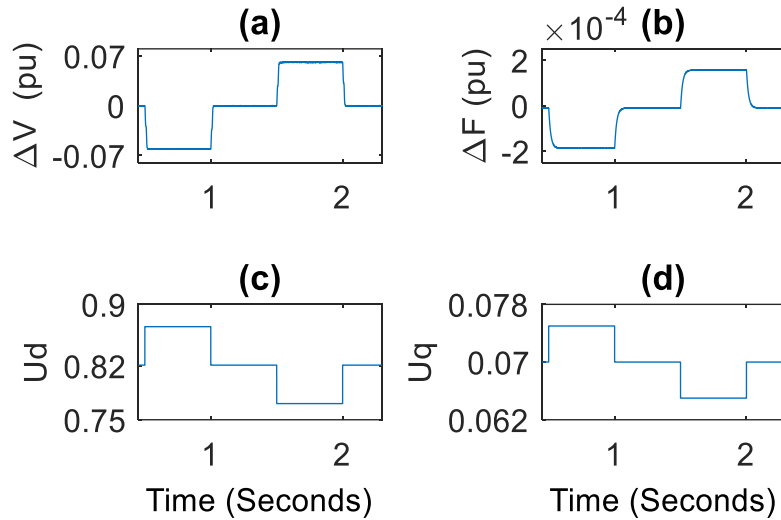


Fig. 6. 4. Input-output data: (a) the deviation of the voltage from the nominal value in pu, ΔV , (b) the deviation of the frequency from the nominal value in pu, Δf ; (c) the d-axis control signal, U_d , and (d) the q-axis control signal, U_q .

6.5 Performance Analysis

This section focuses on the four key steps during the model development: 1) input delay calculation; 2) model order selection; 3) initialization technique; and 4) optimization approaches. To conduct all analysis under the same simulation environment, the tolerance and the maximum number of iterations are set to 1μ and 400, respectively, to comply with the lower tolerance requirement by TRR [23].

6.5.1 Input Delay Calculation

Input delay is often known as the “system’s dead time”. It signifies the number of samples the physical system takes before outputs respond to inputs. The inclusion of input delay into a data-driven model is particularly important if the model is intended to control a physical system. A MATLAB function named “delayest” is used to estimate the input delay. The function takes the input-output data as input, and returns the input delay as sample numbers. For the proposed model, there are four input-output combinations, and for all combinations, the function returns an input delay of 2 sample numbers.

6.5.2 Model Order Selection

The selection of a suitable model order is crucial in developing a data-driven system identification model. To select the optimum coefficient’s order without digging into the initialization technique and the optimization algorithm, the two parameters are set to “auto”. For an “auto” initialization technique, the software assumes that a suitable initialization technique is among “Zero”, “Estimate” and “Backcast” initialization techniques by analyzing the estimation data. For an “auto” optimization technique, the software chooses the optimization algorithm that first shows a decent direction in reducing the estimated cost. For both voltage and frequency models, all possible combinations up to the 8th model order are considered. A total of 135,902 number of models are resulted, and the most suitable one is chosen based on their data fitting accuracies. The selected orders of the model coefficients are given as follows in this study:

$$nB = \begin{bmatrix} 3 & 1 \\ 3 & 1 \end{bmatrix}; nC = \begin{bmatrix} 6 \\ 6 \end{bmatrix}; nD = \begin{bmatrix} 7 \\ 7 \end{bmatrix}; nF = \begin{bmatrix} 7 & 5 \\ 7 & 5 \end{bmatrix} \quad (29)$$

6.5.3 Initialization Technique

The three initialization techniques under analysis are: Zero, Estimate, and Backcast. The BJ models are created using the four optimization algorithms (GN, AGN, LM and TRR) and the three initialization techniques. The suitable initialization technique is chosen by analyzing the data fitting accuracies of the developed models given in Table 6. 2, where the first value represents the data fitting accuracy for the voltage model, and the second one represents the data fitting accuracy for the frequency model. It is found that Zero cannot maintain satisfactory fitting accuracies for the voltage or frequency models for GN and TRR; Estimate shows low fitting accuracies for the voltage or frequency models for GN, AGN and TRR; while Backcast maintains consistent and acceptable data fitting accuracies for both models using all four optimization algorithms. Therefore, “Backcast” is chosen as the suitable initialization technique.

Table 6. 2: Data Fitting Accuracy (%) for Different Initialization Techniques for the Four Optimization Algorithms (GN, AGN, LM and TRR)

	Zero	Estimate	Backcast
GN	42.25,98.16	99.6, 72.01	99.68, 98.01
AGN	97.69,98.14	58.98, 98.03	97.63, 98.07
LM	97.71, 98.14	98.06, 98.03	97.68, 98.01
TRR	97.72, 17.62	99.66,19.74	99.67, 76.35

6.5.4 Optimization Algorithms

Using the “Backcast” initialization technique, models are developed using GN, AGN, LM, and TRR and are analyzed. Data fitting accuracies of the developed models are depicted in Fig. 6.5. The data fitting accuracies for the voltage model for both GN and TRR are similar, whereas AGN

and LM for the voltage model show slightly lower fitting accuracies. The data fitting accuracies for the frequency model for GN, AGN, and LM are similar, but shows a much lower fitting accuracy for TRR. Therefore, TRR is determined to be an unsuitable algorithm.

Now we need to select the best algorithm among GN, AGN and LM as they show similar fitting accuracies in Fig. 6.5. The models' performance matrices are analyzed as shown in Table 6.3. It is found that GN has lower values for NRMSE and MSE than AGN and LM, which indicate a better model. Therefore, GN outperforms other three considered optimization algorithms using the training dataset.

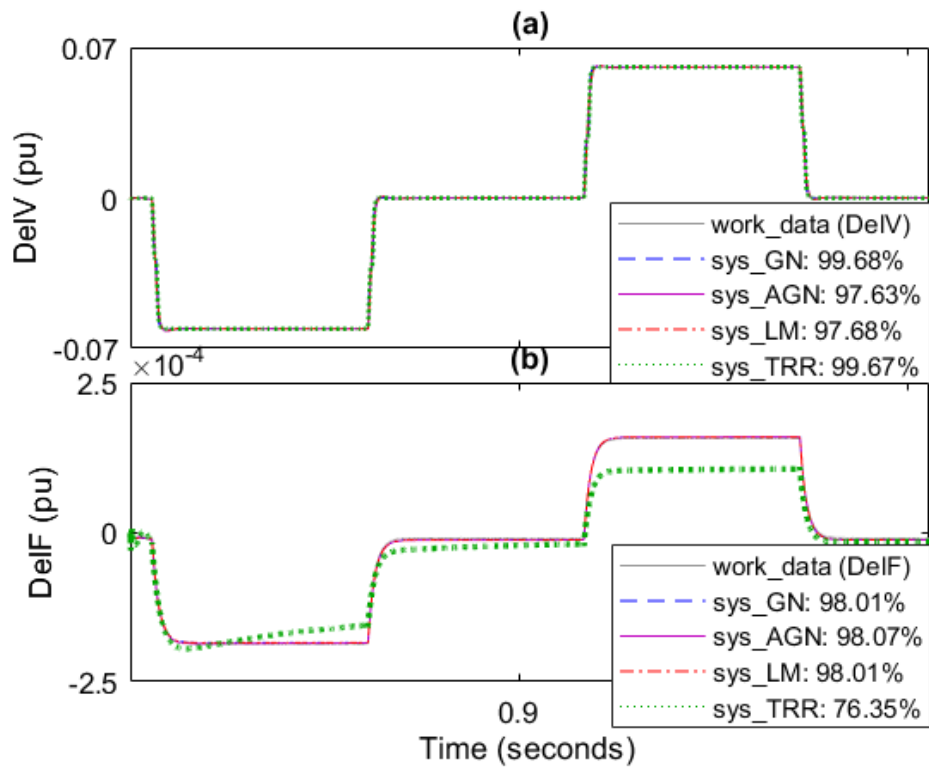


Fig. 6. 5. The fitted models for four optimization algorithms along with their fitting accuracies for the training dataset: (a) DeIV; (b) DeIF.

Table 6. 3: The Model’s Performance Matrices

Focus	NRMSE	MSE
GN	0.32, 1.9	2.1×10^{-8}
AGN	2.37, 1.9	1.1×10^{-6}
LM	2.32, 1.9	1.1×10^{-6}
TRR	0.33, 23.65	2.2×10^{-8}

To further validate the models, fitting accuracies are re-examined using the validation dataset as shown in Fig. 6.6. Similar to the training dataset, GN maintains better performance for the validation dataset than other three optimization algorithms.

Therefore, GN performs better to trace the data trend for the system under analysis and is chosen as the most suitable optimization algorithm in this study.

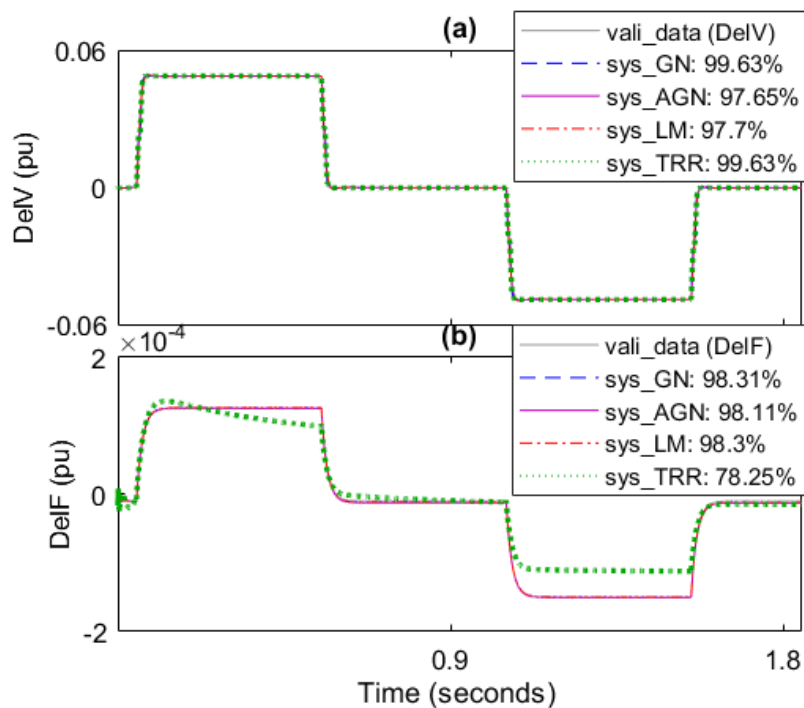


Fig. 6. 6. The fitted models for four optimization algorithms along with their fitting accuracies for the validation dataset: (a) DeIV; (b) DeIF.

6.6 The Final GN-Based Box-Jenkins Model

In this section, before presenting the final Box-Jenkins model, the residual analysis is conducted on the final model to check the model's data overfitting issue.

6.6.1 Residual Analysis

An accurate model has residuals uncorrelated with past inputs and scattered. For the developed model, the residuals plot in Fig. 6.7 shows that the residuals are scattered and not following any trend.

To further verify the model, the cross-correlation analysis between the input and residuals for each input-output pair is conducted. In practice, residuals always hold to some degree of cross-correlation; as a remedy, a confidence interval is used. Any cross-correlation falls within the confidence interval of a chosen probability is treated as statistically insignificant. The evidence of the cross-correlation beyond the confidence interval indicates that the model fails to explain the relation of that particular input-output pair, and the model suffers from data overfitting. The cross-correlation study results for the proposed final model are shown in Fig. 6.8, where the shaded area in blue represents the 99% confidence interval, and the blue circles are the cross-correlation readings. Since all cross-correlation readings fall within the confidence interval, so the model is accurate, and no data overfitting is present.

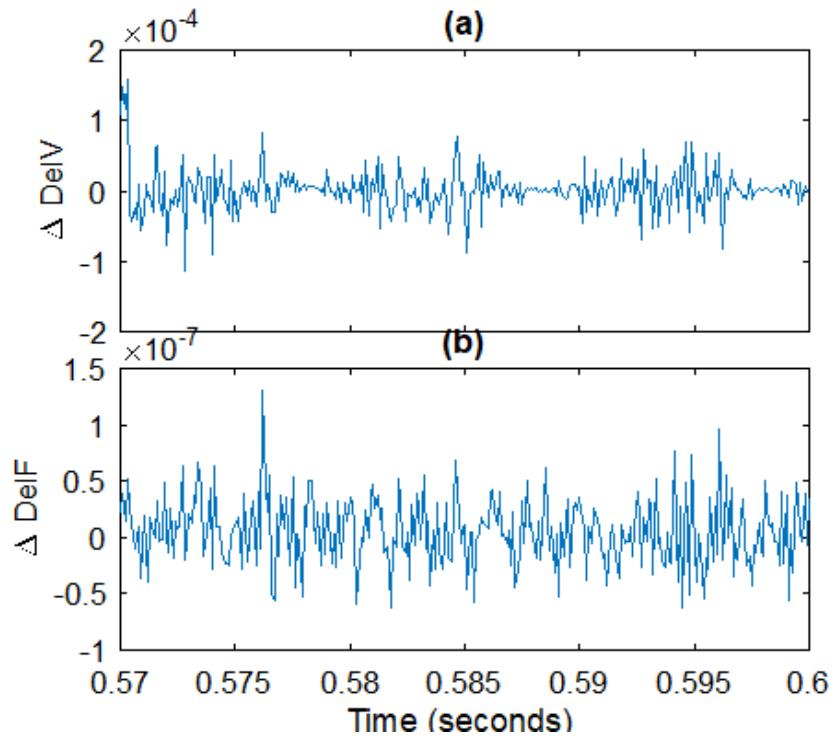


Fig. 6. 7. The residual plot of the final BJ model.

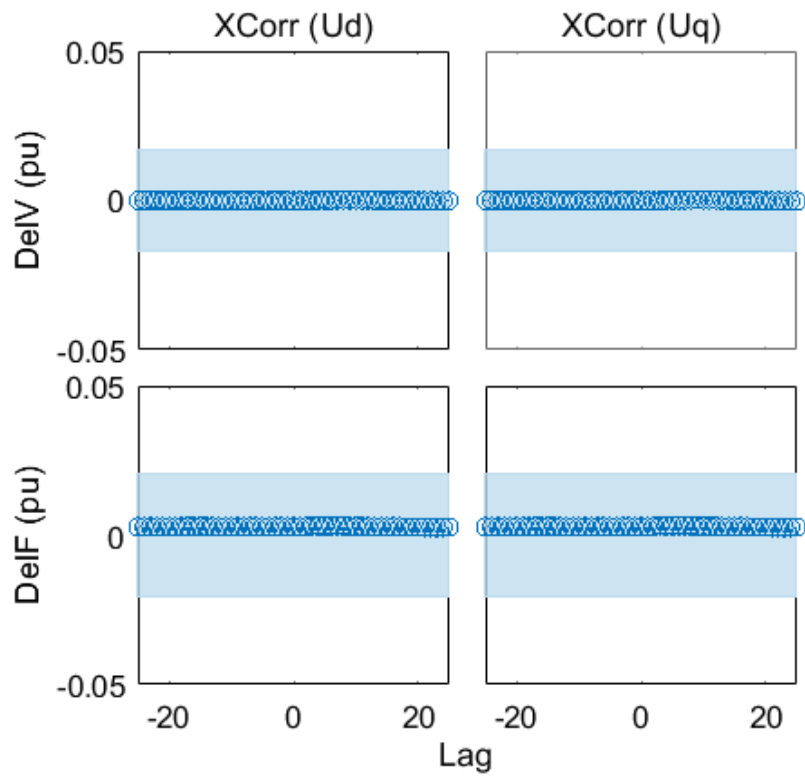


Fig. 6. 8. The cross-correlation readings for the final BJ model.

6.6.2 The Final Box-Jenkins Model

The final Box-Jenkins model expressed in (20) is developed for the test system, and its coefficients A, B, C, D, and F are obtained as follows:

$$A = \begin{bmatrix} 1 & 0 \\ 0 & 1 \end{bmatrix} \quad (30)$$

$$B = \begin{bmatrix} (0, 0, -0.0024, 0.0039, -0.0011) & (0, 0, -8.98 \times 10^{-4}) \\ (0, 0, 2.1 \times 10^{-5}, -7.9 \times 10^{-6}, -2.5 \times 10^{-6}) & (0, 0, -1.5 \times 10^{-5}) \end{bmatrix} \quad (31)$$

$$C = \begin{bmatrix} (1, -0.04, 0.2, 0.43, -0.61, 0.08, -0.01) \\ (1, -0.73, 0.15, -0.49, 0.06, -0.3, 0.48) \end{bmatrix} \quad (32)$$

$$D = \begin{bmatrix} (1, -1.26, 0.58, 0.09, -1.13, 1.02, -0.41, 0.14) \\ (1, -1.97, 1.47, -1.15, 0.63, -0.25, 0.8, -0.54) \end{bmatrix} \quad (33)$$

$$F = \begin{bmatrix} (F_{11}) & (F_{12}) \\ (F_{21}) & (F_{22}) \end{bmatrix} \quad (34)$$

$$F_{11} = [1, -1.86, -0.48, 1.88, 0.35, -0.59, -0.85, 0.54] \quad (34.1)$$

$$F_{12} = [1, -3.69, 4.91, -2.61, 0.22, 0.16] \quad (34.2)$$

$$F_{21} = [1, -1.27, -0.43, 0.59, 0.03, 0.19, 0.02, -0.13] \quad (34.3)$$

$$F_{22} = [1, -2.5, 3.1, -2.88, 1.57, -0.29] \quad (34.4)$$

The step response within the 3rd standard deviation is plotted in Fig. 6.9. The shorter span of the step response within the 3rd standard deviation indicates a minimal covariance in the model parameters.

The developed model can be used to design and tune a DG controller to regulate the voltage and frequency at the PCC of an islanded microgrid. Being a multi-input multi-output model (MIMO), the controller with the MIMO structure handling competency, such as Model Predictive Control (MPC)-based controller, should be considered.

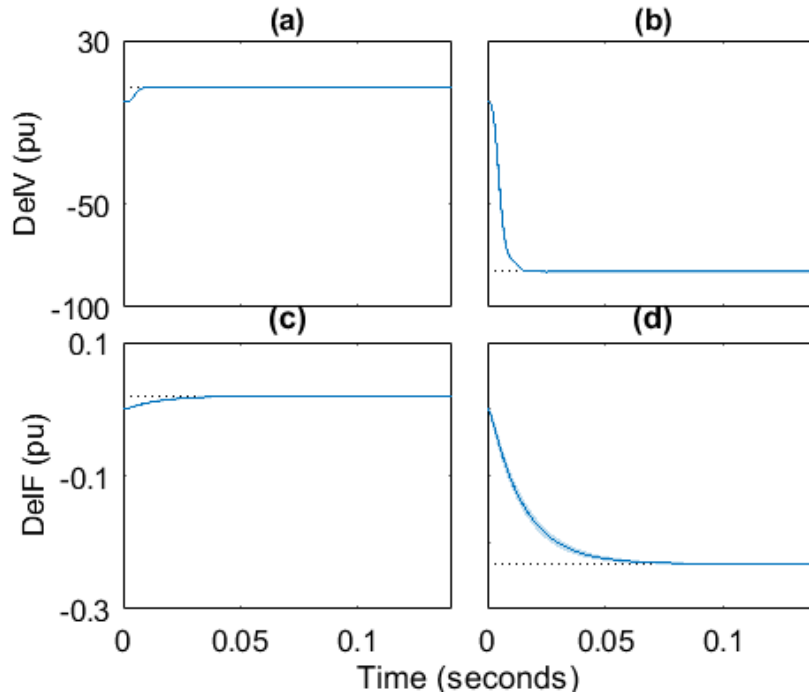


Fig. 6. 9. Step response of the model along with the 3rd confidence bound: (a) U_d vs DeIV; (b) U_q vs DeIV; (c) U_d vs DeIF; and (d) U_q vs DeIF.

6.7 Conclusion

In this paper, a novel DG control algorithm to regulate the voltage and frequency at the PCC in an islanded microgrid is proposed and developed. The algorithm correlates the deviation of voltage and frequency at the PCC with the d- and q- axis components of the DG control signal. A data-driven system identification approach using nonlinear least square method is proposed to parameterize the control model. Due to the flexibility in formulating the system and noise model, the polynomial Box-Jenkins model is chosen as the model structure. Four NLS optimization algorithms, where two are line search-based (Gauss-Newton and Adaptive Gauss-Newton), and two are trust region-based (Levenberg-Marquardt and Trust Region Reflective) are studied to determine the optimum model coefficients. In all performance matrices, GN along with Backcast initialization maintains a consistent and better performance over the other methods for both

training and validation datasets, and thus, is chosen to develop the control model. The developed model can be used for DG control without requiring the secondary controller and virtual impedance loop.

References

- [1] H. Golpîra, H. Seifi, and M. R. Haghifam, “Dynamic equivalencing of an active distribution network for large-scale power system frequency stability studies,” *IET Gener. Transm. Amp Distrib.*, vol. 9, no. 15, pp. 2245–2254, Nov. 2015.
- [2] K.-H. Tan and T.-Y. Tseng, “Seamless Switching and Grid Reconnection of Microgrid Using Petri Recurrent Wavelet Fuzzy Neural Network,” *IEEE Trans. Power Electron.*, pp. 1–1, 2021.
- [3] R. Perez-Ibacache, A. Cedenó, C. Silva, G. Carvajal, J. Agüero, and A. Yazdani, “Decentralized Model-based Predictive Control for DER units Integration in AC Microgrids Subject to Operational and Safety Constraints,” *IEEE Trans. Power Deliv.*, pp. 1–1, 2020.
- [4] C. Dou, Z. Zhang, D. Yue, and M. Song, “Improved droop control based on virtual impedance and virtual power source in low-voltage microgrid,” *IET Gener. Transm. Distrib.*, vol. 11, no. 4, pp. 1046–1054, 2017.
- [5] R. An, Z. Liu, and J. Liu, “Successive-Approximation-Based Virtual Impedance Tuning Method for Accurate Reactive Power Sharing in Islanded Microgrids,” *IEEE Trans. Power Electron.*, vol. 36, no. 1, pp. 87–102, Jan. 2021.
- [6] J. Chen, D. Yue, C. Dou, L. Chen, S. Weng, and Y. Li, “A Virtual Complex Impedance Based $P-V$ Droop Method for Parallel-Connected Inverters in Low-Voltage AC Microgrids,” *IEEE Trans. Ind. Inform.*, vol. 17, no. 3, pp. 1763–1773, Mar. 2021.
- [7] X. Liang, C. Andalib-Bin-Karim, W. Li, M. Mitolo, and M. N. S. K. Shabbir, “Adaptive Virtual Impedance-Based Reactive Power Sharing in Virtual Synchronous Generator Controlled Microgrids,” *IEEE Trans. Ind. Appl.*, vol. 57, no. 1, pp. 46–60, Jan. 2021.

- [8] L. Wang, Y. Qin, Z. Tang, and P. Zhang, "Software-Defined Microgrid Control: The Genesis of Decoupled Cyber-Physical Microgrids," *IEEE Open Access J. Power Energy*, vol. 7, pp. 173–182, 2020.
- [9] P. N. Papadopoulos, T. A. Papadopoulos, P. Crolla, A. J. Roscoe, G. K. Papagiannis, and G. M. Burt, "Measurement-based analysis of the dynamic performance of microgrids using system identification techniques," *IET Gener. Transm. Distrib.*, vol. 9, no. 1, pp. 90–103, 2015.
- [10] B. Zaker, G. B. Gharehpetian, and M. Karrari, "A Novel Measurement-Based Dynamic Equivalent Model of Grid-Connected Microgrids," *IEEE Trans. Ind. Inform.*, vol. 15, no. 4, pp. 2032–2043, Apr. 2019.
- [11] S. A. R. Konakalla, A. Valibeygi, and R. A. de Callafon, "Microgrid Dynamic Modeling and Islanding Control With Synchrophasor Data," *IEEE Trans. Smart Grid*, vol. 11, no. 1, pp. 905–915, Jan. 2020.
- [12] C. N. L. Eu, "Numerical Analysis in Nonlinear Least Squares Methods and Applications," PhD Thesis, Curtin University, 2017.
- [13] J. J. Moré, "The Levenberg-Marquardt algorithm: implementation and theory," in *Numerical analysis*, Springer, 1978, pp. 105–116.
- [14] T. M. Le, B. Fatahi, H. Khabbaz, and W. Sun, "Numerical optimization applying trust-region reflective least squares algorithm with constraints to optimize the non-linear creep parameters of soft soil," *Appl. Math. Model.*, vol. 41, pp. 236–256, Jan. 2017.
- [15] B. Gao and Z. Xu, "Phaseless Recovery Using the Gauss–Newton Method," *IEEE Trans. Signal Process.*, vol. 65, no. 22, pp. 5885–5896, 2017.

- [16] R. Pourbagher and S. Y. Derakhshandeh, "Application of high-order Levenberg–Marquardt method for solving the power flow problem in the ill-conditioned systems," *IET Gener. Transm. Distrib.*, vol. 10, no. 12, pp. 3017–3022, 2016.
- [17] M. Ahsan and M. A. Choudhry, "System identification of an airship using trust region reflective least squares algorithm," *Int. J. Control Autom. Syst.*, vol. 15, no. 3, pp. 1384–1393, Jun. 2017.
- [18] J.-F. Bao, C. Li, W.-P. Shen, J.-C. Yao, and S.-M. Guu, "Approximate Gauss–Newton methods for solving underdetermined nonlinear least squares problems," *Appl. Numer. Math.*, vol. 111, pp. 92–110, Jan. 2017, doi: 10.1016/j.apnum.2016.08.007.
- [19] M. Gan, C. L. P. Chen, G.-Y. Chen, and L. Chen, "On Some Separated Algorithms for Separable Nonlinear Least Squares Problems," *IEEE Trans. Cybern.*, vol. 48, no. 10, pp. 2866–2874, Oct. 2018.
- [20] B. Liu, Z. Liu, J. Liu, R. An, H. Zheng, and Y. Shi, "An Adaptive Virtual Impedance Control Scheme Based on Small-AC-Signal Injection for Unbalanced and Harmonic Power Sharing in Islanded Microgrids," *IEEE Trans. Power Electron.*, vol. 34, no. 12, pp. 12333–12355, Dec. 2019.
- [21] F. Chen, H. Garnier, M. Gilson, J. Agüero, and T. Liu, "Refined instrumental variable parameter estimation of continuous-time Box–Jenkins models from irregularly sampled data," *IET Control Theory Appl.*, vol. 11, no. 2, pp. 291–300, 2017.
- [22] P. Wilson and H. A. Mantooth, "Chapter 10 - Model-Based Optimization Techniques," in *Model-Based Engineering for Complex Electronic Systems*, P. Wilson and H. A. Mantooth, Eds. Oxford: Newnes, 2013, pp. 347–367.

[23] “Option set for bj - MATLAB bjOptions.”

<https://www.mathworks.com/help/ident/ref/bjoptions.html> (accessed Nov. 15, 2020).

Chapter 7

A Novel Data-Driven Predictive Model for Distributed Generation Control in Islanded Microgrids

Md Nasmus Sakib Khan Shabbir¹, *Student Member*, IEEE, Xiaodong Liang², *Senior Member*, IEEE, Weixing Li³, *Senior Member*, IEEE, and Syed Imtiaz⁴

¹Department of Electrical and Computer Engineering, Memorial University of Newfoundland, St. John's, Newfoundland, Canada.

²Department of Electrical and Computer Engineering, University of Saskatchewan, Saskatoon, Saskatchewan, Canada.

³Department of Electrical Engineering, Harbin Institute of Technology, Harbin, Hilongjiang, China.

⁴Department of Process Engineering, Memorial University of Newfoundland, St. John's, Newfoundland, Canada.

A version of this chapter is to be submitted to a journal. Md Nasmus Sakib Khan Shabbir co-authored the paper under the supervision of Dr. Xiaodong Liang. Sakib's contributions in this paper are listed as follows:

- Performed literature review for data driven system identification approaches for distributed generation system.
- Developed the novel control structure for distributed generation control.
- Examined results and reported findings.
- Involved in writing the paper draft as the first author.

Dr. Xiaodong Liang provided continuous technical guidance, checked the results, reviewed the manuscript, provided suggestions to accomplish the work, and modified the final version of the manuscript. Dr. Weixing Li modified the manuscript. Dr. Syed Imtiaz reviewed the manuscript and provided suggestions.

In this chapter, the manuscript is presented with altered figure numbers, table numbers and reference formats in order to maintain the thesis formatting guidelines set out by the Memorial University of Newfoundland.

In Chapter 6, the most suitable optimization algorithm is chosen among Gauss-Newton, Adaptive Gauss-Newton, Levenberg-Marquardt and Trust Region Reflective to parameterize the proposed control model through the data driven approach. In this chapter, the suitable focus for the optimization (the two optimization focuses are simulation and prediction) is chosen to be prediction.

Abstract- A data-driven input-output Box-Jenkins polynomial predictive model for a Distributed Generation (DG) control in an islanded microgrid is developed using the Gauss-Newton-based nonlinear least square method to regulate the voltage and frequency at the Point of Common Coupling (PCC). The model inputs are direct- and quadrature-axis components of the control signal, and the model outputs are deviations of the voltage and frequency from their nominal values at the PCC. To initialize the iteration for nonlinear least square, the Backcast technique is chosen by comparing with Zero and Estimate techniques. Two optimization methodologies are evaluated: “simulation” focus and “prediction” focus. The prediction focus shows much better performance, such as a high prediction accuracy and faster convergence; it also avoids the necessity of data

prefiltering by introducing a built-in weighted filter in the objective function. The developed model is validated using noisy and noiseless datasets.

Keywords- Box-Jenkins model, distributed generation, Gauss-Newton, nonlinear least square, prediction model.

7.1 Introduction

Due to integration of renewable energy sources, microgrid has become a fundamental element in smart grids, enabling bidirectional power flow and advanced control for distributed generation (DG) and load. A microgrid can operate in grid-connected or island mode. The voltage and frequency of a microgrid are governed by the grid in grid-connected mode and regulated by DG controllers in island mode. In this paper, we focus on DG control for islanded microgrids.

Droop control, which mimics steady-state characteristics of synchronous generators, is the most adopted primary control method for DGs in islanded microgrids. To compensate voltage or frequency deviations, droop control estimates adjustments of power flow by updating control signal references for voltage regulators [1] or current regulators [2] through its control architecture. The output of voltage/current regulators then feeds a signal generator to generate Pulse Width Modulation (PWM) signals. Droop control adopts P - f / Q - V [3] or P - V / Q - f [4] control (active power P , reactive power Q , frequency f , voltage V), depending on inductive or resistive nature of distribution lines.

Inherent limitations of droop control include steady-state errors in voltage and frequency regulation and disproportional reactive power sharing among DGs due to the mismatch of line impedances. Therefore, improved droop control schemes were proposed in the literature by implementing secondary controllers [5] and virtual impedance loops [1] to overcome such

problems, but the size and complexity of DG controllers are increased substantially, as a result, retuning of the controller due to microgrid's topological and parametric uncertainty becomes more difficult, expensive and time-consuming [6].

A DG controller depends on accurate estimation of control signals, and existing methods undergo a very complex process to realize it. In this paper, a novel data-driven input-output model is developed through system identification by directly correlating deviations of the voltage and frequency at the PCC (outputs) with deviations of direct(d)- and quadrature(q)-axis components (U_d and U_q) of control signals (inputs). Unlike droop control only considering either line resistance or line reactance, the proposed model considers both resistance and reactance of distribution lines, which leads to simultaneous control of P-f/Q-V and P-V/Q-f, so it can be applied in controllers that need to handle a coupled relationship between active and reactive power. The model formulates the impact of line parameters on the model outputs, secondary controllers and virtual impedance loops are no longer needed, which substantially reduces volume and complexity of the controller. The proposed model can be implemented by a Model Predictive Controller, whose design will be addressed in a separate paper. By using a data-driven approach, the knowledge of line impedances is not required, which greatly simplify the problem.

Recently, data-driven approaches for system identification have attracted significant research interest in modeling dynamic characteristics of a DG or microgrid as a whole [7]–[12]. The developed models represent dynamic characteristics of active and reactive power of a grid-connected microgrid due to variations of the voltage and frequency [7], [8], and due to changes of power dispatch commands (P_{ref} and Q_{ref}) [9]–[12]. To the authors' best knowledge, there are no developed models directly correlating deviations of voltage and frequency at the PCC with variations of control signals.

In this paper, the Box-Jenkins model structure is adopted, which is parameterized through Gauss-Newton (GN)-based nonlinear least-square (NLS) method. GN is frequently used to solve nonlinear least-square problems. With the assumption of reduced-order Hessian of the objective function, GN reduces the computational burden significantly [13]. However, it takes large and uncontrolled steps and sometimes may fail to converge if a large residual occurs during optimization [14].

The optimization method conventionally used in the NLS is the “simulation” focus[15]. During the parametric optimization, the objective function with “simulation” focus cannot update itself according to measurement data [16], which can enlarge the residual and force GN to take more iterations or even prevent it to converge. In this paper, we found that another optimization method, known as the “prediction” focus, can update the objective function according to measurement data, and thus, can keep the residual small and ensure faster convergence. In addition, the built-in noise-canceling weighted filter in the “prediction” focus helps GN to find right frequencies from a noisy dataset and eliminate the needs of data preprocessing[17]. This is particularly important for a dataset containing transient data with high-frequency dynamics, where preprocessing can eliminate crucial dynamics.

The main contributions of the paper include: 1) a novel data-driven input-output Box-Jenkins polynomial predictive model for DG control in islanded microgrids to regulate the voltage and frequency at the PCC is developed using GN-based nonlinear least square method, and it directly correlates deviations of the voltage and frequency at the PCC with d- and q-axis components of control signals; 2) the model is developed by considering both resistance and reactance of distribution lines; 3) for optimization methods used in the GN-based NLS, the effectiveness of the “prediction” focus over the “simulation” focus is demonstrated.

The paper is arranged as follows: mathematical derivations and steps to develop the proposed data-driven model are introduced in Section 7.2; the fundamental theory is explained in Section 7.3; the test system is given in Section 7.4; two key steps during the model development are explained in Sections 7.5; the final model is developed in Section 7.6, and conclusions are drawn in Section 7.7.

7.2 The Proposed Approach

Mathematical derivations and stepwise evolution of the proposed model are provided in this section.

7.2.1 Mathematical Formulation for the Proposed Model

For a microgrid depicted in Fig. 7.1, the generated active and reactive power at the point S can be expressed by

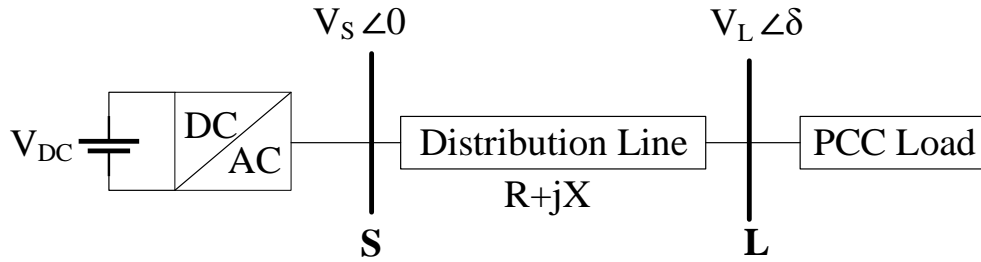


Fig. 7. 1. A microgrid with a DG's interfacing inverter.

$$P = \frac{V_s}{R^2+X^2} [R(V_s - V_L \cos \delta) + XV_L \sin \delta] \quad (1)$$

$$Q = \frac{V_s}{R^2+X^2} [X(V_s - V_L \cos \delta) - RV_L \sin \delta] \quad (2)$$

Assuming a very small power angle, δ , (1) and (2) can be rewritten as follows:

$$\delta = \frac{1}{XV_L} \left[\frac{R^2+X^2}{V_s} P - R(V_s - V_L) \right] \quad (3)$$

$$V_s - V_L = \frac{1}{X} \left(\frac{R^2 + X^2}{V_s} Q + R V_L \delta \right) \quad (4)$$

With the further analysis, (3) and (4) can be expressed by

$$\delta = \frac{1}{V_s V_L} (X P - R Q) \quad (5)$$

$$V_s - V_L = \frac{1}{V_s} (X Q + R P) \quad (6)$$

From (5) and (6), fundamental formulas of conventional droop control equations are derived: Eq. (7.1) is derived by assuming $X \gg R$, so R is ignored, which leads to P-f/Q-V control; Eq. (7.2) ignores X by assuming $R \gg X$, which leads to P-V/Q-f control. R and X are resistance and reactance of distribution lines, respectively.

$$\delta, (V_s - V_L) = \begin{cases} \frac{X P}{V_s V_L}, \frac{X Q}{V_s}, \text{ when } X \gg R & (7.1) \\ -\frac{R Q}{V_s V_L}, \frac{R P}{V_s}, \text{ when } R \gg X & (7.2) \end{cases}$$

Ref [1] shows the derivation of droop equations and adjustment of the voltage reference settings of the virtual impedance loop in droop control for DG controllers [1]. Generally, the control of power angle, δ , dynamically controls the system frequency, f . Thus, droop equations in (5) and (6) can be expressed by

$$f - f_0 = -k_{p1}(P - P_0) + k_{p2}(Q - Q_0) \quad (8)$$

$$V_s - V_{s0} = -k_{q1}(Q - Q_0) - k_{q2}(P - P_0) \quad (9)$$

From (8) and (9), the DG control considering both line resistance R and line reactance X requires a simultaneous P-f/Q-V and P-V/Q-f control.

The active and reactive power can be expressed by

$$P = \frac{3}{2}(U_d I_d + U_q I_q) \quad (10)$$

$$Q = \frac{3}{2}(-U_d I_q + U_q I_d) \quad (11)$$

Where subscripts d and q represent d- and q-axis components of the parameters. Eqs. (10) and (11) transform (5) and (6) into

$$\delta = \frac{3}{2} \frac{1}{V_s V_L} [(X I_d + R I_q) U_d + (X I_q - R I_d) U_q] \quad (12)$$

$$V_s - V_L = \frac{3}{2} \frac{1}{V_s} [(R I_d - X I_q) U_d + (R I_q + X I_d) U_q] \quad (13)$$

For the sake of simplicity, let's assume that the alteration of U_d and U_q is not going to affect I_d and I_q , so the control formulas developed in (12) and (13) can be expressed by

$$f - f_0 = \frac{3}{2} \frac{1}{V_s V_L} [(X I_d + R I_q)(U_d - U_{d0}) + (X I_q - R I_d)(U_q - U_{q0})] \quad (14)$$

$$V_L - V_{L0} = \frac{3}{2} \frac{1}{V_s} [(R I_d - X I_q)(U_d - U_{d0}) + (R I_q + X I_d)(U_q - U_{q0})] \quad (15)$$

Where f and V_L are reference voltage and frequency, and f_0 and V_{L0} are nominal voltage and frequency, respectively. U_d and U_q are the reference of the parameters at f and V_L ; and U_{d0} and U_{q0} are the pre-disturbance reference of the parameters.

The relationship between (deviations of the voltage and frequency) and (U_d and U_q) is formulated in (14) and (15). The major challenge to implement these formulas is that the line resistance and reactance of distribution lines are needed. To solve the issue, a data-driven system identification approach is adopted in this paper. To obtain the datasets, U_d and U_q are varied over a short-range, which is large enough to influence the system dynamics but small enough to ignore

nonlinearities; the subsequent impact on the voltage and frequency at the PCC are recorded in the datasets. Using the datasets, two system identification models are developed as follows:

$$\Delta f = k_1 \Delta U_d + k_2 \Delta U_q \quad (16)$$

$$\Delta V = k_3 \Delta U_d + k_4 \Delta U_q \quad (17)$$

where coefficients k_1 to k_4 are derived through the proposed data-driven system identification approach. This way, the equivalent model in (14) and (15) is developed without quantifying parameters of distribution lines.

The data-driven model shown in (16) and (17) are intended to control DG units using intelligent controllers, such as a model predictive controller. The model supports the controller to decide how much reference adjustments for U_d and U_q are required to compensate the voltage and frequency deviations.

7.2.2 Main Idea of the Proposed Approach

The proposed approach is to develop a data-driven Box-Jenkins prediction model for DG control in islanded microgrids to regulate the voltage and frequency at the PCC. It is developed through 7 steps below, as shown in the flowchart in Fig. 7.2:

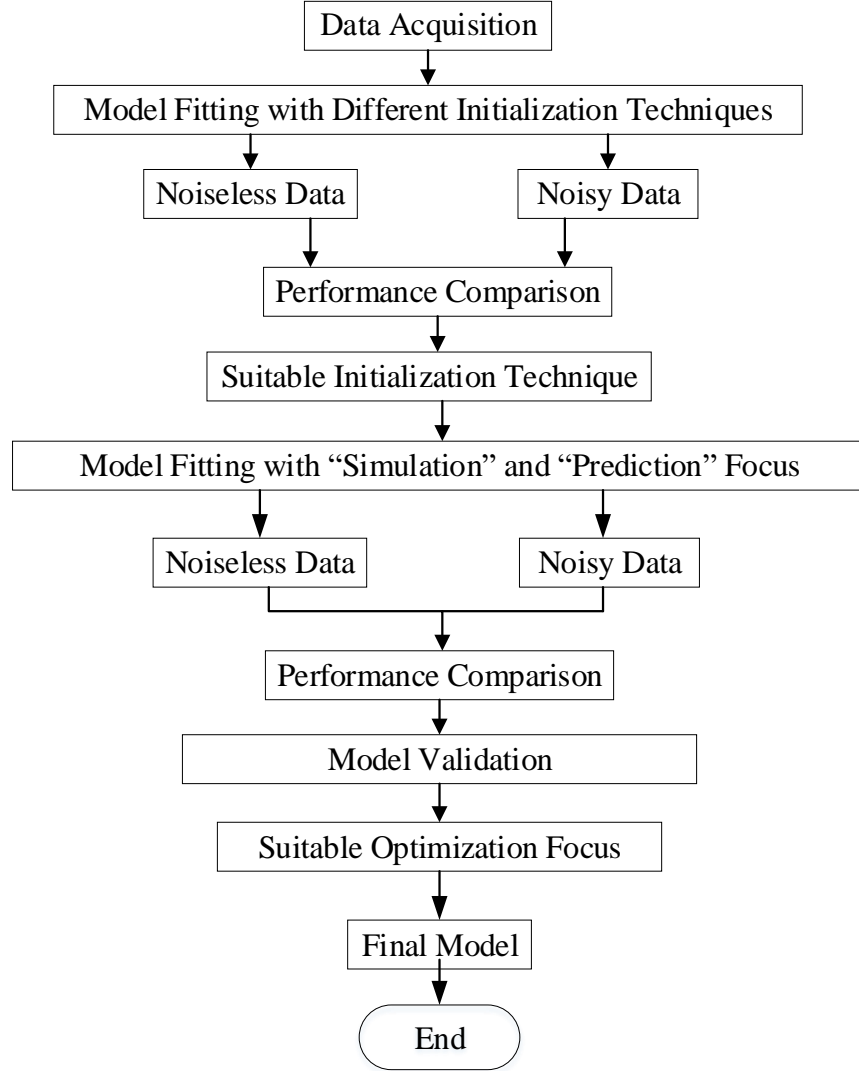


Fig. 7. 2. Flow chart of the proposed approach.

Step 1: Data acquisition for system identification. To develop a data-driven model, datasets must be obtained first. To obtain the datasets, d- and q-axis components of the control signal (U_d and U_q) are varied in the simulation model, and corresponding deviations of the voltage and frequency from their nominal values in pu at the PCC (ΔV and Δf) are tabulated. For each of training and validation datasets, we also produce two sets of data: 1) noiseless data, which is the direct simulation results; and 2) noisy data, which is created by adding Gaussian noise to the noiseless data (Details are given in Section IV).

Step 2: *Selection of initialization techniques.* Optimization algorithms in nonlinear least square are sensitive to initial conditions, affecting convergence speed and fitting accuracy of the model. Three initialization techniques, zero, estimate and backcast, are evaluated in this paper. “zero” is to set the initial condition to zero regardless of the data trend; “estimate” is to treat the initial condition as an independent estimation parameter, and “backcast” is to estimate the initial condition by the “auto-regressive with external input” method. A suitable technique is selected based on the model performance matrices.

Step 3: *Model development with optimization focus.* Using GN-based nonlinear least square approach, models are developed using “prediction” and “simulation” optimization focus for noiseless and noisy datasets (Details are given in Section III.D).

Step 4: *Performance analysis.* To study the performance of the two optimization focus, the precision of the models is analyzed using the data fitting accuracies, Akaike's Final Prediction Error (FPE), Normalized Root Mean Square Error (NRMSE), Mean Square Error (MSE), first-order optimality, and auto and cross-correlation analysis of the residuals.

Step 5: *Model validation.* The developed models are validated by validation datasets, which shows how precisely the developed model agrees with the original system for a different combination of input-output.

Step 6: *Suitable optimization focus.* Based on the above analysis, the most suitable optimization focus is chosen.

Step 7: *Develop the final Box-Jenkins model.* The final Box-Jenkins model is developed for a given system.

7.3 Fundamental Theory

7.3.1 Box-Jenkins Model

A Box-Jenkins model is a polynomial mathematical model that provides the flexibility of independent parameterization of a system's dynamics and associated noises using rational polynomial functions [18]. The general expression of the Box-Jenkins model with nu inputs and ny outputs is

$$\sum_{i=1}^{nu} \sum_{j=1}^{ny} A_{ij}(q) y_j(t) = \sum_{i=1}^{nu} \sum_{j=1}^{ny} \frac{B_{ij}(q)}{F_{ij}(q)} u_i(t - nk_{ij}) + \sum_{j=1}^{ny} \frac{C_j(q)}{D_j(q)} e_t(t) \quad (18)$$

Where A, B, C, D, and F are polynomial coefficients; q is the time shift operator; $u(t)$ and $y(t)$ are the input and the output, respectively; nk_{ij} is the transport delay in between the i^{th} input and j^{th} output; and $e_t(t)$ is the noise. C and D are $ny \times 1$ matrices, and related to the noise and can be modeled independently, regardless of B and F. A, B, F, and K are $ny \times nu$ matrices. The number of coefficients in the denominator in (18) represents the pole number, and the numerator polynomials are one unit more than the number of zeros. A, B, C, D, and F can be obtained by the nonlinear least-square approach.

7.3.2 Mathematical Formulation of Non-linear Least Square

In a regression analysis, the nonlinear least square approach is adopted, where a nonlinear mathematical model, $y = f(\theta, t)$, $\theta = [\theta_1, \theta_2, \dots, \theta_n]^T$ with n unknown vector parameters (coefficients of the model), is used to fit a set of m observed data points $(t_1, y_1), (t_2, y_2), \dots, (t_m, y_m)$, where $m > n$. To find the best fit, the minimum value of the vector parameters, θ , are selected by optimizing an objective function, $V(\theta)$, formulated as the sum of the squared residual functions, $r_i(t, \theta)$, of the m observed data. The minimum point of θ , θ^* , is calculated by.

$$\theta^* = \underset{\theta}{\operatorname{argmin}} V(\theta) \quad (19)$$

7.3.3 The Gauss-Newton Method

GN is a line search-based quasi newton approach. For a search direction of p_k^{GN} and a step size of α_k^{GN} , the iterative equation of GN can be expressed as follows [19]:

$$\theta_{k+1} = \theta_k + \alpha_k p_k^{GN} \quad (20)$$

GN approximates the objective function's Hessian matrix to its truncated form of $J(x_k)^T J(x_k)$, and the search direction

p_k^{GN} is given by

$$[J(x_k)^T J(x_k)] p_k^{GN} = -J(x_k)^T r(x_k) \quad (21)$$

Where $J \in \mathbb{R}^{m \times n}$ is the Jacobian of $r(x)$.

If the number of data points m , the number of parameters n , both m and n , or the residual $r_i(t, \theta)$ is large, the truncated Hessian is no longer a valid approximation. In such a situation, GN takes a significantly higher amount of iterations to converge, or even fails to solve a NLS problem [19].

7.3.4 Impact of Optimization Focus

In system identification, model parameters are estimated by minimizing the objective function, which is a weighted sum of squares of the residuals. The time-domain representation of the objective function can be expressed as follows:

$$V(\theta) = \frac{1}{N} \sum_{t=1}^N r^T(t, \theta) W(\theta) r(t, \theta) \quad (22)$$

Where N is the number of data samples, and $W(\theta)$ is a weighted semi-definite matrix of the vector parameter θ .

The optimization focus mainly impacts how the residuals in the objective function are computed. The general expression to compute the residuals can be expressed by

$$r(t, \theta) = y_m(t) - y_r(t, \theta) \quad (23)$$

Where, $y_m(t)$ is the measured output, $y_r(t, \theta)$ is the predicted or simulated response of the model, parameterized with prediction or simulation focus, respectively.

A simulated response calculated using present measured inputs and initial states can be expressed by

$$y_r(t, \theta) = f(u_m(t), u_m(0); y_m(0)) \quad (24)$$

Where, $u_m(t)$ is the present measured input, $u_m(0)$ and $y_m(0)$ are initial states.

A predicted response is computed certain steps ahead in time using the present input, and the past measured input and output, including initial states. To calculate a predicted response k step ahead into the future from the present time t , where $k \geq 1$, all the inputs up to $(t + k)$ and all output up to t must be available. The general expression for the predicted response is

$$y_r(t + k, \theta) = f(u_m(t + k), u_m(t + k - 1), \dots, u_m(t), u_m(t - 1), \dots, u_m(0); y_m(t), y_m(t - 1), \dots, y_m(0)) \quad (25)$$

This unique competency of considering the previous measured input-output enables the prediction model to respond with more narrow but reliable confidence bounds over a shorter time period [16]. The time span should be long enough for the controller, but unnecessarily long prediction horizon increases the computational burden and controller response time substantially. This updating characteristic of the prediction focus keeps residuals ($r(t, \theta)$) in (22) low, which subsequently supports GN's approximation of the truncated Hessian for all iterations. This way, the prediction focus ensures a faster and guaranteed convergence of GN. On the contrary, non-

updating nature of the simulation focus may trigger larger residuals for some data points, which penalizes GN's truncated Hessian approximation, and GN may take longer or fail to converge.

To illustrate how the “prediction” or “simulation” focus works on noisy data, let's first transform the objective function with the prediction focus into the frequency domain using Parseval's identity as follows:

$$\vartheta(\omega, \theta) = \frac{1}{N} \left\| \frac{Y(\omega)}{U(\omega)} - G(\omega, \theta) \right\|^2 \frac{\|U(\omega)\|^2}{\|H(\omega, \theta)\|^2} \quad (26)$$

Where $Y(\omega)$, $U(\omega)$, and $E(\omega)$ are the frequency domain representation of output, input, and noise, respectively. $G(\omega, \theta)$ and $H(\omega, \theta)$ represent the frequency response of the input-output, and noise coefficients, respectively.

Eq. (26) is the objective function $\vartheta(\omega, \theta)$, minimized by fitting $G(\omega, \theta)$ with the empirical function $\frac{Y(\omega)}{U(\omega)}$ using a weighted filter $\frac{\|U(\omega)\|^2}{\|H(\omega, \theta)\|^2}$. The filter emphasizes frequencies where the input has more power, and de-emphasizes frequencies where the noise has more power. This way, the algorithm tunes the objective function to the right frequencies by itself. Thus, the original dataset no longer needs prefiltered, which avoid the accidental removal of critical information.

On the other hand, the frequency domain representation of the objective function with the simulation focus is

$$\vartheta(\omega, \theta) = \frac{1}{N} \left\| \frac{Y(\omega)}{U(\omega)} - G(\omega, \theta) \right\|^2 \|U(\omega)\|^2 \quad (27)$$

In the simulation focus, the noise term $H(\omega, \theta)$ is ignored in the weighted filter. The objective function emphasizes only the input spectrum to weigh relative importance of the estimation in a specific frequency range despite the presence of noises.

7.3.5 Model Quality Matrices

The model quality matrices in this paper include Akaike's Final Prediction Error (FPE), Normalized Root-Mean-Square Error (NRMSE), Mean Square Error (MSE), the model data fitting accuracy, the first order optimality (FOO), and residual analysis. FPE quantifies the prediction error among a group of models [20]. NRMSE represents the normalized square root of the second sample moment of the difference between the model's predicted and observed values. MSE is a non-negative quality matrix of an estimated model and the second moment of the error. MSE incorporates both the variance and the bias of an estimated model. FOO represents how much the model parameters are close to the optimal. A better model comes with a lower FPE, NRMSE, MSE, and FOO.

Both simulated and predicted response is calculated from a model irrespective of their "prediction" or "simulation" focus during the parametric optimization. However, it is suggested in [16] that, due to the difference in estimating the two responses, data fitting accuracies resulted from the simulated response should not be compared with that of the predicted response. As in most cases, a controller performance depends on how aptly the model, on which the controller relies, responds at the present time frame, therefore, the simulated response is used to calculate the data fitting accuracy in this paper.

Residuals are the portion of the dataset not explained by a developed model. An accurate model has uncorrelated and scattered residuals. To verify the developed models, a residual analysis is conducted through two tests: whiteness test and independence test. The whiteness test's criteria imply that a good model has the residual autocorrelation function inside the confidence interval (99%) of the corresponding estimates [21]. For independence test, a good model has residuals uncorrelated with the past inputs. A cross-correlation beyond the confidence indicates that the

model does not describe how part of the output relates to the corresponding input. In short, autocorrelation depicts the correlation between the residual and its respective output, and cross-correlation analyzes the correlation between the input and the residuals for each input-output pair. The real system lies within the developed model's confidence interval if the model passes the residual analysis [21].

7.4 The Test System

The test system's simulation model (an islanded microgrid) is shown in Fig. 7.3. The DG under analysis is a PV system rated at 10 kVA, modeled as a constant DC voltage source. System parameters used in the simulation are tabulated in Table 7.1.

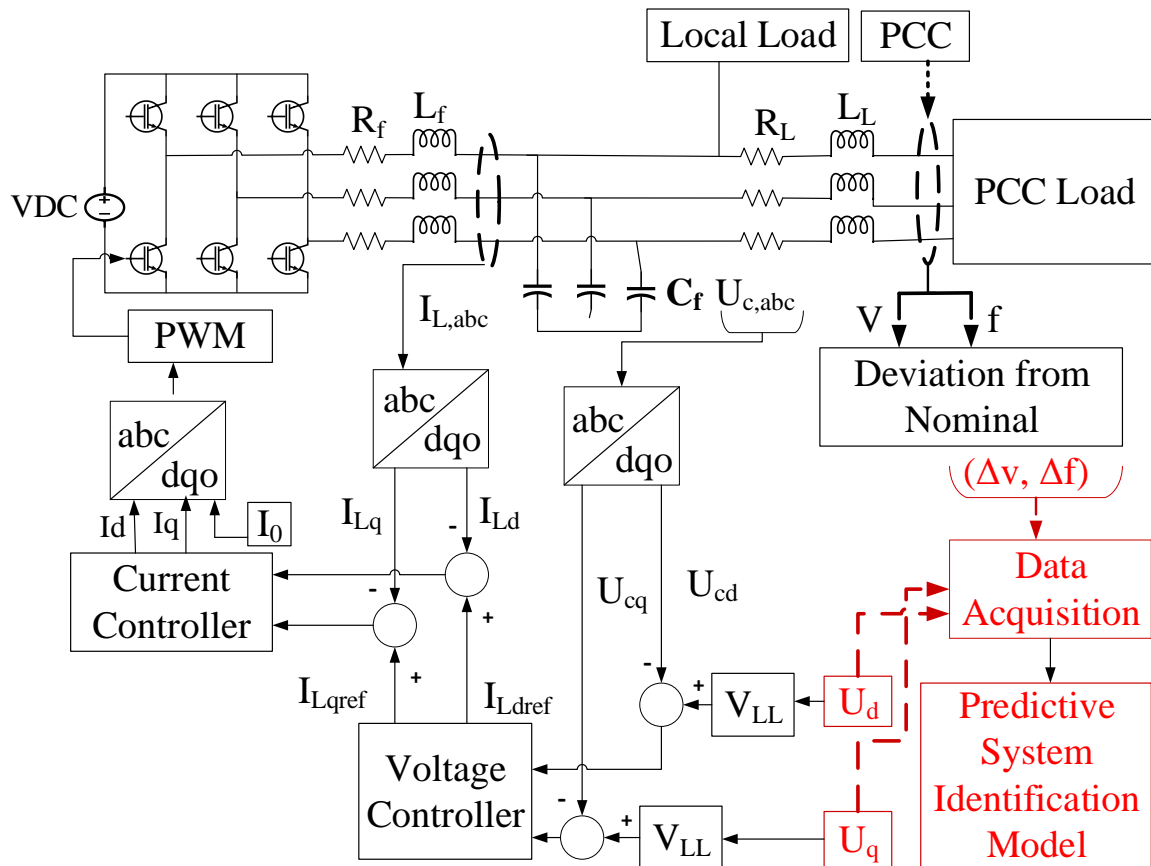


Fig. 7. 3. The test system's simulation model.

Table 7. 1: Test System's Parameters

Parameters		Values
Nominal DC bus voltage (V)		700
Nominal AC bus RMS line voltage (V)		380
AC system frequency (f)		50
DG's Nameplate capacity (kVA)		10
Local Load		5 kW, 1 kVar
PCC Load		2 kW, 0.4 kVar
Inverter filter	Resistance, R_f (Ω)	0.2
	Inductance, L_f (H)	3×10^{-3}
	Capacitance, C_f (F)	15×10^{-6}
Line impedance	Line resistance, R_L (Ω)	0.641
	Line reactance, X_L (Ω)	0.08

The test system is first initialized to the nominal steady-state situation. Initialization sets 0.821 for the d-axis component (U_d) and 0.07 for the q-axis component (U_q) for the control signal. To generate the training dataset for system identification, U_d and U_q are perturbed around their nominal values by ± 0.05 and ± 0.005 , respectively. The duration of each step change is 0.5 s. Deviations of the voltage and frequency from their nominal values in pu at the PCC (ΔV and ΔF) for the aforementioned variations of U_d and U_q are tabulated. Input-output data collection points are marked in red in Fig. 7.3. To calculate deviations, the measured parameter values (voltage and frequency) are subtracted from their nominal values. The magnitude of step variations is carefully chosen to influence system dynamics without causing nonlinearity. The sampling frequency of data acquisition is 10 kHz.

In system identification, in addition to a “training” dataset, a “validation” dataset is usually used to test the robustness of the developed model. To generate a validation dataset, U_d and U_q are varied around their nominal value by ± 0.04 and ± 0.004 , respectively. The duration of the step input and data acquisition frequency remains the same as that for the training dataset.

The control signal (U_d and U_q) pass through the voltage and current controllers before transforming into the abc co-ordinate. Assuming a balanced system, I_0 , the zero-axis component of the controller current is set to zero. The transformed control signal is then used to generate the PWM pulse. The triangular carrier signal in PWM has a switching frequency of 10 kHz and a peak value of 1.03. Input-output data used in the analysis are depicted in Fig. 7.4.

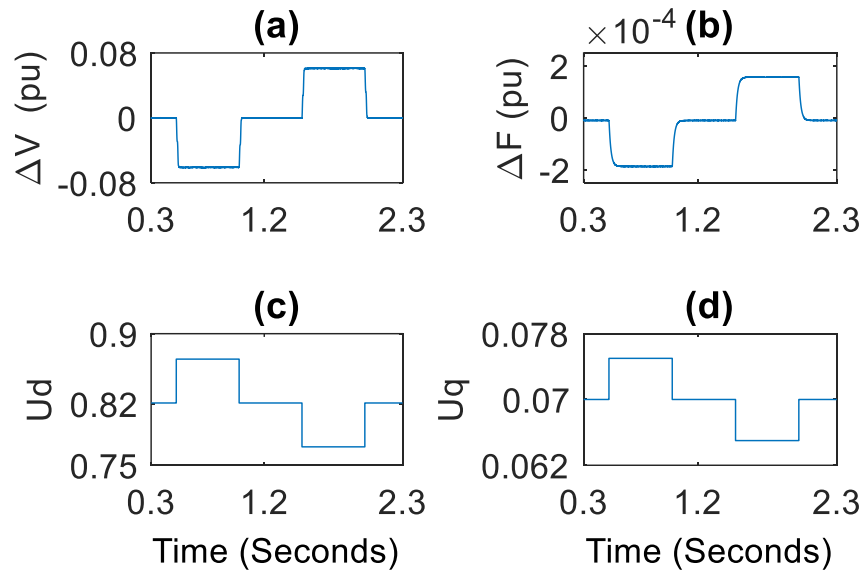


Fig. 7. 4. Input-output data: (a) deviation of the voltage from the nominal value in pu, ΔV , (b) deviation of the frequency from the nominal value in pu, Δf ; (c) the d-axis control signal, U_d , and (d) the q-axis control signal, U_q .

7.5 Performance analysis

This section focuses on two key steps in model development: 1) initialization technique; and 2) optimization focus.

7.5.1 Initialization Technique

To set initial conditions, three initialization techniques are considered in this paper: Zero, Estimate, and Backcast. To choose the most suitable initialization technique, three models are created for each optimization focus (prediction and simulation) using these three initialization techniques (note: the optimization focus affects the performance of an initialization technique). Fitting accuracies of these models are shown in Table 7.2, where each pair of accuracies in % represents the fitting accuracies for the voltage (left) and frequency (right). Zero’s accuracies for both voltage and frequency models are significantly lower than that of Estimate and Backcast; while Backcast shows slightly higher accuracies than Estimate.

To further validate that Backcast is better than Estimate, their respective model performance matrices are analyzed in Table 7.3. Backcast’s FPE, NRMSE and MSE are consistently lower than that of Estimate, indicating better models using Backcast.

The estimated initial states for prediction and simulation focus using the three initialization techniques are depicted in Fig. 7.5. The initial states estimated by “Backcast” are consistently smaller than other two techniques. Finally, the first order optimality of the models is compared for the final iterations as shown in Table 7.4, Backcast provides the lowest first-order optimality, so Backcast is chosen in this paper.

Table 7. 2: Simulation Accuracy (%) for Different Initialization Techniques

Optimization Focus	Zero	Estimate	Backcast
Prediction	97.68, 5.24	97.22, 97.93	98.93, 97.92
Simulation	51.7,98.81	99.59,97.88	99.67, 97.92

Table 7. 3: The Model's Performance Matrices for Different Initialization Techniques

Optimization Focus	Initialization Technique	FPE	NRMSE	MSE
Prediction	Estimate	5.26×10^{-25}	0.03,0.02	7.85×10^{-10}
	Backcast	5.12×10^{-25}	0.01,0.02	7.68×10^{-10}
Simulation	Estimate	1.27×10^{-22}	0.004,0.02	3.05×10^{-8}
	Backcast	3.19×10^{-24}	0.003,0.02	1.99×10^{-8}

7.5.2 Optimization Focus

The developed Box-Jenkins models using prediction focus and simulation focus are compared through noiseless and noisy datasets. As recommended by MATLAB for GN, the tolerance of the optimization is set to 0.01[22].

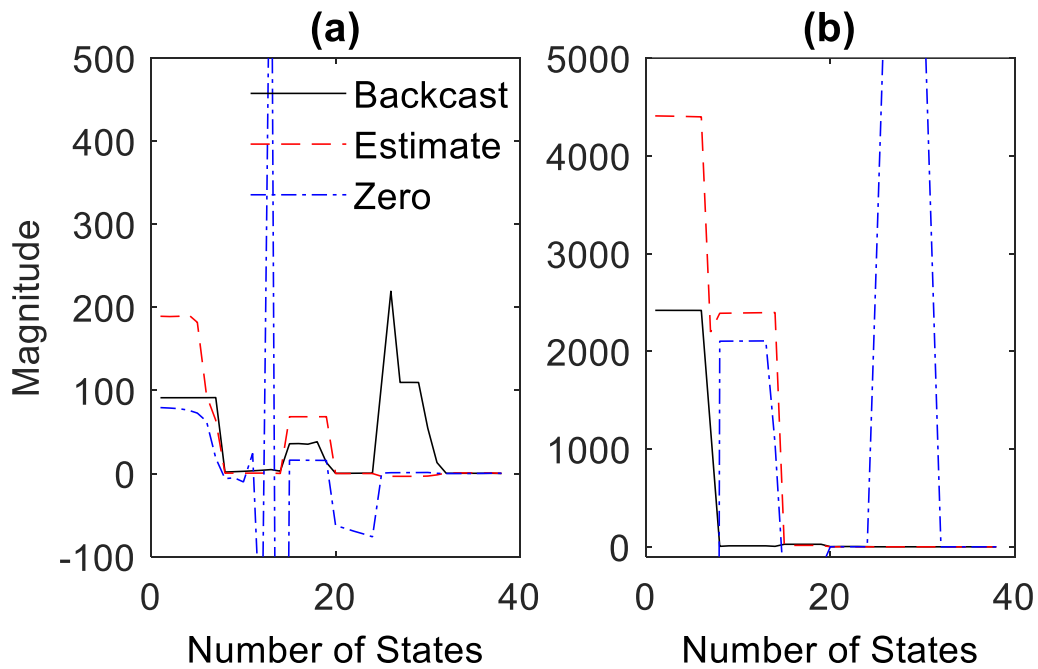


Fig. 7. 5. Initial states: (a) prediction focus; and (b) simulation focus.

Table 7. 4: First Order Optimality for Different Initialization Techniques

Optimization Focus	Estimate	Backcast
Prediction	0.32, 0	0.09, 0
Simulation	$2.27 \times 10^4, 2.9 \times 10^{-3}$	7.49, 1×10^{-4}

7.5.2.1 Noiseless Dataset

At the beginning of each iteration, based on the Gauss-Newton vector computed at the last iteration, an expected improvement in the objective function towards the minima is calculated. If the expected improvement falls below the tolerance value, the iteration converges. To achieve the expected improvement, GN calculates the step size. With larger residuals, iterations start with a larger expected improvement. A larger residual invalidates truncated Hessian approximations, and thus, the algorithm fails to realize the step size accurately. As a result, the expected improvement cannot be achieved, and the algorithm requires more iterations to converge. In extreme cases, the algorithm fails to bring the expected improvement below the tolerance value due to inaccurate step size, and the iteration fails to converge.

In Fig. 7.5, initial states estimated by Backcast using prediction focus are significantly lower than that using simulation focus, so the residuals remain low, and the Hessian approximation remains valid for the prediction focus. GN estimates the step size accurately (Fig. 7.6 (e) and (f)), and meet the expected improvement. As a result, the expected improvement is reduced below the tolerance by 40 and 27 iterations for voltage and frequency models, respectively (Fig. 7.6 (a) and (b)).

On the contrary, higher initial states in Fig. 7.5 (b) estimated by simulation focus makes the residuals significantly higher, which is reflected in the expected improvements in Fig. 7.6 (c) and (d). Consequently, the truncated Hessian approximation becomes invalid, and GN fails to estimate

proper step sizes (α_k^{GN}) to achieve higher expected improvements for most of the iterations (Fig. 7.6 (g) and (h)) in simulation focus. With some bigger step sizes during final iterations in Fig. 7.6 (g), the voltage model with simulation focus manages to converge by 532 iterations. However, due to no such reasonable step sizes (Fig. 7.6 (h)), the frequency model's expected improvements was fixed at 0.1 after 175 iterations and failed to achieve the required tolerance of 0.01. Therefore, to ensure the convergence of the voltage model to the desired level with the simulation focus, the maximum iteration number is set to 600.

Performance matrices of the developed models are shown in Table 7.3 (highlighted in light green). For NRMSE, the data pair represents the fitting performance of the voltage (left) and frequency (right). The fitted models, along with their respective fitting accuracies, are depicted in Fig. 7.7.

The models' residual correlation analysis are shown in Fig. 7.8. Some autocorrelations of simulation focus-based frequency model in Fig. 7.8 (b) go beyond the 99% confidence interval, indicating a considerable correlation in its noise model. Immature termination of optimization for the frequency model causes this correlation, which can be interpreted better by analyzing the first-order optimality of the two models provided in Table 7.4 (highlighted in light green). Models with prediction focus hold the lowest first-order optimality, i.e. their objective functions are very near the minimum during convergence.

To further validate the models, fitting accuracies are re-examined with the validation dataset for noiseless data, as shown in Fig. 7.9. Although the fitting accuracy for both models is similar for both training and validation datasets, in terms of the iteration number, certainty of convergence, and the other performance matrices, the prediction focus model performs better over the simulation focus model.

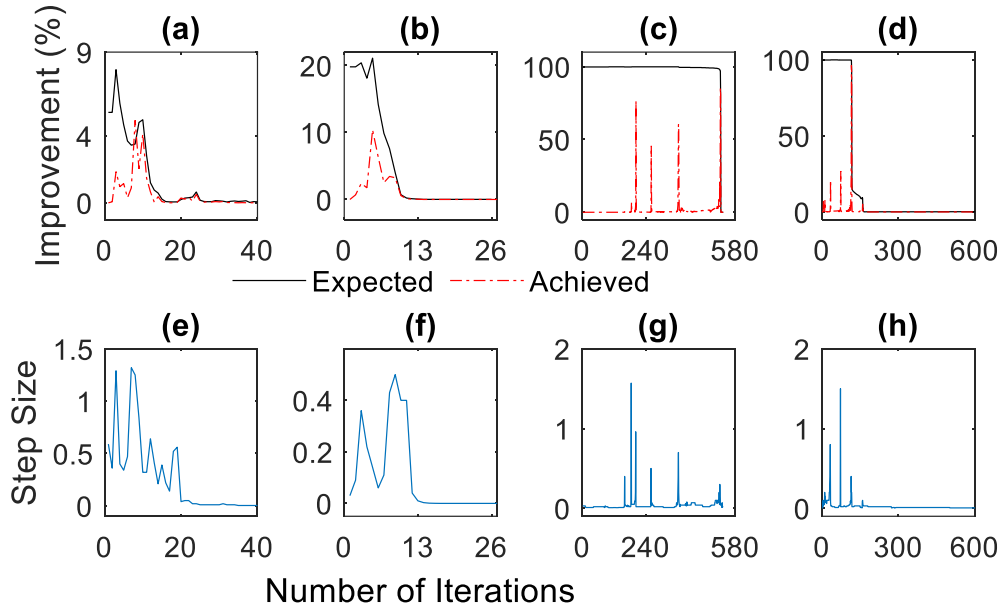


Fig. 7. 6. Iteration wise variation of expected and achieved improvements: (a) DelV (prediction); (b) DelF (prediction); (c) DelV (simulation); (d) DelF (simulation); Iteration wise variation of step sizes: (e) DelV (prediction); (f) DelF (prediction); (g) DelV (simulation); and (h) DelF (simulation)

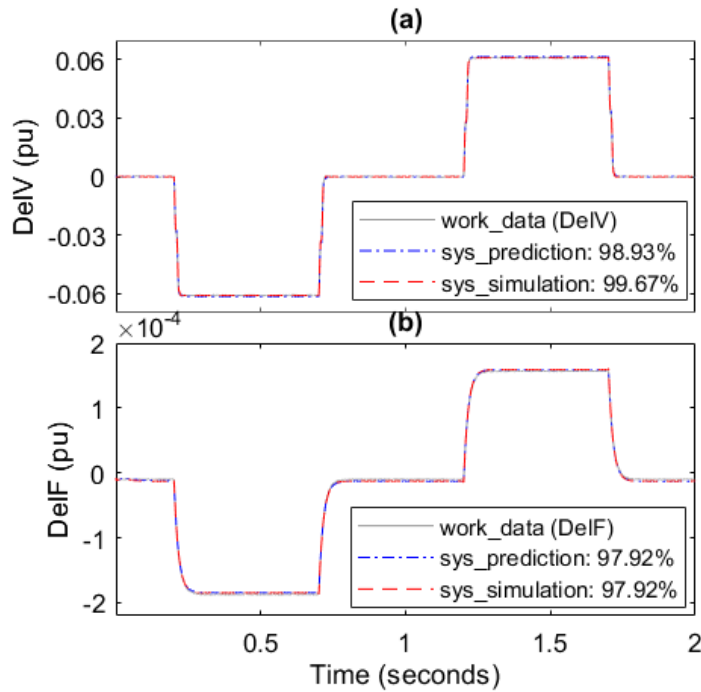


Fig. 7. 7. Fitted models for different optimization focus along with their fitting accuracies for noiseless training data: (a) DelV; (b) DelF.

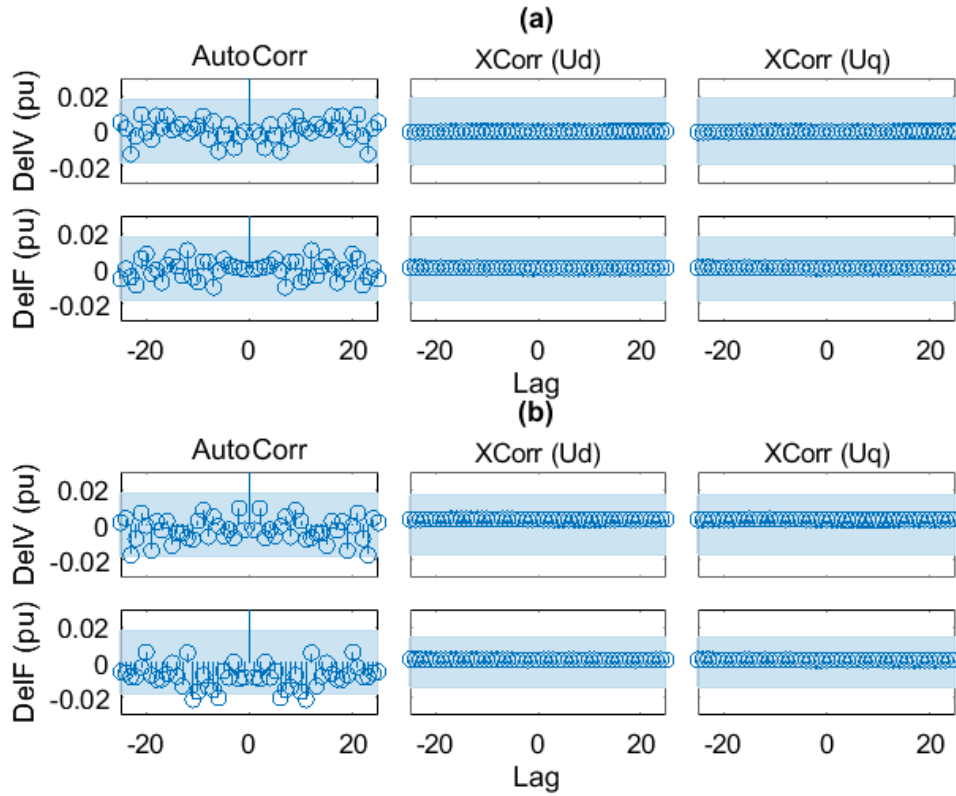


Fig. 7. 8. Auto- and cross-correlation for the two optimization focus: (a) prediction focus; (b) simulation focus.

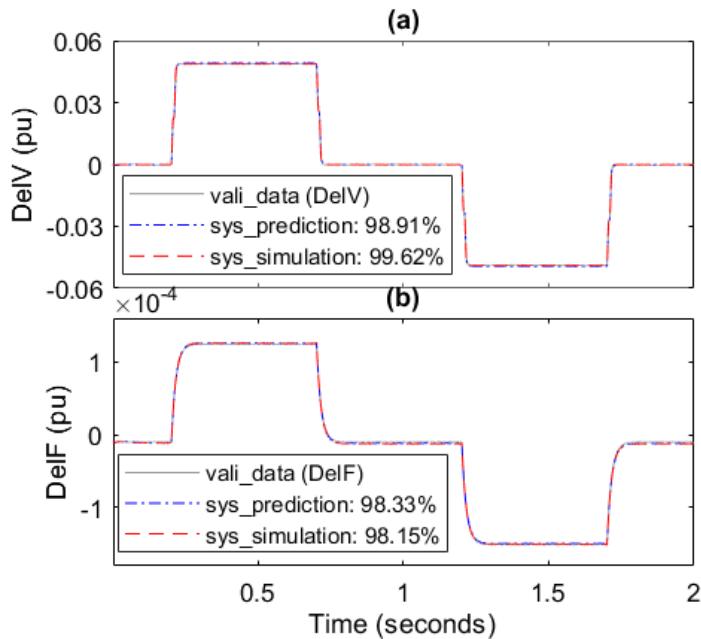


Fig. 7. 9. Fitted models for different optimization focus along with their fitting accuracies for noiseless validation data: (a) DelV; (b) DelF.

7.5.2.2 Noisy Dataset

Real-life data often has noise. To mimic real-life conditions, normally distributed white Gaussian noises shown in Fig. 7.10 are added to the noiseless training dataset. The noise power is 1db; and the signal to noise ratio (SNR) are 33.5 db and 24.14 db for ΔV and ΔF , respectively. In the validation dataset, the SNR for ΔV and ΔF are changed to 31.5 db and 22.2 db, respectively.

The simulation focus takes 271 and 131 iterations for the voltage and frequency models to converge, while the prediction focus takes only 42 and 19 iterations, respectively. Performance matrices of the models are shown in Table 7.5.

Fig. 7.11 shows how precisely the developed models follow the present trend of the noisy data. The residual correlation analyses of the fitted models are shown in Fig.12. Despite higher fitting accuracy, simulation focus-based models hold auto- and cross-correlations beyond the 99% confidence interval, indicating possible data overfitting. This implies that the models have failed to capture the trend of the dataset, which can be verified by the validation dataset. The noise-canceling weighted filter in the objective function helps the prediction focus algorithm distinguish between the noise and the information frequencies. This way, the prediction focus-based model can catch the system's actual trend from a noisy dataset.

To further validate the models' performance, fitting accuracies are re-examined by the validation dataset (Fig. 7.13). Due to the noise canceling weighted filter, the prediction model is developed and tuned to the information frequencies, so changing noise characteristics doesn't affect the model performance. Without such a filter, the simulation model is sensitive to the change of noise characteristics. Therefore, simulation focus models perform poorly to generate a stable response, while the prediction focus models have a stable response with superior accuracies.

Based on the analysis for noisy and noiseless datasets, the prediction focus-based GN algorithm is chosen as the line search algorithm in this study.

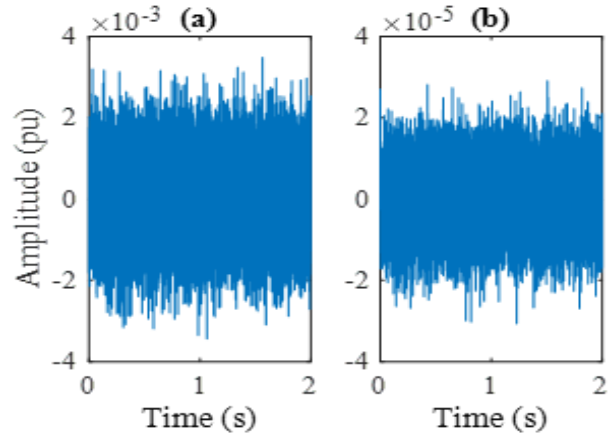


Fig. 7. 10. White Gaussian noise: (a) noise added to the ΔV data; and (b) noise added to the Δf data.

Table 7. 5: The Model’s Performance Matrices for Noisy Dataset

Optimization Focus	FPE	NRMSE	MSE
Prediction	5.12×10^{-17}	0.03, 0.07	9.06×10^{-7}
Simulation	5.55×10^{-17}	0.02, 0.07	8.46×10^{-7}

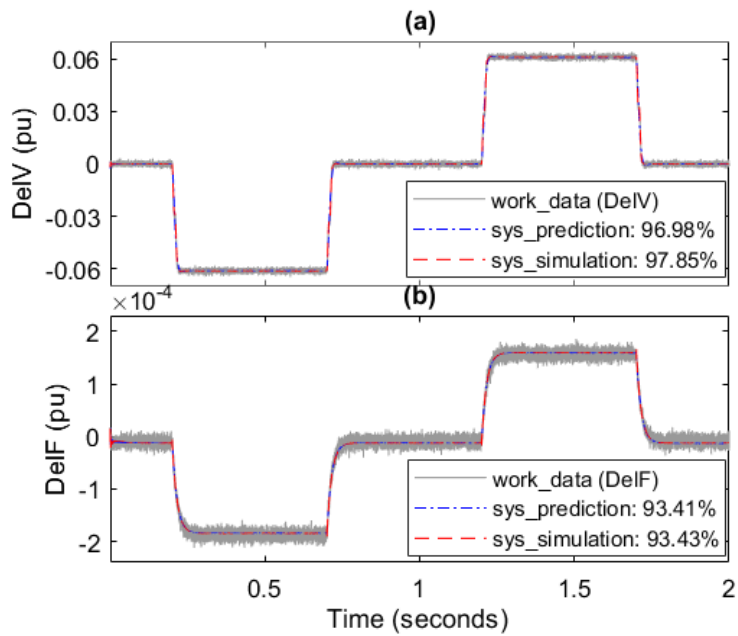


Fig. 7. 11. Fitted models for different optimization focus along with their fitting accuracies for noisy training data: (a) DeIV; (b) DeIF.

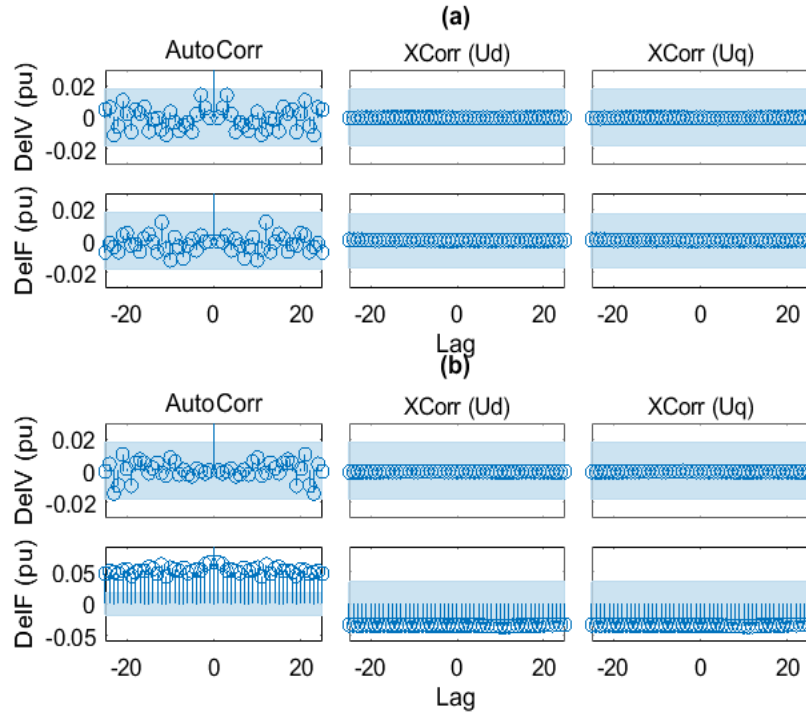


Fig. 7. 12. Auto- and cross-correlation for the two optimization focus: (a) prediction focus; (b) simulation focus.

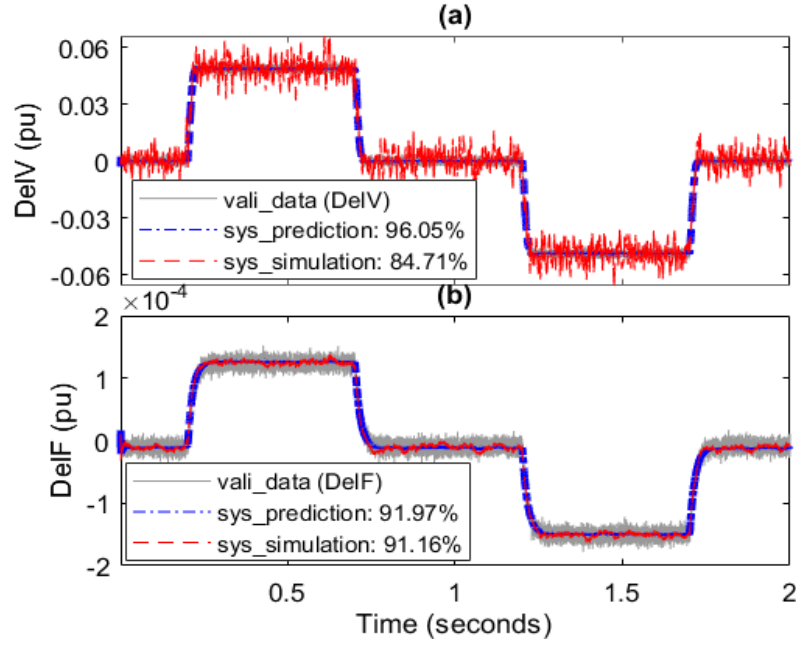


Fig. 7. 13. Fitted models for different optimization focus along with their fitting accuracies for noisy validation data: (a) DeIV; (b) DeIF.

7.6 The Final GN-Based Box-Jenkins Model

The final prediction focus-based Box-Jenkins model expressed in (18) is developed for the test system, and its coefficients A, B, C, D, and F are obtained as follows:

$$A = \begin{bmatrix} 1 & 0 \\ 0 & 1 \end{bmatrix} \quad (28)$$

$$B = \begin{bmatrix} (0, 0.1189, 0.0682, 0.0932) & (0, -0.967) \\ (0, 0, 0, 5.26 \times 10^{-6}, 7.95 \times 10^{-5}, -7.59 \times 10^{-5}) & (0, 0, 0, -0.0013) \end{bmatrix} \quad (29)$$

$$C = \begin{bmatrix} (1, -0.198, -0.456, -0.479, -0.618, 0.664, 0.174) \\ (1, -0.364, -1.009, -0.149, 0.662, 0.096, -0.182) \end{bmatrix} \quad (30)$$

$$D = \begin{bmatrix} (1, -0.313, -0.547, -0.495, -0.581, 0.777, 0.185, -0.017) \\ (1, -0.421, -1.047, -0.14, 0.692, 0.092, -0.179, 0.003) \end{bmatrix} \quad (31)$$

$$F = \begin{bmatrix} (F_{11}) & (F_{12}) \\ (F_{21}) & (F_{22}) \end{bmatrix} \quad (32)$$

$$F_{11} = [1, -0.49, -0.355, 0.047, 0.286, -0.181, -0.557, 0.291]$$

$$F_{12} = [1, -1.599, 0.589, 0.713, -1.025, 0.335]$$

$$F_{21} = [1, -0.702, 0.075, -0.865, 0.115, 0.288, -0.014, 0.112]$$

$$F_{22} = [1, -0.051, 0.422, -0.699, -0.157, -0.476]$$

The step response within the 3rd standard deviation is plotted in Fig. 7.14. The shorter span of the step response within the 3rd standard deviation indicates a minimal covariance in the model parameters. Fig. 7.15 depicts the prediction accuracies and prediction errors.

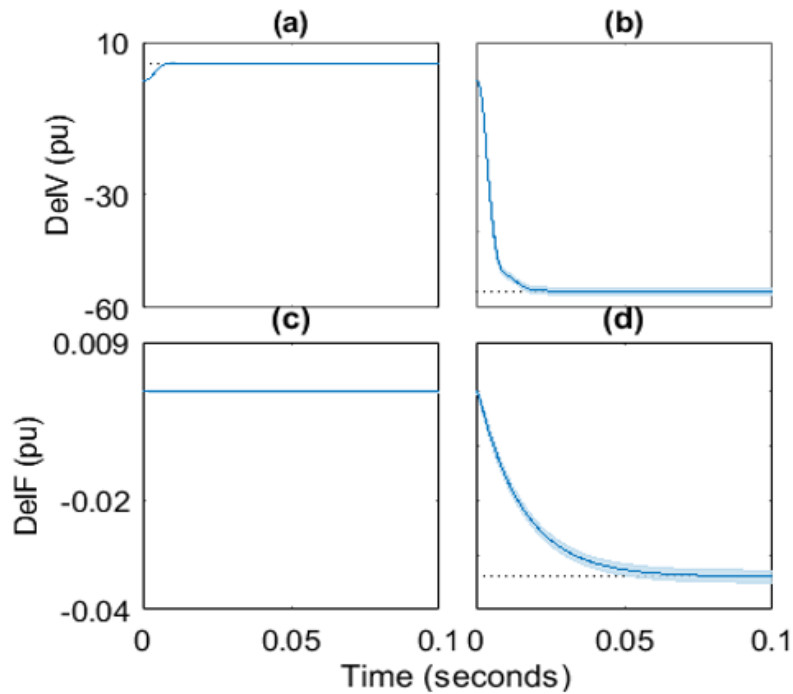


Fig. 7. 14. Step responses of the model along with their 3rd confidence bound: (a) U_d vs DeIV; (b) U_q vs DeIV; (c) U_d vs DeIF; and (d) U_q vs DeIF.

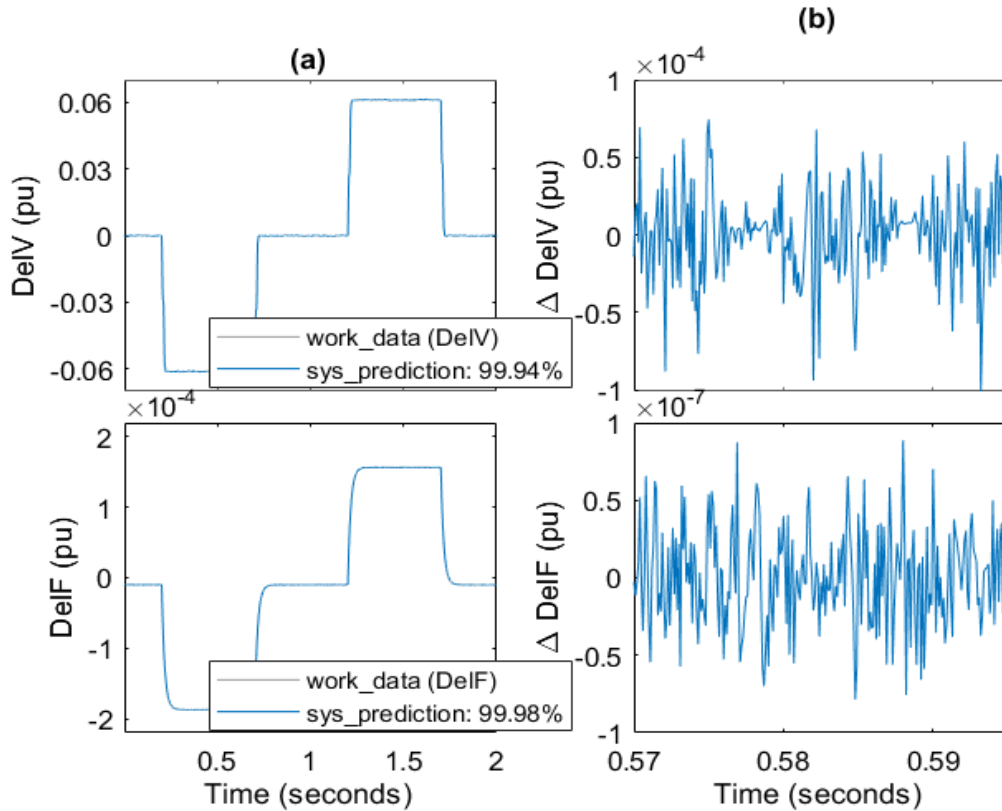


Fig. 7. 15. One-step ahead prediction: (a) prediction fitting; (b) prediction error

7.7 Conclusion

In this paper, a novel data-driven Box-Jenkins predictive model for DG control in an islanded microgrid is proposed to regulate voltage and frequency at the PCC. It formulates the relationship between (deviations of the voltage and frequency at PCC) and (deviations of d- and q-axis components of the control signal). Both resistance and reactance of distribution lines are considered in the model. The model is parameterized through nonlinear least-square optimization using Gauss-Newton method, where the Backcast initialization technique is chosen, and two estimation methods (“prediction” focus and “simulation” focus) are compared. The prediction focus has built-in weighted filters and deals with noisy data more efficiently; while the simulation focus generates large errors and has poor convergence. Therefore, the prediction focus is recommended to develop the proposed model.

References:

- [1] B. Liu, Z. Liu, J. Liu, R. An, H. Zheng, and Y. Shi, "An Adaptive Virtual Impedance Control Scheme Based on Small-AC-Signal Injection for Unbalanced and Harmonic Power Sharing in Islanded Microgrids," *IEEE Trans. Power Electron.*, vol. 34, no. 12, pp. 12333–12355, Dec. 2019, doi: 10.1109/TPEL.2019.2905588.
- [2] S. d J. M. Machado, S. A. O. da Silva, J. R. B. d A. Monteiro, and A. A. de Oliveira, "Network Modeling Influence on Small-Signal Reduced-Order Models of Inverter-Based AC Microgrids Considering Virtual Impedance," *IEEE Trans. Smart Grid*, vol. 12, no. 1, pp. 79–92, Jan. 2021, doi: 10.1109/TSG.2020.3012475.
- [3] R. An, Z. Liu, and J. Liu, "Successive-Approximation-Based Virtual Impedance Tuning Method for Accurate Reactive Power Sharing in Islanded Microgrids," *IEEE Trans. Power Electron.*, vol. 36, no. 1, pp. 87–102, Jan. 2021, doi: 10.1109/TPEL.2020.3001037.
- [4] J. Chen, D. Yue, C. Dou, L. Chen, S. Weng, and Y. Li, "A Virtual Complex Impedance Based $P-V$ Droop Method for Parallel-Connected Inverters in Low-Voltage AC Microgrids," *IEEE Trans. Ind. Inform.*, vol. 17, no. 3, pp. 1763–1773, Mar. 2021, doi: 10.1109/TII.2020.2997054.
- [5] X. Liang, C. Andalib-Bin-Karim, W. Li, M. Mitolo, and M. N. S. K. Shabbir, "Adaptive Virtual Impedance-Based Reactive Power Sharing in Virtual Synchronous Generator Controlled Microgrids," *IEEE Trans. Ind. Appl.*, vol. 57, no. 1, pp. 46–60, Jan. 2021, doi: 10.1109/TIA.2020.3039223.
- [6] L. Wang, Y. Qin, Z. Tang, and P. Zhang, "Software-Defined Microgrid Control: The Genesis of Decoupled Cyber-Physical Microgrids," *IEEE Open Access J. Power Energy*, vol. 7, pp. 173–182, 2020, doi: 10.1109/OAJPE.2020.2997665.

- [7] S. M. Zali and J. V. Milanović, “Generic Model of Active Distribution Network for Large Power System Stability Studies,” *IEEE Trans. Power Syst.*, vol. 28, no. 3, pp. 3126–3133, Aug. 2013, doi: 10.1109/TPWRS.2012.2233223.
- [8] J. V. Milanović and S. M. Zali, “Validation of Equivalent Dynamic Model of Active Distribution Network Cell,” *IEEE Trans. Power Syst.*, vol. 28, no. 3, pp. 2101–2110, Aug. 2013, doi: 10.1109/TPWRS.2012.2227844.
- [9] P. N. Papadopoulos, T. A. Papadopoulos, P. Crolla, A. J. Roscoe, G. K. Papagiannis, and G. M. Burt, “Black-box dynamic equivalent model for microgrids using measurement data,” *IET Gener. Transm. Distrib.*, vol. 8, no. 5, pp. 851–861, May 2014, doi: 10.1049/iet-gtd.2013.0524.
- [10] P. N. Papadopoulos, T. A. Papadopoulos, P. Crolla, A. J. Roscoe, G. K. Papagiannis, and G. M. Burt, “Measurement-based analysis of the dynamic performance of microgrids using system identification techniques,” *IET Gener. Transm. Distrib.*, vol. 9, no. 1, pp. 90–103, 2015, doi: 10.1049/iet-gtd.2014.0555.
- [11] B. Zaker, G. B. Gharehpetian, and M. Karrari, “A Novel Measurement-Based Dynamic Equivalent Model of Grid-Connected Microgrids,” *IEEE Trans. Ind. Inform.*, vol. 15, no. 4, pp. 2032–2043, Apr. 2019, doi: 10.1109/TII.2018.2856852.
- [12] S. A. R. Konakalla, A. Valibeygi, and R. A. de Callafon, “Microgrid Dynamic Modeling and Islanding Control With Synchrophasor Data,” *IEEE Trans. Smart Grid*, vol. 11, no. 1, pp. 905–915, Jan. 2020, doi: 10.1109/TSG.2019.2948815.
- [13] S. Gratton, A. S. Lawless, and N. K. Nichols, “Approximate Gauss–Newton Methods for Nonlinear Least Squares Problems,” *SIAM J. Optim.*, vol. 18, no. 1, pp. 106–132, Jan. 2007, doi: 10.1137/050624935.

- [14] P. E. Gill and W. Murray, “Algorithms for the solution of the nonlinear least-squares problem,” *SIAM J. Numer. Anal.*, vol. 15, no. 5, pp. 977–992, 1978.
- [15] M. Verhaegen and V. Verdult, *Filtering and system identification: a least squares approach*. Cambridge university press, 2007.
- [16] A. Breinholt, J. K. Møller, H. Madsen, and P. S. Mikkelsen, “A formal statistical approach to representing uncertainty in rainfall–runoff modelling with focus on residual analysis and probabilistic output evaluation – Distinguishing simulation and prediction,” *J. Hydrol.*, vol. 472–473, pp. 36–52, Nov. 2012, doi: 10.1016/j.jhydrol.2012.09.014.
- [17] “Loss Function and Model Quality Metrics - MATLAB & Simulink.” <https://www.mathworks.com/help/ident/ug/model-quality-metrics.html> (accessed Mar. 12, 2021).
- [18] F. Chen, H. Garnier, M. Gilson, J. Agüero, and T. Liu, “Refined instrumental variable parameter estimation of continuous-time Box–Jenkins models from irregularly sampled data,” *IET Control Theory Appl.*, vol. 11, no. 2, pp. 291–300, 2017.
- [19] C. N. L. Eu, “Numerical Analysis in Nonlinear Least Squares Methods and Applications,” PhD Thesis, Curtin University, 2017.
- [20] M. Niedźwiecki and M. Ciołek, “On Noncausal Identification of Nonstationary Multivariate Autoregressive Processes,” *IEEE Trans. Signal Process.*, vol. 67, no. 3, pp. 769–782, Feb. 2019, doi: 10.1109/TSP.2018.2885480.
- [21] “What Is Residual Analysis? - MATLAB & Simulink.” <https://www.mathworks.com/help/ident/ug/what-is-residual-analysis.html> (accessed Mar. 07, 2021).

[22] “Option set for bj - MATLAB bjOptions.”

<https://www.mathworks.com/help/ident/ref/bjoptions.html> (accessed Nov. 15, 2020).

Chapter 8

A Novel Design of Model Predictive Control-Based Distributed Generation Controller in Islanded Microgrids

Md Nasmus Sakib Khan Shabbir¹, *Student Member*, IEEE, Xiaodong Liang², *Senior Member*, IEEE, Weixing Li³, *Senior Member*, IEEE, and Syed Imtiaz⁴

¹Department of Electrical and Computer Engineering, Memorial University of Newfoundland, St. John's, Newfoundland, Canada.

²Department of Electrical and Computer Engineering, University of Saskatchewan, Saskatoon, Saskatchewan, Canada.

³Department of Electrical Engineering, Harbin Institute of Technology, Harbin, Hilongjiang, China.

⁴Department of Process Engineering, Memorial University of Newfoundland, St. John's, Newfoundland, Canada.

A version of this chapter is to be submitted to a journal. Md Nasmus Sakib Khan Shabbir co-authored the paper under the supervision of Dr. Xiaodong Liang. Sakib's contributions in this paper are listed as follows:

- Performed literature review for distributed generation controller in islanded microgrid.
- Developed the model predictive controller based distributed generation controller in islanded microgrid.
- Performed simulation analysis, examined results and reported findings.
- Involved in writing the paper draft as the first author.

Dr. Xiaodong Liang provided continuous technical guidance, checked the results, reviewed the manuscript, provided suggestions to accomplish the work, and modified the final version of the manuscript. Dr. Weixing Li modified the manuscript. Dr. Syed Imtiaz reviewed the manuscript and provided suggestions.

In this chapter, the manuscript is presented with altered figure numbers, table numbers and reference formats in order to maintain the thesis formatting guidelines set out by the Memorial University of Newfoundland.

Abstract- To regulate the voltage and frequency at the Point of Common Coupling (PCC) in an islanded microgrid, a novel model predictive control (MPC)-based distributed generation (DG) controller is proposed in this paper. A data-driven predictive model that directly correlates deviations of the voltage and frequency at the PCC with direct- and quadrature-axis components of the control signal is used as MPC's plant model. This predictive model is developed using Gauss-Newton-based non-linear least-square approach with the prediction optimization focus. The proposed MPC controller operates on the PCC data and does not require microgrid's central controllers or DG-to-DG communication networks. It can effectively compensate voltage and frequency deviations at the PCC and ensure proportional power sharing among DGs without a secondary controller and a virtual impedance loop. The integrated Kalman filter in the MPC structure makes the controller robust to impedance variations and measurement noises. Effectiveness and robustness of the proposed MPC controller are validated through case studies and the robustness analysis.

Keywords- Distributed generation, islanded microgrid, Kalman filter, model predictive control (MPC).

8.1 Introduction

Microgrid serves as a fundamental unit for smart grids containing distributed generation (DG) units and load. Microgrid can operate in grid-connected or island mode. Island mode is most challenging as DGs are responsible to maintain the system stability, voltage and frequency profile.

To coordinate the power dispatched among DGs, droop control is mostly adopted by mimicking steady-state characteristics of synchronous generators and compensates voltage and frequency deviations by dispatching necessary active and reactive power through updating control signal references for the voltage regulator [1] or the current regulator [2] in the control scheme. To realize control signal references, depending on the assumption of highly inductive or resistive distribution lines, droop control incorporates either P-f/Q-V [3] or P-V/Q-f [4],[5] control by ignoring line resistance or line inductance, respectively. Droop control has its inherent limitations, such as steady-state errors in voltage and frequency, and disproportional reactive power sharing among DGs. To overcome the limitations, the secondary controller and virtual impedance technique have been integrated into droop control.

Secondary controllers adjust the controller references so that additional power necessary for compensating steady-state errors are dispatched while ensuring active power sharing among DGs. Secondary controllers in droop-controlled microgrid can be categorized as centralized, distributed, and decentralized control schemes [6]. In centralized control, a microgrid central controller (MGCC) is required, that collects information from the point of common couplings (PCC) and distribute commands among DGs' local controllers via a communication network. Despite superior compensation of steady-state errors, the reliance on MGCC and one to all communication structure makes the centralized control less reliable and costly [6]. Distributed control, on the other

hand, doesn't require MGCC, but its mandatory DG-to-DG communication's latency and accidental cut-off can initiate contingency [7]. Decentralized control doesn't require DG-to-DG communication, but an intra-DG communication might be required. Decentralized secondary control (SC) can be categorized as proportional regulator-based (P-SC), proportional-integral regulator-based (PI-SC), and a switched secondary control which is a combination of P-SC and PI-SC [6]. Despite relaxing the necessity of communication system, decentralized methods have limitations: P-SC cannot fully compensate the steady-state errors [8]; although PI-SC completely compensates steady-state errors, it deteriorates active power sharing; and the switched secondary control has the risk of switching failure, which can deteriorate the microgrid's stability [6].

Virtual impedance determines controller references according to impedance mismatch and ensures accurate reactive power sharing. This technique adopts virtual resistance [9], virtual inductance [10] or combination of both [11]. Accurate realization of virtual impedance is a very complex process and requires low bandwidth DG-to-DG communication in most cases [11]. In addition, improper and unbounded virtual impedance may violate bus voltage limits although reactive power sharing is ensured [12].

Therefore, the secondary controller and virtual impedance technique in droop control substantially increase the controller size and complexity. A simple and effective approach that can accurately realize the control reference based on critical system parameters is urgently needed.

To solve this problem, in this paper, a novel model predictive control (MPC)-based DG controller is proposed and designed for islanded microgrids to regulate the voltage and frequency at the PCC. This MPC controller does not require complex secondary controllers and virtual impedance loops, which can significantly reduce the cost and complexity of the controller. The proposed MPC controller uses a data-driven predictive model developed from system

identification as MPC's plant model, where deviations of the PCC's voltage and frequency from the nominal values (controlled variables) are directly correlated with direct(d)- and quadrature(q)-axis components (U_d and U_q) of the control signal (control variables). Instead of ignoring line resistance or line inductance as in droop control, the proposed MPC's plant model considers the presence of both resistance and reactance of distribution lines and enables simultaneous P-f/Q-V and P-V/Q-f control. The model is developed using Gauss-Newton (GN) based non-linear least-square approach with the prediction optimization focus. To ensure better control over the system and noise model, Box-Jenkins structure is adopted for the model [13].

Model predictive controller has been traditionally used in industrial process control. Recent advancement of parallel computing in CPU and GPU arena resolves constraints due to computational requirements of the MPC, as a result, MPC gains interest in airlines, automotive and power systems, where fast responses are required. In microgrids, MPC is mostly used for load forecasting [14], [15] and energy management [16], [17]. In [18], MPC is implemented at a secondary controller to realize secondary voltage control by incorporating forecasted behaviors of local and neighboring DGs; MPC regulates the secondary voltage and frequency in [19]; and MPC reduces eddy current losses in the inner control loop in [20].

In this paper, a reference is set for each controlled parameter for the proposed MPC-based DG controller; when deviations from a reference occur, MPC reads the polarity and depth of such deviations, solves the system model to achieve an optimum trajectory of control signals to get the controlled parameters back to their reference values. This way, the proposed approach completely compensates any deviations by accurately updating the reference for U_d and U_q , which indirectly ensures the dispatch of necessary power. MPC's predictive competency ensures the controller's

redundancy, which boosts up the microgrid stability. Each MPC-based DG controller responds using the respective PCC data, so no MGCC or DG-to-DG communication network is necessary.

The main contributions of this paper include: 1) a novel model predictive control-based DG controller is developed using a data-driven predictive model from system identification, directly correlating the deviation of voltage and frequency with the direct(d)- and quadrature (q)-axis components of the DG control signal; 2) the proposed controller can achieve simultaneous P-f/Q-V and P-V/Q-f control, and the secondary controller is not needed; and 3) the proposed controller can update the control signal reference according to the line voltage drop, and thus, the virtual impedance loop is not needed.

The paper is arranged as follows: the proposed approach is introduced in Section 8.2; the fundamental theory is explained in Section 8.3; the data-driven predictive model is presented in Section 8.4; the proposed model predictive control-based DG controller is developed in Section 8.5; the proposed controller is validated through case and sensitivity studies in Sections 8.6 and 8.7; and conclusions are drawn in Section 8.8.

8.2 The Proposed Approach

The mathematical formulation for the proposed control system and the stepwise development of the proposed MPC-based DG controller is described in this section.

8.2.1 Mathematical Formulation for Proposed Control System

For a microgrid depicted in Fig. 8.1, the generated active and reactive power at the point S can be expressed as follows:

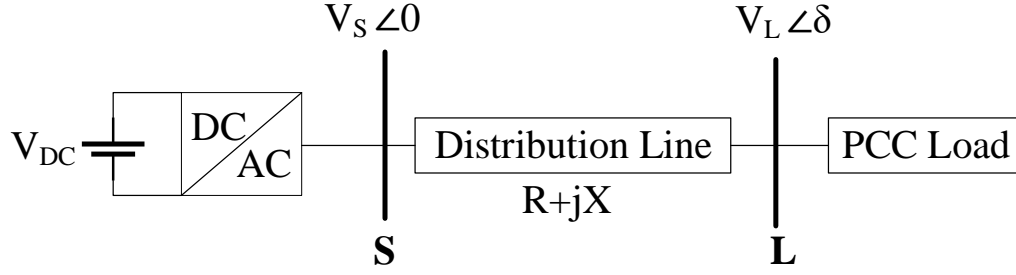


Fig. 8. 1. A microgrid with an interfaced inverter system.

$$P = \frac{V_s}{R^2 + X^2} [R(V_s - V_L \cos \delta) + XV_L \sin \delta] \quad (1)$$

$$Q = \frac{V_s}{R^2 + X^2} [X(V_s - V_L \cos \delta) - RV_L \sin \delta] \quad (2)$$

Assuming a very small power angle, δ , (1) and (2) can be rewritten by

$$\delta = \frac{1}{V_s V_L} (XP - RQ) \quad (3)$$

$$V_s - V_L = \frac{1}{V_s} (XQ + RP) \quad (4)$$

The system frequency f is dynamically controlled by the power angle, δ , therefore, droop equations resulted from (3) and (4) including both resistance and reactance of distribution lines can be expressed by

$$f - f_0 = -k_{p1}(P - P_0) + k_{p2}(Q - Q_0) \quad (5)$$

$$V_s - V_{s0} = -k_{q1}(Q - Q_0) - k_{q2}(P - P_0) \quad (6)$$

Eqs. (5) and (6) indicate that the control algorithm enables a simultaneous P-f/Q-V and P-V/Q-f control due to consideration of both line resistance and line reactance. Therefore, active and reactive power can be expressed by

$$P = \frac{3}{2} (U_d I_d + U_q I_q) \quad (7.1)$$

$$Q = \frac{3}{2}(-U_d I_q + U_q I_d) \quad (7.2)$$

where subscript d and q represent the d- and q-axis components of the respective parameters. Eqs. (7.1) and (7.2) transform (3) and (4) into the following form:

$$\delta = \frac{3}{2} \frac{1}{V_s V_L} [(X I_d + R I_q) U_d + (X I_q - R I_d) U_q] \quad (8)$$

$$V_s - V_L = \frac{3}{2} \frac{1}{V_s} [(R I_d - X I_q) U_d + (R I_q + X I_d) U_q] \quad (9)$$

For simplicity, it is assumed that variations of U_d and U_q do not change I_d and I_q , therefore, the control formula developed in (8) and (9) can be expressed as follows:

$$f - f_0 = \frac{3}{2} \frac{1}{V_s V_L} [(X I_d + R I_q)(U_d - U_{d0}) + (X I_q - R I_d)(U_q - U_{q0})] \quad (10)$$

$$V_L - V_{L0} = \frac{3}{2} \frac{1}{V_s} [(R I_d - X I_q)(U_d - U_{d0}) + (R I_q + X I_d)(U_q - U_{q0})] \quad (11)$$

where f and V_L are reference voltage and frequency, and f_0 and V_{L0} are nominal voltage and frequency, respectively. U_d and U_q are the reference of the respective parameters at f and V_L , and U_{d0} and U_{q0} are the pre-disturbance reference of the respective parameters.

The major challenge to implement the formulas is the required resistance and reactance values of distribution lines, which is often impractical to obtain in real-life. As a remedy, a data-driven system identification approach is adopted, and Eqs. (10) and (11) are re-formulated by

$$\Delta f = k_1 \Delta U_d + k_2 \Delta U_q \quad (12)$$

$$\Delta V = k_3 \Delta U_d + k_4 \Delta U_q \quad (13)$$

where coefficients k_1 to k_4 are derived through data-driven system identification approach.

The impacts of distribution line parameters on voltage and frequency due to variations of U_d and U_q are embedded in (12) and (13), so the control algorithm can response accordingly and does not require a virtual impedance loop. In addition, it can be inferred from (12) and (13) that the compensation of the voltage and frequency can be expressed as a function of ΔU_d and ΔU_q . Based on (5), (6), (12) and (13), a complete compensation of voltage and frequency by directly regulating U_d and U_q ensures necessary adjustments of power flow ($(P - P_0)$ and $(Q - Q_0)$). This way, $(P - P_0)$ and $(Q - Q_0)$ are proportionally correlated with ΔV and Δf through ΔU_d and ΔU_q . In a multi-DG scenario, the net deviation can be distributed among DGs according to their nameplate ratings, which will ensure proportional power sharing among them. The control algorithm becomes

$$\sum_{i=1}^{N_{DG}} k_{s,i} \Delta f = \sum_{i=1}^{N_{DG}} (k_{1,i} \Delta U_{d,i} + k_{2,i} \Delta U_{q,i}) \quad (14)$$

$$\sum_{i=1}^{N_{DG}} k_{s,i} \Delta V = \sum_{i=1}^{N_{DG}} (k_{3,i} \Delta U_{d,i} + k_{4,i} \Delta U_{q,i}) \quad (15)$$

where $k_{s,i}$ is the sharing factor of the i^{th} DG, and N_{DG} is the total number of DGs. $k_{s,i}$ is determined according to the nameplate rating of the respective DG. This way, the overall required compensation is distributed among DGs according to their capacity, and DGs then dispatch power accordingly.

8.2.2 Stepwise Evolution of the Proposed Controller

Before describing the stepwise development of the proposed controller, we describe a few terminologies of MPC:

- **Controlled variable (CV):** CVs are the measured variables that the MPC controls at the desired set point to achieve the controller's objectives. In this controller, Δf and ΔV at the PCC are two CVs.

- Manipulated variable (MV). MVs are the controller outputs that MPC adjusts to force CVs to follow the references. In this controller, U_d and U_q are MVs.
- Plant Model: It is a mathematical model correlating MVs and CVs of the system.

The proposed controller is developed in the following 8 steps, as shown in the flowchart in Fig. 8.2:

Step 1: *Offline system identification model.* To develop the model expressed in (12) and (13), d- and q-axis components (U_d and U_q) of the control signal are varied over a narrow region so that the system dynamics are influenced without initiating the non-linearity, and the corresponding deviations of the PCC's voltage and frequency are recorded. The input-output parameters and points of data acquisition are marked in red in Fig. 8.3. The details about the collected input-output data for the system identification are provided in Section IV. The model is developed using Gauss-Newton-based nonlinear least-square method with the prediction optimization focus.

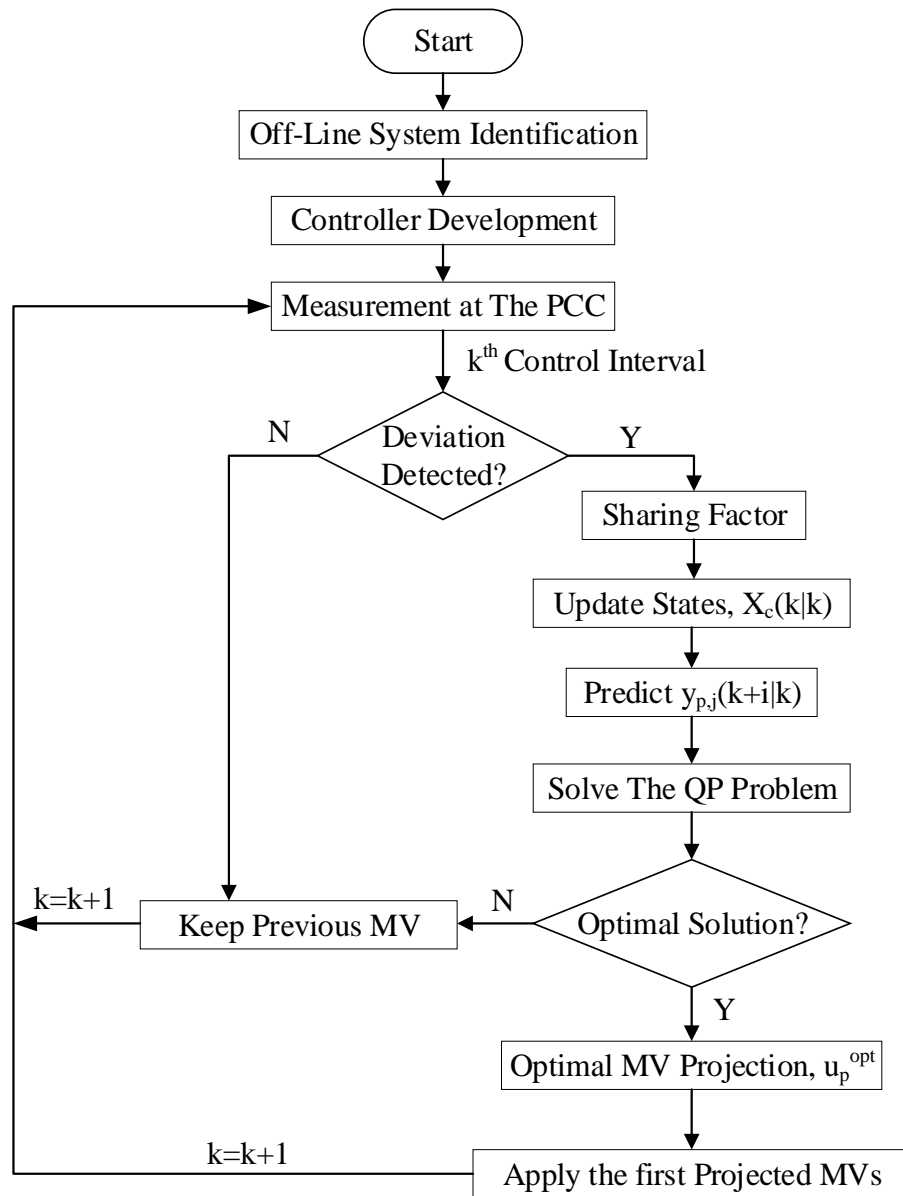


Fig. 8. 2. Flow chart of the proposed controller design.

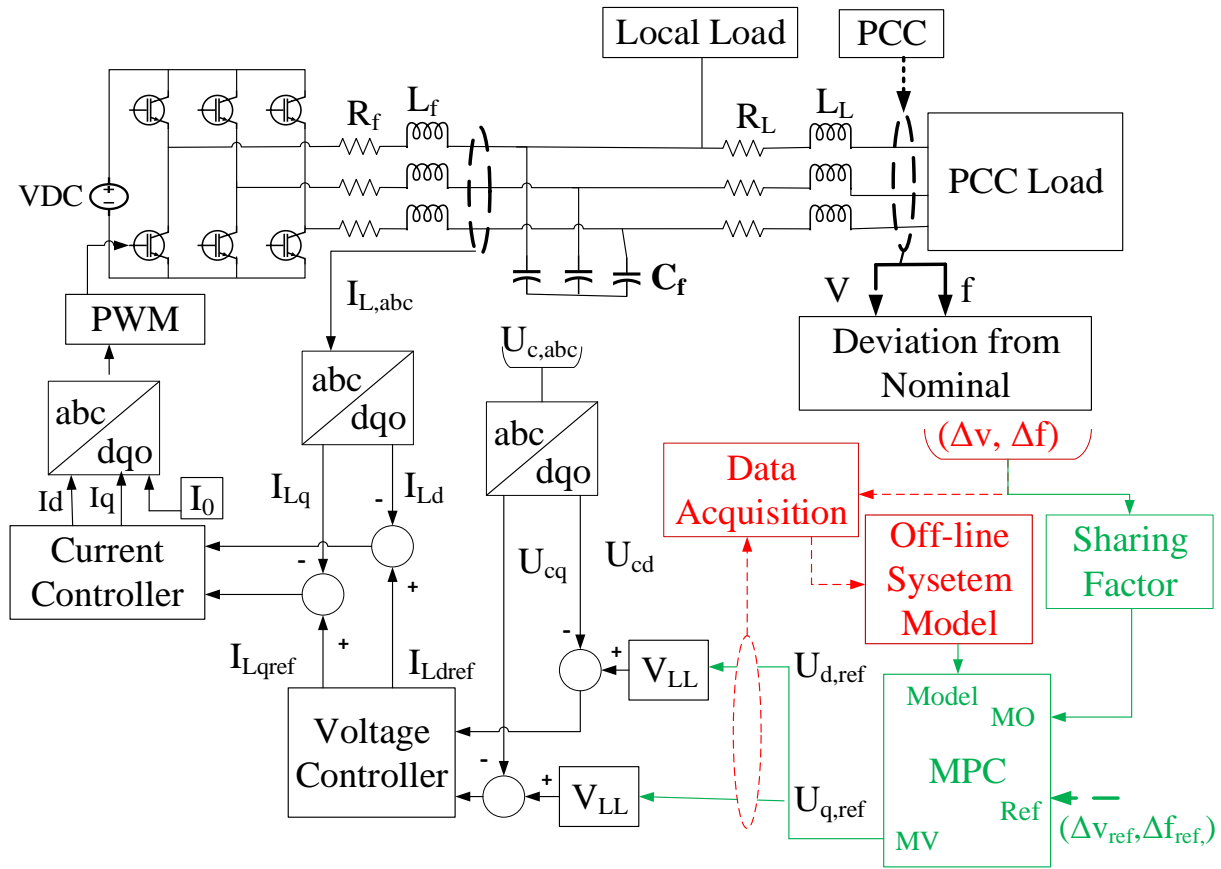


Fig. 8. 3. Schematic diagram of the test system simulation model.

Step 2: MPC-based DG controller. Using the developed system identification model in Step 1 as a plant model, the MPC-based DG controller is developed. The schematic diagram of the proposed control approach is given in Fig. 8.3. Details about the controller developments are provided in Section V. Both ΔV_{ref} and Δf_{ref} in Fig. 8.3 are set to “zero”, which means the controller maintains the voltage and frequency at their nominal values.

Step 3: Detection of deviations. At every control interval, MPC reads the deviations of the voltage and frequency from their nominal values at the PCC. If no deviations are detected, MPC continues with the MVs applied in the previous control interval.

Step 4: *Sharing the overall compensation.* If a deviation is detected, DGs assess their respective portion from the overall required compensation using the sharing factor (k_s). k_s is determined according to the nameplate rating of DGs to ensure proportional power sharing among the DGs.

Step 5: *Updating the current states.* After deciding the required contribution, each individual DG updates current states of the plant using a steady-state Kalman filter-based state observer.

Step 6: *Prediction of the future plant response.* With the past trajectory of the MVs up to current time and current states, MPC predicts the plant outputs up to the prediction horizon.

Step 7: *Solve the quadratic programming (QP) Problem.* With the predicted states and outputs, MPC solve the QP problem using KWIK algorithm based Active-set QP solver. The solution predicts the optimal trajectory of the MVs that will bring the voltage and frequency back to their respective nominal values. If the solver detects infeasibility or reach to the maximum iteration limit before converging to the optimal trajectory, MPC adopts the optimal trajectory from the previous control interval.

Step 8: *Apply the first projected MVs.* Although MPC projects the optimal MVs trajectory up to the prediction horizon, only the first projected MVs movement is applied in the immediate next control interval.

The process keeps cycling from Steps 3 to 8 until the deviation is compensated. When compensated, MPC continues with the MVs applied in the previous control interval until a new deviation is detected.

8.3 Fundamental Theory

The theories used to develop the system identification model and MPC controller are stated in this section.

8.3.1 System Identification

8.3.1.1 Box-Jenkins model

A Box-Jenkins (BJ) model is a polynomial mathematical model that provides the flexibility of independent parameterization of a system's dynamics and associated noises using rational polynomial functions [13]. The general expression of the Box-Jenkins model with nu inputs and ny outputs is

$$\sum_{i=1}^{nu} \sum_{j=1}^{ny} A_{ij}(q) y_j(t) = \sum_{i=1}^{nu} \sum_{j=1}^{ny} \frac{B_{ij}(q)}{F_{ij}(q)} u_i(t - nk_{ij}) + \sum_{j=1}^{ny} \frac{C_j(q)}{D_j(q)} e_t(t) \quad (16)$$

Where A, B, C, D, and F are polynomial coefficients; q is the time shift operator; $u(t)$ and $y(t)$ are the input and the output, respectively; nk_{ij} is the transport delay in between the i^{th} input and j^{th} ; and $e_t(t)$ is the noise. C and D are related to the noise and can be modeled independently, regardless of B and F. A, B, F, and K are $ny \times nu$ matrices; C and D are $ny \times 1$ matrices. The number of coefficients in the denominator in (1) represents the pole number, and the numerator polynomials are one unit more than the number of zeros. A, B, C, D, and F can be obtained by the nonlinear least-square approach.

8.3.1.2 The Gauss-Newton method

GN is a line search-based quasi newton approach. For a search direction of p_k^{GN} and step size of α_k^{GN} , the iterative equation of GN can be expressed by [21]

$$\theta_{k+1} = \theta_k + \alpha_k p_k^{GN} \quad (17)$$

GN approximates the objective function's Hessian matrix to its truncated form of $J(\theta_k)^T J(\theta_k)$, and the search direction p_k^{GN} is given by

$$[J(\theta_k)^T J(\theta_k)] p_k^{GN} = -J(\theta_k)^T r(\theta_k) \quad (18)$$

Where, $J \in \mathbb{R}^{m \times n}$ is the Jacobian of $r(\theta)$.

8.3.1.3 The objective function

In system identification, model parameters are estimated by minimizing the objective function, which is a weighted sum of squares of the residuals expressed as follows.

$$V(\theta) = \frac{1}{N} \sum_{t=1}^N r^T(t, \theta) W(\theta) r(t, \theta) \quad (19)$$

Where N is the number of data samples, and $W(\theta)$ is a weighted semi-definite matrix of the vector parameter θ .

The focus of the parametric optimization is set to “Prediction”. It mainly impacts how the residuals in the objective function are computed. The general expression to compute the residuals can be expressed as follows:

$$r(t, \theta) = y_m(t) - y_p(t, \theta) \quad (20)$$

Where, $y_m(t)$ is the measured output, $y_p(t, \theta)$ is the predicted response of the mode.

The predicted response is computed certain steps ahead in time using the current input and past measured input and output, including initial states. To calculate a predicted response k step ahead into the future from the current time t , where $k \geq 1$, all the inputs up to $(t + k)$ and all outputs up to t must be available. The general expression for the predicted response can be expressed by

$$y_r(t + k, \theta) = f(u_m(t + k), u_m(t + k - 1), \dots, u_m(t), u_m(t - 1), \dots, u_m(0); y_m(t), y_m(t - 1), \dots, y_m(0)) \quad (21)$$

This updating characteristic of the prediction focus keeps residuals ($r(t, \theta)$) low, which subsequently supports the GN’s approximation of the truncated Hessian for all iterations. The prediction focus ensures faster and guaranteed convergence of GN method.

8.3.1.4 Model quality matrices

The model quality matrices used in this paper include Akaike's Final Prediction Error (FPE), Mean Square Error (MSE), and the model data fitting accuracy. FPE represents the prediction error among a group of models [22]. MSE is the second moment of the error. A good model comes with a lower value of FPE and MSE, representing a higher fitting accuracy.

8.3.2 MPC Controller

8.3.2.1 Plant Model

To comply with the MPC's requirement, the developed BJ plant model is converted into a delay free, linear time-invariant (LTI) state-space model with dimensionless input and output. The "SS" function available in MATLAB converts the BJ model into state space; later, another function, "absorbDelay", which converts a delay of k sampling period into k poles at $z = 0$, is used to make the model delay free. Then, the inputs and outputs of the converted state-space model is made dimensionless by taking the following form:

$$x_p(k + 1) = A_p x_p(k) + B_{pu} u_p(k) \quad (22)$$

$$y_p(k) = C_p x_p(k) + D_{pu} u_p(k) \quad (23)$$

Where $A_p, B_{pu}, C_p,$ and D_{pu} are the delay free dimensionless matrices of the plant model. $x_p, u_p,$ and y_p are the dimensionless states, manipulated variables (inputs), and outputs of the plant model. $C_p = (S_p^y)^{-1} C$. B_{pu} and D_{pu} are the corresponding column of BS_p^u and $(S_p^y)^{-1} DS_p^u$, respectively. S_p^u and S_p^y are the scale factors of the plant inputs and outputs, respectively. $B, C,$ and D are the state-space matrices of the plant model with delay.

8.3.2.2 Noise model

The proposed controller rejects measurement noises according to noise models given during the controller development. Similar to the plant model, the noise model also has to be the delay free, LTI state-space model. The noise model can be expressed by

$$x_n(k + 1) = A_n x_n(k) + B_n w_n(k) \quad (24)$$

$$y_n(k) = C_n x_n(k) + D_n u_n(k) \quad (25)$$

Where A_n , B_n , C_n , and D_n are the delay-free dimensionless matrices of the noise model. x_n , w_n , and y_n are the delay-free states, inputs, and outputs of the noise model.

8.3.2.3 Controller state observer model

A steady-state Kalman filter-based state observer is used to estimate unmeasured states of the system. The state observer combines the plant and noise models, and update the states through the steady-state Kalman filter in every control interval. To set the Kalman coefficients, Kalman gains calculation approach described in [23] is adopted. The state-space representation of the state observer is given as follows:

$$x_c(k + 1) = A_c x_c(k) + B_c u_c(k) \quad (26)$$

$$y_c(k) = C_c x_c(k) + D_c u_c(k) \quad (27)$$

where,

$$A_c = \begin{bmatrix} A_p & 0 \\ 0 & A_n \end{bmatrix} \quad (28)$$

$$B_c = \begin{bmatrix} B_{pu} & 0 \\ 0 & B_n \end{bmatrix} \quad (29)$$

$$C_c = \begin{bmatrix} C_p & \begin{bmatrix} C_n \\ 0 \end{bmatrix} \end{bmatrix} \quad (30)$$

$$D_c = \begin{bmatrix} 0 & [D_n] \\ & 0 \end{bmatrix} \quad (31)$$

$$u_c^T = [u_p^T \quad w_n^T] \quad (32)$$

$$x_c^T = [x_p^T \quad x_n^T] \quad (33)$$

8.3.2.4 Constraints

The proposed controller ensures constrained optimization of the plant's outputs and MVs during operation. The constraints are expressed by

$$\frac{y_{p,j,min}}{S_{p,j}^y} - \varepsilon_k V_{p,j,min}^y \leq \frac{y_{p,j}(k+i|k)}{S_{p,j}^y} \leq \frac{y_{p,j,max}}{S_{p,j}^y} + \varepsilon_k V_{p,j,max}^y \quad (34)$$

$$\frac{u_{p,e,min}}{S_{p,e}^u} - \varepsilon_k V_{p,e,min}^u \leq \frac{u_{p,e}(k+i|k)}{S_{p,e}^u} \leq \frac{u_{p,e,max}}{S_{p,e}^u} + \varepsilon_k V_{p,e,max}^u \quad (35)$$

Where, $1 \leq i \leq p$, $1 \leq j \leq n_y$, and $1 \leq e \leq n_u$. $y_{p,j,min}$ or max is the lower or upper bound of the j^{th} plant outputs, whereas $u_{p,e,min}$ or max is the lower and upper bound of the e^{th} MVs. ε_k is the slack variable that represents the worst-case constraint violation. $y_{p,j}(k+i|k)$ is the predicted response of the j^{th} plant output at the i^{th} prediction horizon.

The parameter, V , in the above equations represents the equal concern of relaxation (ECR) of the respective parameters, which decides whether a constraint is hard or soft. The quadratic programming solutions must satisfy the hard constraints under any circumstance. Failing to do so, an infeasible solution results, which could lead to a loss of control. Whereas, if required, QP can violate the soft constraints.

At the very beginning of a disturbance, due to lower inertia of islanded microgrids, deviations of the voltage and frequency at the PCC (plant output) may momentarily go beyond the bounds.

Therefore, to prevent the loss of control, output bounds are softened. This softening could initiate steady-state errors in the voltage and frequency. As a remedy, tuning weights on the outputs are set to a higher value. Tuning weights penalize the deviation from the references, and thus, MPC allows the outputs to go beyond their bounds, but bring back to the reference as fast as it can. Softening both input and output bounds guarantees the QP's feasible solution, but significantly deteriorates the controller's performance [24]. Therefore, all the input bounds are set as hard constraints.

8.3.2.5 Controller Working Principle

Suppose the state observer senses a deviation of the voltage and frequency at the beginning of the k^{th} control interval. The sharing factor updates the MPC of each of the DGs about what proportion of the overall deviation they are supposed to compensate. Later, the state observer updates the states of the system using the following formulas.

$$x_c(k|k) = x_c^{rev}(k|k-1) + Me(k) \quad (36)$$

Where,

$$x_c^{rev}(k|k-1) = x_c(k|k-1) + B_u[u_p^{act}(k-1) - u_p^{opt}(k-1)] \quad (37)$$

$$e(k) = y_m(k) - C_m x_c^{rev}(k|k-1) \quad (38)$$

where B_u and C_m are rows of the state observer parameters B_c and C_c corresponding to $u_p(k)$ and $y_m(k)$, respectively. $y_m(k)$ is the measured plant outputs at the k^{th} control interval. $u_p^{act}(k-1)$ and $u_p^{opt}(k-1)$ are the implemented and predicted MVs for (k-1) to k control interval.

Later, the state observer predicts the plant outputs up to the prediction horizon using (39).

$$y_{p,j}(k + i|k) = S_x x_c(k|k) + S_u u(k - 1) \quad (39)$$

Where,

$$S_x = \begin{bmatrix} C_c A_c \\ C_c A_c^2 \\ \dots \\ C_c A_c^p \end{bmatrix} \in \mathbb{R}^{pn_y \times n_x} \quad (40.1)$$

$$S_u = \begin{bmatrix} C_c B_u \\ C_c B_u + C_c A_c B_u \\ \dots \\ \sum_{h=1}^{p-1} C_c A_c^h B_u \end{bmatrix} \in \mathbb{R}^{pn_y \times n_u} \quad (40.2)$$

and $1 \leq i \leq p$.

At any control interval k , the controller minimizes the following objective function:

$$J(z_k) = \sum_{j=1}^{ny} \sum_{i=1}^p \left\{ \frac{w_{p,j}^y}{s_{p,j}^y} [r_{p,j}(k + i|k) - y_{p,j}(k + i|k)] \right\}^2 + \rho_\epsilon \epsilon_k^2 \quad (41)$$

Where $w_{p,j}^y$, is the tuning weight for the j^{th} plant output, and $r_{p,j}(k + i|k)$ is the reference value of the j^{th} plant output.

Later, the objective function is then passed to the MPC's QP solver. The QP solver transforms it into the general form of the QP problem expressed as follows:

$$\min_{z_k} \left(\frac{1}{2} z_k^T H z_k + f^T z_k \right) \quad (42)$$

The adopted QP solver is a KWIK algorithm-based Active-set solver. The working principle of the adopted solver is explained in [25]. The solver prerequisites a positive definite Hessian matrix, H . It uses the warm start approach, where the initial guesses are the active constraint sets determined in the previous control step. The maximum number of iterations is 120. If the solver detects infeasibility or iterations maxed-out without an optimal solution, the controller keeps the

last successful MVs. The solver returns z_k , which is a set of recommended optimal movements for the manipulated variables, expressed as follows:

$$z_k = u_p^{opt}(k) = [u_p(k|k)^T \quad u_p(k+1|k)^T \quad \dots \quad u_p(k+p-1|k)^T \quad \varepsilon_k] \quad (43)$$

Only the first recommended MV movements are implemented, then the whole process is repeated at $(k+1)$ control step.

8.4 The GN-Based Box-Jenkins Model

The test system simulation model shown in Fig. 8.3 is an islanded microgrid. The DG under analysis is a 10 kVA PV system, modeled as a constant DC voltage source. System parameters used in the simulation are tabulated in Table 8.1.

Table 8. 1: Test System's Parameters

Parameters		Values
Nominal DC bus voltage (V)		700
Nominal AC bus RMS line voltage (V)		380
AC system frequency (f)		50
DG's Nameplate capacity (kVA)		10
Local Load		5 kW, 1 kVar
PCC Load		2 kW, 0.4 kVar
Inverter filter	Resistance, Rf (Ω)	0.2
	Inductance, Lf (H)	3×10^{-3}
	Capacitance, Cf (F)	15×10^{-6}
Line impedance	Line resistance, RL (Ω)	0.641
	Line reactance, XL (Ω)	0.08

First, output parameters of the test system are initialized to their nominal steady-state value. Initialization sets 0.821 and 0.07 for the d-axis component (U_d) and the q-axis component (U_q) of the DG's control signal. To generate the training dataset for the system identification, U_d is varied around its nominal value by ± 0.05 and U_q is varied around its nominal value by ± 0.005 . To generate the validation dataset, U_d is varied around its nominal value by ± 0.04 , and U_q by ± 0.004 . The corresponding deviations of the PCC voltage and frequency from their nominal values in pu (ΔV and ΔF) are tabulated. The duration of each step change is 0.5 s, and the data acquisition sampling frequency is 10 kHz. The magnitudes of the step variations are carefully chosen to influence system dynamics without initiating nonlinearity.

Using the GN-based nonlinear least-square approach, the final Box-Jenkins model expressed in (16) is developed using the prediction optimization focus. The model's data fitting performance for training and validation dataset are depicted in Fig. 8.4. The model's FPE and MSE are 5.12×10^{-25} and 7.68×10^{-10} , respectively. The high fitting accuracies for both training and validation datasets and low FPE and MSE indicate that the model is in good agreement with the datasets.

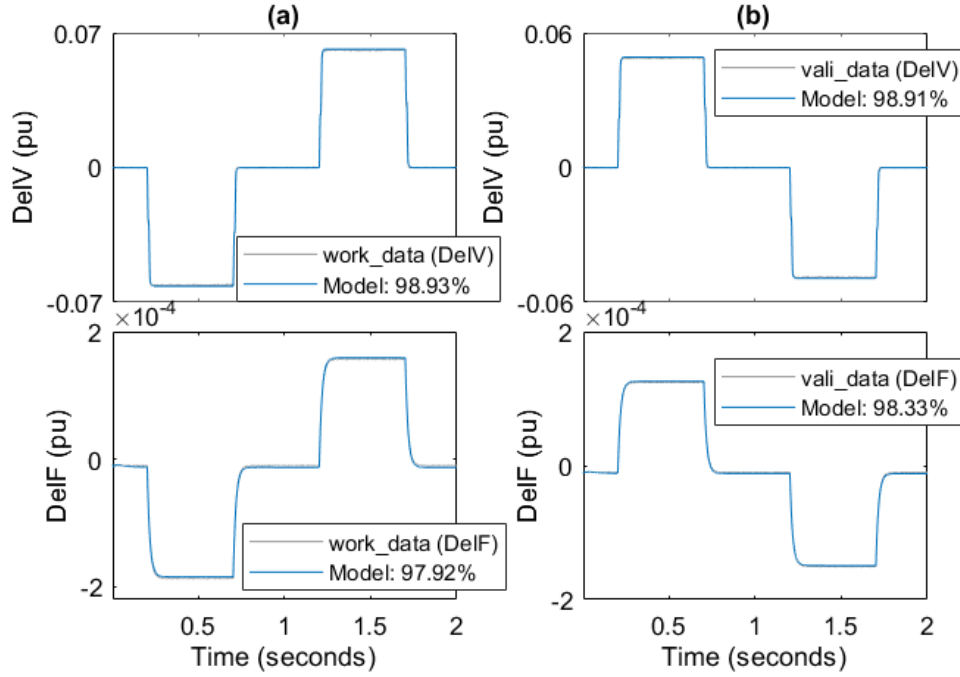


Fig. 8. 4. The fitted model along with their fitting accuracies for different datasets: (a) training dataset; and (b) validation dataset.

Finally, the model's coefficients A, B, C, D, and F are determined as follows:

$$A = \begin{bmatrix} 1 & 0 \\ 0 & 1 \end{bmatrix} \quad (44)$$

$$B = \begin{bmatrix} (0, 0.1189, 0.0682, 0.0932) & (0, -0.967) \\ (0, 0, 0, 5.26 \times 10^{-6}, 7.95 \times 10^{-5}, -7.59 \times 10^{-5}) & (0, 0, 0, -0.0013) \end{bmatrix} \quad (45)$$

$$C = \begin{bmatrix} (1, -0.198, -0.456, -0.479, -0.618, 0.664, 0.174) \\ (1, -0.364, -1.009, -0.149, 0.662, 0.096, -0.182) \end{bmatrix} \quad (46)$$

$$D = \begin{bmatrix} (1, -0.313, -0.547, -0.495, -0.581, 0.777, 0.185, -0.017) \\ (1, -0.421, -1.047, -0.14, 0.692, 0.092, -0.179, 0.003) \end{bmatrix} \quad (47)$$

$$F = \begin{bmatrix} (F_{11}) & (F_{12}) \\ (F_{21}) & (F_{22}) \end{bmatrix} \quad (48)$$

$$F_{11} = [1, -0.49, -0.355, 0.047, 0.286, -0.181, -0.557, 0.291]$$

$$F_{12} = [1, -1.599, 0.589, 0.713, -1.025, 0.335]$$

$$F_{21} = [1, -0.702, 0.075, -0.865, 0.115, 0.288, -0.014, 0.112]$$

$$F_{22} = [1, -0.051, 0.422, -0.699, -0.157, -0.476]$$

8.5 The MPC-Based DG Controller Design

Using the developed system identification model, the MPC-based DG controller is developed. The controller sample time is set to 0.001s and output parameters are constrained within ± 0.05 pu of deviations around the nominal values [26]. Equal concern of relaxation (ECR) for upper and lower bounds of the MVs are 0, whereas, the same for the outputs are 1. A 0 ECR makes the input bounds hard, whereas a non-zero ECR makes the output bounds soft. Critical parameters used to develop the controller are tabulated in Table 8.2.

Table 8. 2: MPC controller's Parameters

Parameters	Values
Nominal Value of U_d and U_q	0.821 and 0.07
Nominal value for DelV and DelF	0 and 0
Scale Factor for U_d and U_q	0.95 and 0.3
Scale factor for DelV and DelF	13.6 and 0.0102
Operational range for U_d	0 to 0.95
Operational range for U_q	0 to 0.3
Tuning Weight on DelV and DelF	20 and 20
Prediction Horizon	10
Control Horizon	2

As the state observer updates the states of the noise and plant models in every control interval, any change in system parameters is automatically reflected on the updated states (Fig. 8.5). This

way, the proposed controller updates the plant model itself, reduce the necessity of redevelopment of the plant models for every individual DGs.

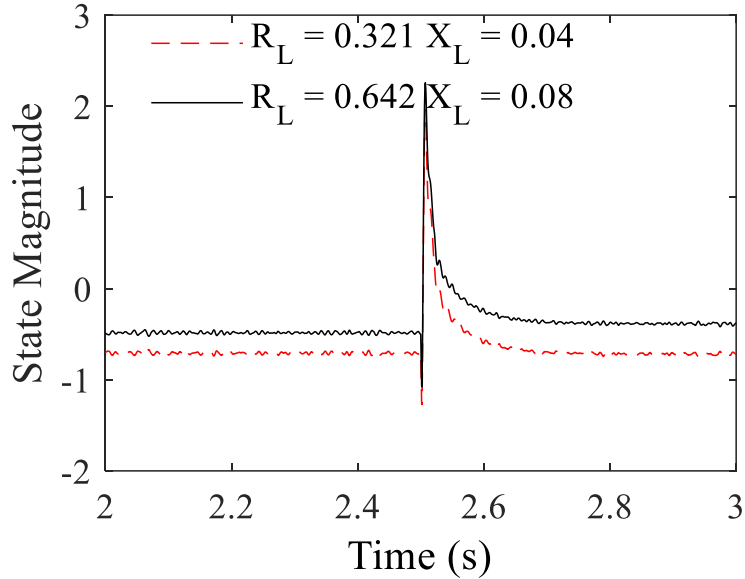


Fig. 8. 5. Change of plant state with line impedances.

8.6 Case Studies

To validate the proposed controller, several case studies are conducted in this section. Fig. 8.6 shows an islanded microgrid used in case studies. Both DGs have a local load of 5 kW and 1 kVar. In all case studies, the local load is not varied; for the PCC load, only “PCC Load 1” is connected in the beginning, and “PCC Load 2” comes online at 2.5 s. A delay of 20 sampling period (2 ms) representing the communication delay between the PCC and the inverter is considered. All MPC-based DG controllers are fed by the same plant model developed earlier, although they have different line impedances.

The specifications of the two lines and the two PCC loads are given as follows: $R_L = 0.321 \Omega$ and $X_L = 0.04 \Omega$ for Line 1; $R_L = 0.642 \Omega$ and $X_L = 0.08 \Omega$ for Line 2; 2 kW and 0.4 kVar for PCC Load 1; and 1 kW and 0.2 kVar for PCC Load 2.

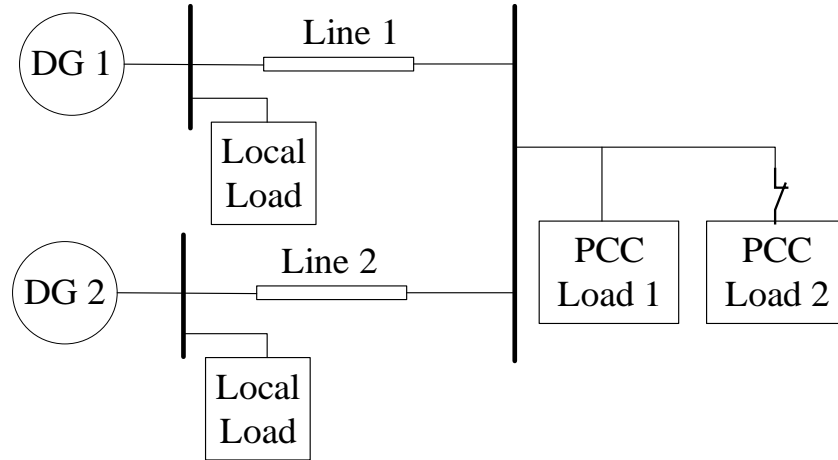


Fig. 8. 6. The single line diagram of the test microgrid configuration.

8.6.1 Case Study 1: Comparison with the Existing Methods

In Case Study 1, each DG has a name plate capacity of 10 kW, and a sharing factor (k_s) of 0.5. To demonstrate the effectiveness of the proposed controller over existing methods, its performance is compared with two existing methods: one is droop control with a secondary controller in [6]; and another is droop control with a secondary controller and the virtual impedance in [27].

The existing controller in [6] shows good performance with accurate active power sharing and complete restoration of the frequency without any DG-to-DG communication network; however, due to the absence of virtual impedance, it fails to ensure reactive power sharing as shown in Fig. 8.7(b).

On the other hand, although the existing controller in [27] has ensured active and reactive power sharing, and compensation of voltage and frequency deviations, it requires a DG-to-DG communication network. The communication latency induces very low magnitude, high frequency ripples, which deteriorates the power quality.

As shown in Fig. 8.7, the proposed method ensures complete restoration of the voltage and frequency and share active and reactive power equally between the two DGs without any secondary controller, virtual impedance loop and DG-to-DG communication network. In terms of the power quality, the proposed controller and the existing controller in [6] maintain better power quality with only 0.2% voltage total harmonic distortion (VTHD) at the PCC; however, the existing controller in [27] has lower power quality with 1.5% VTHD at the PCC.

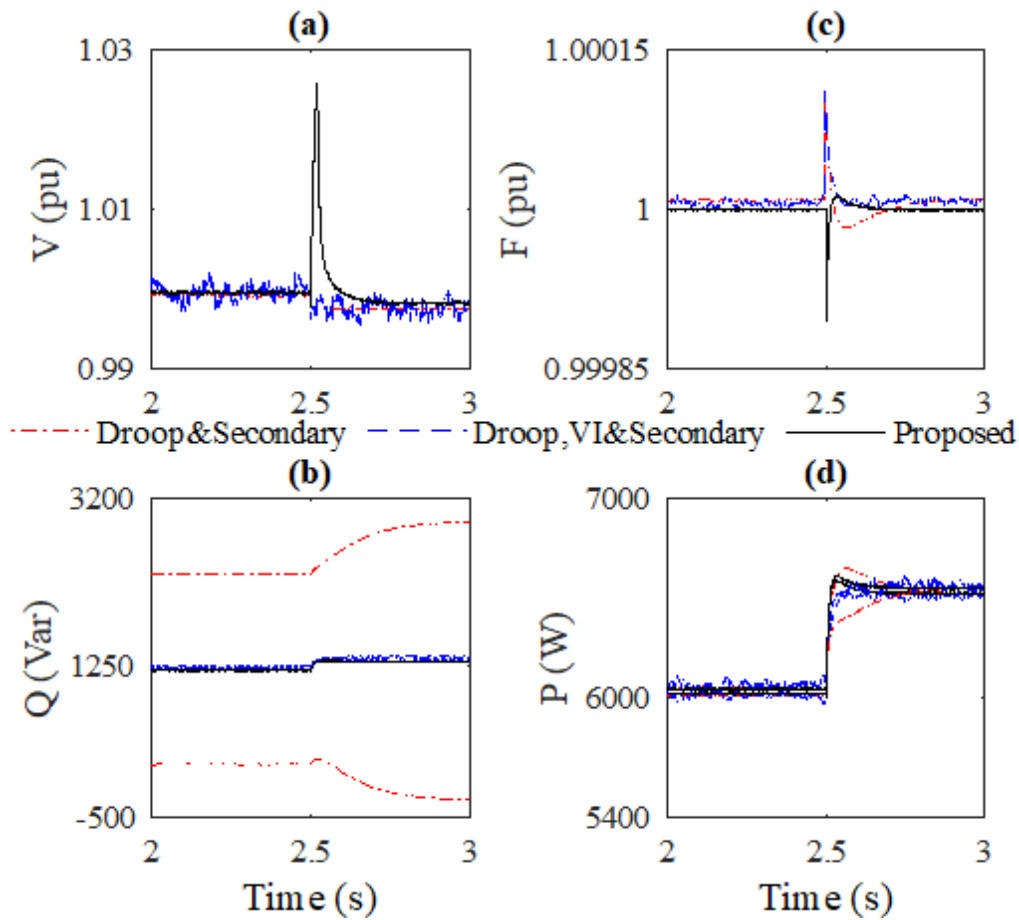


Fig. 8. 7. Performance comparison of the proposed and two existing controllers; (a) PCC voltage in pu; (b) reactive power supplied by DGs in Var; (c) PCC frequency in pu; (d) active power supplied by DGs in W (Case Study 1).

8.6.2 Case Study 2: Equal Power Sharing

In Case Study 2, each DG has a name plate capacity of 10 kW, and a sharing factor (k_s) of 0.5. Before “PCC Load 2” gets connected, each DG is supplying power at 6 kW and 1.2 kVar. Due to the DGs’ equal ratings, the control signals generated by the MPC are very near to each other but keep a little bit difference because of their impedance mismatch (Fig. 8.8 (d) and (h)). Following the connection of “PCC Load 2” at 2.5 s, both MPC controllers analyze the sags and adjust control signals. The adjustments compensate the voltage and frequency deviations and ensure equal power sharing between the DGs. The post-disturbance power flow from each DG is 6.5 kW and 1.3 kVar (Fig. 8.8 (c) and (g)).

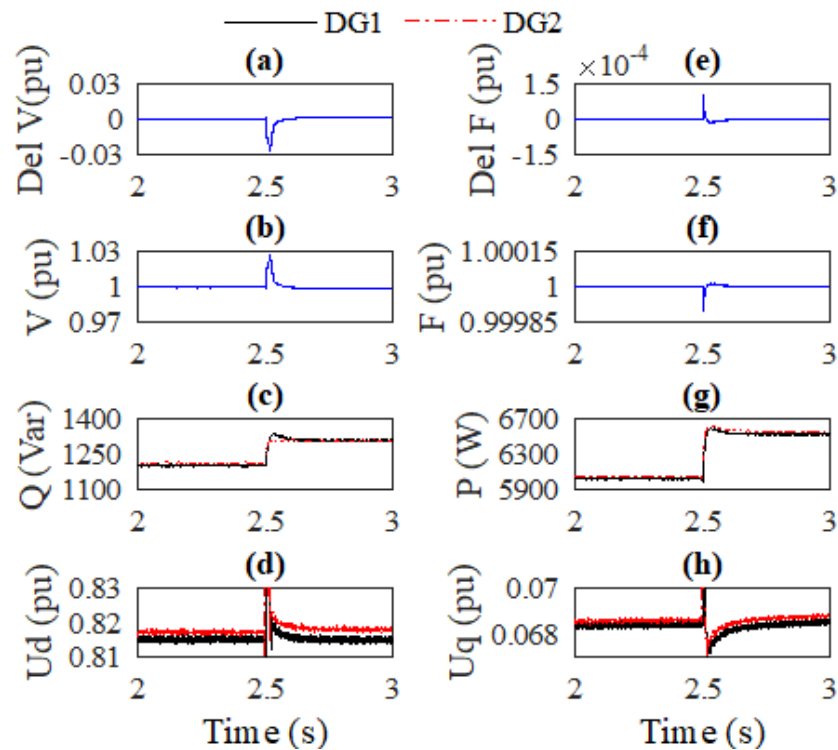


Fig. 8. 8. Controller performance: (a) PCC voltage deviation from the nominal in pu; (b) PCC voltage in pu; (c) Reactive power supplied by DGs in Var; (d) d-axis component of the control signal; (e) PCC frequency deviation from the nominal in pu; (f) PCC frequency in pu; (g) active power supplied by DGs in w; (h) q-axis component of the control signal (Case Study 2).

8.6.3 Case Study 3: Proportional Power Sharing

In Case Study 3, the name plate capacity for DG1 and DG2 are 30 kW and 10 kW, respectively; and their sharing factor (k_s) are 0.75 and 0.25, respectively. The pre-disturbance power flow from DG1 and DG2 are (9 kW, 1800 Var) and (3 kW, 600 Var), respectively. Following the connection of PCC Load 2, controllers respond according to their capacity and impedance mismatch and compensate the deviations promptly. The post-disturbance power dispatch from DG1 and DG2 are (9.9 kW, 1950 Var) and (3.3 kW, 650 Var), respectively (Fig. 9 (c) and (g)). The proposed controller ensures the proportional power sharing between the DGs before and after the connection of PCC Load 2.

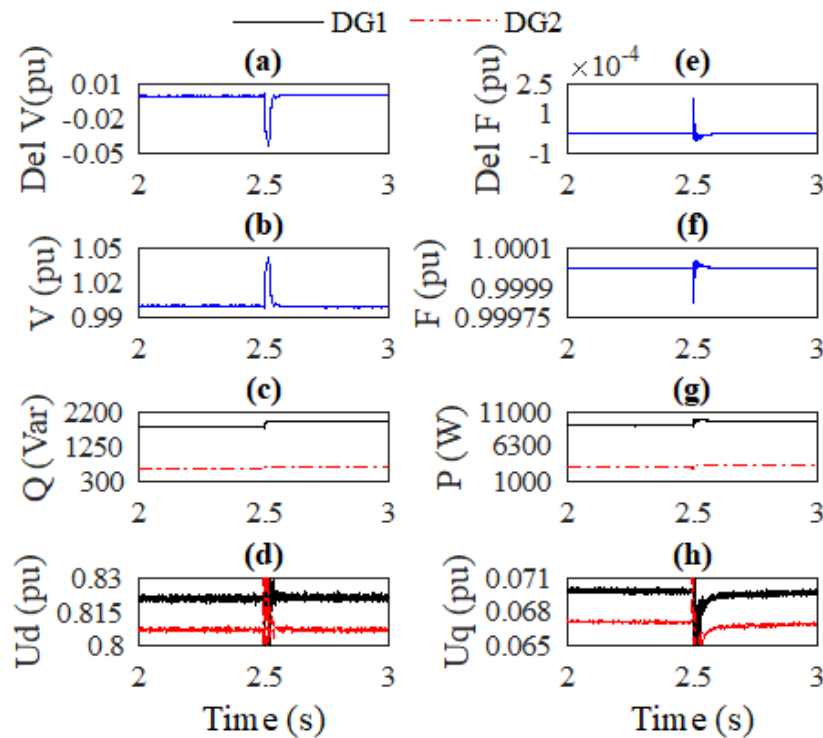


Fig. 8. 9. Controller performance: (a) PCC voltage deviation from the nominal in pu; (b) PCC voltage in pu; (c) Reactive power supplied by DGs in Var; (d) d-axis component of the control signal; (e) PCC frequency deviation from the nominal in pu; (f) PCC frequency in pu; (g) active power supplied by DGs in w; (h) q-axis component of the control signal (Case Study 3).

8.6.4 Case Study 4: Performance with one added DG

Case Study 4 is conducted to evaluate the performance of the proposed controller if an additional DG is connected. Therefore, an additional DG, identical to DG 1 are connected in parallel with the two existing DGs. All three DGs have 10 kW nameplate rating, and their sharing factor (k_s) is $\frac{1}{3}$. Before 2.5 s, the total connected load is 17 kW and 3.4 kVar; and at 2.5 s, PCC Load 2 is connected. It is found that the three DGs share the total load demand equally, and each of them supplies 5.7 kW and 1.14 kVar of power till 2.5 s (Fig. 8.10 (c) and (g)). After the connection of PCC Load 2, the controllers adjust their references by analyzing the depth of deviations, and each DG contribute power at 6 kW and 1.2 kVar.

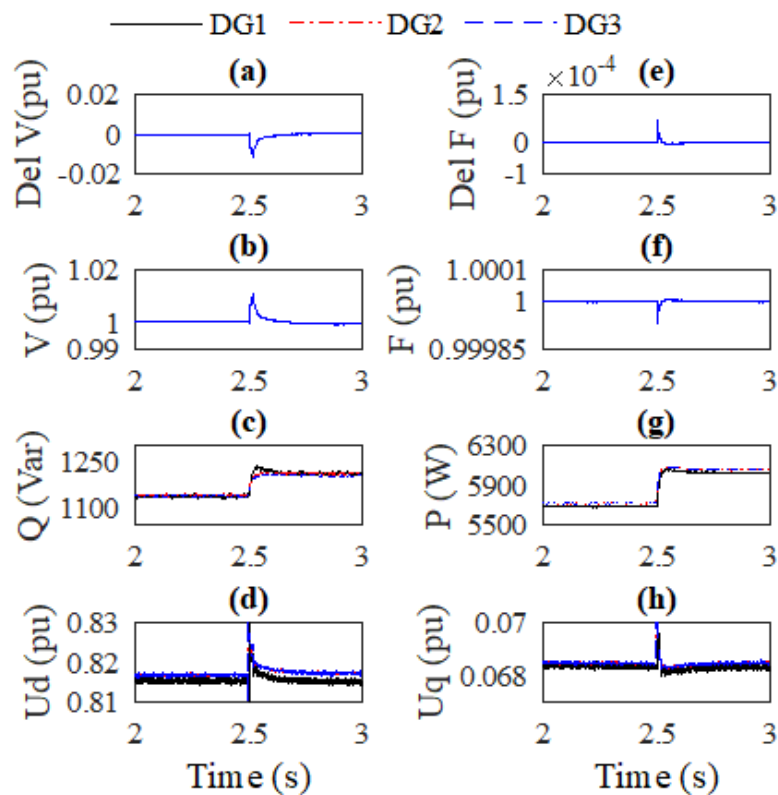


Fig. 8. 10. Controller performance: (a) PCC voltage deviation from the nominal in pu; (b) PCC voltage in pu; (c) Reactive power supplied by DGs in Var; (d) d-axis component of the control

signal; (e) PCC frequency deviation from the nominal in pu; (f) PCC frequency in pu; (g) active power supplied by DGs in w; (h) q-axis component of the control signal (Case Study 4).

8.7 Robustness Analysis

To study the robustness of the proposed controller, parameters critically influence the controller's performance are studied. Parameters under analysis are distribution line impedance (Z_L), communication delay, and measurement noises. To conduct the analysis, the microgrid configuration used in Case Study 2 is considered.

8.7.1 Distribution Line Impedance Variation

In real life, the impedance of a distribution line can be influenced by ambient conditions, aging and change of conductors. Therefore, a microgrid controller should be robust to the impedance variations. The impedance can be varied uniformly for all lines, or different lines could face different rate of variations. Therefore, the performance of the proposed controller is studied for both conditions.

In the first study, for both "Line 1" and "Line 2", a uniform 50% rise and drop are considered; while in the second study, Line 1 is varied by 50%, and Line 2 is varied by 40%. Although for day-to-day operation, these range of variations are highly unlikely, however, due to aging, faulty conductor or change of conductor, this situation may arise. The performance of the proposed controller for the two studies are depicted in Figs. 11 and 12, respectively.

As the controller automatically adapt itself with the changing impedance by updating the states, therefore, its performance is robust even for such huge deviations. For study 1, the maximum active and reactive power sharing errors for the increased impedance are 39 W and 6 Var, respectively; whereas for the decreased impedance, they are 11 W and 11 Var, respectively. On the other hand, in study 2, the maximum sharing errors for the risen impedance are 34 W and 5

Var, and for the decreased impedance are 7 W and 7 Var. From Fig. 8.11, 12(a) and 12(c), it is found that the impedance change has very minimal impact on the controller's voltage and frequency recovery performance. Therefore, the proposed controller is robust to sudden impedance variations, and doesn't need frequent retuning.

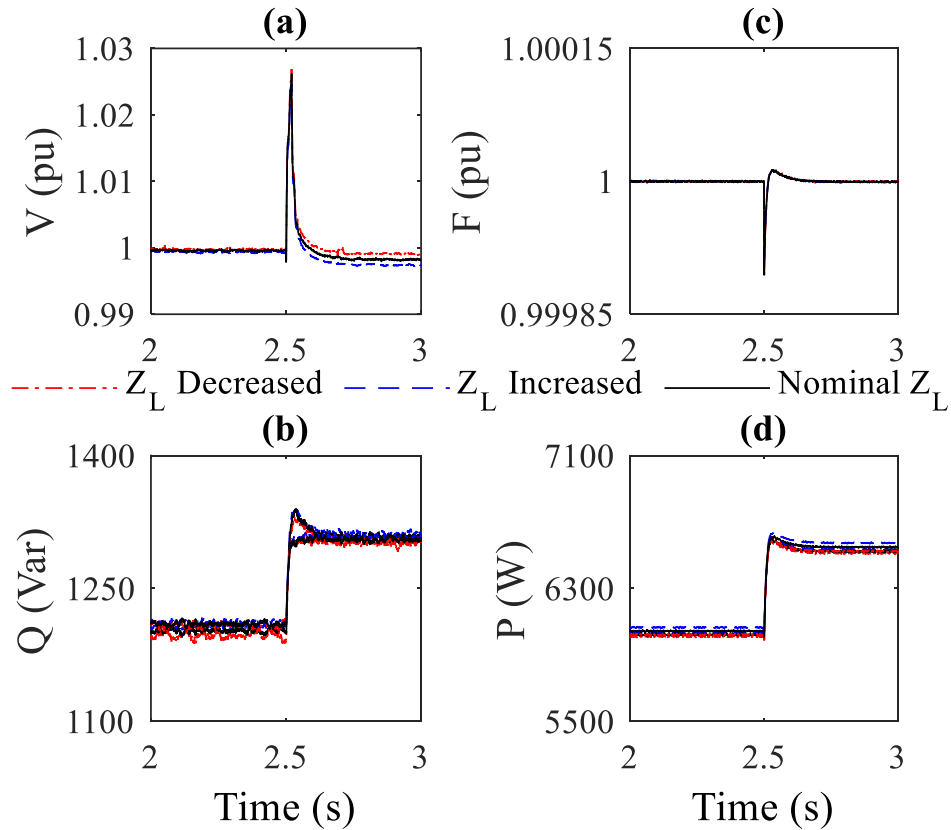


Fig. 8. 11. The proposed controller for uniform impedance variation of Line 1 and Line 2; (a) PCC voltage in pu; (b) Reactive power supplied by DGs in Var; (c) PCC frequency in pu; (d) active power supplied by DGs in W.

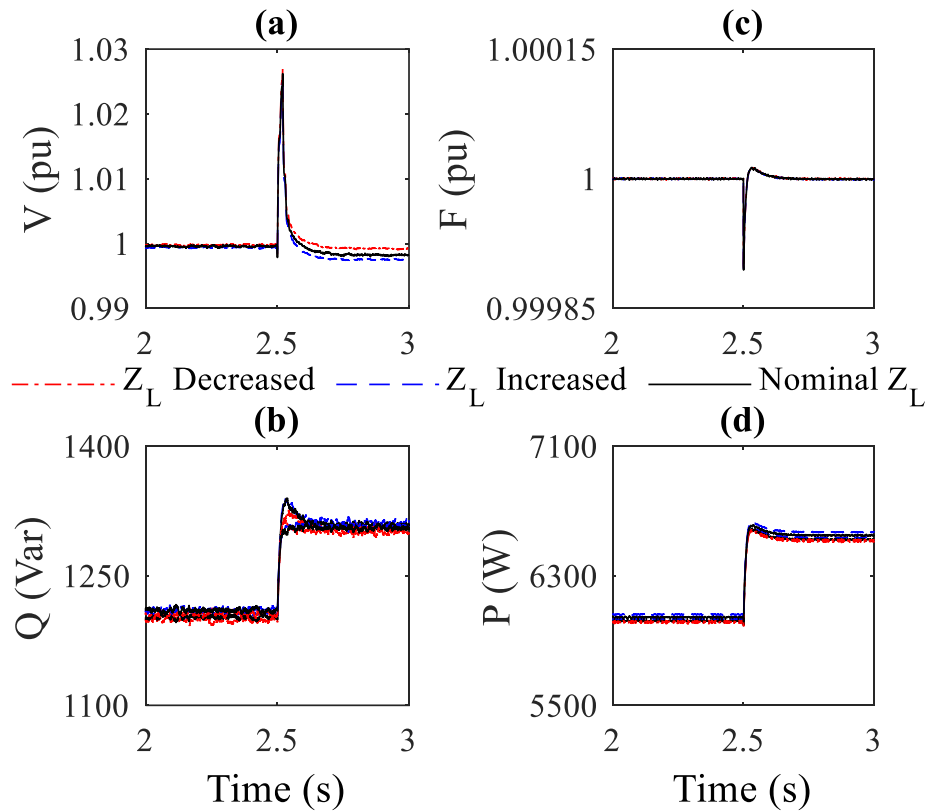


Fig. 8. 12. The proposed controller for un-uniform impedance variation of Line 1 and Line 2; (a) PCC voltage in pu; (b) Reactive power supplied by DGs in Var; (c) PCC frequency in pu; (d) active power supplied by DGs in W.

8.7.2 Communication Delay

The proposed controller responds based on the PCC data; doesn't require DG-to-DG communication. However, to realize any deviations, a communication link from the PCC to the inverter terminal is required. Subjected to the length of distribution lines and the communication architecture, this communication link may introduce delays in the controller response. Therefore, the robustness of the controller to communication delays should be evaluated.

The analysis shows that the proposed controller can maintain the stable and unaltered performance up to 210-sampling delay (N_{DELAY}), which is equivalent to 21 ms of communication

delay (Fig. 8.13). The tolerance time is significantly better than 2.55 ms in [28]. As a result, the proposed approach doesn't require costly faster communication network, and thus, ensures more economical operation.

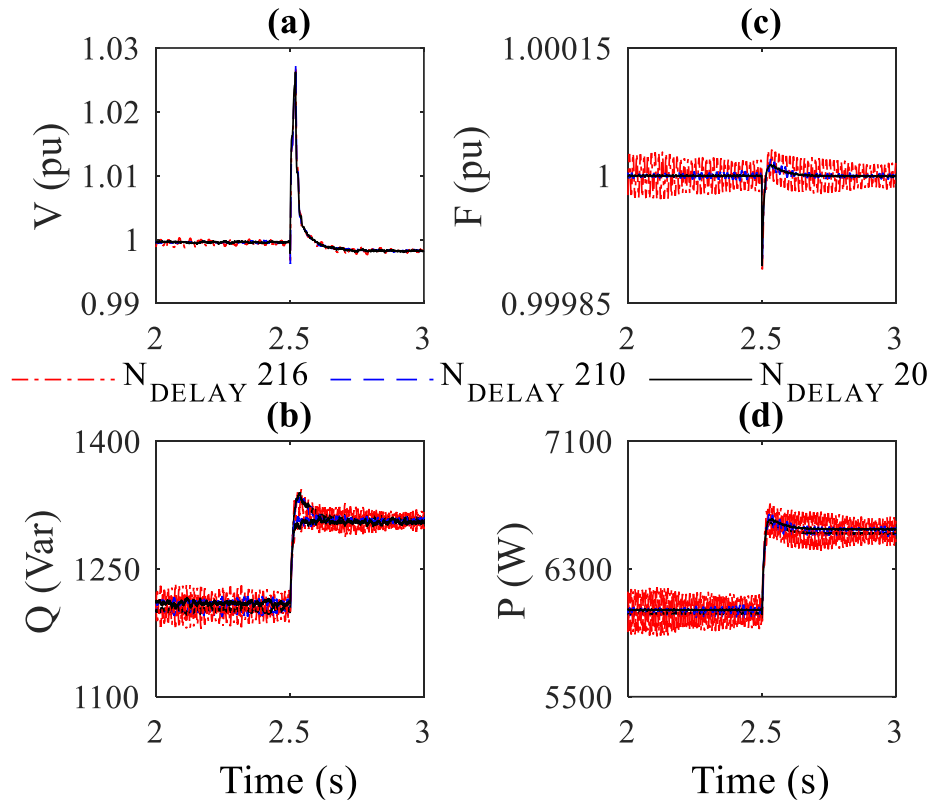


Fig. 8. 13. The proposed controller for different communication delays; (a) PCC voltage in pu; (b) Reactive power supplied by DGs in Var; (c) PCC frequency in pu; (d) active power supplied by DGs in W.

8.7.3 Measurement Noise

Noises are an integral part of the real-life measurements; therefore, usually data are prefiltered before feed into the controller. The proposed controller has a built-in Kalman filter which is effective in filtering the white Gaussian measurement noise, so no additional prefiltering is required before the data are feed into the controller.

To demonstrate the controller's robustness against measurement noises, white Gaussian noise are added with ΔV and ΔF (Fig. 8.14(b) and (e)) and passed to the controller. Fig. 8.14(a) and (d) depict that the controllers successfully cancel out the noises and keep the performance unaffected.

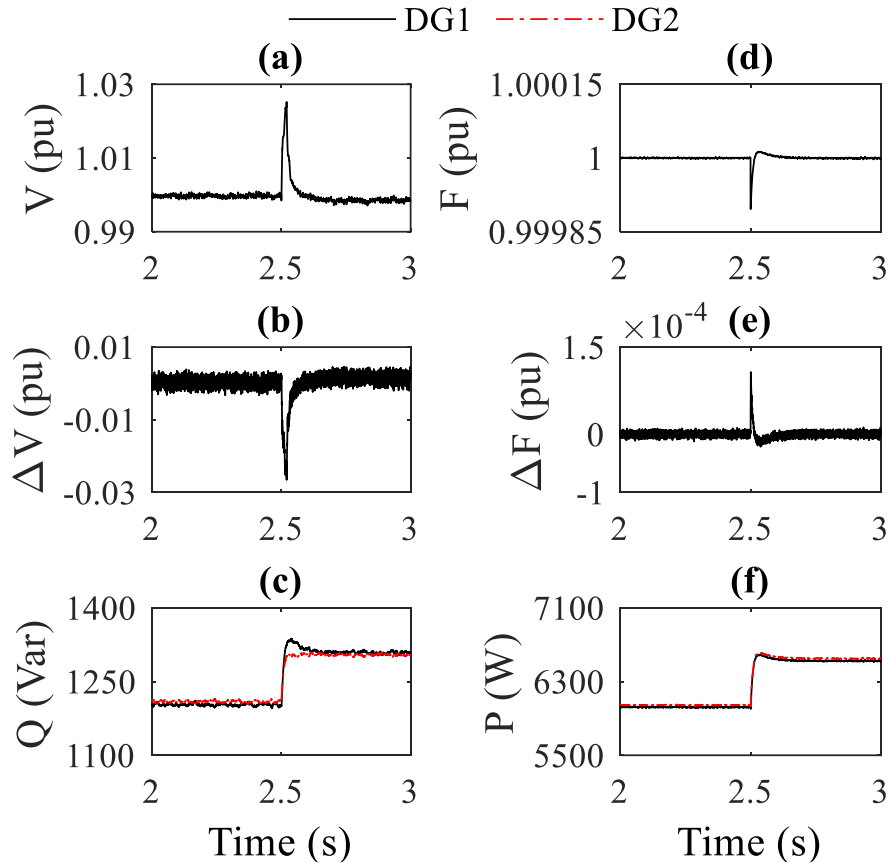


Fig. 8. 14. The proposed controller with unfiltered measurement noises; (a) PCC voltage in pu; (b) Noisy deviation of voltage data, ΔV in pu; (c) Reactive power supplied by DGs in Var; (d) PCC frequency in pu; (e) Noisy deviation of frequency data, ΔF in pu; and (f) active power supplied by DGs in W.

8.8 Conclusion

In this paper, a novel MPC-based DG controller in islanded microgrids is proposed by controlling deviations of the voltage and frequency at the PCC using the d- and q-axis components of the DG control signal. The control model is developed using non-linear least-square approach

with Gauss-Newton line search method. The proposed approach can fully compensate the voltage and frequency deviations and ensure proper active and reactive power sharing among DGs without any secondary controller and virtual impedance loop. The proposed controller doesn't require DG-to-DG communication network and is robust to line impedance variations and measurement noises.

References

- [1] B. Liu, Z. Liu, J. Liu, R. An, H. Zheng, and Y. Shi, "An Adaptive Virtual Impedance Control Scheme Based on Small-AC-Signal Injection for Unbalanced and Harmonic Power Sharing in Islanded Microgrids," *IEEE Trans. Power Electron.*, vol. 34, no. 12, pp. 12333–12355, Dec. 2019, doi: 10.1109/TPEL.2019.2905588.
- [2] S. d J. M. Machado, S. A. O. da Silva, J. R. B. d A. Monteiro, and A. A. de Oliveira, "Network Modeling Influence on Small-Signal Reduced-Order Models of Inverter-Based AC Microgrids Considering Virtual Impedance," *IEEE Trans. Smart Grid*, vol. 12, no. 1, pp. 79–92, Jan. 2021, doi: 10.1109/TSG.2020.3012475.
- [3] R. An, Z. Liu, and J. Liu, "Successive-Approximation-Based Virtual Impedance Tuning Method for Accurate Reactive Power Sharing in Islanded Microgrids," *IEEE Trans. Power Electron.*, vol. 36, no. 1, pp. 87–102, Jan. 2021, doi: 10.1109/TPEL.2020.3001037.
- [4] J. Chen, D. Yue, C. Dou, L. Chen, S. Weng, and Y. Li, "A Virtual Complex Impedance Based P - V Droop Method for Parallel-Connected Inverters in Low-Voltage AC Microgrids," *IEEE Trans. Ind. Inform.*, vol. 17, no. 3, pp. 1763–1773, Mar. 2021, doi: 10.1109/TII.2020.2997054.
- [5] B. John, A. Ghosh, and F. Zare, "Load Sharing in Medium Voltage Islanded Microgrids With Advanced Angle Droop Control," *IEEE Trans. Smart Grid*, vol. 9, no. 6, pp. 6461–6469, Nov. 2018, doi: 10.1109/TSG.2017.2713452.
- [6] B. Liu, T. Wu, Z. Liu, and J. Liu, "A Small-AC-Signal Injection-Based Decentralized Secondary Frequency Control for Droop-Controlled Islanded Microgrids," *IEEE Trans. Power Electron.*, vol. 35, no. 11, pp. 11634–11651, Nov. 2020, doi: 10.1109/TPEL.2020.2983878.

- [7] Y. R. Rodrigues, M. Abdelaziz, and L. Wang, "D-PMU Based Secondary Frequency Control for Islanded Microgrids," *IEEE Trans. Smart Grid*, vol. 11, no. 1, pp. 857–872, Jan. 2020, doi: 10.1109/TSG.2019.2919123.
- [8] M. Hua, H. Hu, Y. Xing, and J. M. Guerrero, "Multilayer Control for Inverters in Parallel Operation Without Intercommunications," *IEEE Trans. Power Electron.*, vol. 27, no. 8, pp. 3651–3663, Aug. 2012, doi: 10.1109/TPEL.2012.2186985.
- [9] X. Liang, C. Andalib-Bin-Karim, W. Li, M. Mitolo, and M. N. S. K. Shabbir, "Adaptive Virtual Impedance-Based Reactive Power Sharing in Virtual Synchronous Generator Controlled Microgrids," *IEEE Trans. Ind. Appl.*, vol. 57, no. 1, pp. 46–60, Jan. 2021, doi: 10.1109/TIA.2020.3039223.
- [10] Y. C. C. Wong, C. S. Lim, A. Cruden, M. D. Rotaru, and P. K. Ray, "A Consensus-Based Adaptive Virtual Output Impedance Control Scheme for Reactive Power Sharing in Radial Microgrids," *IEEE Trans. Ind. Appl.*, vol. 57, no. 1, pp. 784–794, Jan. 2021, doi: 10.1109/TIA.2020.3031884.
- [11] M.-D. Pham and H.-H. Lee, "Effective Coordinated Virtual Impedance Control for Accurate Power Sharing in Islanded Microgrid," *IEEE Trans. Ind. Electron.*, vol. 68, no. 3, pp. 2279–2288, Mar. 2021, doi: 10.1109/TIE.2020.2972441.
- [12] X. Wu, C. Shen, and R. Iravani, "Feasible Range and Optimal Value of the Virtual Impedance for Droop-Based Control of Microgrids," *IEEE Trans. Smart Grid*, vol. 8, no. 3, pp. 1242–1251, May 2017, doi: 10.1109/TSG.2016.2519454.
- [13] F. Chen, H. Garnier, M. Gilson, J. Agüero, and T. Liu, "Refined instrumental variable parameter estimation of continuous-time Box–Jenkins models from irregularly sampled data," *IET Control Theory Appl.*, vol. 11, no. 2, pp. 291–300, 2017.

- [14] J. Sachs and O. Sawodny, "A Two-Stage Model Predictive Control Strategy for Economic Diesel-PV-Battery Island Microgrid Operation in Rural Areas," *IEEE Trans. Sustain. Energy*, vol. 7, no. 3, pp. 903–913, 2016.
- [15] A. Ouammi, H. Dagdougui, L. Dessaint, and R. Sacile, "Coordinated Model Predictive-Based Power Flows Control in a Cooperative Network of Smart Microgrids," *IEEE Trans. Smart Grid*, vol. 6, no. 5, pp. 2233–2244, Sep. 2015, doi: 10.1109/TSG.2015.2396294.
- [16] U. C. Yilmaz, M. E. Sezgin, and M. Gol, "A Model Predictive Control for Microgrids Considering Battery Aging," *J. Mod. Power Syst. Clean Energy*, pp. 1–9, 2019.
- [17] T. Pippia, J. Sijs, and B. D. Schutter, "A Single-Level Rule-Based Model Predictive Control Approach for Energy Management of Grid-Connected Microgrids," *IEEE Trans. Control Syst. Technol.*, pp. 1–13, 2019.
- [18] G. Lou, W. Gu, W. Sheng, X. Song, and F. Gao, "Distributed Model Predictive Secondary Voltage Control of Islanded Microgrids With Feedback Linearization," *IEEE Access*, vol. 6, pp. 50169–50178, 2018.
- [19] J. S. Gómez, D. Sáez, J. W. Simpson-Porco, and R. Cárdenas, "Distributed Predictive Control for Frequency and Voltage Regulation in Microgrids," *IEEE Trans. Smart Grid*, vol. 11, no. 2, pp. 1319–1329, 2020.
- [20] T. Nguyen, H. Yoo, and H. Kim, "Applying Model Predictive Control to SMES System in Microgrids for Eddy Current Losses Reduction," *IEEE Trans. Appl. Supercond.*, vol. 26, no. 4, pp. 1–5, 2016.
- [21] C. N. L. Eu, "Numerical Analysis in Nonlinear Least Squares Methods and Applications," PhD Thesis, Curtin University, 2017.

- [22] M. Niedźwiecki and M. Ciolek, “On Noncausal Identification of Nonstationary Multivariate Autoregressive Processes,” *IEEE Trans. Signal Process.*, vol. 67, no. 3, pp. 769–782, Feb. 2019, doi: 10.1109/TSP.2018.2885480.
- [23] “Controller State Estimation - MATLAB & Simulink.”
<https://www.mathworks.com/help/mpc/ug/controller-state-estimation.html#bujxvp9-51>
(accessed Apr. 22, 2021).
- [24] “Specify Constraints - MATLAB & Simulink.”
<https://www.mathworks.com/help/mpc/ug/specifying-constraints.html> (accessed Apr. 21, 2021).
- [25] C. Schmid and L. T. Biegler, “Quadratic programming methods for reduced hessian SQP,” *Comput. Chem. Eng.*, vol. 18, no. 9, pp. 817–832, 1994.
- [26] B. Zhang, C. Dou, D. Yue, Z. Zhang, and T. Zhang, “A Cyber-Physical Cooperative Hierarchical Control Strategy for Islanded Microgrid Facing With Random Communication Failure,” *IEEE Syst. J.*, vol. 14, no. 2, pp. 2849–2860, Jun. 2020, doi: 10.1109/JSYST.2019.2956774.
- [27] Y. Xu and H. Sun, “Distributed Finite-Time Convergence Control of an Islanded Low-Voltage AC Microgrid,” *IEEE Trans. Power Syst.*, vol. 33, no. 3, pp. 2339–2348, May 2018, doi: 10.1109/TPWRS.2017.2743011.
- [28] H. Yan, X. Zhou, H. Zhang, F. Yang, and Z. Wu, “A Novel Sliding Mode Estimation for Microgrid Control With Communication Time Delays,” *IEEE Trans. Smart Grid*, vol. 10, no. 2, pp. 1509–1520, Mar. 2019, doi: 10.1109/TSG.2017.2771493.

Chapter 9

Conclusions and Future Work

9.1 Summary and Conclusions

In this research, advanced control schemes for grid-connected wind power plants and model predictive control-based controller for DG control in islanded microgrids are investigated. The following summarizes the work that has been done in this thesis.

For developing control techniques for WPPs, two regression models have been developed through surface fitting using MATLAB curve fitting toolbox: one model based on simulation data is to determine the required reactive power for grid voltage compensation; another model based on field measurement data is to determine reactive power characteristics of the WPP. A central control architecture to control the dispatch of reactive power during over-, under-, and normal-voltage conditions has been developed. The effectiveness of the developed two regression models and the central WPP control architecture has been validated through MATLAB/Simulink simulations. A capacitor bank controller that regulates the switching of capacitor banks and ensures optimum switching has been developed.

Moreover, an analytical model for the maximum reactive power capability curve at the plant-level of DFIG-based WPPs has been developed considering several constraint variables at DFIGs and the plant-level. The reactive power capability curve for individual DFIGs is derived, considering the effect of stator currents, rotor currents, rotor voltages, winding factors, magnetic saturation, and losses associated with converter switches. The plant level reactive power capability curve has been developed considering the wake effect and distribution feeder losses.

Finally, using the developed maximum reactive power capability model, an adaptive droop coefficient-based WPP controller is developed. The controller consists of a central WPP controller and a local WTG controller. Both controllers operate in voltage control mode. An updated droop coefficient estimation model considering the depth of voltage deviations and the range of reactive power capability is proposed. A GSC controller is developed to utilize the reactive power capability of GSC. The proposed WPP controller can extract more reactive power and maximize WPP's contribution to the voltage compensation action.

A new methodology to control distributed generation units in an islanded microgrid is proposed. The model inputs are direct- and quadrature-axis components of the control signal, and the model outputs are deviations of the voltage and frequency from their nominal values at the PCC. The model is parameterized through data-driven approach using nonlinear least-square optimization. Due to the flexibility in formulating the system and noise model, the polynomial Box-Jenkins model is chosen as the model structure. To initialize the iteration for nonlinear least square, the Backcast technique is chosen by comparing with Zero and Estimate techniques. Four NLS optimization algorithms, where two are line search-based (Gauss-Newton (GN), and Adaptive Gauss-Newton (AGN)), and two are trust region-based (Levenberg-Marquardt (LM), and Trust Region Reflective (TRR)) are studied to get the optimum model coefficients. GN shows consistent and superior performance over the others and is chosen as the suitable optimization technique. Two optimization methodologies for the chosen GN method are evaluated: "simulation" focus and "prediction" focus. The prediction focus shows much better performance, such as a high prediction accuracy and faster convergence; it also avoids the necessity of data prefiltering by introducing a built-in weighted filter in the objective function.

Finally, to regulate the voltage and frequency at the PCC in an islanded microgrid, a model predictive control-based DG controller is developed. The controller adopts the developed data-driven DG control algorithm. The control algorithm executes simultaneous control of P - f / Q - V and P - V / Q - f by considering both resistance and reactance of distribution lines. As a result, the proposed controller can completely compensate the voltage and frequency deviation and ensure accurate power sharing among DGs without the secondary controller and virtual impedance loop.

9.2 Major Contributions of the Research Work

Major Contributions of the research work are summarized below.

Part 1:

1. Developed a WPP controller that could extract the maximum amount of reactive power from a DFIG-based WPP.
2. Developed the maximum reactive power capability model for an individual WTG and the whole WPP plant using a wide range of practical and influential parameters.
3. Developed a steady-state reactive power capability model of a DFIG-based WPP using SCADA measurement data.

Part 2:

2. Developed a novel DG control algorithm to regulate the voltage and frequency at the PCC of an islanded microgrid. The algorithm's inputs are direct(d)- and quadrature(q)- axis components of the control signal and outputs are deviations of the voltage and frequency at the PCC. The control algorithm considers both resistance and reactance of the distribution lines and their subsequent impacts in between input and output parameters.
3. Developed a model predictive control (MPC)-based DG controller. The controller ensures the complete restoration of the voltage and frequency, and accurate sharing of active and

reactive power among DGs without using a secondary controller, a virtual impedance loop and DG-to-DG communication networks.

9.3 Future Work

The following are future work that can be conducted:

- The proposed WPP controller can be further developed into a fully distributed controller. This way, the central controller can be removed and the WPP can be controlled by the local controller in a cooperative distributed manner. As a result, the controller response time can be reduced substantially.
- The proposed WPP controller can be further modified to handle unbalance voltage conditions.
- The developed microgrid controller can be re-coded to make it compatible for GPU along with parallel computing, which will increase the execution speed and enhance the controller redundancy.
- The proposed microgrid controller can be further developed to facilitate plug and play capabilities.
- The steady state Kalman filter based state observer can be improved using an extended Kalman filter. It will increase the state observer competency to capture the state transitions more accurately.
- An adaptive model predictive control-based DG controller can be developed. It will increase the controller competency to withstand a wider operating range and various microgrid configurations.
- DG's instantaneous capacity can be added into the control algorithm. This will ensure more accurate power sharing among DGs.

List of Publications (Since Fall 2017)

Refereed Journal Papers (published or submitted) Since Fall 2017:

- [1] **Md Nasmus Sakib Khan Shabbir**, Xiaodong Liang, and Saikat Chakrabarti, "An ANOVA-Based Fault Diagnosis Approach for Variable Frequency Drive-Fed Induction Motors," *IEEE Transactions on Energy Conversion*, vol. 36, no. 1, pp. 500-512, March 2021.
- [2] Xiaodong Liang, Chowdhury Andalib-Bin-Karim, Weixing Li, Massimo Mitolo, and **Md Nasmus Sakib Khan Shabbir**, "Adaptive Virtual Impedance-Based Reactive Power Sharing in Virtual Synchronous Generator Controlled Microgrids," *IEEE Transactions on Industry Applications*, vol. 57, no. 1, pp. 46-60, Jan.-Feb. 2021.
- [3] Mohammad Zawad Ali, **Md Nasmus Sakib Khan Shabbir**, Shafi Md Kawsar Zaman, and Xiaodong Liang, "Single- and Multi-Fault Diagnosis Using Machine Learning for Variable Frequency Drive-Fed Induction Motors", *IEEE Transactions on Industry Applications*, vol. 56, no. 3, pp. 2324-2337, May-June 2020.
- [4] Xiaodong Liang, **Md Nasmus Sakib Khan Shabbir**, Nahidul Khan, and Xiaodi Yan, "Measurement-Based Characteristic Curves for Voltage Stability and Control at Point of Interconnection of Wind Power Plants", *IEEE Canadian Journal of Electrical and Computer Engineering*, vol. 42, no. 3, pp. 163-172, Summer 2019.
- [5] **Md Nasmus Sakib Khan Shabbir**, Xiaodong Liang, Weixing Li, Nahidul Khan, and Anh Minh Le, "A Novel Data-Driven Voltage Control Approach for Grid-Connected Wind Power Plants", *IEEE Transactions on Industry Applications*, vol. 55, no. 4, pp. 3376-3393, July-August 2019.

- [6] Mohammad Zawad Ali, **Md Nasmus Sakib Khan Shabbir**, Xiaodong Liang, Yu Zhang, and Ting Hu, "Machine Learning based Fault Diagnosis for Single- and Multi-Faults in Induction Motors Using Measured Stator Currents and Vibration Signals", *IEEE Transactions on Industry Applications*, vol. 55, no. 3, pp. 2378-2391, May-June 2019.
- [7] **Md Nasmus Sakib Khan Shabbir**, Muhammad Sifatul Alam Chowdhury, and Xiaodong Liang, "A Guideline of Feasibility Analysis and Design for Concentrated Solar Power Plants", *IEEE Canadian Journal of Electrical and Computer Engineering*, vol. 41, no. 4, pp. 203 - 217, Fall 2018.
- [8] **Md Nasmus Sakib Khan Shabbir**, Mohammad Zawad Ali, Xiaodong Liang, and Muhammad Sifatul Alam Chowdhury, "A Probabilistic Approach Considering Contingency Parameters for Peak Load Demand Forecasting", *IEEE Canadian Journal of Electrical and Computer Engineering*, vol. 41, no. 4, pp. 224 - 233, Fall 2018.
- [9] **Md Nasmus Sakib Khan Shabbir**, Xiaodong Liang, Weixing Li, and Syed Imtiaz, "A Novel Design of Model Predictive Control-Based Distributed Generation Controller in Islanded Microgrids", to be submitted.
- [10] **Md Nasmus Sakib Khan Shabbir**, Xiaodong Liang, Weixing Li, and Syed Imtiaz, "A Novel Data-Driven Predictive Model for Distributed Generation Control in Islanded Microgrid", to be submitted.
- [11] **Md Nasmus Sakib Khan Shabbir**, Xiaodong Liang, Weixing Li, and Syed Imtiaz, "A Novel Data Driven Distributed Generation Control Algorithm for Islanded Microgrids: Development and Parameterization", to be submitted.

- [12] **Md Nasmus Sakib Khan Shabbir**, Xiaodong Liang, and Saikat Chakrabarti, "An Adaptive Droop Coefficient Based Wind Power Plant Voltage Control Approach Through Enhanced Reactive Power Support", to be submitted.

Referred Conference Papers Since Fall 2017

- [13] **Md Nasmus Sakib Khan Shabbir**, Xiaodong Liang, Weixing Li and Nahidul Khan, "Analytical Approach-Based Reactive Power Capability Curve for DFIG Wind Power Plants," *2020 IEEE Industry Applications Society Annual Meeting*, 2020, pp. 1-9,
- [14] **Md Nasmus Sakib Khan Shabbir**, and Xiaodong Liang, "A DFFT and Coherence Analysis-Based Fault Diagnosis Approach for Induction Motors Fed by Variable Frequency Drives," *33rd Canadian Conference on Electrical and Computer Engineering (CCECE)*, pp. 1-4, London, Ontario, Canada, April 26-29, 2020.
- [15] Chowdhury Andalib-Bin-Karim, Xiaodong Liang, Weixing Li, Massimo Mitolo, and **Md Nasmus Sakib Khan Shabbir**, "Improving Reactive Power Sharing in Microgrids by Adaptive Virtual Impedance Approach," *56th IEEE Industrial and Commercial Power System (I&CPS) Technical Conference*, Las Vegas, Nevada, United States, April 27-30, 2020.
- [16] Mohammad Zawad Ali, **Md Nasmus Sakib Khan Shabbir**, Shafi Md Kawsar Zaman, and Xiaodong Liang, "Machine Learning Based Fault Diagnosis for Single- and Multi-Faults for Induction Motors Fed by Variable Frequency Drives", *54th IEEE Industry Applications Society (IAS) Annual Meeting*, Baltimore, Maryland, United States, September 29th - October 3rd, 2019.

- [17] Yu Zhang, Ting Hu, Xiaodong Liang, Mohammad Zawad Ali, and **Md Nasmus Sakib Khan Shabbir**, "Fault Detection and Classification for Induction Motors using Genetic Programming", 22nd European Conference on Genetic Programming (EuroGP), Leipzig, Germany, 24-26 April, 2019.
- [18] Mohammad Zawad Ali, **Md Nasmus Sakib Khan Shabbir**, Xiaodong Liang, Yu Zhang, and Ting Hu, "Experimental Investigation of Machine Learning Based Fault Diagnosis for Induction Motors", Proceedings of 2018 IEEE Industry Applications Society (IAS) Annual Meeting, pp. 1-14, Portland, OR, USA, September 23 - 27, 2018.
- [19] **Md Nasmus Sakib Khan Shabbir**, Xiaodong Liang, Weixing Li, Anh Minh Le, and Nahidul Khan, "A Data-Driven Voltage Control Approach for Grid-Connected Wind Power Plants", Proceedings of 2018 IEEE Industry Applications Society (IAS) Annual Meeting, pp. 1-14, Portland, OR, USA, September 23 - 27, 2018.
- [20] **Md Nasmus Sakib Khan Shabbir**, Mohammad Zawad Ali, Muhammad Sifatul Alam Chowdhury, and Xiaodong Liang, "A Probabilistic Approach for Peak Load Demand Forecasting", Proceedings of the 31st Annual IEEE Canadian Conference on Electrical and Computer Engineering (CCECE 2018), pp. 1-4, Québec City, Québec, Canada, May 13-16, 2018.
- [21] **Md Nasmus Sakib Khan Shabbir**, and Xiaodong Liang, "Feasibility Analysis and Design of a Concentrated Solar Power Plant", Proceedings of the 31st Annual IEEE Canadian Conference on Electrical and Computer Engineering (CCECE 2018), pp. 1-4, Québec City, Québec, Canada, May 13-16, 2018.

- [22] Mohammad Zawad Ali, **Md Nasmus Sakib Khan Shabbir**, Muhammad Sifatul Alam Chowdhury, Arko Ghosh, and Xiaodong Liang, "Regression Models of Critical Parameters Affecting Peak Load Demand Forecasting", Proceedings of the 31st Annual IEEE Canadian Conference on Electrical and Computer Engineering (CCECE 2018), pp. 1-4, Québec City, Québec, Canada, May 13-16, 2018.

Non-Refereed Conference Papers Since Fall 2017

- [23] **MD Nasmus Sakib Khan Shabbir**, and Xiaodong Liang, "A Soft-switching Charging System Design for Electric Vehicles", 2018 Annual IEEE Newfoundland Electrical and Computer Engineering Conference (NECEC), pp. 1-5, St. John's, Canada, November 2018.
- [24] **Md Nasmus Sakib Khan Shabbir**, and Xiaodong Liang, "Feasibility Analysis and Design of a Parabolic Trough CSP Power Plant in Bangladesh", 2017 Annual IEEE Newfoundland Electrical and Computer Engineering Conference (NECEC), pp. 1-5, St. John's, Canada, November 2017.